KATHOLIEKE UNIVERSITEIT LEUVEN
FACULTEIT INGENIEURSWETENSCHAPPEN
DEPARTEMENT WERKTUIGKUNDE
AFDELING TOEGEPASTE MECHANICA
EN ENERGIECONVERSIE
Celestijnenlaan 300A - B-3001 Leuven (Heverlee) - België

SELECTIVE COOLING OF ELECTRONICS USING ELECTROSTATICALLY ACTUATED LIQUID DROPLETS

Promotoren :
Prof. dr. ir. M. Baelmans
Prof. dr. G. Borghs

Proefschrift voorgedragen tot
het behalen van het doctoraat
in de ingenieurswetenschappen

door

Ir. Herman Oprins

Augustus 2010

In samenwerking met

imec

Kapeldreef 75
B-3001 Leuven (Heverlee) - België

KATHOLIEKE UNIVERSITEIT LEUVEN
FACULTEIT INGENIEURSWETENSCHAPPEN
DEPARTEMENT WERKTUIGKUNDE
AFDELING TOEGEPASTE MECHANICA
EN ENERGIECONVERSIE
Celestijnenlaan 300A - B-3001 Leuven (Heverlee) - België

SELECTIVE COOLING OF ELECTRONICS USING ELECTROSTATICALLY ACTUATED LIQUID DROPLETS

Jury :
Prof. dr. ir. P. Moldenaers, voorzitter
Prof. dr. ir. M. Baelmans, promotor
Prof. dr. G. Borghs, promotor
Prof. Dr.-Ing. habil. Dr. h.c. K. Hameyer (RWTH Aachen)
Prof. dr. ir. E. Van den Bulck
Prof. dr. F.G. Mugele (Universiteit Twente)
Dr. ir. E. Beyne (IMEC)
Prof. dr. ir. J. Driesen
Prof. dr. I. De Wolf

Proefschrift voorgedragen tot
het behalen van het doctoraat
in de ingenieurswetenschappen

door

Ir. Herman Oprins

Wet. Depot : D/2010/7515/77
ISBN 978-94-6018-238-9

Augustus 2010

In samenwerking met

imec

Kapeldreef 75
B-3001 Leuven (Heverlee) - België

ISBN 978-94-6018-238-9
D/2010/7515/77

Voorwoord

Het einde van dit doctoraatsonderzoek is het ideale moment om even stil te staan bij alle hulp die ik gekregen heb en om iedereen te bedanken die heeft bijgedragen om dit multidisciplinaire onderzoek tot een goed einde te brengen.

In de eerste plaats wil ik mijn promotor, prof. Tine Baelmans bedanken voor de kans die ze mij geboden heeft om dit boeiende onderzoek te kunnen uitvoeren. Het eindwerk van de ingenieursopleiding in haar onderzoeksgroep, was een eerste kennismaking met metingen en modellering van thermische fenomenen. In dit doctoraatsonderzoek in samenwerking met IMEC, kreeg ik de mogelijkheid om deze kennis toe te passen en verder te ontwikkelen in de wondere wereld van de elektronica en chip verpakkingen. Tine, bedankt voor de hulp en discussies, suggesties en ideeën om me weer op weg te helpen wanneer ik vast zat. Verder wil prof. Gustaaf Borghs bedanken om als co-promotor dit doctoraatswerk te begeleiden.

Prof. Eric Van den Bulck en prof. Kay Hameyer wil ik bedanken om als assessoren deel uit te maken van mijn begeleidingscommissie en het doctoraatswerk op te volgen. Ook de andere leden van de examencommissie, dr. Eric Beyne, prof. Frieder Mugele, prof. Johan Driesen en prof. Ingrid De Wolf wil ik bedanken voor de interesse, het kritisch nalezen van mijn doctoraatstekst en de interessante discussies tijdens de preliminaire verdediging. Door hun opmerkingen en suggesties vanuit hun respectievelijke specialisatie is de kwaliteit van dit manuscript sterk verbeterd. Prof. Paula Moldenaers bedank ik voor het opnemen van de taak van voorzitter van de examencommissie.

Verder wens ik dr. Bart Vandevelde te bedanken voor de dagelijkse begeleiding en vooral zijn blijvende steun bij de moeilijkere momenten van dit onderzoek. Verder apprecieer ik de kans die ik gekregen heb van hem om mee te mogen werken aan onderzoeksprojecten buiten het doctoraat. Dit vormde voor mij een grote meerwaarde in mijn ontwikkeling, niet alleen op technisch-wetenschappelijk vlak maar ook op project-technisch gebied.

Ik wil ook het Agentschap voor Innovatie door Wetenschap en Technologie in Vlaanderen (IWT-Vlaanderen) bedanken dat mij door middel van een specialisatiebeurs 4 jaar financieel gesteund heeft.

Vervolgens wens ik vele mensen te bedanken die in min of meerdere mate een bijdrage hebben geleverd tot dit werk. Evelien, Dominiek en Mario wil ik bedanken voor de hulp met de eindige elementen simulaties. De voormalige thesisstudenten Geert Van der Veken, Johan Danneels en Brecht Van Ham wil ik bedanken voor hun goede prestaties tijdens hun eindwerk, wat tot een belangrijke bijdrage in dit werk leidde. I would like to thank Benjamin Jones (Purdue University), for the development of the fixture for the droplet sliding experiments during his internship in IMEC. Vervolgens wil ik volgende mensen danken: Jens Rip voor hulp met contacthoekmetingen, Josine Loo voor hulp bij aanbreng van de hydrofobe coatings, Myriam en Veerle voor de sample preparatie en ruwheidsmetingen, Christophe Winters voor het ontwerp van de testborden en Marion voor de administratieve hulp. Furthermore, I would like to thank Jean-Christophe Baret for the

interesting discussions on the liquid filament flow in microchannels, Alicia Linde Sanchez for providing super-hydrophobic surfaces and Paolo Fiorini, Joeri De Vos and Brivragh Majeed for the development of the processing of the droplet cooler.

Tijdens een doctoraat moet er niet alleen hard gewerkt worden maar moet er ook tijd gemaakt worden voor ontspanning. I would like to thank Dominiek, Paresh, Nele, Chukwudi, Yu, Melina and Konstantza for the nice time in the office. There was always time for a chat and a laugh, even late at night or in the weekends. Ook alle collega's van REMO en TME hebben met een aangename samenwerking bijgedragen tot een toffe doctoraatstijd. Daarnaast waren er Tomas, Nele, Evelien, Dominiek, Mario, Christophe, Riet, Steven, Xavier, Xiao en Aitor die voor vele leuke momenten zorgden tijdens de koffie- en middagpauzes en de activiteiten buiten de werkuren. Verder wil ik ook mijn vrienden bedanken voor de broodnodige ontspanning in de weekends. Daarbij denk ik vooral aan Peter en Frederik voor de reizen die we samen hebben ondernomen. Dat zorgde ervoor dat de batterijen weer opgeladen waren en we er weer tegen aan konden gaan.

Mijn familie wil ik bedanken voor hun steun en bemoedigende woorden wanneer het wat tegenzat: Annemie, Frederik en Michel dank ik voor hen steun, hulp en interesse en mijn petekindje Brecht voor zijn lieve motiverende lach. In het bijzonder bedank ik mijn ouders voor alle kansen en steun die ze mij gegeven hebben en nog altijd volop geven. Ze staan altijd klaar om mij met raad en daad bij te staan.

Tenslotte wil ik Els bedanken voor de liefde, steun en warmte die ze me de laatste jaren heeft gegeven. Ook ben ik haar dankbaar voor het vele geduld dat ze heeft gehad tijdens de lange eenzame avonden en weekenden toen ik bezig was met het schrijven van deze thesis. Haar steun en hulp waren heel belangrijk voor mij om het schrijven van deze tekst tot een goed einde te brengen.

Heverlee, Herman Oprins
Augustus 2010

Abstract

The continuous miniaturisation and increase in component integration lead to a continuing increase in power dissipation of electronic components. Furthermore, the increase in functionality and integration of components lead to strong non-uniform power dissipation. Therefore, there is a need for the development of new cooling techniques, capable of cooling this ever increasing heat fluxes and capable to efficiently deal with hot spots. In this work, a novel cooling technique based on electrostatically actuated liquid droplets is presented. In this system, individual liquid droplets are transported over an array of electrodes. The major advantages of this system over conventional cooling systems are the ability for selective cooling of hot spots and the low power consumption.

The main objective of this PhD study is to develop a modelling framework to characterise the droplet motion in a droplet based cooling system and to assess the cooling performance of this system. This methodology can be applied to optimise the system parameters to maximise the flow rate and the thermal performance.

In this work, a decoupled modelling approach is presented to assess the droplet behaviour. This approach consists of three parts:

1. Electrical analysis: this part describes the electrostatic force acting on a droplet for an applied voltage at the electrode.
2. Mechanical analysis: in this part the macroscopic droplet motion is predicted, based on the forces acting on the droplet.
3. Thermal analysis: this part describes the internal flow and heat transfer and provides an estimate for the thermal performance of an integrated droplet based cooling system.

Throughout the work, the methodology has been applied to two electrode configuration systems: (1) a planar parallel plate electrode system and (2) an annular electrode system.

First, the droplet deformation under a symmetric electric field has been studied experimentally, both on a flat surface as well as on a rough surface. For the droplet on a flat surface, the relation between the contact angle and the applied voltage was studied. The rough surface is mimicked by 100 x 100 μm^2 microchannels. For a droplet on these structures, a morphological transition between two meta-stable states occurs when a voltage is applied. Theoretical transition criteria, derived from energy considerations, correspond well to the experimental contact angle data before and after the transition. Furthermore, a general metrology has been developed to calculate the electrostatic actuation force based on the results of 2D and 3D electrostatic finite element simulations. Formulations for the actuation force are derived both from a force approach (method of Maxwell stresses) as well as an energy approach (method of virtual work). For both electrode configuration systems, parameter studies have been performed to assess the impact of material properties and geometrical parameters on the actuation force. The parameterised finite element models allow optimising these parameters to achieve a maximal actuation force for a given voltage.

When an external force is applied on a droplet, this force needs to be sufficiently high to overcome a threshold force in order to move the droplet. This threshold force is caused by the contact angle hysteresis. This force has been studied experimentally by performing

contact angle measurements during the droplet deformation and motion in tilt tests. For both sessile and confined droplets sliding on hydrophobic surfaces, empirical correlations have been derived for this retentive force.

A general methodology for the dynamic modelling of the macroscopic electro-actuated droplet motion has been presented. This model uses the results of the electrostatic force calculation and the experimental results of the static and dynamic contact line friction force as input to predict the droplet motion. The dynamic model has been used to study the droplet response to the application of a voltage at a single electrode and an array of consecutive electrodes. Using this dynamic model, a robust switching profile design of voltage and frequency can be derived to ensure a continuous droplet motion through the channel. Finally, the methodology has been successfully validated for the planar electrode system using experimental data on average droplet velocities from literature.

Detailed numerical flow calculations have been performed to study the flow patterns and heat transfer inside a moving droplet between two parallel plates. It is shown that the internal droplet flow exhibits a parabolic characteristic and that the flow pattern consists of two separate convection cells. The presence of these two convection cells decreases the heat transfer to the lower part of the droplet, thereby limiting the overall heat transfer from the heat source to the droplet. A typical enhancement of the heat transfer with a factor 2 is achieved with respect to the minimal value that would be obtained assuming heat conduction in the liquid only. Further, an analytic lumped model based on the steady state detailed simulations has been presented to estimate the transient average droplet temperature with an accuracy of 5% compared to the full transient CFD modelling.

Finally, the thermal performance of two droplet based cooling systems has been assessed. In the first system, the thermal enhancement of electrowetting assisted pulsating flow in microchannels is assessed. A theoretical study, based on experimental filling data of the heat transfer reveals that this implementation can induce an enhancement in cooling capacity of 55%. Based on the transient lumped model, it has been shown that the cooling performance of the droplet based cooling system with planar horizontal electrodes, is in the order of several W to a few tens of W, while the power consumption only amounts to several μW.

The low energy consumption and the flexibility for reconfigurable hot spot cooling, make the droplet based cooling system an attractive cooling option. The cooling performance is in the range of several to tens of W/cm², while the power consumption is only in the order of μW. Therefore, the targeted applications are low to medium power systems with highly non-uniform power dissipation.

Korte samenvatting

De doorgedreven miniaturisatie en stijging van het aantal componenten in geïntegreerde schakelingen leiden tot een toename van de vermogensdissipatie van elektrische componenten. Bovendien leidt de toename in functionaliteit en integratie tot een niet-uniforme warmteverdeling. Daardoor is er nood aan de ontwikkeling van nieuwe koelsystemen, die deze hoge warmteproductie en niet-uniforme verdeling efficiënt kunnen koelen. In dit doctoraatswerk is een nieuwe koeltechniek, gebaseerd op elektrostatisch aangedreven vloeistofdruppeltjes onderzocht. In dit koelsysteem worden de druppels getransporteerd over een matrix van elektroden. De belangrijkste voordelen van dit koelsysteem zijn het lage energiegebruik en de mogelijkheid om hot spots selectief te koelen.

De voornaamste doelstelling van dit doctoraatsonderzoek is de ontwikkeling van een modelleringsomgeving om de druppelstroom en het koelvermogen te karakteriseren. Deze methodologie kan dan toegepast worden om de systeemparameters te optimaliseren voor een maximaal debiet of een maximale koelcapaciteit.

In dit doctoraatsonderzoek is er een ontkoppelde modelleringsmethodologie voorgesteld om het druppelgedrag te onderzoeken. Deze ontkoppelde aanpak bestaat uit drie delen:

1. elektrische analyse: dit deel beschrijft de elektrostatische aantrekkingskracht op de druppel als functie van een aangelegde spanning aan de elektrode.
2. mechanische analyse: in dit deel wordt de macroscopische druppelbeweging voorspeld aan de hand van de krachten die op de druppel inwerken.
3. thermische analyse: dit deel beschrijft de interne stroming en warmteoverdracht in een druppel en maakt een schatting van het koelvermogen van een koelsysteem gebaseerd op elektrostatisch aangedreven vloeistofdruppeltjes.

Doorheen de doctoraatsthesis wordt de methodologie toegepast op twee verschillende systemen: (1) een systeem met evenwijdige vlakke elektrodes en (2) een systeem met ringvormige elektrodes.

Eerst is de druppelvervorming onder invloed van een symmetrisch aangelegd uitwendig elektrisch veld experimenteel bepaald voor vlakke en ruwe oppervlakken. Voor de vlakke oppervlakken is de relatie tussen de contacthoek en de aangelegde spanning bestudeerd. De ruwe oppervlakken worden nagebootst door microkanalen met een grootte van 100 µm x 100 µm. Bij het aanleggen van een spanning aan een druppel op dergelijke structuren, wordt er een morfologische overgang tussen twee meta-stabiele toestanden waargenomen. Theoretische voorspellingen hiervoor, gebaseerd op energiebeschouwingen, komen goed overeen met de opgemeten waarden voor en na de overgang. Verder is er een algemene methodologie ontwikkeld om de elektrische kracht te bepalen op basis van resultaten van 2D en 3D eindige-elementen simulaties. Formuleringen voor deze kracht zijn zowel afgeleid op basis van een kracht-methode als van een energie-methode. Voor beide druppelsystemen zijn parameterstudies uitgevoerd om de invloed ervan op de kracht te onderzoeken. Op deze manier kunnen de systeemparameters geoptimaliseerd worden om een maximale kracht te verkrijgen.

Om een druppel te bewegen moet de aangelegde kracht groot genoeg zijn om een drempelkracht, veroorzaakt door de hysteresis van de contacthoeken, te overwinnen. Deze drempelkracht is experimenteel onderzocht met behulp van contacthoekmetingen tijdens het vervormen en bewegen van de druppel op een hellend oppervlak. Op deze manier zijn er correlaties voor deze drempelkracht afgeleid, voor zowel druppels op een vrij oppervlak als voor druppels tussen twee parallelle oppervlakken.

Voor de dynamische modellering van de elektrostatisch geactueerde druppelbeweging, is een algemene methodologie voorgesteld. Hiermee wordt de macroscopische druppel-beweging voorspeld aan de hand van de krachten die op de druppel inwerken. Voor de elektrostatische actuatiekracht worden de simulatieresultaten gebruikt en voor de beschrijving van de drempelkracht, de afgeleide correlaties. Met dit model is de druppelreactie bij het aanleggen van een spanning aan een enkele elektrode of een rij van opeenvolgende elektrodes onderzocht. Dit model laat toe een robuust ontwerp te maken van het schakelschema van de spanningen en de frequentie waarmee ze aan de elektroden worden aangelegd. Tenslotte is dit dynamische model gevalideerd met behulp van experimentele data over druppelsnelheden, beschikbaar in de literatuur.

Om de inwendige stroming en warmteoverdracht in een druppel tussen twee parallelle platen te onderzoeken, zijn gedetailleerde numerieke 2D stromingssimulaties uitgevoerd. De simulaties tonen aan dat de interne stroming opgedeeld is in twee circulatiezones. Deze zones beperken de warmteoverdrachtsverbetering die bekomen kan worden door de snelheidstoename van de druppel. Voor een snelheid van 10 cm/s, is een typische verdubbeling van de warmteoverdracht met een factor twee gevonden, vergeleken met een stilstaande druppel waar de warmtestroom enkel op geleiding gebaseerd is. Verder is er een vereenvoudigd analytisch 4 cellen model voorgesteld dat gebaseerd is op de simulaties in regimetoestand. Dit model laat toe de transiënte gemiddelde druppeltemperatuur te bepalen met een nauwkeurigheid van 5% ten opzicht van de gedetailleerde numerieke transiënte simulaties, maar met een veel kortere berekeningstijd.

Tenslotte is het koelvermogen van twee concepten, gebaseerd op de elektrostatisch aangedreven vloeistofdruppels, theoretisch onderzocht. Het eerste concept gebruikt de elektrische actuatie om een pulserende vloeistofstroming in microkanalen te genereren om zo de thermische spreiding te verbeteren. Een theoretische studie, gebaseerd op experimentele gegevens van de vulling van de microkanalen, geeft aan dat een warmteoverdrachtsverbetering van 55% mogelijk is voor een goed gekozen frequentie. Voor de druppelstroming tussen twee parallelle platen is er met behulp van het transiënte 4 cellen model aangetoond dat een koelcapaciteit in de orde van enkele W tot enkele tientallen W kan gehaald worden. Het hiervoor noodzakelijke energieverbruik bedraagt slechts enkele μW.

Het lage energieverbruik en de mogelijkheid tot herconfigureerbare hot spot koeling maken van het voorgestelde druppelgebaseerde koelsysteem een aantrekkelijke koeloplossing. Het koelvermogen van deze techniek bedraagt enkele tot enkele tientallen W/cm², terwijl het energieverbruik slechts in de grootteorde van μW ligt. Deze koeltechniek is daardoor uitermate geschikt om toepassingen, met een laag tot gemiddeld koelvermogen en een sterke niet-uniforme warmteverdeling, te koelen.

List of Symbols

Symbol	Description	Units
a	Acceleration	m s^{-2}
A	Area	m²
A_{ij}	Contact area between the cell i and j	m²
C	Capacitance	F
c_p	Specific thermal capacity	J kg^{-1} K^{-1}
d	Depth	m
d_{ij}	Characteristic distance between cell i and j	m
d	Distance	m
D	Diameter	m
D_h	Hydraulic diameter	m
D	Electric displacement	C m^{-2}
E	Electric field	V m^{-1}
E	Energy	J
F	Force	N
F_{CL}	Contact line force	N
F_D	Drag force	N
F_{el}	Electrostatic force	N
F_W	Friction Force	N
f	Frequency	Hz
g	Gravitational constant	m s^{-2}
g_e	Gap between control electrodes	m
h	Heat transfer coefficient	W m^{-2} K^{-1}
h	Specific enthalpy	J kg^{-1}
H	Droplet height	m
I	Current	A
k	Thermal conductivity	W m^{-1} K^{-1}
L	Filling length	m
$\dot{m}_i$	Mass flow rate in cell i	kg s^{-1}
M	Droplet mass	kg
P	Perimeter	m
P	Power	W
P_{hydr}	Hydrostatic pressure	Pa
P_{in}	Internal pressure	Pa
P_{amb}	Ambient pressure	Pa
P_γ	Pressure due to the surface tension	Pa
Q	Heat flow	W
R	Electrical resistance	Ohm
R	Thermal resistance	K W^{-1}
R	Radius	m
Ra	Average roughness	m
$Res_{tot,con}$	Residual for the continuity equation	kg s^{-1}

$Res_{tot,en}$	Residual for the energy equation	J s^{-1}
$Res_{tot,mom}$	Residual for the momentum equation	kg m s^{-1}
t	Thickness	m
t	Maxwell stress tensor	N m^{-2}
T	Temperature	K
u	Streamwise fluid velocity	m s^{-1}
U_{av}	Average droplet velocity	m s^{-1}
V	Voltage	V
Vol	Droplet volume	m²
W	Energy	J
$\dot{W}$	Power	W
w_e	Width of an electrode	m
x	Position	m

Greek symbols

Symbol	Description	Units
α	Tilt angle	rad
α_c	Critical tilt angle	rad
α	Thermal diffusivity	$m^2 s^{-1}$
ν	Fluid kinematic viscosity	$m^2 s^{-1}$
γ	Surface tension	N m^{-1}
γ_{ls}	Surface tension 'liquid to solid'	N m^{-1}
γ_{lg}	Surface tension 'liquid to gas'	N m^{-1}
γ_{gs}	Surface tension 'gas to solid'	N m^{-1}
ε_d	Discretisation error	
ε_0	Permittivity of vacuum	F m^{-1}
ε_R	Relative permittivity	-
ζ	Coefficient of contact line friction	Pa s
θ_Y *or* θ_0	Young's contact angle	rad
θ_a	Apparent contact angle	rad
θ_A	Advancing contact angle	rad
θ_R	Receding contact angle	rad
κ^0	Equilibrium frequency of random molecular displacements	Hz
λ	Average length of the random molecular displacement	m
μ	Fluid dynamic viscosity	N s m^{-2}
μ_f	Dynamic viscosity of the filler medium	N s m^{-2}
ρ	Density	kg m^{-3}
ρ_f	Charge density	kg m^{-3}
τ	Filling period	s
ϕ	Area fraction (Chapter 2)	-
χ	Droplet filling ratio	-
ω_0	Natural angular frequency	rad/s

Non-dimensional numbers

Symbol	Description
C_D	Drag coefficient
G	Geometrical constant
k	Geometrical constant
N	Number of components
p	Order of the numerical method
r_w	Cassie ratio
r_w	Wenzel ratio
β	Width to length ratio
κ	Non-dimensional droplet radius

Non-dimensional groups

Symbol	Description
Gr	Grashof number
Gr_H	Grashof number based on the droplet height
Nu	Nusselt number $Nu=hD/k$
Nu_H	Nusselt number based on the droplet height $Nu=hH/k$
Pe	Péclet number
Pr	Prandtl number
Ra	Rayleigh number
Ra_H	Rayleigh number based on the droplet
Re	Reynolds number $Re=UD/\nu$
Re_H	Reynolds number based on the droplet height $Re_H=UH/\nu$
$Re_{critical}$	Critical Reynolds number for laminar to turbulent transition

Subscripts

Symbol	Description
A	Advancing
c	Cassie
ch	Channel
el	Electric
fl	Fluid
p	Pump
lv	Liquid-vapour interface
sl	Solid-liquid interface
sv	Solid-vapour interface
R	Receding
w	Wenzel

Table of Contents

Chapter 1

General introduction

Abstract

This chapter provides a general introduction to this PhD thesis. First, the origin of the heat sources in electronics and the need for cooling of the electronic devices is discussed. Further, the general aspects of a cooling system are reviewed. Next, an overview of existing conventional and advanced cooling systems is given. It is shown that the limits of the conventional cooling methods are being reached for several applications and that there is a clear need for the development of advanced high performance cooling techniques to cool next generations of electronic components. In the second part of this chapter, the objectives of this PhD thesis are discussed. A methodology for the assessment of the thermal performance of a droplet based cooling system is presented. The chapter concludes with an overview of the outline of the thesis.

1.1 Introduction to cooling of electronic components

During the operation of electronics, heat is generated. If this heat is not properly removed, excessive temperatures can be reached in the electronic components, which might lead to failures or performance degradation. Driven by miniaturisation and the continuing increase in clock speed and data transfer, power dissipation in electronic components has surpassed the limits for conventional cooling methodologies in many applications. As a result, there is a need for the development of advanced cooling and packaging solutions to remove the generated heat.

1.1.1 Power dissipation in electronic components

Sources of power dissipation

Heat generation is an unavoidable by-product during the operation of electronics. The heat is generated by current flowing through active and passive devices and interconnections. The passive components, where power dissipation occurs, include resistors, capacitors and inductors. The active devices include transistors and integrated circuits. For DC current, the power dissipation P in the passive components and the interconnections can be described as follows :

$$P = I \cdot V = IR^2 \tag{1.1}$$

where I is the current, V is the voltage drop across the device, and R is the resistance. Examples of interconnections where heat can be dissipated, are wire bonds, package pins and metallisation in substrates. The amount of power dissipated by an integrated circuit depends on the type of the technology of the device, the geometry, the frequency and voltage at which it is operated. For bipolar devices, the power dissipation is constant with respect to frequency, while for CMOS devices, the power dissipation scales linearly with the frequency. The power dissipation in CMOS devices consists of three components (Yeh and Chu 2002): (1) the switching power, (2) the dynamic short-circuit power and (3) the DC leakage power. The switching power is caused by the charging and discharging of the capacitance of the transistor gates during the changing of the logic states. This contribution to the power dissipation can be expressed as follows:

$$P = \frac{1}{2} CV^2 \cdot f \cdot N \tag{1.2}$$

where C is the capacitance of a transistor, f is the operation frequency and N is the number of transistors. The dynamic short-circuit power is due to the non-zero rise and fall times. As a result, the transistors are briefly on during a change of logic state. The leakage power is caused by the leakage current. Traditionally, the contribution of the switching power amounts to 70 – 90% of the total power dissipations. However, for smaller technology nodes, the contribution of the leakage power increases rapidly. For sub-100 nm CMOS technologies, leakage power forms a significant component of the total power dissipation.

Trends in power dissipation

The scaling trends in microelectronics have a strong impact on the power dissipation of the electronic components. This scaling is described by Moore's law: the number of transistors doubles every 18 months (Moore 1965). This leads to an exponential increase in the density of solid-state integrated circuits. Decreasing the feature size of the unit transistor has allowed a dramatic improvement of the overall circuit performance and an equally significant reduction of cost per manufactured component. This miniaturisation and continuing increase in clock speed and data transfer, lead to a very strong increase in the power dissipation, both in the total power dissipation as in the power density. The left hand side of Figure 1.1 shows the increase in power density as function of time for several commercial processors. The graph shows that the power density was a major factor to replace the bipolar transistor by CMOS technology, which has a lower inherent power dissipation. The right hand side of Figure 1.1 shows the increase of the power density in CMOS technology for decreasing technology nodes. From this figure, it can be seen that the projections of a continuing scaling will lead to very high power densities. In the near future, no new mature technology is available to allow a technology switch, similar to the bipolar to CMOS transition. Therefore, the innovations to deal with these power dissipation levels must come from the thermal management research.

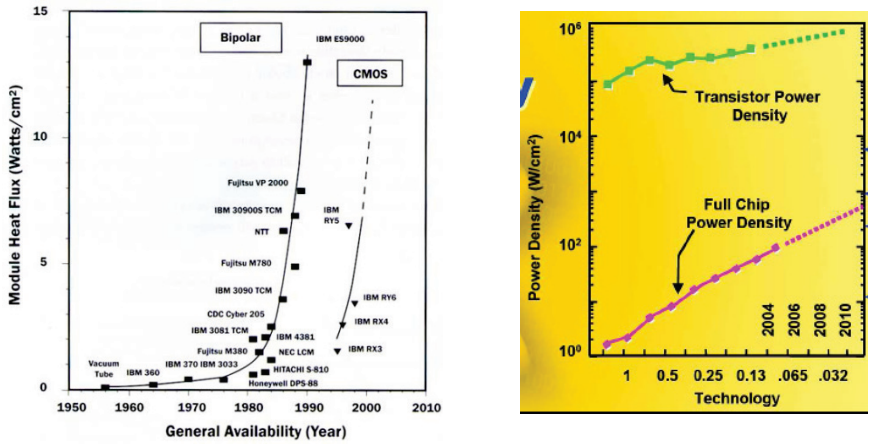

Figure 1.1. Power dissipation trends (Intel): evolution of heat flux over the years (left) and evolution of the power density as function of the technology node (right).

Another thermal challenge is the increasing non-uniformity of the power dissipation due to the increase in integration and functionality on a single component. The effect of localised regions of significantly higher temperatures, referred to as hot spots, is becoming more pronounced as process technology is further scaled down (to 32 nm in the near future) and total power dissipation increases. Hot spots limit the IC's performance, reliability and yield, which are all very sensitive to small changes in temperature. The efficiency of a cooling system is significantly reduced if the power density is not uniformly distributed on the chip. Mahajan *et al.* (2006) introduced the concept of the density factor *DF* to characterise the reduction of the cooling efficiency in the presence of hot spots. The density factor is defined as "*the ratio of the actual package thermal resistance at the hottest spot to the die-area-normalised uniform power resistance or thermal impedance*". Figure 1.2 illustrates

this effect. As the non-uniformity increases, the overall cooling capability of a thermal solution decreases for a constant temperature difference. This effect indicates the need for cooling solutions dedicated to non-uniform heat dissipation to efficiently cool the components.

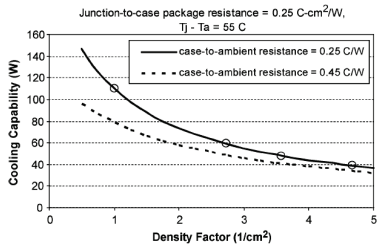

Figure 1.2. Impact of die power non-uniformity on cooling capability: increasing non-uniformity of the power dissipation reduces the cooling capability (Mahajan et al. 2006).

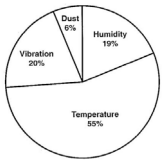

Figure 1.3. Major causes of electronic failure (Yeh and Chu 2002).

1.1.2 Temperature related failures and performance degradation in electronic components

If the heat generating electronic components are not sufficiently cooled, excessive temperatures will be reached. Both performance and reliability of electronic circuits are strongly influenced by temperature. The electrical **performance** is adversely impacted by high temperatures:

- Carrier mobility is degraded at higher temperatures, resulting in slower devices.
- The dissipated power is a function of temperature. In certain conditions, this might lead to thermal runaway and eventual failure of the circuit.
- The interconnect resistivity increases with temperature. This leads to higher voltage drops and longer delays and causes performance degradation.
- Timing uncertainty increases at elevated temperatures.

The temperature related **reliability** concerns are located on three levels: the chip level, the package level, and the system level. Without carefully engineered cooling methods, an increased power density from more ICs means a lower overall reliability. Excessive temperature is considered to be the major cause of electronic failures (Yeh and Chu 2002). Temperature effected reliability problems include electromigration, gate-oxide breakdown, increased leakage power, temperature accelerated failures and thermal stresses due to thermal expansion.

1.1.3 General aspects of cooling systems for electronic components

The main objective of a cooling system, or more general a thermal management system, is to ensure that the maximum temperature in an electronic component remains below a specified limit. If the temperature exceeds this limit, both electrical performance and reliability are not guaranteed, as discussed above. The cooling system moves the heat, generated by the electronic component, from the heat source to the environment using the different means of heat transfer (conduction, convection, radiation). The performance of a cooling system can be expressed as a thermal resistance R (K/W). A low value for the thermal resistance indicates a high thermal performance. The use of a cooling system with a lower overall thermal resistance R, will lead to a lower temperature for the same power dissipation. On the other hand, an electronic system, equipped with a cooling system with a lower overall thermal resistance R, can dissipate more power before reaching the maximum temperature. Three main parts can be distinguished in the system: (1) the chip package, (2) the external heat sink or other cooling system, (3) the interface connection between the different levels of packaging. To optimise the cooling system, each thermal resistance between the heat source and the ambient environment needs to be minimised.

Figure 1.4 gives a schematic representation of a cooling system for both an air cooling and a liquid cooling based system. In a typical example of an air cooling configuration, the chip is flip-chip mounted to a substrate. At the back side, a heat sink, with a much larger surface area is connected to the chip. Between the die and the heat spreader, a thermal interface material (TIM) is introduced to improve the thermal connection. An additional heat spreader can be added between the chip and the heat sink to reduce the effect of the hot spots. The heat removal is a multi-scale process, including both conduction and convection. The heat is generated in the small heat sources in the active region of the die. Next, the heat is spread in the die and heat spreader. As such, the heat is removed by conduction through the die and package to a heat sink, and by convection and radiation to the ambient environment.

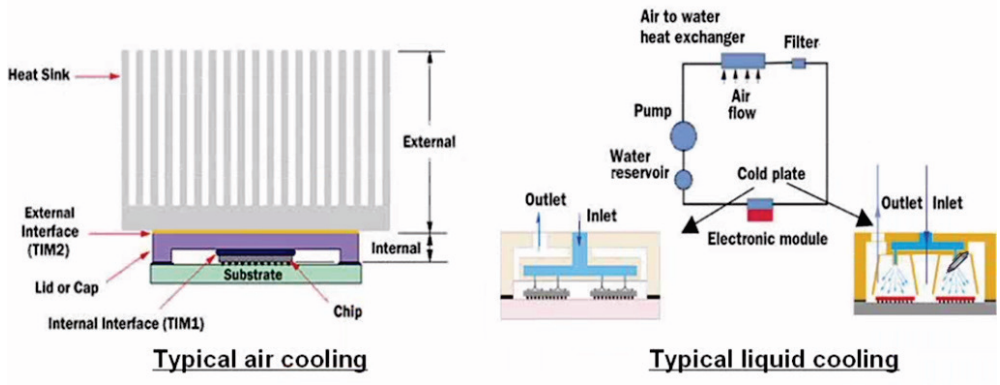

Figure 1.4 Schematic representation of a typical air cooling (left) and liquid cooling system (right) for electronic components (Azar 2003).

A similar heat path exists in the liquid cooling set-up. A primary cooler is attached to the die or package, depending on the level of integration. The heat, generated by the heat sources, reaches the surface of the package by conduction. The package is then cooled with a coolant in the primary cooler. This primary coolant convects the heat to a secondary heat exchanger. In turn, the secondary heat exchanger is cooled by a secondary coolant at a position where more heat transfer area is available. At this heat exchanger, the heat absorbed by the coolant is transferred to the ambient by convection. In the next section, an overview of cooling solutions based on this conductive and convective heat paths are discussed.

An extensive range of cooling solutions for electronic components is currently available. There are several ways to categorise the cooling techniques. A first distinction is based on energy required to operate the cooling system. The options for cooling technologies can be divided into two broad categories:

- Passive cooling, where no additional power is required for the fluid movement or heat is transported by conduction and/or radiation heat transfer. Passive air cooling is also referred to as natural convection cooling.
- Active cooling, where the fluid motion is assisted by an external source, a fan in a forced air cooled system, or a pump in a liquid cooled system.

Alternatively, the cooling solutions can be divided into categories based on the coolant (air cooling and liquid cooling) or based on the packaging level on which the cooling solution is applied (device level, package level or system level cooling). In the next section, an overview of existing cooling techniques, covering all these categories is given.

1.2 Overview of cooling techniques for electronic components

In this section, an overview of existing cooling techniques is given. First, the passive cooling techniques, including conduction, are discussed. Next, cooling systems based on air and liquid cooling are reviewed. Finally, several advanced cooling techniques are discussed. This overview focuses on the limitations of conventional cooling methods and the transition to closed-loop liquid cooling systems. Electronic cooling systems such as solid state cooling (thermo-electric cooling), refrigeration cooling, cryogenics cooling and immersion cooling are not discussed.

The need for new cooling techniques is driven by the continuing miniaturisation and increases in power dissipation and power densities of electronic parts and systems. In many cases standard techniques, such as heat sinks and fans, can not achieve the required cooling performance for the high end applications. For those applications, there is a need for innovative, high performance cooling solutions. Figure 1.5 shows a comparison of various cooling techniques based on air or liquid, plotted as a function of the achievable heat transfer in terms of the heat transfer coefficient. From this figure, it is clear that with liquid cooling higher heat transfer coefficients can be achieved. As a result, it will be possible to cool higher heat fluxes using liquid cooling, compared to air cooling for the same temperature difference.

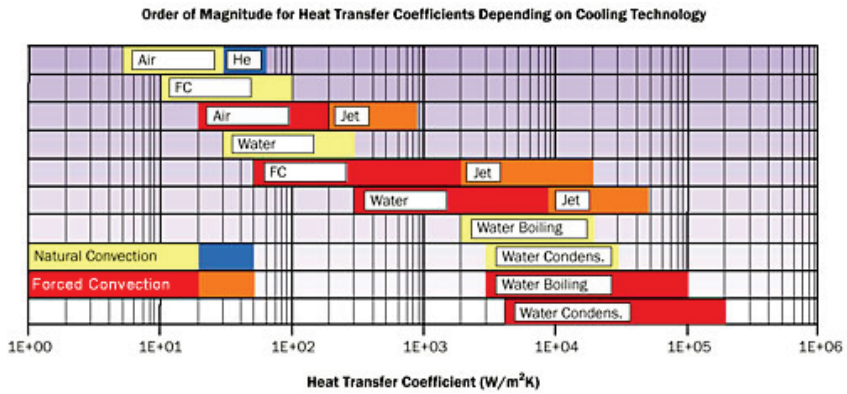

Figure 1.5 Heat transfer coefficient attainable with natural convection, single-phase liquid forced convection and boiling for different coolants (Lasance 2005).

1.2.1 Passive cooling

1.2.1.1 Natural convection air cooling

Passive air cooling is based on the circulation of the fluid due to the density difference caused by a temperature difference. Therefore, this technique only works in the presence of gravity. Advantages of this technique are the simplicity and reliability of the cooling design, and the low cost for both production and maintenance, the lack of moving parts and noise. The technique can be used in applications where heat dissipation is not dependent on designated supply of air flows. The draw backs of air cooling are inherent to the thermal properties of air. Using air as a coolant is inefficient as heat removal (low thermal conductivity k and low Prandtl number Pr), and air has a low thermal capacitance (low density and low specific heat). Consequently, an air based cooling system will have a large thermal resistance and will not be able to cool high heat fluxes.

To increase the thermal performance of natural convection, heat sinks can be attached to the heat generating component. With this heat sink, a larger surface area for heat transfer with the air is created. To further optimise the passive heat sink, the fin surface can be interrupted. These discontinuities break up the boundary layer and significantly enhance the heat transfer to the air while only moderating the increase in pressure drop across the heat sink (Johnson 2004). Despite these improvements, the maximum cooling performance for natural convection is limited. To increase the cooling, forced convection can be used (see Section 1.2.2).

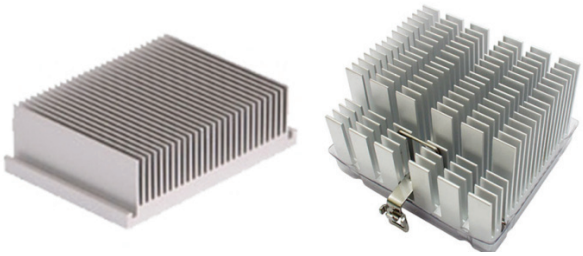

Figure 1.6. Examples of heat sinks for natural convection cooling.

1.2.1.2 Heat pipes and thermal vapour chambers

Currently, heat pipes are the standard cooling solution in mobile electronic applications (e.g. heat pipe – heat sink combinations in laptops) to move the heat from the CPU to a small heat sink. These are completely passive devices based on conduction and phase transition with an extremely high effective thermal conductivity (Faghri 1995). A heat pipe is a hermetically sealed, vacuum pumped tubular container, partially filled with a liquid. The liquid is chosen to match the operating temperature of the electronic component. The evaporator side of the heat pipe is attached to the heat generating component. When heat is applied, the liquid evaporates and flows to the cold side due to the pressure difference. At the cold side (condenser), the vapour condenses and flows back through the capillary wick at the internal walls of the heat pipe. Since the return of the liquid is governed by capillary forces, the operation of the heat pipe is independent of its orientation. In these applications the evaporator is attached to the heat source and the condenser is attached to an external heat sink, at a location where more space is available. Since the heat pipe is only a device to transfer heat, the thermal capacity of a heat pipe is restricted by the heat sink's ability to remove the heat through convection. In electronic cooling applications, copper/water heat pipes are typically used to limit the temperature to 125 °C or below. Heat pipes can transfer much higher powers for a given temperature difference than even the best metallic conductors. When too much heat is applied, either the capillary pressure is too low to provide enough liquid to the evaporator from the condenser, or the heat flux into the heat pipe causes the liquid in the wick to boil and evaporate. Both cases will lead to a dry-out of the heat pipe and the effective thermal conductivity of the heat pipe will be significantly reduced to the conduction of the metal casing.

Several types of heat pipes are commonly used for electronics cooling applications including micro heat pipes, loop heat pipes, flat plate heat pipes. In loop heat pipes (LHP), the vapour and liquid paths are separated, enabling a much better performance of the liquid return loop (Kim and Golliher 2002). Two dimensional planar heat pipes are referred to as vacuum chambers. They are based on the same principle and have the same components as tubular heat pipes. The wick structure is formed around the vacuum chamber. This provides a very effective spreading of the heat on the surface at the condenser side. The vacuum chambers act as very effective, thin heat spreaders (down to 0.5 mm) with an effective thermal conductivity close to the one of diamond. Micro heat pipes are small heat pipes that are non-circular and use angled corners in stead of the capillary wick structure to circulate the liquid back (Peterson 1994). Due to their small size, they are very suitable to cool components with very limited space available.

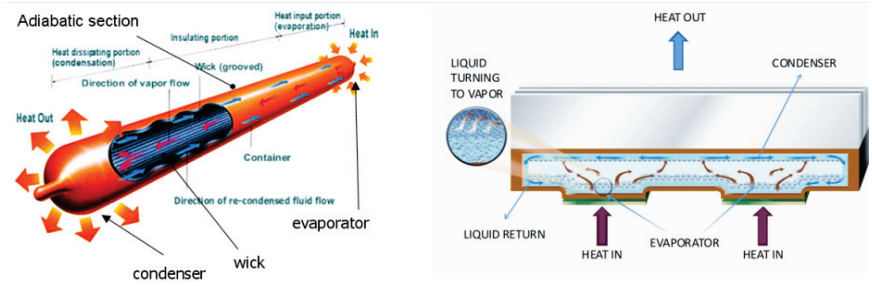

Figure 1.7. Schematic representation of a heat pipe (left) and a vacuum chamber (right).

1.2.2 Active air cooling

Currently, air cooling is widely used as standard solution for the cooling of micro-electronics. However, this cooling technique has clearly reached its limits in high power applications. State-of-the-art air heat sinks make use of impinging jet technology with optimised fin geometry. To extend the usefulness of this technology, heat sinks with integrated heat spreading are used at the expense of increased space requirements. Further improvement can only be achieved by using higher air velocities, which will lead to even more noise generation.

1.2.2.1 Heat sink – fan combination

The heat transfer for forced convection between a heated surface and a fluid depends on the velocity of this fluid flow. Higher velocities give rise to higher heat transfer coefficients h at the surface. In an active air cooling system, this fluid flow is generated by fans. These fans can be placed at the entrance of a system level cooling or attached directly to the heat sink. Figure 1.8 shows two examples of this heat sink – fan combination. The reliability of these systems depends on the moving parts. Other draw backs are the generated noise by the fan and the additional occupied space. Using these types of fans, a maximum heat transfer coefficient of the order of 100− 150 W/m ^{2}K can be reached with acceptable noise levels, which is 0.5 to 1 W/cm^2 for a 50 °C temperature difference. Additional improvements to the heat transfer by forced convection cooling on system level, can be made by an optimised air flow management. This includes smart placement of the components, reorientation of the flow to create vortices or the introduction of turbulators to break up the boundary layer.

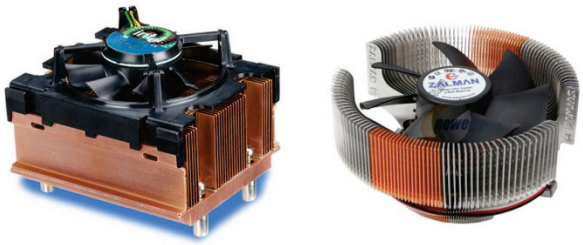

Figure 1.8. Examples of heat sink with integrated fan for forced convection cooling: axial fan (left:Intel) and radial fan (right: Zalman).

1.2.2.2 Synthetic jet cooling

The heat transfer from the hot surface to the air flow can be improved by impinging the flow on the surface. This can be implemented by jet of air impacting the surface to be cooled. These jets can be steady state or pulsating. Examples of this approach are the pulsating synthetic micro jets, where the pulsation is caused by an oscillating diaphragm (Beratlis *et al*. 2003). Due to the pulsating nature of the flow, synthetic jets introduce a stronger entrainment than conventional steady-state jets. The synthetic jet entrains cool air from ambient, impinges on the top hot surface and circulates the heated air back to the ambient. The technique offers a higher heat transfer, lower noise levels and lower flow rate compared to standard heat sinks for the same cooling performance.

1.2.2.3 Micro scale air movers

Several advanced micro scale air moving devices have been developed to create a local air flow close to the heat source, without generating unacceptable noise levels. A first example is the **piezoelectric fan**. Piezoelectric fans consist of oscillating, flexible blades covered with piezoceramic material. The blade is actuated at its resonance frequency using a piezoelectric device, and creates an airflow motion directed to the electronic component. A heat transfer enhancement of 100% over natural convection has been reported for this technique (Acikalin *et al.* 2004).

A second example of micro scale air movers are the **solid state fans**. This technology is based on 'micro-scale ion-driven airflow' using very high electric fields. These fields ionise the air. The ionised air molecules are attracted by another electric field, and induce a secondary airflow. Cooling a heat flux level of 40 W/cm^2 has been reported (Peterson *et al*. 2003). This technique is also referred to as 'nanolightning' or ionic wind cooling or electro-aerodynamic pumping.

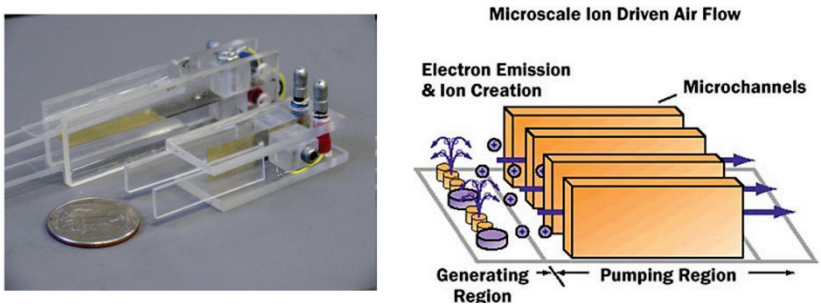

Figure 1.9. Piezoelectric fan (left, Acikalin et al. 2004). Ion wind cooling (right, Peterson et al. 2003).

1.2.3 Active liquid cooling

For heat flux densities up to and potentially even beyond 50 W/cm^2, air cooling may remain the standard cooling solution. For heat fluxes over 100 W/cm^2, some form of liquid-cooling appears to be the most viable option. Most liquids have a much higher thermal conductivity compared to the one of air (e.g. water has a thermal conductivity of 0.598 W/mK at room temperature compared to 0.0237 W/mK for air). Therefore, a major improvement in heat transfer coefficient can be achieved by using liquid cooling systems for applications where air cooling is no longer sufficient. As can be seen in Figure 1.5, the heat transfer coefficient that can be obtained using liquids is much higher compared to air. The ideal coolant used for liquid cooling should fulfil several requirements: high thermal conductivity, high specific heat to limit the flow rate, low viscosity to limit the pumping power, high surface tension to prevent leakage, chemical inert to prevent corrosion and compatible for a large temperature range. Commonly used liquids are water, ethylene glycol, liquid metals, fluorcarbonates (e.g. FC-72) and refrigerants (e.g. R134a).

A distinction of the cooling techniques can be made based on the presence of phase transition. The cooling techniques can be divided in **single-phase** cooling or **two-phase** cooling techniques. Liquid cooling for application to electronics can also be divided into the two main categories of **indirect** and **direct** liquid cooling. In indirect cooling, the liquid does not come in direct contact with the electronic component. This category includes cold plate and microchannel cooling. In the case of direct cooling, the coolant directly contacts with the electronics. Therefore, the liquid should be dielectric. This category includes jet impingement and immersion cooling.

A typical configuration of a closed-loop liquid cooling system is shown in Figure 1.4. The primary cooler is attached to the heat generating component. This component is cooled by the liquid coolant moving through the primary cooler. This primary cooler could be a cold plate heat sink, a microchannel heat sink, a jet impingement cooler, or any other type of liquid cooling. The heated coolant is circulated in a closed-loop to a secondary heat exchanger (e.g. liquid-air heat exchanger), where the coolant is cooled by a secondary coolant, usually the ambient air. Circulation of the primary coolant can be achieved by passive means (density difference, capillary forces, …) or by pumping action. Both centralised and distributed pumping systems are possible.

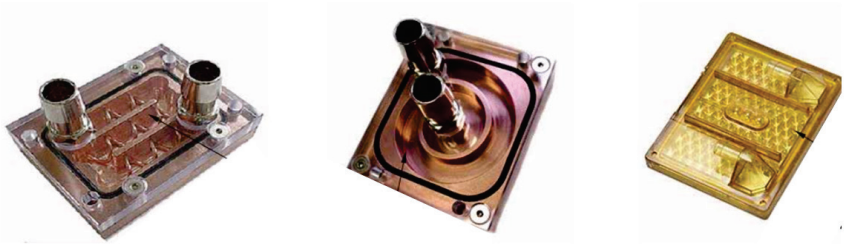

Figure 1.10 Examples of cold plates used for component level liquid cooling.

1.2.3.1 Cold plate heat sink

Liquid-cooled cold plates are fixed on top of the heat generating component like air heat sinks and use water as primary coolant. It consists of a box with flow in- and outlet and can have an internal fin structure. To force the coolant through the device, a pump is used. Cold plates typically have a large flow rate at a relatively low pressure drop. Liquid cooled cold plates are commonly used in high end applications to cool high power multi-chip processor modules. Dedicated cold plate coolers are available to provide cooling at device, component or system level. In Figure 1.10, a few examples of cold plates are shown.

1.2.3.2 Microchannel heat sinks

In many practical cases, the flow within the cold plate coolers is laminar for commonly used flow rates. For laminar flow, the heat transfer coefficient h is inversely proportional to the hydraulic diameter D_h :

$$h = \frac{Nu \cdot k}{D_h} \tag{1.3}$$

where k is the thermal conductivity of the coolant. This means that smaller channels result in higher heat transfer coefficients and suggest replacing the channel in the cold plate by hundreds of smaller channels in parallel. Additionally, microchannels provide a larger heat exchanging surface area to remove the heat. As such, micro-structured cold plates give high performance and occupy a very low volume (typically about 1 mm high) in comparison to the classic cold plate coolers. Typically, the hydraulic diameter of microchannels is in the range of tens to several hundreds of micrometers. The price to pay for this heat transfer enhancement, is an increase in pressure drop that needs to be overcome by the pump. For laminar flow, the pressure drop Δp increases with the inverse of the second power of the channel dimension. This pressure drop, due to forcing a fluid through a small channel, may produce design limitations. Microchannel heat sinks can be fabricated either in the chip itself or they can be fabricated into a substrate, which is then attached to the chip. In the first case, there is no additional thermal resistance of the adhesive to bond the cooler to the chip. The microchannels can be etched in Si (either the chip itself, or in an additional cooler) or micromachined in materials with a high thermal conductivity (typically in Al or Cu) .

These microchannel heat sinks were first proposed for electronics cooling applications by Tuckerman and Pease (1981). The microchannel heat sink was able to dissipate 790 W/cm^2 with a maximum substrate to inlet water temperature difference of 71 °C. However, the pressure drop was quite large at 200 kPa with plain microchannels and 380 kPa with pin fin enhanced microchannels. This classical design has been studied exhaustively during the last decade and recently some improved designs have been suggested and manufactured using multiple manifolds and enhanced internal fin structures (Palm 2001; Kandlikar and Grande 2004).

By allowing the coolant to evaporate when flowing through a cooler, much more heat can be extracted at a lower flow rate compared to single-phase cooling by taking advantage of the latent heat at the phase transition (Gambill and Lienhard 1989). In addition, evaporation occurs at near isothermal conditions. This gives two-phase cooling methods a fundamental advantage over single-phase cooling where the temperature rise of the coolant eventually becomes the limitation of the latter technology. However, two-phase flow in microchannels is highly unpredictable and can produce large voids and multiple flow regimes inside the channels.

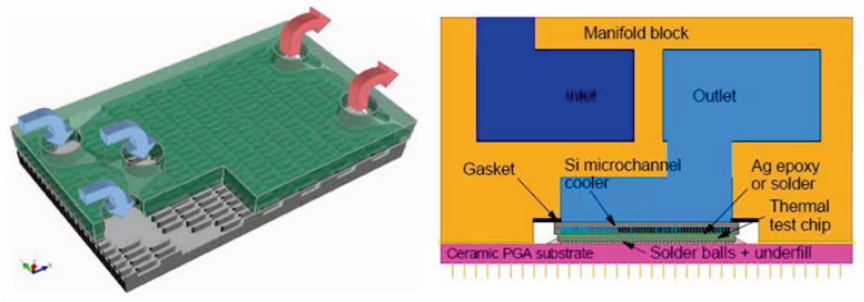

Figure 1.11. Microchannel based heat sinks (Colgan et al. 2006).

1.2.3.3 Integrated micropumps

Forced convection liquid cooling through microchannels can achieve very high heat removal rates. The draw back for these microchannels is the high pressure drop that needs to be overcome by the external pump to force the coolant through the heat sink (Garimella and Sobhan 2003). To overcome the problem with the high pressure drop in the microchannels where the pressure is provided by an external pump, extensive research is carried out to develop integrated pumps in the channels. In literature, comprehensive reviews of micropumps are available which cover the whole range of actuation mechanisms and applications (Nguyen *et al*. 2002; Laser and Santiago 2004; Woias 2005; Singhal *et al*. 2004; Zhang *et al*. 2007; Iverson and Garimella 2008). In these review papers, the micropumps are classified in two categories :

1. Mechanical displacement pumps
2. Electro- and magneto-kinetic micropumps

The mechanical pumps exert pressure forces on the fluid generated by the motion of a solid or a liquid. These pumps include rotary pumps, vibrating diaphragms, and peristaltic micropumps. The electro- and magneto-kinetic micropumps convert magnetic or electric energy into continuous or discrete liquid motion. These pumps include electrohydrodynamic (EHD), electro-osmotic, and magnetohydrodynamic (MHD) micropumps. This categorisation of micropumps is shown in Figure 1.12.

Iverson and Garimella (2008) compared the achievable flow rates and back pressures for all these types of micropumps. They concluded that pumps with high flow rates per unit area include piezoelectric diaphragm pumps, induction- and injection-type EHD, rotary-disk viscous, and electro-osmotic pumps and that pumps with high back pressure include vibrating diaphragm and electro-osmotic pumps.

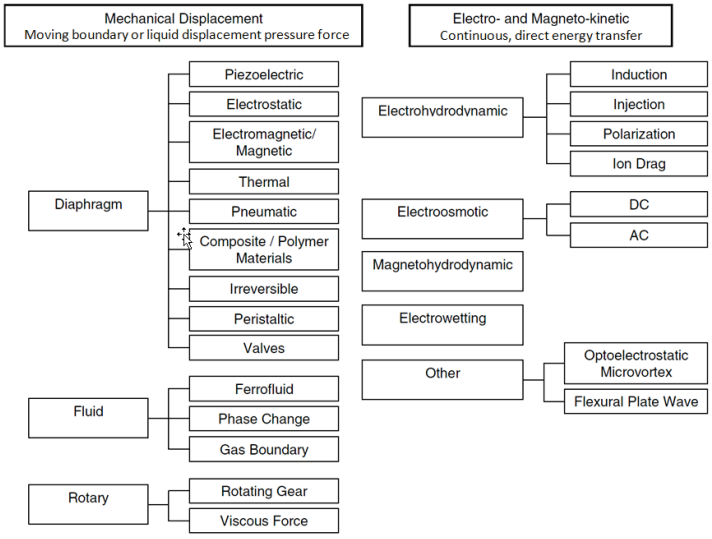

Figure 1.12. Categorisation of pumping mechanisms (Adapted from Iverson and Garmilla 2008).

The reported values of the micropump performances with respect to the achievable flow rate and achievable back pressure show a large scatter in the review papers (Nguyen *et al*. 2002; Laser and Santiago 2004; Woias 2005; Singhal *et al*. 2004; Zhang *et al*. 2007; Iverson and Garimella 2008; Nisar *et al.* 2008). Since most of the pumps cover a range of several decades for the flow rate and pressure, it is not possible to draw clearly defined operating ranges of the several pumps in a flow rate versus back pressure performance diagram. Nisar *et al.* (2008) present the achievable flow rate and the required operation voltage for a series of electro- and magneto- kinetic micropumps (Figure 1.13). From this figure, it can be observed that the electrohydrodynamic and the magnetohydrodynamic pumps are capable of realising a very high flow rate. The electroosmotic micropumps on the other hand are capable to generate a high back pressure. The disadvantage however of both the electro-osmotic (EO) and the electrohydrodynamic (EHD) pumps is the high required voltage to operate the pump. EHD pumps typically require a voltage in the range of 700 V, whereas for EO pumps even higher voltages are required.

The electrowetting based pump is capable of generating a flow rate in the order of several hundreds µl/min and only requires several tens of Volts to be operated. This low required voltage, and consequently low power consumption are very important. An additional advantage of the electrowetting technique, and the electrostatic actuation techniques in general, is the full integrating capability with microelectronics processing and packaging techniques. Those two main advantages make the electrowetting pumping a very interesting potential technique to apply for microelectronics cooling.

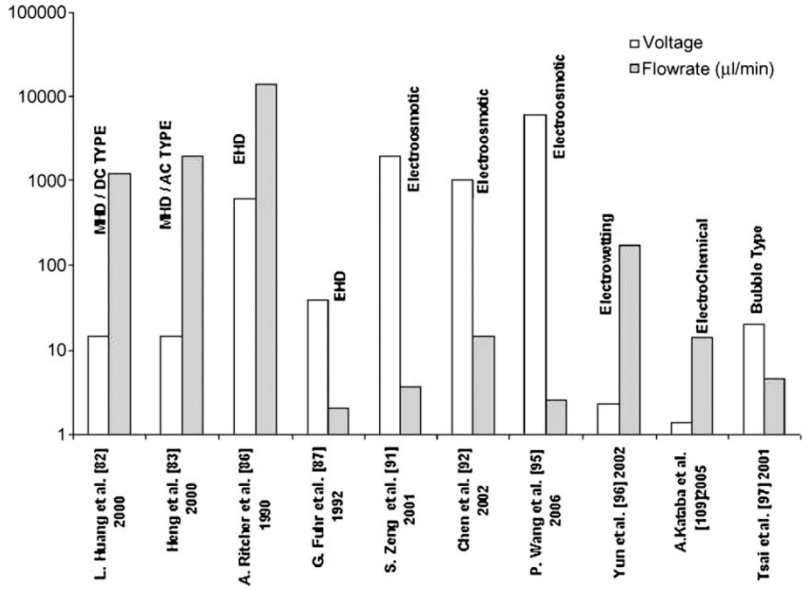

Figure 1.13. Comparison of flow rate and required voltage for several electro- and magneto- kinetic micropumps (Nisar et al. 2008).

1.2.3.4 Liquid jet impingement and spray cooling

In **jet impingement** cooling devices, liquid is directly ejected to the backside of the electronic component. The heat transfer under an impinging jet is extremely high in the stagnation zone, but decays quickly with distance from the centre of the jet (Martin 1977; Webb and Ma 1995). Impingement cooling may involve a single jet or an array of jets directed at the electronic component. Possible heat transfer modes for jet impingement are forced convection alone and localised flow boiling, with or without net vapour generation. A high-performance impingement jet cooler requires a high number of small, closely-spaced jets and alternating outlets, which requires complex feeding and draining duct networks (see Figure 1.14). Several of these complex coolers have been proposed with arrays up to 10000 jets (Brunschwiler *et al.* 2006). For microjet arrays (MJA) heat transfer coefficients up to 500,000 W/m²K and heat removal rates up to 1000 W/cm² (Shedd 2007) and 1200 W/cm² (Garimella 2000) are reported. Managing and controlling the jets and the interaction with the neighbouring jets, as well as the packaging is challenging. In comparison with microchannels, jet impingement systems are more difficult to fabricate and implement but achieve better cooling uniformity over the surface of the component to cool.

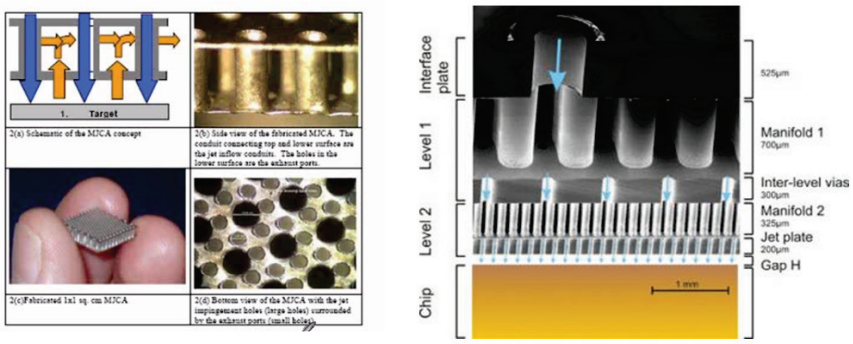

Figure 1.14. Examples of jet impingement array systems: Mezzo Technologies (left: Shedd 2007), IBM (right: Brunschwiler et al. 2006)

Figure 1.15. Examples of the impingement flow for a jet impingement cooler (left : Cotler et al. 2004) and a spray cooling system (right: Bash et al. 2003).

In **spray cooling,** liquid is broken up into fine droplets that individual impinge on the surface and evaporate upon impact. The vapour is then collected, re-condensed, and then pumped back to the nozzles. Different spray technologies may be used, e.g. pressure nozzles (Cotler *et al.* 2004) and inkjet technology (Bash *et al.* 2003).

1.2.3.5 Liquid metal cooling

Instead of water, liquid metals can be used as coolant, e.g. Ga-Sn-In eutectics are in liquid form at room temperature. These metals have superior thermophysical properties compared to water (high vapour pressure, high thermal conductivity, high heat transfer coefficients, low coefficient of thermal expansion, very large operating temperature range) and can be pumped efficiently with silent, non-moving pumps using magnetohydrodynamic (MHD) pumping. Miner and Ghosal (2004) and Ghosal *et al.* (2005) have reported a cooling capacity of 200 W/cm² for a flow rate of 0.25 l/min.

1.3 General description of the work

In this work, the principle of electrostatically actuated liquid droplets is applied as a cooling technique for electronic components. This technique is applied as a micropump to actuate discrete liquid droplets through a channel close to the heat generating electronic component. The droplets are actuated by means of electrostatic forces, which are generated by individual addressable electrodes.

1.3.1 Introduction to the droplet based cooling system

1.3.1.1 Droplet actuation principle

The actuation principle used for the droplet transport in a cooling channel of the proposed cooling system is electrostatic actuation of droplet. The principle is also referred to as ‘electrowetting’. Electrowetting is a technique to manipulate fluids on a millimetre or micrometre scale by altering the wetting properties under the application of an electrical field. At microscale dimensions, the surface forces are dominant over the body forces (de Gennes *et al.* 2004). Therefore, the control of surface energies can be used to manipulate droplet interfaces or induce bulk motion of liquid. By locally changing the interfacial energy, deformation or even motion of the droplet can be induced. This change in interfacial energy can be created by applying a surface tension gradient (Marangioni effect), a temperature gradient (thermocapillary effect) or an electric field (electrowetting effect).

The two major groups of applications of electrowetting are microfluidic lab on chip devices and optical applications. In lab on chip devices, electrowetting is used for microfluidic actuation and manipulation. Droplet manipulations such as transporting, creating, merging and splitting using this electrowetting effect are demonstrated in single plate or parallel plate systems (Pollack *et al*. 2002; Cho *et al*. 2003; Srinavasan *et al.* 2004; Fouillet and

Achard 2004; Chakrabarty and Su 2006). The optical applications include tuneable liquid lenses (Berge and Peseux 2000; Yang *et al.* 2003; Kuiper and Hendriks 2004) and reflective (Hayes and Feenstra 2003) and fluorescence displays (Heikenfeld and Steckl 2005). Instead of an aqueous solution, liquid metals can also be used in electrostatic actuation with applications as switches, latching relays and optical shutters (Washizu 1998; Lee and Kim 2000; Yun *et al*. 2002). Quilliet and Berge (2001) and Mugele and Baret (2005) provide a comprehensive review discussing the principle of electrowetting and its applications.

Researchers from Duke University (Pamula and Chakrabarty 2003; Paik *et al*. 2004, 2005) proposed to apply this actuation technique as a cooling method to cope with the thermal issue of hot spots in electronic devices. In order to further enhance the cooling capability, Mohseni (2005) proposed cooling with liquid metal droplets that have superior thermal properties in combination with more favourable operating temperature ranges.

1.3.1.2 Droplet cooling principle

In this work, a cooling system based on individually actuated liquid droplets is studied. The objective of the cooling system is to remove the heat dissipated in the electronic component. The left hand side of Figure 1.16 shows a schematic representation of this cooling technique. From this figure, the main parts of the system can be identified. The chip is at the top of the structure. During operation this chip generates heat. The objective of the droplet flow is to take away the heat from the chip and remove this heat from the system. In this case, the channel for the liquid droplet is formed by the gap between the substrate and the chip. The height of this gap is determined by spacers. The liquid of the droplet should be either electrically conductive or polarisable. The channel is filled with a host medium, also referred to as filler liquid. This could be air or a low-viscosity silicone oil. The droplets are actuated by the application of an electric field across the droplet. This electric field is generated by the electrodes in the system. At the bottom side, control electrodes are integrated in the substrate over the length of the channel. The voltage on each of these control electrodes can be controlled independently to create a local voltage difference. The top plate consists of a single grounded electrode. The electrodes on both top and bottom plate are covered with an insulating dielectric layer. This dielectric layer prevents electric current flowing from the energised electrode to the liquid droplet which would cause chemical reactions, such as electrolysis. As a result, this dielectric material should have a sufficiently high dielectric strength. Moreover, the dielectric constant of the material should be high and the layer thickness should be thin, in order to generate a high actuation force. Typical materials that could be used are BCB, Parylene, SiO_2 or Si_3N_4. Both top and bottom plate are coated with a thin hydrophobic layer. This hydrophobic layer reduces the friction between the droplet and the walls. A large contact angle of the liquid on the hydrophobic layer allows larger contact angle reduction as reaction to the application of an electric field and therefore a larger effect for the same voltage. As a result, a lower force, and actuation voltage is required for the droplet motion. Therefore, the top coating should be as hydrophobic as possible.

When a voltage is applied to a control electrode at the bottom plate close to the droplet, while the other control electrodes and the ground electrode at the top side are kept at 0 V, the droplet will feel an actuation force. If the actuation force is sufficiently high, the droplet will move towards the activated electrode. In order for the droplet to start moving, the

actuation force must overcome the retentive force by the surface tension, discussed in Chapter 2. The presence of this retentive force leads to a threshold value for the actuation force and the applied voltage. For voltages lower than this threshold, the droplet will only deform but not move. For an actuation force above the threshold force, a droplet motion towards the activated electrode will be induced, until the droplet is on top of the activated electrode. At this position, the actuation force is zero, and the droplet will stop. At this point, the voltage of the electrode can be set to 0 V, while the next electrode is put at the actuation voltage. Consequently, the droplet will move towards the next electrode. With a good choice of the frequency to switch the voltage between succeeding electrodes, the droplet can be transported along the path of electrodes to cover the length of the channel. By addressing multiple electrodes at the same time, multiple droplets will be transported. Thus, a continuous flow of droplets through the channel between the two plates can be generated. During this motion through the channel, the droplets will heat up while taking away the heat from the chip.

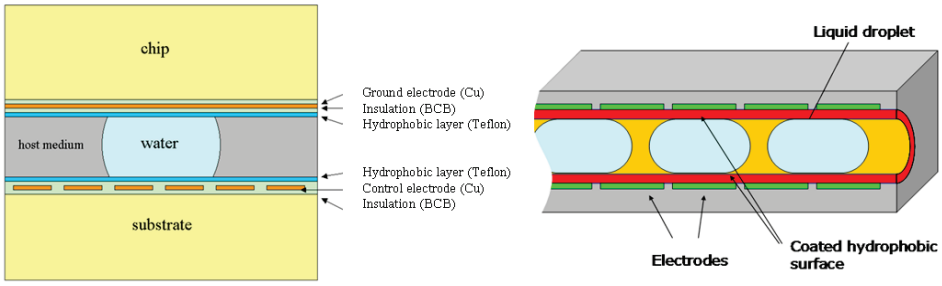

Figure 1.16. Concepts for the electrode configurations of the droplet actuation; planar electrode system (left), cylindrical channel with annular electrodes (right).

In this work, two different integration configurations of the electrodes will be studied. The first one consists of two parallel plates, as described above. In the bottom plate, a matrix of control electrodes is integrated. With these electrodes, the droplets can be guided on the chip surface to the location of hot spots. In the following chapters of the thesis, this system is referred to as '*planar parallel electrode system*'. The other system consists of a cylindrical channel with integrated annular electrodes that are covered with an insulating and hydrophobic layer. This system will be referred to as '*annular electrode system*'. This system is schematically illustrated at the right hand side of Figure 1.16. For both systems, the electrostatic actuation force and droplet motion through the cooling channel are studied.

1.3.1.3 Cooling system overview

The droplet actuation principle will actuate the droplets through the channel below the chip. This is only part of the global system. This global system is an autonomous closed-loop cooling system. Figure 1.17 shows a schematic representation of such a global cooling system. First, cold liquid droplets are extracted from a reservoir. The dispensing of droplets from the reservoir can be realised using similar electrodes (Cho *et al.* 2003; Pollack *et al.* 2002). Next, the droplets are actuated through the channel, while removing the heat from the chip. At the end of the channel, the heated droplets are collected. Subsequently, the liquid can be cooled by a secondary cooler using a secondary coolant (e.g. liquid-air heat

exchanger). This heat exchanger can be at another location in the system. Afterwards, the liquid is fed back to the first reservoir from which new droplets will be dispensed to enter the channel again. Using a 2D matrix of electrodes to actuate the liquid, this principle can be used to achieve efficient uniform cooling of the chip. But it is also possible to direct more droplets to a specific location of interest (e.g. a hot spot). In this way, a targeted cooling of hot spots on the chip can be provided. The droplets are guided from electrode to electrode. This means the channel is reconfigurable and no walls are used to divide parallel droplet flows. Therefore, the control of the droplet flows is rather software-controlled than hardware-implemented as walls in the channel. This allows a large flexibility for different cooling strategies.

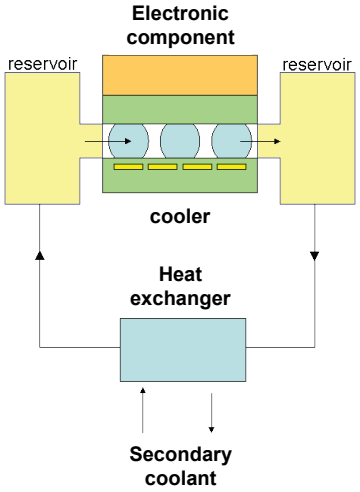

Figure 1.17. Schematic representation of the closed-loop cooling system including the elecrostatic droplet actuation in the cooler.

Compared to the cooling systems discussed in Section 1.2, this droplet based cooling system has important advantages. The main advantages are listed below.

- The paths for the droplet flow are defined by the electrodes. Therefore, the droplet trajectories are reconfigurable. This allows multiple control strategies to direct the droplet towards locations with a high need for cooling. This is of interest to cool thermal hot spots, or non-uniform power dissipation in general.
- Since the pump is integrated in the channels, no pressure drop needs to be overcome by a bulky external pump.
- The cooler can be integrated in the microsystem using microelectronic fabrication technologies. In this way, additional thermal resistances between the electronic component and the cooling system are avoided.
- The operation of the system is independent on the orientation or gravity. For the dimensions considered, the surface tension related forces are large compared to the gravitational force (see Section 2.1.1).
- The integrated cooler can be fabricated as a compact and light construction.
- The actuation of the droplets consumes a very low power in the range of mW (Pollack *et al*. 2002; Baelmans *et al*. 2007).

- No mechanical valves or pumps are required to actuate the droplets in the cooler. This has a beneficial effect on the reliability of the system.

The focus of this PhD work is on the electrical, mechanical and thermal behaviour of the droplet in the primary cooler itself. The other parts of the cooling loop are outside the scope of this thesis.

1.3.2 Methodology for the study of electrostatically actuated droplets

In this work, a modelling framework for the cooling performance of the droplet based cooling system is presented. This framework allows estimation of the cooling performance as function of the system parameters. These parameters include the actuation voltage, the geometrical properties of the channel and insulation and hydrophobic layers, the droplet volume and the material properties. The modelling presented here, provides a methodology to assess the influence of parameters on the cooling performance and to optimise the system. Using the methodology, the system parameters could be optimised to achieve a maximum flow rate for the constraint of a maximum specified voltage, or vice versa, to achieve a minimum actuation voltage for a required flow rate or cooling performance.

The electrostatic actuation of liquid droplets is a very complex system to model. Many coupled and not completely understood phenomena are involved. A first aspect is the coupling between the droplet shape and the applied electric field. A second aspect is a pinning force caused by the contact angle hysteresis. This results in a threshold value for the actuation force to overcome this critical pinning force. A third complicating aspect is the contact angle saturation. Different simplifying approaches have been suggested to estimate the actuation force and other forces acting on the droplet. These approaches are either based on the minimisation of potential energy (Shapiro *et al*. 2003; Ren *et al.* 2002) or on the electrostatic Maxwell stresses (Torkkeli *et al*. 2001).

In this work, a simplified modelling approach is used, to approximate the complex reality. The modelling of the electrostatically actuated droplets is decoupled into three separate parts:

- **Electrical**: This part describes the electrostatic force acting on a droplet for an applied voltage at the control electrode. For each position of the droplet, a quasi-static approach is used for the calculation of the electrostatic force.
- **Mechanical**: This part involves the macroscopic droplet motion and the internal motion inside the moving liquid droplet.
- **Thermal**: In this part, the heat removal by the liquid droplets is modelled using the results of the previous parts as input.

The decoupling of these effects is justified since the effect of the droplet motion on the droplet shape is limited. Indeed, the inertial forces on the droplet are small compared to the viscous dissipation forces. The assumption that the heat transfer does not influences the flow is justified by the ratio of the natural convection to the forced convection in the flow. When the ratio Gr/Re^2, where Gr is the Grashof number and Re in the Reynolds number, is sufficiently low (< 0.1), it can be assumed that the natural convection does not influence the flow (Guyer 1999). For the dimensions (order of magnitude mm) and velocities (several

tens of cm/s) considered here, this ratio is sufficiently low. An additional justification for the decoupling is the time scale on which the phenomena occur. The time scale of the electrical rearrangement of the ions or dipoles is of the order of 10^{-5} s or smaller. For the mechanical model, the dynamic response of the droplet is in the range of 10^{-3} to 10^{-2} s. In case of the thermal effect on the droplets, time constants of 10^{-1} s to several s are observed. From this, it is clear that the effects are each separated by an order of magnitude.

1.3.3 Outline of the thesis

In this work, a modelling framework for a droplet based cooling technique is presented. This methodology allows parameter studies and optimisation of the cooling performance. This methodology is applied to a planar and a cylindrical system. In Chapter 2, the friction force of droplets on surfaces is studied experimentally. Further, an empirical model is derived for the static and the dynamic part of this friction force. The electrostatic actuation force acting on a droplet in the channel is calculated by finite elements modelling in Chapter 3. In this chapter, the influence of material and geometrical parameters on the actuation force is studied for both cooling systems. Chapter 4 presents a simplified analytical model for the dynamic droplet response, using the information on the friction force from Chapter 2 and the electrostatic actuation force from Chapter 3 as input. In Chapter 5, the flow and heat transfer internally in a moving droplet are studied. Finally, in Chapter 6 all information is combined to assess the cooling performance of the proposed cooling systems using simplified analytical formulations. In Figure 1.18, a schematic overview of the structure of the thesis is shown.

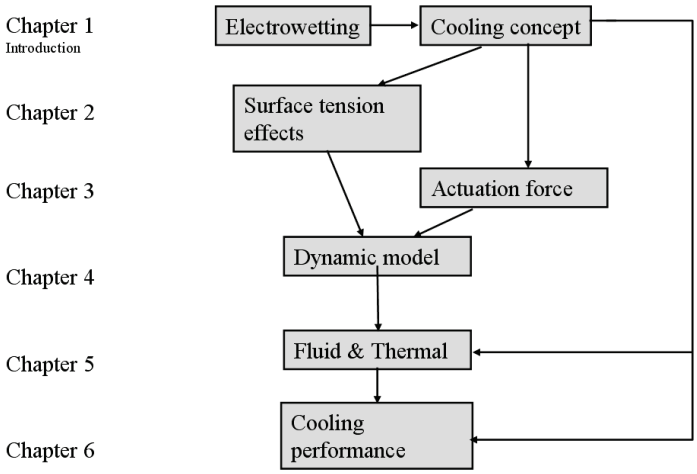

Figure 1.18. Schematic overview of the outline of the thesis.

Chapter 2

Characterisation of the impact of surface tension on droplet motion

Abstract

In this chapter, the impact of surface tension and gravity on the behaviour and shape of liquid droplets is investigated. The aim of this chapter is to determine the retentive force that prevents the droplet from moving. This is the force that the electrostatic force has to overcome in order to actuate the droplets. First, the aspects of surface tension, which are necessary to understand the droplet behaviour, are introduced. Contact angle measurements and analytical models are used to study the shape, deformation and start of motion of the droplets. The effect of surface roughness is studied analytically and validated experimentally. The insight in the droplet deformation from the modelling and experimental study is then applied to determine the retentive force on droplets when sliding down a surface or between two surfaces.

2.1 Introduction

2.1.1 Contact angle of a liquid droplet on a solid substrate

When an amount of liquid is placed on a solid surface, it forms a droplet whose shape is determined by the liquid volume and the contact angle θ between the liquid and the surface (Figure 2.1). This angle is a measure for the wettability of the liquid on the solid surface. A contact angle of 0° means complete wetting of the surface, a surface with an angle between 0° and 90° is called hydrophilic (wetting) and a contact angle higher than 90° means that the surface is hydrophobic or non-wetting (water repellent).

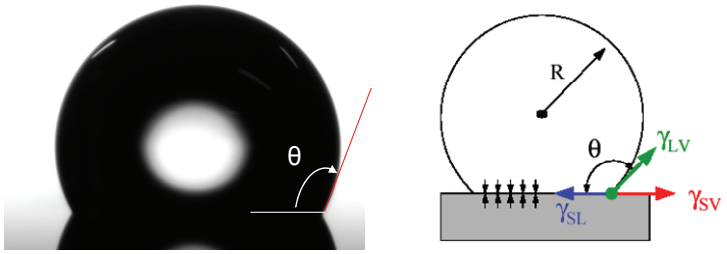

Figure 2.1. Picture of a typical droplet shape on a hydrophobic surface (left). Schematic representation of the interfacial force components acting on the contact line (right).

The contact angle depends on surface tension of the liquid, the surface tension of the solid substrate and the surface condition. The surface tension γ [N/m] is defined as the force F acting per unit length L of the line drawn on the surface of the liquid, the direction of the force being at right angles to this line and tangential to the surface of the liquid.

$$\gamma = \frac{F}{L} \tag{2.1}$$

An alternative definition for the surface tension is the amount of work done per unit area to create or expand a surface. As such, in order to increase the surface area of a mass of liquid by an amount, dA, a quantity of work, γdA, is needed. This work is stored as potential energy. Consequently, surface tension can also be measured in the SI system as J/m^2. Therefore the surface tension is also a measure of surface energy per unit area.

$$\gamma = \frac{dU}{dA} \tag{2.2}$$

For an ideal surface (smooth, planar, rigid and homogeneous), the equilibrium contact angle is equal to Young's angle, which can be determined from the force balance between the interfacial tensions at the three-phase contact line formed by solid, liquid and vapour (Figure 2.1). The horizontal projection of the force balance on the contact line can be written as follows:

$$\gamma_{SL} + \gamma_{SV} + \gamma_{LV} \cos\theta = 0 \tag{2.3}$$

where γ_{SL} , γ_{SV} and γ_{LV} are surface tensions at solid-liquid, solid-vapour (air) and liquid-vapour interfaces. The horizontal projection of this force balance leads to the Young equation of the contact angle:

$$\cos\theta = \frac{\gamma_{SV} - \gamma_{SL}}{\gamma_{LV}}. \tag{2.4}$$

The projection of the capillary forces onto the vertical axis is balanced out by a force of reaction exerted by the solid material (de Gennes *et al.* 2004). The same relation between the contact angle and the interfacial components of the surface tension can be derived from an energy analysis. At equilibrium, the droplet shape changes to a situation such that the free energy of the system is minimal. The total free energy for the droplet on a solid substrate can be written as follows:

$$E = \gamma_{SL} A_{SL} + \gamma_{LV} A_{LV} + \gamma_{SV} A_{SV}; \tag{2.5}$$

where A_{SL} , A_{SV} and A_{LV} are areas of the solid-liquid, solid-vapour (air) and liquid-vapour interfaces respectively. The change in interfacial area can be expressed as a function of the change in the solid-liquid interfacial area, referred to as *dA :*

$$\begin{aligned} dA_{SV} &= -dA_{SL} \\ dA_{LV} &= dA_{SL}\cos\theta \end{aligned} \tag{2.6}$$

To express an increase of the droplet base or increase of the solid-liquid interface, expressed with *dA*, the change in energy *dE* associated with the change in area *dA*, can be written as follows:

$$dE = \gamma_{SL} dA - \gamma_{SV} dA + \gamma_{LV} dA\cos\theta. \tag{2.7}$$

At equilibrium, the shape and interface of the droplet are such that the energy is minimal or whenever *dE/dA = 0*. This leads to the same expression for the contact angle as equation (2.4).

Table 2.1. Overview of surface tension values of common materials.

Liquid surface tension	**γ_{LV} (N/m)**	**Critical surface tension**	**γ_c (N/m)**
Benzene (20 °C)	0.029	Cu	1
Blood (37 °C)	0.058	Al	0.5
Glycerine (20 °C)	0.063	Glass	0.17
Mercury (20 °C)	0.47	Au	0.0574
Water (20 °C)	0.072	Teflon®	0.0156
Water (100 °C)	0.059	Si	0.0144

Unfortunately, not all the components of the surface tension are known. Practically, γ_{SL} and γ_{SV} are not known and the wetting of a solid by a liquid can only be approximated using correlations by means of the interfacial surface tension γ_{LV} of the liquid with respect to the air and the critical surface tension of the solid γ_c. The critical surface tension is the surface tension of a liquid that would have a contact angle of 90° on the solid surface. The liquids with surface tension γ_{LV} below the γ_c value of the solid, will simply spread on the solid. A low critical surface tension means that the surface has a low energy per unit area. The larger the difference between the surface tension of the liquid γ_{LV} and the critical surface tension of the solid, the larger the contact angle. To obtain a hydrophobic surface, the difference $(\gamma_{LV} - \gamma_c)$ should be chosen as large as possible. Plastics usually have a low critical surface tension. Table 2.1 gives an overview of the surface tension of common liquids and the critical surface tension of common solids. In Appendix A.3 several

correlations are listed that can be used to estimate the contact angle of a droplet based on the surface tension γ_{LV} of the liquid and the critical surface tension γ_C of the solid.

2.1.2 Scaling analysis of body and surface forces

The relative importance of the different volume and surface energies working on an amount of liquid, depends on the dimensions considered. When a liquid droplet is large in volume, its behaviour will be characterised by conversion between its gravity potential energy and the kinetic energy of the liquid flow. When the droplet of interest is much smaller, the surface energy dominates the evolution process. For a simplified geometry a scaling analysis can be performed to illustrate the contribution of the different types of forces as a function of the droplet volume. For a spherical drop of liquid, the order of magnitude of both energies can be assessed as follows. The potential energy of the gravity can be written as:

$$E_v = mgR = \rho VgR = \frac{4\pi}{3} R^4 \rho g \; ; \tag{2.8}$$

where ρ is the density, V the volume, g the gravitational constant and R the radius of the droplet. The surface energy E_s can be estimated as:

$$E_s = 4\pi\gamma_{LV} R^2 \tag{2.9}$$

Where γ_{LV} is the surface tension of the liquid. The value of the surface energy is equal to the one of the potential energy of the gravity for a droplet radius of

$$R = \sqrt{\frac{3\gamma_{LV}}{\rho g}} \; . \tag{2.10}$$

For water with material properties γ_{LV} = 72 mN/m and ρ = 1000 kg m^{-3}, this radius is 2.7 mm. This means that for droplet sizes smaller than 2.7 mm in radius, the surface energy is dominant, and vice versa for larger droplets the effect of the volume forces will be stronger. If the droplet size is further reduced, the so-called line tension τ [N] should be included in the description. Values for the line tension are reported in literature in the range of a few orders of magnitude (in the order of 10^{-10} N). From an analogous comparison, the transition between the dominance of the surface energy and line energy can be found. A droplet radius in the range of 1 nm–10 μm is found below which the line energies are dominant. These dimensions are outside the scope of this PhD study; the influence of the line tension will therefore not be considered. The energy contributions of the volume, surface and line forces are schematically represented as a function of the droplet volume in Figure 2.2. The inset shows the relevant range of volumes for microscale droplets. The graph indicates that, in the case of water, the surface force is dominant for microlitres down to picolitres.

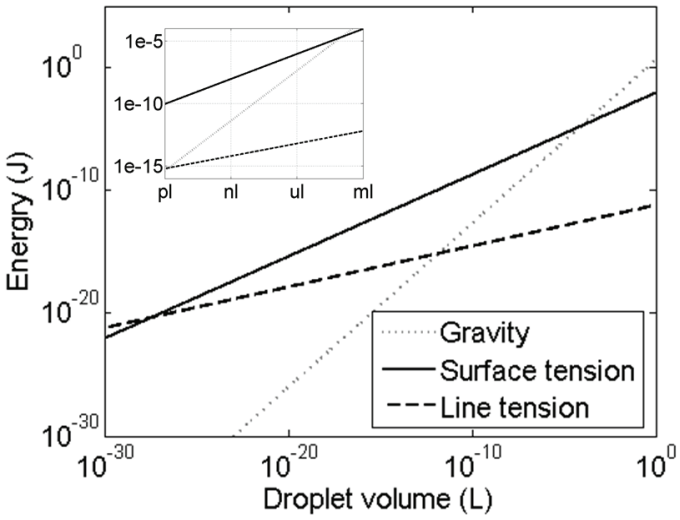

Figure 2.2. Scaling analysis of energies of the gravity, surface tension and line tension respectively as a function of the droplet volume for a surface tension γ of 72 mN/m and a line tension τ of 10^{-10} N. Inset: Detail for the range of microscale droplets.

2.1.3 Contact angle hysteresis

On an ideal surface (smooth, planar, rigid and homogeneous) only one equilibrium contact angle will exist, the Young's angle (Johnson and Dettre 1964). On a real, non-ideal surface however a whole range of multiple equilibrium angles can exist, which represent local minima of the total potential energy. The difference between the minimum and the maximum contact angle values that can be observed is called the contact angle hysteresis. Contact angle hysteresis is generally attributed to surface roughness, surface heterogeneity, solution impurities adsorbing on the surface, or swelling. For surfaces which are not homogeneous, there will exist domains on the surface which present barriers to the motion of the contact line. For the case of chemical heterogeneity, these domains represent areas with different contact angles than the surrounding surface. For situations in which surface roughness generates hysteresis, the actual microscopic variations of slope in the surface create the barriers which pin the motion of the contact line and alter the macroscopic contact angles. Contact angle hysteresis is of particular interest for moving liquids and thus moving contact lines. Contact angles measured for a liquid advancing across a surface exceed those of a liquid receding from the surface. This contact angle is called the advancing contact angle θ_A. On the other hand, the contact angle at the receding side of the droplet is smaller than the one from the surface. This is the so called receding contact angle, θ_R. Usually θ_A is significantly higher than θ_R. The difference θ_A - θ_R is called contact angle hysteresis.

For a droplet on a tilted surface, the rear angle (θ_R) is smaller than the front one (θ_A). Therefore a net force, which opposes the gravity force is exerted on the droplet. The force is compensated for by the deformation of the droplet. In order to initiate droplet movement,

the gravity should overcome the threshold force for which the deformed angles reach the maximum advancing and minimum receding angle of that specific liquid on the solid material.

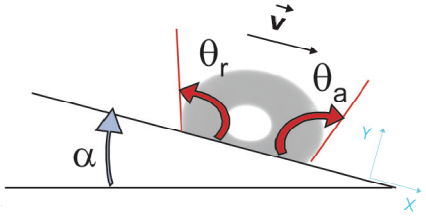

Figure 2.3. Advancing and receding contact angle of a droplet on a tilted substrate.

For a moving droplet, a dynamic contact angle is defined; this means the receding and advancing contact angle are function of the local velocity of the contact line (Figure 2.4). On an ideal surface, the velocity of the contact line V_{CL} is zero only when the contact angle is equal to the Young's angle. On a real surface V_{CL} is equal to zero in an interval $[\theta_R, \theta_A]$ which is called the hysteresis domain.

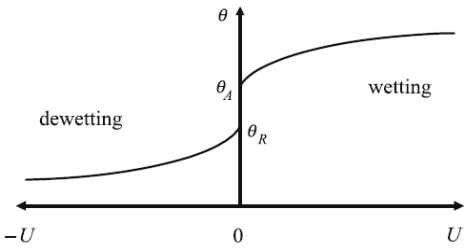

Figure 2.4. The dynamic contact angles of a droplet with a moving contact line speed V_{CL} (Yeo and Chang 2008).

2.1.4 Retentive force due to contact angle hysteresis

Consider a force acting on the droplet. This could be an electrostatic actuation force or the gravitation force in case the surface on which the droplet is lying is tilted. When the droplet is exposed to this external force, the droplet will deform and lean into the direction of the attraction force. As this happens, the advancing contact angle increases and the receding contact angle decreases. The contact line of the droplet however stays pinned to the surface. Only after the force exceeds a certain threshold, the droplet will move as a whole. In this case, the droplet deformation exceeds a critical contact angle hysteresis and the contact line will move. This behaviour results in a friction force caused by the contact angle hysteresis. This force is referred to as retentive force. In order to move the droplet, the actuation force needs to overcome this threshold force. Bonn *et. al* (2009) provide a comprehensive review of the recent progress description of moving contact line dynamics. Extrand and Kumagai (1995) stated that retentive force can be described as a function of the advancing and receding contact angle and the geometrical properties of the droplet:

$$F = \gamma_L wk\left(\cos\theta_R - \cos\theta_A\right) \tag{2.11}$$

where w is the width of the droplet in the direction perpendicular to the droplet motion and k is a numerical constant that depends on the geometry of the droplet. This constant is a result from the integration of the contact angle profile over the contact line. In case of a circular droplet, $k = 4/\pi$ and for a parallel sided droplet with constant θ_A and θ_R $k=2$. Generally, the numerical factor is found to be (Extrand and Kumagai 1995):

$$k = 0.23 + 1.04\beta \tag{2.12}$$

where β is the width-to-length ratio of the droplet. In the case of a droplet with a circular contact line $\beta = 1$ and $k = 4/\pi$.

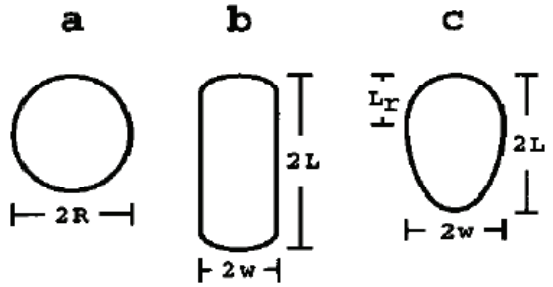

Figure 2.5. Top view of droplet with different contact line shapes: (a) circular drop, (b) a parallel-sided drop, and (c) a drop with front to back asymmetry (Extrand and Kumagai 1995) .

Dynamic model

As discussed in the previous section, the contact angle at the advancing and receding side of the droplet depends on the local velocity of the contact line. This dynamic effect should be included in the formulation of the retentive force. Many different theories exist on dynamic wetting modelling. Blake (2006) stated that current models of dynamic wetting can be divided into three categories:

1. hydrodynamic models which are based on empirical relations (Ren *et al*. 2002; Wang and Jones 2005; Chen and Hsieh 2006; Decamps and De Coninck 2000),
2. molecular-kinetic theory; (Blake 2006). This approach is able to clarify the molecular details of wetting as experimental observations reveal that the contact line motion takes place on a microscopic molecular scale,
3. Shikhmurzaev (1993) model.

The implementation of these models is outside the scope of this work. However, simplified expressions, capturing the dynamic effect can be derived from these theories. In the molecular-kinetic theory of Blake (2006), the relationship between the contact line velocity and the dynamic contact is introduced:

$$U_{CL} \approx 2\kappa^0 \lambda^3 \gamma \left(\cos\theta_{static} - \cos\theta_{dynamic}\right) / k_B T \tag{2.13}$$

where U_{CL} , k_B and T are velocity of the contact line, the Boltzmann constant and absolute temperature, respectively and where κ^0 and λ are the equilibrium frequency of the random molecular displacements and the average length of each displacement, respectively.

By introducing the coefficient of contact line friction ζ, equation (2.13) can be rewritten as follows:

$$U_{CL} \approx \left(\cos\theta_{static} - \cos\theta_{dynamic}\right)/\zeta \tag{2.14}$$

with

$$\zeta = k_B T/\left(2\gamma\kappa^0\lambda^3\right) \tag{2.15}$$

where the coefficient of contact line friction ζ, κ^0 and λ are experimentally determined (Keshavarz-Motamed *et al.* 2009). Equation (2.14) provides a simple relationship between the contact line velocity and the dynamic contact angle, for which the coefficient of contact line friction ζ (Pa.s) can be extracted from simple experiments. The dynamic part of the retentive force can therefore be written as follows:

$$F_{dyn} = \zeta U_{CL} L\,, \tag{2.16}$$

where L is the length of the contact line.

2.1.5 Objectives of this chapter

The objective of the work, presented in this chapter, is to characterise the retentive force of a droplet on the surfaces used for the electrostatic droplet actuation. This characterisation will lead to empirical models, to be used as input for dynamic droplet motion modelling in Chapter 4. Those models relate the retentive force to the droplet volume, the material of the coating, the surface roughness and in case of a confined channel, the distance between the surfaces. For the characterisation, tilt tests will be used to monitor the contact angles and retentive force during a sliding motion of the droplet. This is a simplification of the electrostatic induced motion. However, it will give interesting information on the retentive force on a certain surface and on the dynamic behaviour of the contact line and contact angles.

2.2 Measurement methods and materials

In this section, the tools and materials used to perform the sliding drop experiments are discussed. Only DI-water is used as a liquid to characterise the retentive force of the different substrates.

2.2.1 Contact angle measurements

Contact angle meter

The goal of the experiments is to characterise the contact angles and estimate the retentive force of droplets on surfaces. Therefore, a contact angle meter with a tiltable platform, including the CCD camera, sample platform and dispensing unit, is used (see Figure 2.6). In this way, the deforming and moving droplet stays in the focus of the camera and the influence of the force and droplet speed on the contact angles and droplet motion can be studied. The droplet dispensers control the volume of the droplets on the sample. The CCD camera takes images of the droplet on the sample platform with a frame rate of 25 images

per second to capture the motion of the droplet. Figure 2.7 shows an example of the image taken by the contact angle meter. From such an image the contact angles, the intersection point and the diameter of the contact line can be extracted. In case of a moving droplet the pictures can be analysed for each frame to extract the necessary information for the dynamic contact angles.

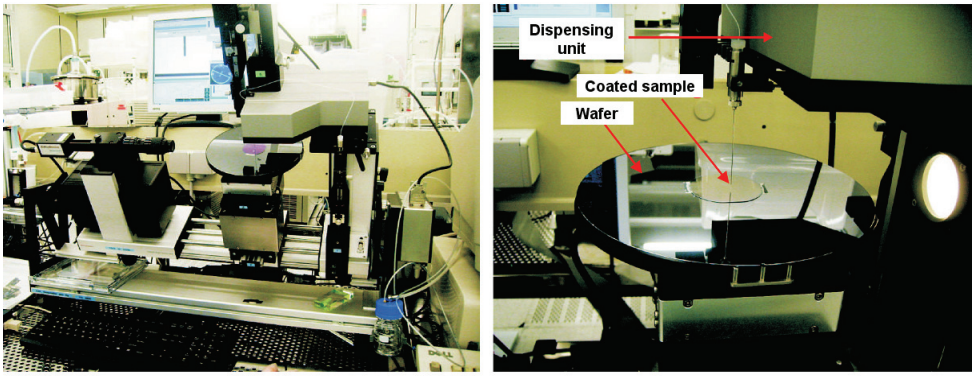

Figure 2.6. Picture of the contact angle measurement set-up. (a) The whole contact angle meter system including the dispensing unit, the sample platform and the camera are tilted during the tilted sliding drop experiments. (b) Detail of the sample platform and the dispensing unit.

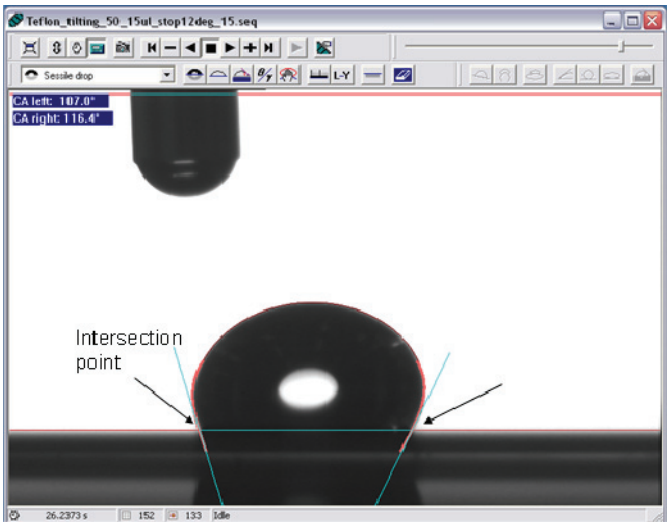

Figure 2.7. Image of droplet shape and indication of the intersection points and the base line.

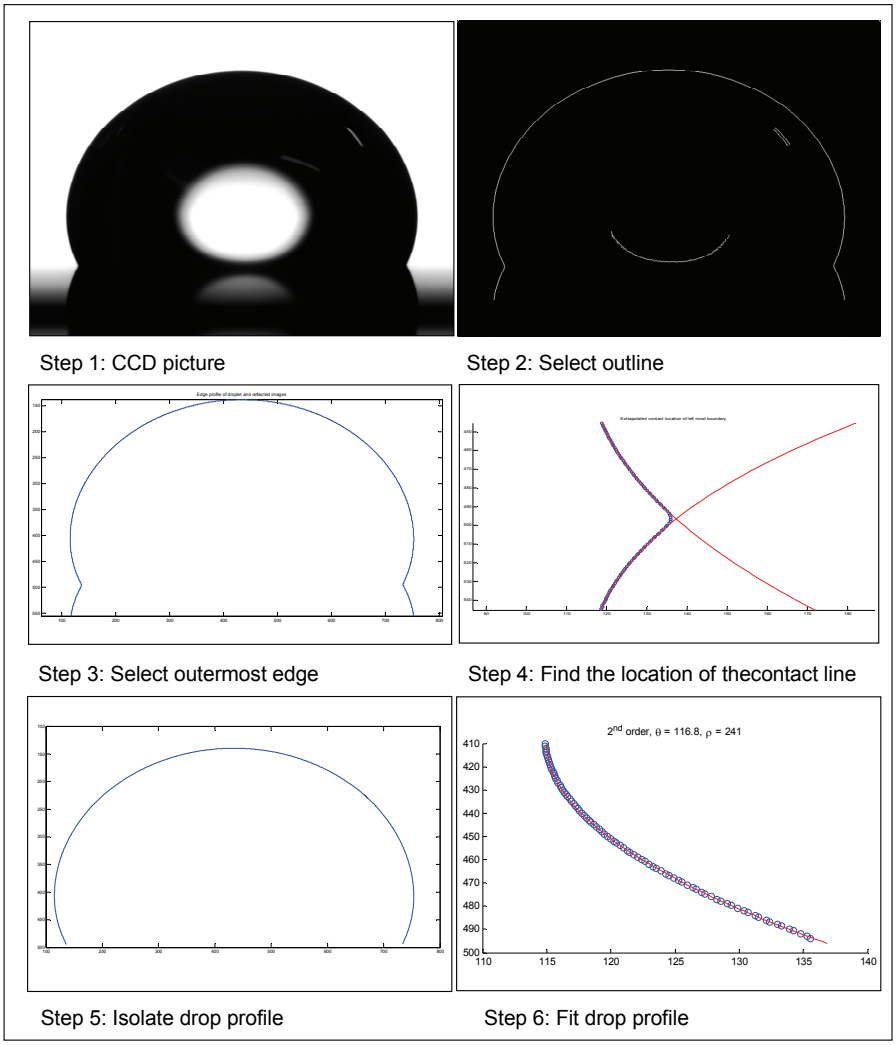

Figure 2.8. Matlab procedure for the accurate contact angle extraction from the images taken by the CCD camera of the contact angle goniometer.

Contact angle extraction

Since the built-in contact angle tool is not sufficiently accurate, a dedicated Matlab routine is developed to accurately extract the droplet profile and contact angles from the acquired images. *Figure 2.8* illustrates the procedure for the extraction of the profile and contact angles: first, the outline is selected based on the contrasts from a droplet image. Next, the outer edge of the droplet is extracted. In the following step, the profile is smoothed and filtered. Then, both the profile and its reflecting counterpart are extrapolated to find the location of the contact line. Next, the reflection is removed and only the profile of the droplet is kept. On the points of this profile, a curve fitting is performed. In the procedure,

the order of the fitting curve can be chosen. The slope of this fitting curve at the intersection with the base line of the droplet provides the contact angle.

2.2.2 Experimental set-up

The sliding droplet experiments are performed for the case of droplets on a surface (‘*sessile droplet*’) and for the case of a droplet confined between two surfaces (‘*confined droplet’*). In the case of the sessile droplet, the sample of interest is attached to the sample platform using double sided tape to prevent sliding of the sample during the tilting of the contact angle meter. The droplet can be directly dispensed on the sample. Due to the surface tension, the droplet remains hanging from the very narrow dispensing needle. The procedure to dispense the droplet is a follows. First, put the needle with the dispensed droplet attached to it, close to the sample. Now move the sample platform upwards until contact with the droplet is made. Then, the platform can be moved downward with the droplet attached to it. When the dispensing needle is removed, the tilt test can start.

For the case of the confined droplet, a dedicated test fixture is designed and fabricated to mount the surfaces of interest at both sides of the droplet. The fixture consists of two main parts: a fixed bottom part and a top part that can be moved up and down, to vary the spacing between the two surfaces. Planarity of both parts is ensured by 4 alignment pins. The gap between top and bottom part is created by spacers. To control the height, several silicon spacers of 330±3 µm thickness are used. Both parts are then clamped together using screws. In the top part, a small removable part is foreseen to enter in a new droplet. In this way the fixture does not need to be unscrewed after one measurement to add a new droplet. It is sufficient to remove the small part to access the bottom sample. In this way, the height of the channel is kept constant for several experiments.

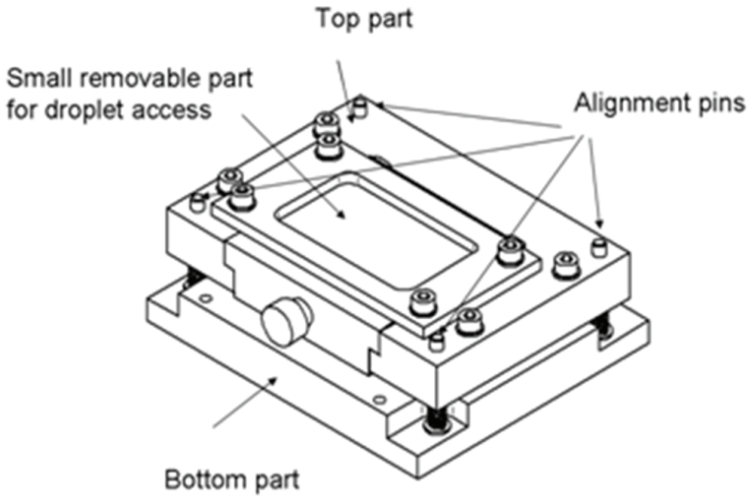

Figure 2.9. Fixture to characterise the droplet motion between two samples.

2.2.3 Description of the test samples

In this section the different tested samples are discussed. After each measurement of a droplet sliding down the surface, the sample surface needs to be cleaned in an ultrasonic bath to remove all traces of liquid on the surface. These potential films of a liquid might influence the droplet motion onset.

Polished Silicon: Teflon® coated

The first coating that has been tested is Teflon® AF1600. This is an amorphous fluoropolymer material that is commonly used in microfluidic applications to provide hydrophobic coatings and electrical insulation layers for electrowetting. For this set of test samples, the coating is deposited on a smooth Si 2" wafer. The surface roughness is assessed using an optical laser profilometry system (Wyco from Veeco®). Using atomic force microscopy (AFM) the local surface roughness can be measured more accurately. However, to reveal the global roughness in roughly 1 x 1 mm² area, the laser profilometry is more suitable. The measured surface roughness R_a of the polished Si is less than 1 nm as can be seen from Figure 2.10. Averaged over 8 samples, the surface roughness is 0.96±0.06 nm. These test samples will be used as a reference case for the retentive force on a "flat" surface.

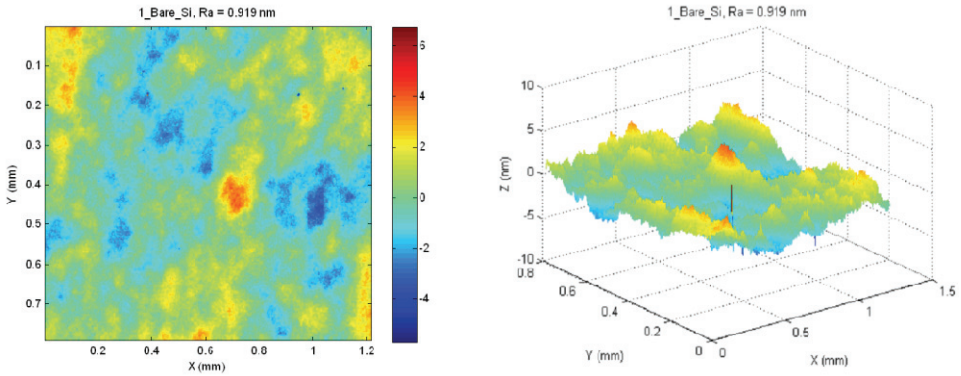

Figure 2.10. Area scan (Wyco) of the surface roughness (expressed in nm) of the surface of a polished Si 2" wafer.

For the coating of Teflon, the Si sample is first cleaned using a 'Piranha Clean' with H_2O_2/H_2SO_4. Afterwards, the sample is put in an oven at 150 °C to dry completely. Next, an adhesion promoter (HMOS) is spin coated on the Si sample at 9000 rpm for 30 s. The adhesive is then cured for 5 minutes in the oven at 100 °C. Finally the Teflon is spin coated at 2000 rpm for 30 s and cured in the oven for 10 minutes at 160 °C to remove the solvent and for another 10 minutes at 330 °C to completely cure the Teflon. For these samples, a Teflon concentration of 6% is used. This results in a coating thickness of 1 to 2 µm. By reducing the Teflon concentration in the solvent, a thinner Teflon coating can be achieved (Saeki *et al*. 2001). To create thinner Teflon coatings on the test samples, the solvent was diluted with the fluorinert FC-40 (3M®). Concentrations of 6%, 3% 1.5% and 0.5% respectively have been used. For these concentrations, the Teflon is spin coated at 1000

rpm for 30 s. The complete procedure for the Teflon coating including the intermediate cleaning steps can be found in Appendix C. The roughness of the coated sample, and the thickness of the polymer coating can not be measured with the laser profilometry since the coating is transparent.

Rough Silicon samples: ground with sand paper

To study the influence of roughness on the contact angle behaviour and the retentive force, Si samples with different level of roughness were created by grinding the surface with different grades of SiC sand paper:

- P400 'extra fine' (average particle size: 35 µm) $R_a = 216 \pm 32$ *nm*
- P1200 'super fine' (average particle size:15.3 µm) $R_a = 140 \pm 13$ *nm*
- P4000 'ultra fine' $R_a = 10.7 \pm 1$ *nm*
- Sand blasted $R_a = 4700 \pm 500$ *nm*

Figure 2.11 gives an overview of the surface roughness of the 4 samples: the average roughness is 216 nm, 140 nm, 11 nm and 5 µm for the P400, P1200, P4000 and sand blasted samples respectively. The roughened samples are coated with a Teflon or Paralyne coating. Appendix C provides the complete procedure for this coating.

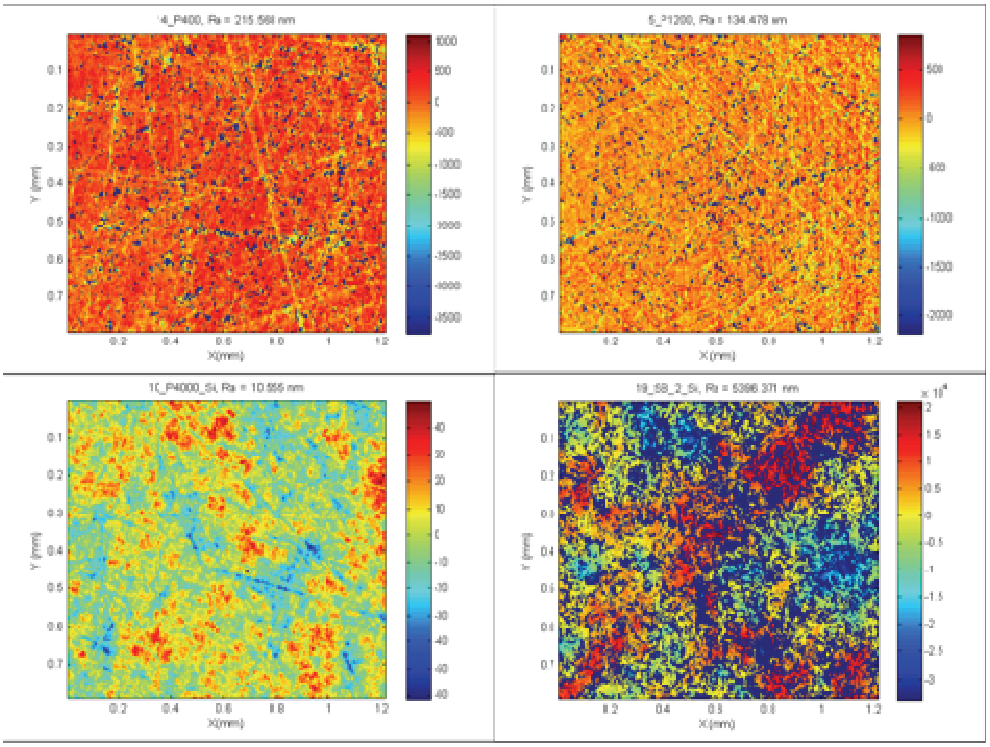

Figure 2.11. Area scan of the surface roughness (nm) of the different ground surfaces: (a) P400, (b) P1200, (c) P4000, (d) sand blasted.

2.3 Sliding on smooth surfaces

In this section, the behaviour of droplets sliding down a tilted Teflon coated surface is studied. During the experiments, the required tilt angle to initiate droplet motion and the evolution of the contact angles are investigated. First, the behaviour is studied for a sessile droplet, and afterwards the case of a confined droplet is investigated. Figure 2.12 shows the convention, used for the contact angle measurements for droplets sliding down tilted surfaces. The direction of motion is towards the right of the picture.

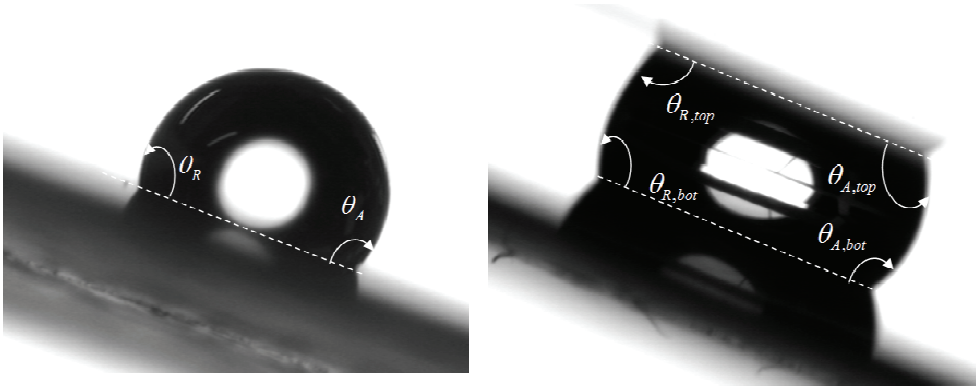

Figure 2.12. Convention of the contact angle measurement in droplets on a tilted surface for: a sessile droplet (left), a confined droplet (right).

2.3.1 Theoretical considerations

The formulation of the retentive force (Extrand and Kumagai 1995) can be used to evaluate the required force needed to move a droplet for a simplified case. Consider a droplet on a tilted solid substrate with a tilt angle α. The static contact angle of the droplet on the horizontal surface is θ_0. The pulling force in the direction of the droplet motion is

$$F_{grav} = \rho \cdot g \cdot Vol \cdot \sin\alpha; \tag{2.17}$$

where Vol is the volume of the liquid droplet. Considering small contact angle hysteresis, the advancing and receding angle can be written as follows:

$$\begin{aligned} \theta_a &= \theta_0 + \Delta\theta/2 \\ \theta_r &= \theta_0 - \Delta\theta/2 \end{aligned} \tag{2.18}$$

with $\Delta\theta$ the contact angle hysteresis. Using equation (2.18) the retentive force (2.11) can be written as:

$$F = 2\gamma Rk \sin\theta_0 \sin\left(\Delta\theta/2\right) \tag{2.19}$$

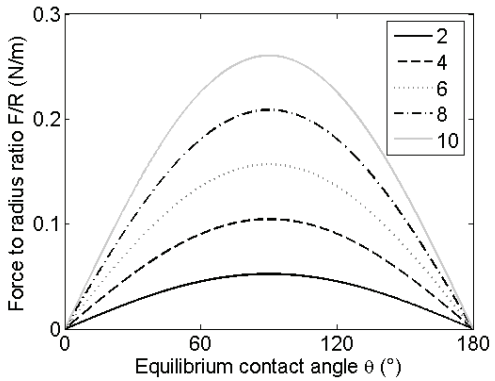

Figure 2.13. Ratio of the required gravitational force to the radius of the contact line of the sessile droplet as a function of the contact angle, for different values of the contact angle hysteresis.

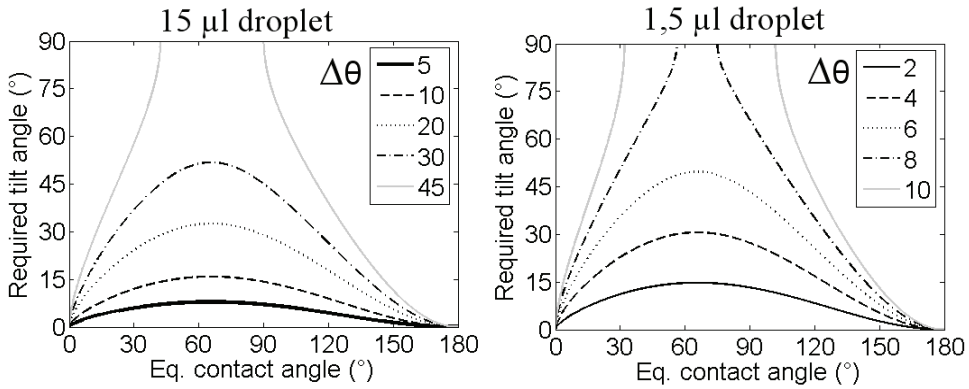

Figure 2.14. Required sliding tilt angle to move a sessile droplet down a tilted surface as a function of the equilibrium contact angle θ_0 for different indicated values of the maximum contact angle hysteresis $\Delta\theta$ and for a droplet volume of 15 µl (left) and 1.5 µl (right).

If the droplet shape is approximated by a truncated sphere, the radius of the contact line R can be expressed as a function of the droplet volume and equilibrium contact angle. For a certain value of the maximum contact angle hysteresis $\Delta\theta$ and droplet volume, the required tilt angle can be calculated. Using equation (2.19), the ratio of the required force to move the droplet to the contact line radius can be expressed as follows :

$$F/R = 2\gamma k \sin\theta_0 \sin\left(\Delta\theta/2\right) \tag{2.20}$$

This ratio is independent of the droplet volume, considered there is no volume dependence of the contact angle. This relationship between this ratio and the contact angle and contact

angle hysteresis is plotted in Figure 2.13. Using the expression of the gravitational force (2.17), the required tilt angle can be expressed as follows :

$$\alpha = \arcsin\left(\frac{2\gamma Rk\sin\theta_0\sin\left(\Delta\theta/2\right)}{\rho g \cdot Vol}\right) \tag{2.21}$$

where the contact line radius R is a function of the droplet volume. Figure 2.14 shows the required tilt angle to overcome the retentive force of a sessile droplet on a tilted surface as a function of the equilibrium contact angle, the maximum contact angle hysteresis for droplet volumes of 1.5 and 15 µl. As mentioned in the scaling analysis in Figure 2.2, for smaller droplets the relative importance of the surface forces is larger than the one of the body forces. From Figure 2.14 can be seen, that for a smaller droplet a higher tilt angle is required to move the droplet for the same contact angle hysteresis (e.g. 10°) compared to the large droplet. The graph also indicates that to minimise the retentive force not only the equilibrium contact angle should be as high as possible (hydrophobic), but also its hysteresis should be minimal.

2.3.2 Sessile droplet on a substrate

Measurements on a horizontal surface

First, the contact angle and droplet shape are studied for a stationary droplet on a flat horizontal substrate. As discussed in Section 2.1.1, the surface tension is the dominant force for small liquid droplets in the µl range, while the influence of the gravity can be neglected. For larger droplets, the contribution of the gravitational energy is increasing. This effect can be noticed from the deformed droplet shape; the droplet flattens due to the gravitational force on the liquid. As a result of this, the contact angle increases as the drop size increases. The Young's contact angle will therefore only be measured in the case of sufficiently small droplets. Contact angles as a function of volume (1 – 35 µl) are measured on the Teflon coated smooth surface to study the volume dependence. The contact angle measurements (Figure 2.15) show that the influence of gravity on the contact angle and droplet shape is visible for volumes larger than 15 µl. Smaller droplets, in the nanolitre range, for which the line tension has a significant influence, are not considered here.

When the droplet is exposed to air, the liquid of the droplet will evaporate. As a result the volume of the liquid droplet will decrease. To study the effect of evaporation, the droplet volume is monitored over time for a liquid droplet on a Teflon surface. From the droplet image, the droplet profile is extracted and the number of pixels inside this profile is calculated. This number of pixels is a measure for the area of the projection of the droplet. As such, the droplet volume can be estimated for an assumed circular contact line. In Figure 2.16 the reduction in droplet volume as a function of time is shown for a 1 µl and a 15 µl droplet. In the case of the large 15 µl droplet, the droplet volume is reduced by 20% after 10 minutes. By that time, 65% of the volume of the 1 µl has evaporated. This needs to be taken into account while performing experiments with liquid droplets. The evolution of the droplet volume is shown for the purpose of illustration. The evaporation rate at a liquid surface scales with the surface area. However, in the case of a pinned sessile droplet, the

evaporation rate scales with the length of the contact line. For the experiments described in the next chapter, glycerol is added to the liquid to prevent this evaporation.

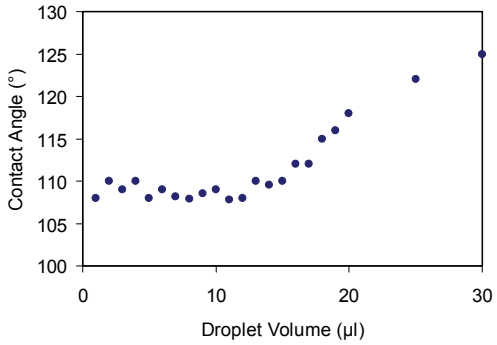

Figure 2.15. Contact angle of a sessile droplet on a Teflon surface as a function of the droplet volume.

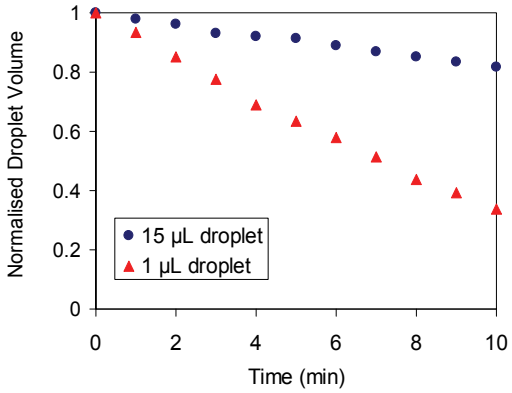

Figure 2.16. Evaporation of the liquid sessile droplets on a Teflon coated surface.

Measurements on a tilted surface

Two types of measurements are performed on the tilted surface. In the first set of experiments, the contact angles and position of the contact line are monitored during the deformation and motion of the droplet. The second set of experiments determines the minimum tilting angle required to move the droplet. This angle corresponds with the maximum force the surface tension can generate, by deforming the droplet shape to compensate the gravitation.

In the first set of experiments, the platform is tilted with a constant rotational speed. During this tilting motion, the advancing and receding contact angles and the location of the intersection points of the droplet profile with the surface are measured.

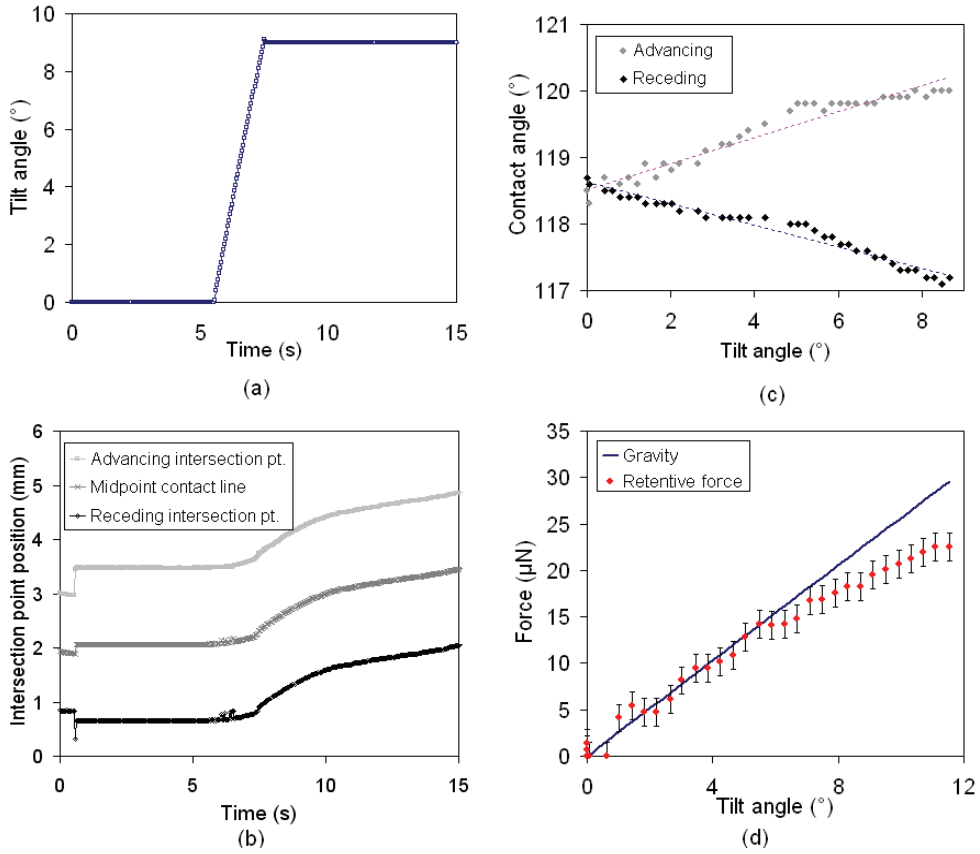

Figure 2.17. Variation of the advancing and receding contact angle of a 20 µl droplet on a Teflon coated surface for increasing tilt angle until the droplet starts sliding.

In Figure 2.17 the results of a typical tilt measurement for a droplet of 20 µl are summarised. The first graph (a) shows the tilt angle of the platform as a function of time. In this case, a maximum tilt angle of 9° is used. A small overshoot and oscillation can be observed in the profile at the moment the maximum tilt angle is reached and the platform is stopped. The oscillation of the droplet causes a vibration of the droplet, which might initiate the droplet motion even though the critical angle is not reached. Therefore the maximum tilt angle is chosen higher than the critical angle. The system takes pictures of the droplets with a frame rate of 25 images per second. The second graph (b) shows the location of the left and right intersection point of the droplet profile extracted from these images. From this graph, both the droplet length and the contact line velocity can be calculated. For the low velocities studied here, the droplet length, which is the distance between the left and right intersection point, does not change during the initial motion of the droplet. Therefore the droplet contact line can be considered circular at low contact line velocities. The third figure shows the evolution of the advancing and receding contact angle as a function of the tilt angle. From these contact angle measurements, the retentive force can be calculated for each tilt angle using equation (2.11) and the assumptions of a circular

contact line. The evolution of this retentive force is presented in the fourth graph of Figure 2.17. The graph indicates that the surface tension of the droplet is able to compensate the gravitational force by deforming the droplet shape. From a tilt angle of 7 − 9°, the retentive force of the surface tension is not sufficient to counteract the gravity and the droplet will start moving. This detailed analysis of the droplet behaviour is repeated for 10 tests. These types of measurements give information about friction force of the surface that has to be overcome and about the deformation of the droplet in the phase before motion.

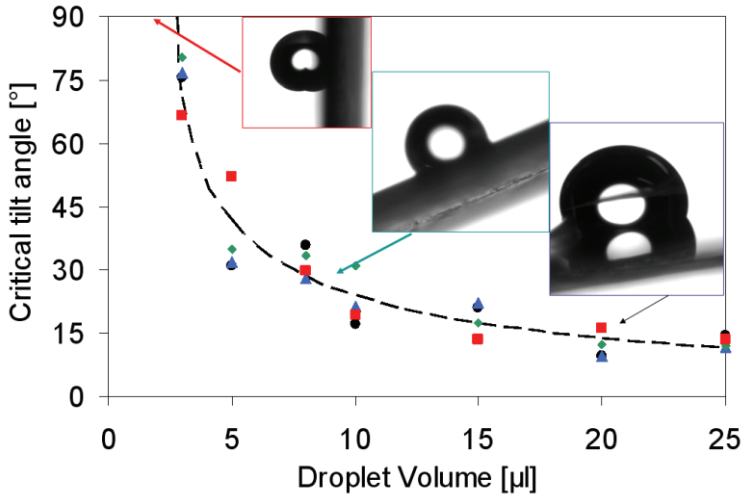

Figure 2.18. Critical tilt angle of droplets on a Teflon coated smooth surface as a function of the droplet volume. The dashed line indicates the predicting of the critical angle based on the measurement of the maximum contact angle. The markers (■, ◊, ▲, ●) represent the measurement results for four different experiments.

In the second set experiments, the critical tilt angle is derived for different volumes of liquid on the Teflon coated smooth surface. The critical tilt angle is defined as the minimal tilt angle for which the droplet starts moving on the surface. These experiments are performed for a volume range of 1 to 25 µl. Droplets smaller than 3 µl will remain stuck to the surface, even when placed vertically. The results of the critical tilt angle measurements are summarised in Figure 2.18 for four sets of experiments.

Using the maximum contact angle hysteresis of a water droplet on the Teflon surface, as determined in Figure 2.15, the critical angle can be predicted as follows:

$$\sin\alpha_c = \frac{2\gamma k R_b \left(\cos\theta_R - \cos\theta_A\right)_{\max}}{\rho g \cdot Vol} \tag{2.22}$$

The radius of the circular contact line can be calculated as a function of the droplet volume and the equilibrium contact angle. For the estimation of the contact angle, the relationship between the contact angle and the droplet, displayed in Figure 2.15 can be used. The relationship of the critical contact angle α_c as a function of the droplet volume is added to Figure 2.18. The agreement between the prediction and the experimental results is

reasonable, considering the large variation in measurement results due to local effects of the surface.

Dynamic analysis

In Section 2.1.3, the dynamic effects of the contact line velocity on the contact angle hysteresis are introduced. These dynamic effects add a velocity dependent term to the expression of the retentive force, in the form of the coefficient of contact line friction ζ (2.14). This coefficient can be extracted from the tilt experiments. Figure 2.19 shows the evolution of the contact line velocity during the droplet motion over the tilted surface. This profile is calculated from the position of the advancing contact line of Figure 2.17(b). The first peak corresponds to the start of the droplet motion. The final peak corresponds to the acceleration of the droplet at the end of the sample.

In Figure 2.20(a) the advancing and receding contact angles are plotted as a function of this velocity. Using equation (2.11), the retentive force can be calculated for each data point. Figure 2.20(b) shows this force as a function of the contact line velocity. Using a linear approximation of the dynamic effect, the coefficient of contact line friction ζ can be estimated for the graph. This linear approximation is indicated as a dashed line in Figure 2.20(b). Averaged over 10 measurement series, a 95% confidence interval of 0.08±0.03 Pa.s is found for the friction coefficient. This coefficient will be used in Chapter 4 for the dynamic modelling of the electrostatic actuated droplet.

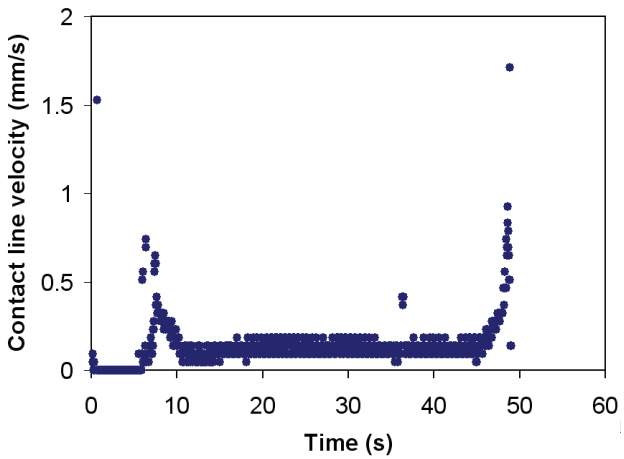

Figure 2.19. Evolution of the contact line velocity as a function of time during the tilting of the surface.

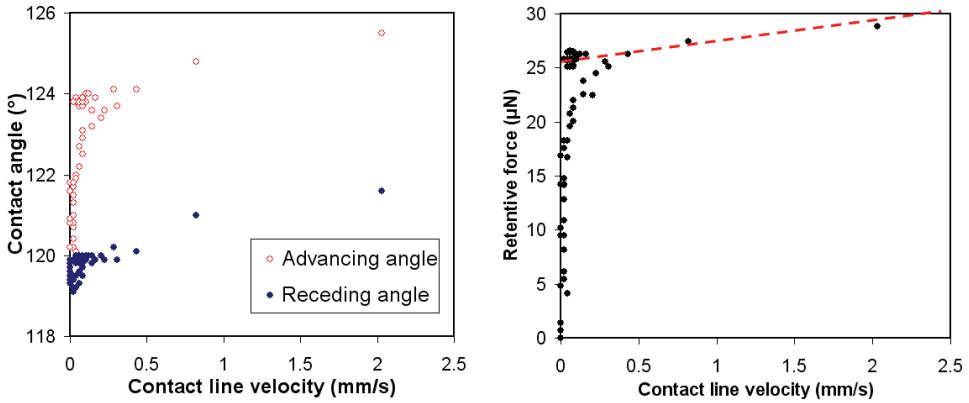

Figure 2.20. Evolution of the receding and advancing contact angles (a) and the retentive force (b) during the tilt motion as a function of the contact line veolocity.

2.3.3 Confined droplets between two surfaces

In this section, the retentive force for a droplet confined between two smooth surfaces is tested. This is the situation that occurs in the case of the two parallel planar electrodes with the droplet in between. The fixture, described in Figure 2.9, is used to mount the two surfaces. The gap between the surfaces is defined by stacking of spacers with a thickness of 330±5 µm. This is schematically represented in Figure 2.21. The automated procedure to detect the droplet interface and estimate the contact angles does not work in that case due to the many reflections on the surface. Therefore, the contact angles have to be extracted manually. This however, leads to larger errors and a larger spread on the results. First, the evolution of the contact angles during deformation before motion is studied. Afterwards, the critical tilt angles are determined.

Droplet volumes of 10 and 20 µl in a channel with a height of 1.32 mm are used to study the behaviour of the contact angles with increasing tilt angle. For the contact angle measurement and nomenclature, the convention of Figure 2.12 is used. In Figure 2.22, the evolution of the 4 contact angles as a function of the tilt angle is presented. The graph indicates that both the advancing angle at the top and bottom side increase with increasing tilt angle, whereas the receding angles at the top and bottom side decrease. When the contact angles are known, the friction force at top and bottom side can be calculated. The combination of the friction force from the top and the bottom side can compensate the gravity until a tilt angle of 39°±4° for the case of the 10 µl droplet. The 20 µl droplet remains stuck to the surfaces until 25°±3°.

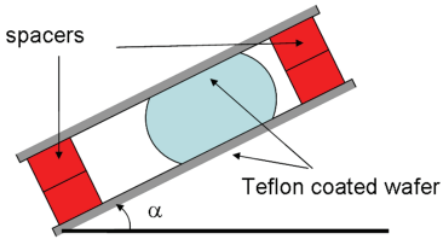

Figure 2.21. Schematic representation of the droplet in the confined channel and the stand off between the two surfaces.

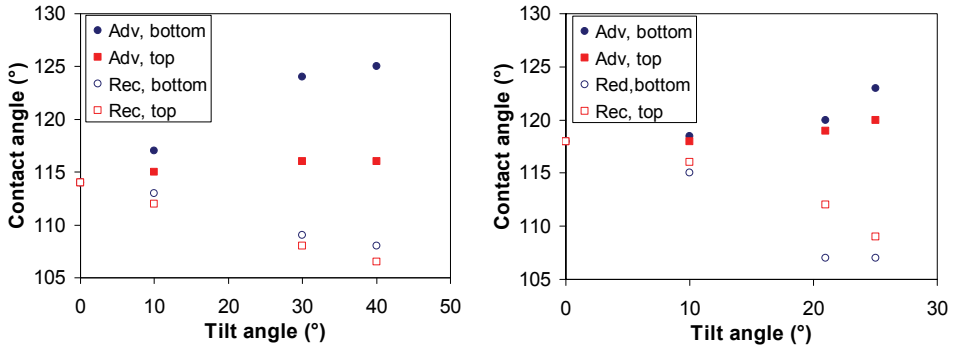

Figure 2.22. Evolution of the contact angles in the droplet in a channel with a height of 1.32 mm for different tilt angles; (a) 10 µl droplet, (b) 20 µl droplet.

In the second set of experiments with the double sided channels, the critical angle is studied for different droplet volumes and different values for the height of the channels. The droplet volumes that are used are 3, 8, 10, 15 and 20 µl. For the height of the channel 2, 3 and 4 spacers are used to create a stand off height of 0.66 mm, 0.99 mm and 1.32 mm respectively.

Figure 2.23 shows a few pictures of combinations of these volumes and heights. In both the 0.99 mm and 0.66 mm channel, the 3 µl droplet remains. In the 1.32 mm channel, the 3 µl droplet starts moving for a tilt angle of 81°±7°. However in this case, the channel is higher than the height of the sessile drop. Therefore, the drop will not touch the top surface and slide down on the bottom surface as presented in the previous section. Only the 15 µl and 20 µl droplets could be pulled down by gravity in the 0.66 mm channel; the three other droplets remained stuck. Figure 2.24 gives an overview of three series of measurements of the critical tilt angles for the described configurations of channel height and droplet volume. The markers present the experimental data for the critical tilt angles. The solid lines are predictions based on the observed hysteresis on the top and bottom face.

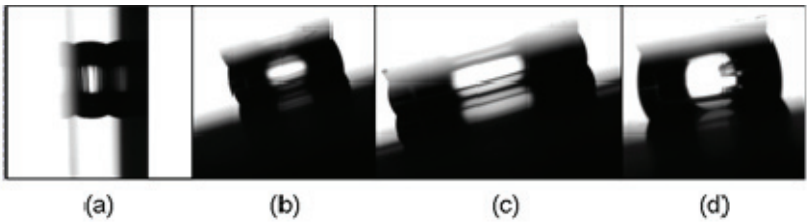

Figure 2.23. Pictures of droplets in a tilted confined channel: (a) 3 µl drop, 0.66 mm gap, (b) 8 µl drop, 1.32 mm gap, (c) 20µl drop, 0.66 mm gap,(d) 20 µl drop, 1.32 mm gap.

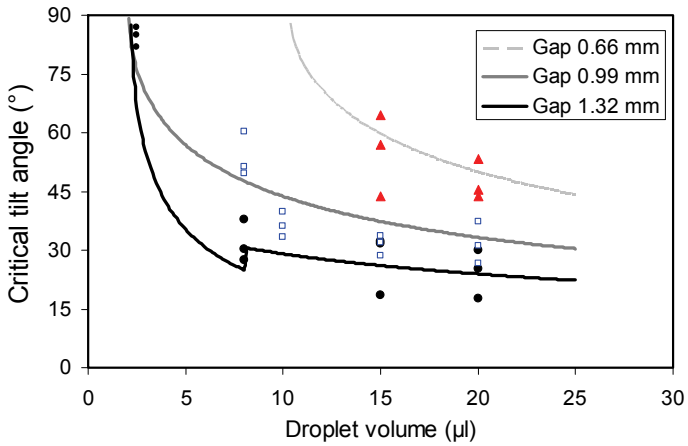

Figure 2.24. Measurement results of the critical tilt angle for a droplet in a confined channel with a height of 0.66 mm (triangles), 0.99 mm (squares) and 1.32 mm (dots) . The solid lines indicate the prediction of the critical tilt angle based on the observed maximum hysteresis.

The predictions are based on a simplified geometry of the droplet between two surfaces. The volume of the droplet can approximately be described as a function of the equilibrium contact angle θ, the height of the channel H and the droplet volume Vol as follows (Appendix A equation A.26):

$$Vol = \pi R_c^2 H + \frac{\pi R_c H^2}{\cos^2\theta}\left(\alpha + \frac{\sin 2\alpha}{2}\right) \tag{2.23}$$

where R is the radius of the circular contact line. From this equation, the radius of the circular contact line can be estimated based on the volume, channel height and contact angle. Combining this with the observed maximum hysteresis at the top and bottom side, the critical tilt angle α_c (2.11) can be written as a function of the droplet volume as follows:

$$\sin\alpha_c = \frac{2\gamma kR \cdot \left[\left(\cos\theta_{R,top} - \cos\theta_{A,top}\right)_{\max} - \left(\cos\theta_{R,bottom} - \cos\theta_{A,bottom}\right)_{\max}\right]}{\rho g \cdot Vol} \tag{2.24}$$

where the radius of the contact line R is a function of the droplet volume. For each volume, this radius can be calculated numerically from the droplet volume using (2.23). For smaller droplets, the height of the droplet might be smaller than the height of the channel. In this case the droplet will not touch the top surface, and will slide down the bottom surface as a sessile droplet. When this happens, formula (2.22) for the sessile case has to be used for the calculation of the critical tilt angle. This jump can be observed in Figure 2.24 in the curve for the 1.32 mm channel. For droplets larger than 7 µl, the confined formulation (2.24) is used, while for smaller droplets the sessile formulation (2.22) is used. The agreement between the experimental data and predictions is good, considering the manual contact angle measurements, which might lead to large errors.

2.3.4 Scaling analysis of the retentive force on a flat surface: extrapolation of the force to small droplet volumes

The smallest droplet that can be moved down on the smooth surface is a 3 µl droplet. For smaller droplets no measurement could be made for the friction force. However, the droplets used in digital microfluidic applications are smaller; typically in the range of 0.5 to 2 µl. Therefore the force formulations need to be scaled down in order to extrapolate to the range of interest. The retentive force of a sessile droplet can be estimated as a function of the droplet volume and the maximum contact angle hysteresis. Substitution of the radius of a sessile droplet (Appendix A.1) in the equation of the retentive force (2.11) leads to:

$$F_{sessile} = 2\gamma k \cdot \sqrt[3]{\frac{3 \cdot Vol}{\pi\left(\cos^3\theta + 3\cos\theta - 2\right)}}\left(\cos\theta_R - \cos\theta_A\right)_{\max} \tag{2.25}$$

In the case of the confined droplet, the force can be expressed as follows:

$$F_{confined} = 2\gamma kR \cdot \left[\left(\cos\theta_{R,top} - \cos\theta_{A,top}\right)_{\max} - \left(\cos\theta_{R,bottom} - \cos\theta_{A,bottom}\right)_{\max}\right] \tag{2.26}$$

where R is calculated as a function of the droplet volume (Appendix A.2). When the droplets are too small to wet the top surface, the droplet sits on the bottom surface as a sessile droplet. In this case, expression (2.25) for the sessile drop should be used. In Figure 2.25(a), these relationships are shown for the critical tilt angles of the cases discussed in the previous section. This critical angle can be more generally translated into a force that is required to move the droplets. This force is extrapolated and indicated on the right hand side of Figure 2.25 for the range of interest of 0.5 to 2 µl. In this graph, the required force is shown as a function of the channel height and the droplet volume. These relationships will be used in the dynamic modelling of the droplet motion in Chapter 4.

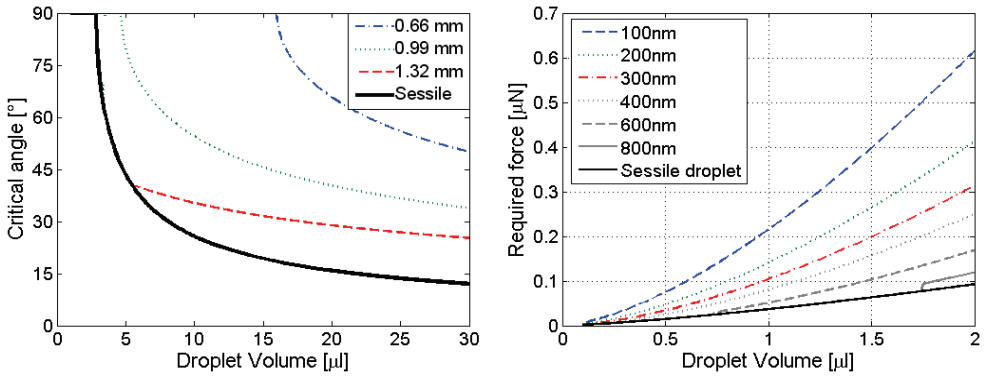

Figure 2.25. (Left) Prediction of the critical tilt angle as a function of the droplet volume for confined and sessile droplets. (Right) Minimal force required to slide a droplet through a channel with indicated height.

2.4 Droplet motion on rough surfaces

In Section 2.3.1, it is shown that the retentive force of a droplet depends on the equilibrium contact angle and the contact angle hysteresis. The hysteresis is influenced by inhomogeneities in the surface chemistry, the surface roughness and the velocity of the contact line. To reduce the force either the contact angle or the hysteresis could be changed, or both. An easy way to change both the apparent contact angle and the hysteresis, is increasing the surface roughness of the surface. In this section, the influence of the surface roughness on the contact angle, contact angle hysteresis and the retentive force is studied.

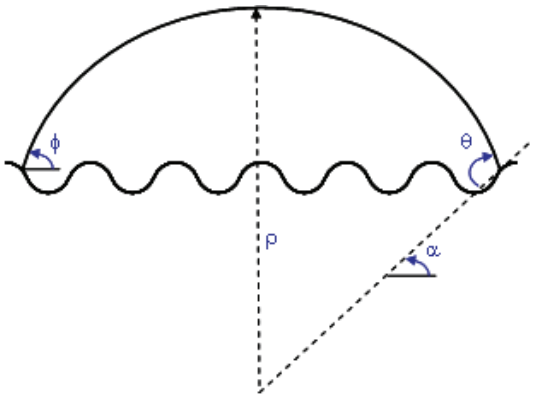

Figure 2.26. Schematic representation of the 1D model of a droplet on a rough surface (Johnson and Dettre 1964).

2.4.1 Theoretical considerations

The roughness of the solid surface will not only influence the apparent macroscopic contact angle θ of the liquid but also the contact angle hysteresis $\Delta\theta$. On a real non-ideal surface, not one equilibrium contact angle will be observed but a range of possible equilibrium situations is possible. This range is the contact angle hysteresis. To study the effect of the roughness on both the apparent contact angle and the contact angle range, Johnson and Dettre (1964) presented an analytical axisymmetric model for contact angle hysteresis on an idealised surface; the profile of the rough solid is assumed to be sinusoidal. The idealised surface is schematically represented in Figure 2.26. In this graph, θ is the Young's contact angle: this is the intrinsic contact angle between the liquid droplet and the horizontal flat surface on which the droplet is placed. ϕ is the apparent contact angle and α is the slope of surface locally at the contact line. With this formulation the apparent contact angle and the range of the contact angle can be predicted as a function of the normalised roughness z_0/x_0, where z_0 is the height of the ridge of the rough surface and x_0 is the period of the sinusoidal surface.

Johnson and Dettre model description

Johnson and Dettre (1964) describe an analytical model to predict the apparent contact angle on an idealised rough surface. Based on the droplet volume, the normalised roughness and the intrinsic contact angle, the apparent contact angle can be predicted. In Appendix B, this model is reproduced and an implementation to lead to a stable, converged solution is presented.

Application of the roughness model

The model, described in Appendix B, is now applied to study the effect of the roughness of an ideal rough surface on the apparent contact angle. For each value of the roughness z_0/x_0, a range of potential apparent contact angles $[\phi_{\min}, \phi_{\max}]$ is calculated. This interval is discretised in a certain number of points. For each of those points, corresponding to a value of the apparent contact angle, the relative free surface energy is calculated. This is illustrated in Figure 2.27 for an intrinsic contact angle θ of 105° and for four values of the normalised surface roughness ($z_0/x_0 =$ 0.001, 0.01, 0.1 and 0.4 respectively) for a droplet volume of 2 µl and an intrinsic contact angle of 110°. The left hand side of Figure 2.27 shows the evolution of the surface energy as a function of the contact angle for the four values of the normalised roughness. The minimum of this curve corresponds with the apparent contact angle that is most likely to be observed. The red dot on the figure indicates this point. However, all points on the curve are potential values of the apparent contact angle. This range of values corresponds to the contact angle hysteresis. Which of those values will be observed depends on the history of the deposition of the droplet. On the right hand side of the figure, for each value of the normalised surface roughness, the minimum $\phi_{\min}$ and the maximum $\phi_{\max}$ of the range of potential apparent contact angle, and the apparent contact angle ϕ, corresponding to the minimum of the surface energy curve are plotted. For this analysis, 100 points are chosen logarithmically between $z_0/x_0 =$ 0.0001 and

0.4. The range $[\phi_{min}, \phi_{max}]$ indicates the range of physically possible contact angles. Therefore, the right hand side of Figure 2.27 corresponds to the evolution of the maximum possible advancing, minimum possible receding, and equilibrium contact angles as a function of the normalised roughness x_0/z_0. It can be observed that as the surface roughness increases, both the apparent contact angle as well as the contact angle hysteresis increase. This simple model shows that it is possible to alter the contact angle and hysteresis by changing the surface roughness and what the expected effect of this change is. An increase in apparent contact angle will lead to a decrease in the retentive force. However an increasing contact angle hysteresis has the opposite effect.

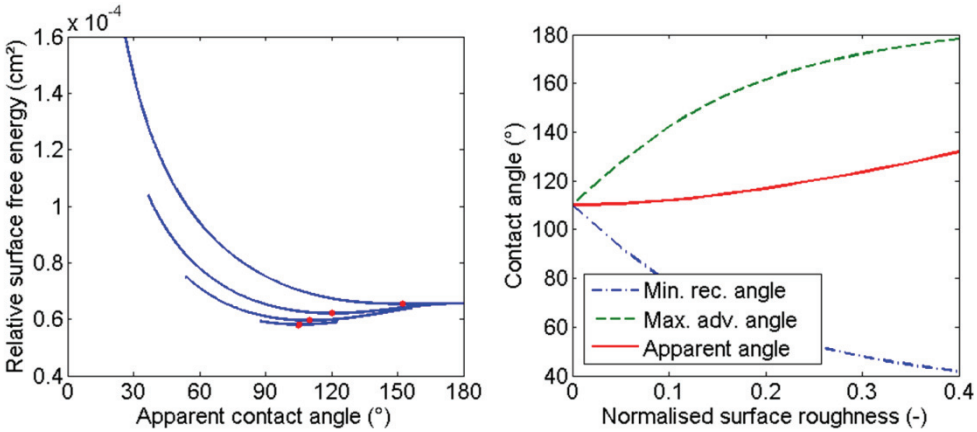

Figure 2.27. Surface energy as a function of the apparent contact angle for different roughness values (left), Apparent contact angle and hysteresis as a function of the surface roughness (right).

2.4.2 Measurements on rough surfaces

In this section, the use of surface roughness to reduce the retentive force is studied. For samples with different coating and roughness, several parameters are extracted using the tilting experiments; (1) the apparent contact angle, (2) the contact angle hysteresis and, (3) the critical tilt angle. A lower tilt angle indicates a reduced retentive force.

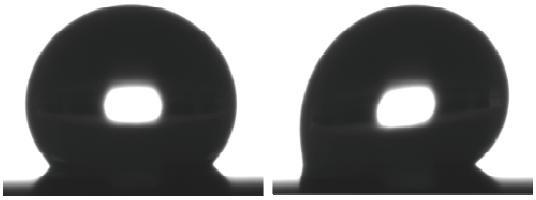

Figure 2.28. Picture of a droplet on a rough sample; (left) horizontal sample, (right) tilted sample.

Teflon coated rough samples

First the effect of the surface roughness is studied for Teflon coated surfaces. The different samples are discussed in Section 2.3.3. These samples are coated using a 6% Teflon concentration in the solution. In this case the thickness of the coating is 1 to 2 µm. Four different values of roughness are tested: a smooth surface, a surface ground with P400, a surface ground with P180 and a sand blasted ('SB') sample. First, the apparent contact angle is measured on a horizontal sample. A typical image of such a droplet is shown on the left hand side of Figure 2.28. Next, the surface is tilted to find the critical tilt angle to initiate droplet motion and the contact angle hysteresis at that moment (see right hand side Figure 2.28). In Figure 2.28, the apparent contact angle (a), the contact angle hysteresis (b), and the critical tilt angle (c) are presented for increasing roughness values of the surface.

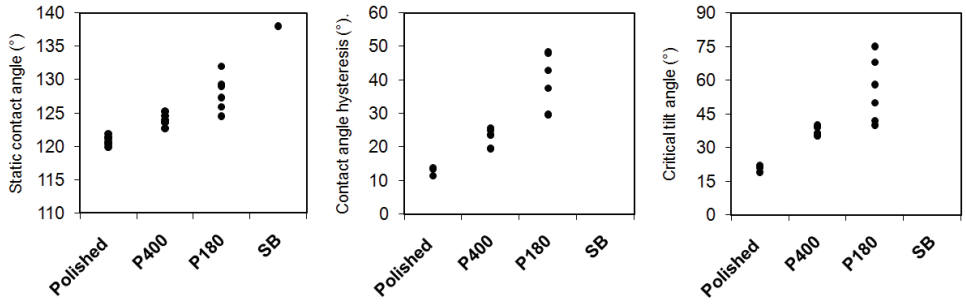

Figure 2.29. Measurement results for the contact angle (a), contact angle hysteresis (b), and critical tilt angle (c) for a 10 µl sessile droplet on a Teflon® coated surface with different surface roughness.

As predicted with the simplified model, the apparent contact angle increases with increasing roughness; the contact angle increases to 138° for the roughest sample (sandblasted, R_a=5 µm), starting from an angle of 121° for the smooth sample. For the contact angle hysteresis, the increase is even more pronounced; the hysteresis increases from 13±1° for the smooth sample, over 23±3° for the P400 sample, to 39±8° in the case of the P180 sample. In graph (c) the critical tilt angle is shown. From this can be seen that the force, required to move the droplet increases for rougher samples. Roughening the surface leads to higher contact angles, which is beneficial to reduce the retentive force for droplets on a hydrophobic surface. However, in this case it happens at the expense of the hysteresis. The negative effect of the increased hysteresis is stronger than the positive effect of the apparent contact angle. Therefore in this case, macroscopic roughening the surface will not reduce the required force to move the droplet. The experimental results can be compared to the 1D analytic surface roughness model. In this model the surface is approximated by a concentric roughness. Compared to the experimental results, the 1D model overpredicts increase in contact angle hysteresis and underpredicts the increase in static contact angle.

Teflon concentration – coating thickness

Coatings, that are used to provide an electrical insulation between the liquid droplet and an activated electrode, should be as thin as possible in order to maximise the actuation force acting on the droplet. Or formulated differently; to generate the same force, a smaller voltage is sufficient in the case of a thinner insulation layer. A thick layer of Teflon coating (2 µm) might smooth out the finer roughness of the surface below, whereas a much thinner coating will follow the roughness instead of covering it. This might lead to a rougher top side of the coating. The thickness of the coating spun on the surface of the silicon is controlled by the concentration of Teflon in the solution, and the spinning parameters. For constant spinning parameters, in this case 1000 rpm for 30 s, a solution with a lower Teflon concentration will lead to a thinner coating after evaporation of the solvent and curing of the coating. Here, concentrations of 6, 3, 1.5 and 0.5% Teflon are used. Table 2.2 shows a relationship between the thickness of the spin coated layer and the concentration of Teflon in the solution (Saeki *et al.* 2001). Although the spinning conditions in that reference are not the same as applied in this work, a similar trend can be expected.

Table 2.2. Relationship between the thickness of the spin coated Teflon layer and concentration of Teflon in the solution (from Saeki et al. 2001).

Concent-ration (wt.%)	Thickness (Å)
6.0	16500
5.5	13500
5.0	12000
4.5	10000
4.0	7000
3.0	5500
2.0	2500
1.5	1000
1.0	800
0.6	500
0.2	**200**
0.1	**130**

In Figure 2.30, the results of the contact angle, contact angle hysteresis and tilt angle measurements are summarised for the different Teflon concentrations. In this set of experiments, the coating is applied on a silicon sample ground with P1200 sand paper. A concentration of 6, 3, 1.5 and 0.5% corresponds roughly to an expected coating thickness of 1.5 µm, 500 nm, 100 nm and 50 nm. The thickness of the two thinnest coatings are therefore from the same order of magnitude as the average roughness (R_a) of the ground sample. For the lowest Teflon concentration, an increase in apparent contact angle of 10° is observed. For the thicker layers, no significant effect is observed. The hysteresis and required force, to move the droplet, increase steadily for thinner coating layers. The required force for the coating with a concentration of 1.5% is about 30% higher than the force for the case of 6%. However, the difference in thickness is expected to be a factor of 10. Therefore, this increase in required force does not outweigh the positive effect of the reduction of the insulation layer, considered no electrical breakdown occurs. The effect of the thickness of the insulation layer on the actuation force acting on the droplet is studied in Chapter 3.

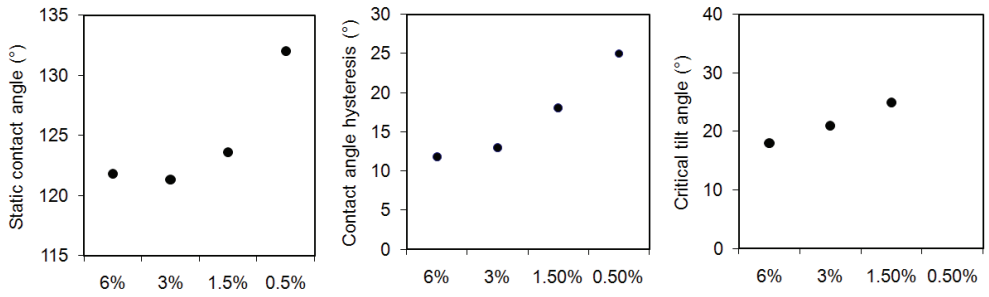

Figure 2.30. Measurement results for the contact angle (a), contact angle hysteresis (b), and critical tilt angle (c) for different concentrations of Teflon® in the spinning solution.

Parylene coating

Another option to increase the actuation force for an applied voltage, is using an insulating material with a higher dielectric constant (see Table 3.1). Both the dielectric constant and the electrical breakdown strength of parylene are higher than those of Teflon. In Figure 2.31 the results of the contact angle, contact angle hysteresis and tilt angle measurements of parylene coated samples are summarised for the different values of the surface roughness. Only for the very rough sample, a small increase in contact angle can be observed. For all samples with low and moderate roughness no significant influence of the roughness on the contact angle, hysteresis and retentive force are observed.

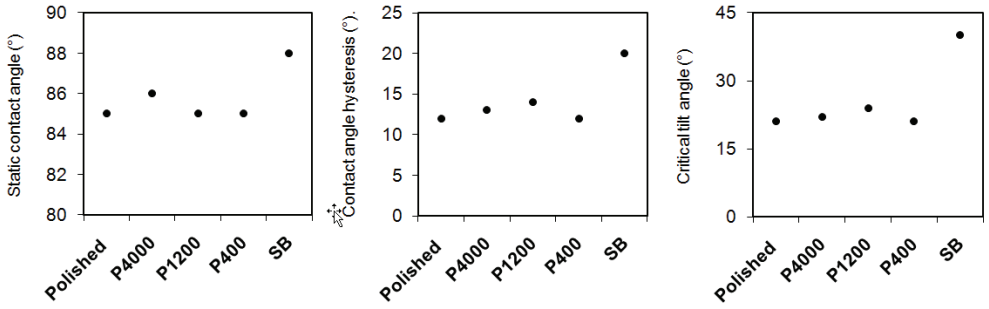

Figure 2.31. Measurement results for the contact angle (a), contact angle hysteresis (b), and critical tilt angle (c) for a 10 µl sessile droplet on a parylene coated surface with different surface roughness.

2.4.3 Other surfaces

In the experimental analysis above, droplets sliding on Teflon and Parylene coatings are investigated. Many other materials could be used to provide (part of) the required properties of the insulation and hydrophobic layers. Materials that could be used include self-assembled monolayers of only a few atoms thick, superhydrophobic materials (contact angle larger than 150°) or other materials with interesting thermal or electrical properties. In this section, several alternative materials or structured surfaces are briefly discussed.

2.4.3.1 Diamond coating

The thermal properties of the coating are important for the application of a droplet flow as a cooling technique. A material with a high thermal conductivity will result in a better heat spreading in the case of local hot spot dissipation and consequently in a lower temperature. Diamond is a material with a very high thermal conductivity: 2000 W/mK at room temperature, which is five times higher than the conductivity of copper. Synthetic diamond can be produced using chemical vapour deposition (CVD) and is already applied as heat spreading material in heat sinks. The thermal properties of the CVD diamond coating depend on the thickness of the layer and the processing details.

In the framework of the IWT-SBO HyperCool-IT project (2008) chemical vapour deposition diamond, deposited with a CH_4/H_2 plasma, is applied as a coating material in channels for electronics cooling. To cover the channels processed in advance in the Si substrates, an ultrasonic pre-treatment will be applied that consists of the immersion of the substrates in a suspension of diamond powder (different grain sizes can be used) in a certain kind of alcohol (e.g. isopropanol) placed in an ultrasonicator (Arnault *et al.* 2007; Haenen *et al.* 2009). When taken out of the reactor, the films are naturally H-terminated. H-termination causes the surface to behave hydrophobic. A simple exposure to an oxidising agent, chemically or through the use of a plasma, replaces the H-atoms by oxygen, switching the surface to a hydrophilic state. Figure 2.32 shows the influence of the exposure time to the oxidant on the droplet shape. Characterisation of the thermal properties (Salebien *et al.* 2009) and the friction properties of the CVD diamond layer is currently ongoing.

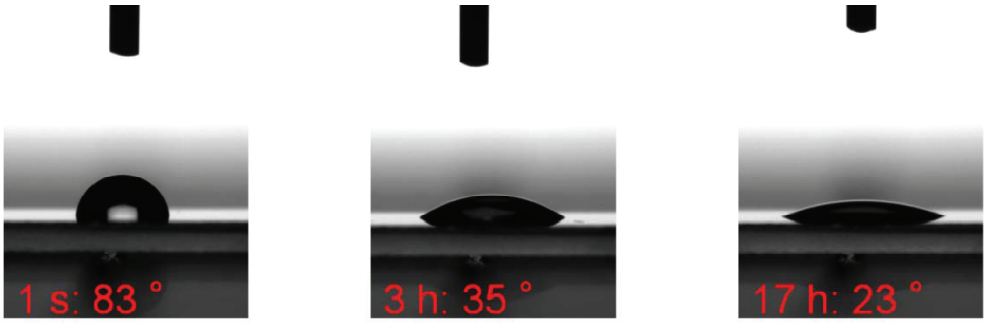

Figure 2.32. Contact angle measurements of a water droplet on a CVD diamond coating, grown with a CH_4/H_2 concentration of 4% and chemically oxidised for different durations (Haenen 2009).

2.4.3.2 Silanised structured surfaces

The retentive force of a droplet on a surface depends on both the static contact angle and the contact angle hysteresis (2.19). Both the static angle and hysteresis are affected by the surface roughness of the solid surface. An increasing roughness leads to a higher contact angle. This results in a lower friction force. On the other hand, an increasing roughness causes a larger contact angle hysteresis, which results in a higher friction force. Therefore, depending on the relative contribution of the contact angle change and the hysteresis change, the effect on the friction force can be positive or negative. In the previous chapter, the effect of mechanically caused roughness was studied. In this section, the influence of a structured roughness is briefly discussed.

Structures with different patterns and pitch are created on a silicon wafer using photolithography techniques and covered with silanes to enhance the hydrophobicity. The details of the processing can be found in (Linde Sanchez 2008). The height of the structures is 25 – 35 µm depending on the etching time. Figure 2.33 shows a SEM picture of the structured surface and several examples of the pillar shapes.

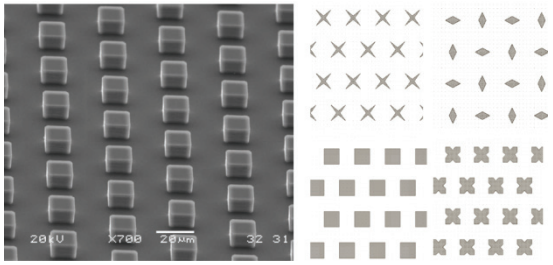

Figure 2.33. SEM picture of the structured surface (left). Mask for the different shapes of pillars (right) (Linde Sanchez 2008).

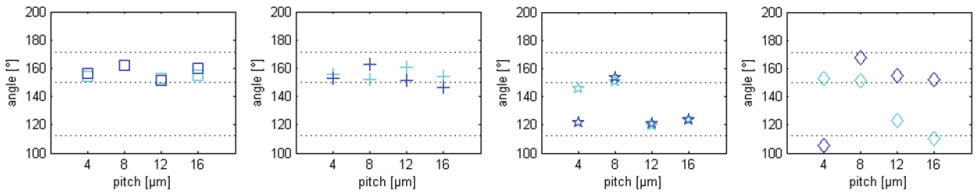

Figure 2.34. Static contact angle measurements for water droplets on different shapes of pillars for a height of 25 µm and 35 µm (Linde Sanchez 2008).

Figure 2.34 shows the static contact angle measurements for the different pillar shapes. For the square and cross-shaped pillars, the static contact angle is between 150° and 160°. Therefore this surface can be qualified as superhydrophobic. However, the tilt measurements reveal that a high force is required to move a droplet on this surface. Figure 2.35 shows the picture of the droplet on a horizontal surface and a tilted surface. The static contact angle is 153°. For this surface, the required tilt for droplet motion angle is 70°. At this angle, the contact angle hysteresis is 28°. For this surface, the negative effect of the contact angle hysteresis increase dominates, leading to a higher retentive force.

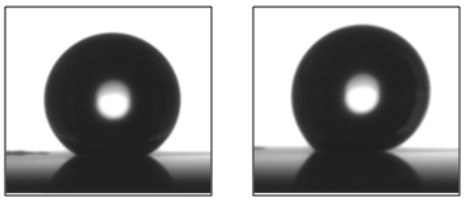

Figure 2.35. (left) Picture of a water droplet on a structured silanised surface. (Right) Picture of a droplet on a tilted surface just before droplet motion. The maximum tilt angle is 70°. At this tilt angle, the contact angle hysteresis is 28°.

2.4.3.3 Black silicon

Black silicon is a needle-shaped surface structure where needles are made of single-crystalline silicon. The black silicon is processed in an inductively coupled plasma multiplex system (STS) (Linde Sanchez 2008). The process is based on a cycle changing between passivation and etching. If the passivation dominates, this very sensitive etching process tends to self-masking effects. The result is a rough surface with peaks of around 7 µm in height and a peak to peak distance of 2 µm. Black silicon acts as a superhydrophobic material. The contact angle of a water droplet on a black silicon surface ranges from 165° to 175°. The critical tilt angle for this material is lower than 1° and cannot be measured using the procedure described in Section 2.2. A droplet deposited on a horizontal black silicon surface immediately rolls away. This means the retentive force of a droplet on such a surface is very low. For this surface, the positive effect of the increase in static contact angle dominates.

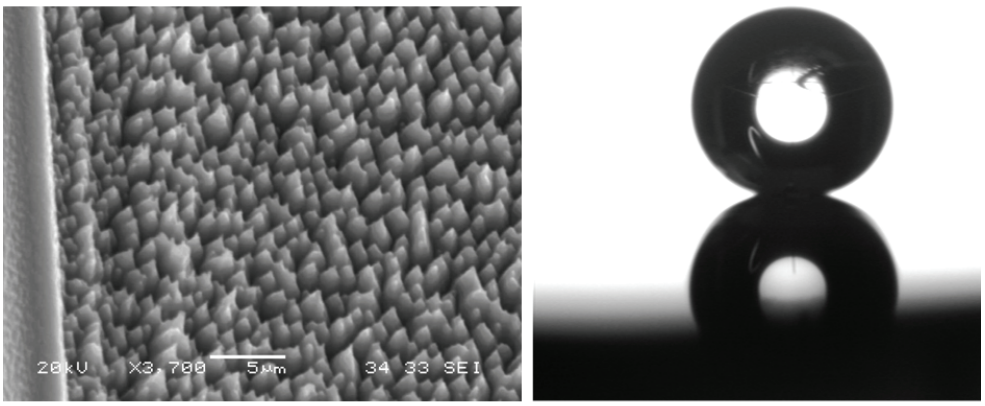

Figure 2.36. SEM picture of the black silicon surface (left). The height of the peaks is around 7 µm and the peak to peak distance is 2 µm. Image of a water droplet on a black silicon surface (right). The contact angle is between 165° and 175°.

2.5 Conclusions

In order to move a droplet, the actuation force needs to overcome a threshold force caused by the contact angle hysteresis. To be able to design an actuation system for droplets, this force needs to be estimated. In this chapter, this retentive force is characterised for a droplet on top of a surface and for droplets between two parallel surfaces. First, the relevant aspects of the surface tension and contact angle hysteresis and their relation to the retentive force are introduced. Theoretical considerations reveal that the retentive force depends both on the contact angle hysteresis and the static contact angle. To reduce the retentive force, the hysteresis should be minimal and the static contact angle should be as high as possible.

An experimental procedure is presented to evaluate the retentive force of droplets on surfaces. A dedicated test fixture is developed to perform droplet sliding experiments for the case of a droplet between two parallel surfaces. Droplet sliding tests are performed for both sessile and confined droplets on Teflon coated smooth silicon surfaces with an average roughness smaller than 1 nm. For these cases an empirical correlation is found to relate the maximum retentive force to the droplet volume, the equilibrium contact angle, the height of the channel and the maximum contact angle hysteresis of the liquid on that specific surface. These empirical relations, both for the static and dynamic part of the retentive force will be used as input for the dynamic droplet modelling in Chapter 4. The tilt tests could only be performed for droplet volumes larger than 3 µl. Smaller droplets remain attached to the Teflon coated surfaces, even when placed vertically. For these droplets, the retentive force exceeds the gravitational force. The derived empirical correlation can be used to extrapolate the measured results on the retentive force in the range from 3 to 25 µl droplets, to the range of droplets used in microfluidic applications.

Furthermore, the effect of roughness on the retentive force is investigated. The analytic 1D roughness model of Johnson & Dettre (1964) predicts an increase of both the static contact angle and the contact angle hysteresis for increasing surface roughness. The increased static contact angle leads to a reduction of the retentive force, whereas an increasing hysteresis results in a higher retentive force. The relative importance of both effects will determine whether the increasing roughness reduces or increases the retentive force. First, the effect of the surface roughness on Teflon coated mechanically roughened surface was investigated. For these samples, increasing roughness leads to a higher retentive force due to the dominant increase in hysteresis. However, no conclusive empirical relation could be determined for the roughness effect due to the large variation of the contact angle measurements. The most important factor to reduce the retentive force is to reduce the contact angle hysteresis. A very static contact angle is not sufficient. In the case of silanised structured surfaces high static contact angles in the range of 150° to 160° were observed. Nevertheless, a drastically increased hysteresis resulted in an increased retentive force. A very low hysteresis (below the limits of detection) was observed in the case of a black silicon surface. On this surface, a very low retentive force was observed.

Chapter 3

Electrostatic manipulation of liquid droplets

Abstract

In this chapter, the electrical actuation of a liquid droplet by means of an external electric field is studied. First, the concept and the main aspects of electrowetting are introduced. Further, the effect on the droplet deformation on flat and rough substrates is studied theoretically and experimentally. Next, the principle is applied to move small amounts of liquid based on the electric field. The electrostatic actuation force is studied numerically for both dielectric and conductive liquid droplets using two different mathematical expressions; a force approach (Maxwell stresses) and an energy approach (method of virtual work). The formulations are applied to study the evolution of the actuation force during the droplet transport over an activated electrode. This analysis is performed for two different electrode configuration systems: (1) the planar electrode system, and (2) the cylindrical channel with integrated annular electrodes. For both systems, the shape of the force profile during the droplet motion is explained. Finally, for both systems a parameter study is performed to study the effect of the properties of the insulation layer (thickness and dielectric constant), droplet volume, channel height and applied voltage on the actuation voltage.

3.1 Introduction to electrostatic droplet actuation

3.1.1 Actuation principle

Electrostatic actuation of droplets or 'electrowetting' is a well-known technique to manipulate fluids on a millimetre or micrometre scale. Electrowetting can be described as the modification of the apparent liquid-solid contact angle of the droplet on a solid substrate due to the application of externally applied electric field (Mugele and Baret 2005). The principle of electrowetting is illustrated in Figure 3.1. When a voltage difference is applied between an insulated substrate and the liquid droplet, the droplet shape will change. The shape of the droplet is expressed by the contact angle θ. In this case, due to the applied electric field, the wetting of the surface by the droplet will improve. As a result from the increased spreading, the contact angle will decrease. This effect is governed by the Lippmann-Young equation:

$$\cos\theta = \cos\theta_Y + \frac{\varepsilon_0 \varepsilon_r}{2t\gamma_{LV}} V^2 \tag{3.1}$$

where θ is the apparent contact angle, θ_Y is the Young's contact angle (see Section 2.1), V is the applied voltage difference, t is the insulation layer thickness, ε_0 the dielectric permittivity of vacuum, ε_r the dielectric constant of the insulation material and γ_{LV} the liquid-vapour surface tension. Curves of this relationship between the applied voltage U and contact angle are referred to as Lippmann curves. The equation indicates that an increase in voltage leads to an increase of $\cos\theta$, and as a result a decrease of the contact angle θ. If the contact angle decreases, the wetting of the liquid on the substrate will improve and the droplet will spread out over the substrate. When an imbalance is created in the surface energies, a net force is induced. If this force is sufficiently high, droplet motion will be initiated. Such an imbalance can be created by the application of an asymmetric electric field.

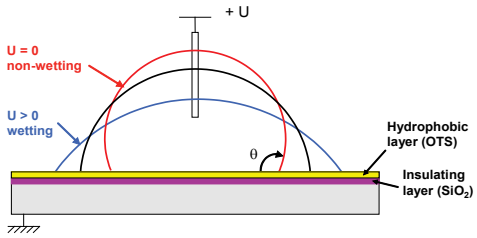

Figure 3.1. Principle of electrowetting on dielectric (EWOD). A voltage is applied between an electrode immersed in a liquid droplet and an electrode, insulated from the droplet.

3.1.2 Materials for droplet actuation

From equation (3.1), it can be seen that several material properties influence the effect of the applied voltage on the droplet; the dielectric constant and thickness of the insulation layer, and the interfacial properties between the liquid and the substrate. The choice of materials will therefore determine the effect of the electrostatic actuation.

Wetting properties

The application of a voltage results in a reduction of the contact angle. This contact angle reduction is limited by the contact angle saturation phenomenon (Vallet *et al*. 1999, Quillet and Berge 2001, Verheijen and Prins 1999). Beyond a certain voltage, no further contact angle reduction is observed. To achieve a maximum effect of the contact angle reduction, one should start from a contact angle as high as possible. This means that the surface should be hydrophobic. Examples of commonly used coatings with hydrophobic properties are amorphous fluoropolymers, such as Teflon® AF or Cytop® or self assembled monolayers (SAM), such as OTS.

Insulation materials

The insulation layer prevents electric currents between the activated electrode and the liquid droplet. Such currents would lead to undesirable chemical reactions in the liquid, e.g. water would decompose into oxygen and hydrogen through electrolysis. The maximum electric field strength the insulation material can withstand is called the dielectric breakdown strength of the material. For higher values of the electric field the dielectric will loose its insulating properties and the material will be damaged. The parameters that can be controlled for an insulation layer are the choice of the material and the thickness of the layer. The most important material properties in this context are the dielectric permittivity and the dielectric strength. Table 3.1 presents an overview of these properties for materials, commonly used as insulators. This table includes both thin polymer coatings as well as metal oxides. The values for water are shown for reference.

Table 3.1. Dielectric constant and dielectric breakdown strength of insulating materials.

Material	Dielectric constant (-)	Breakdown strength (MV/cm)
Teflon® AF1600	2.1	1.93
BCB	2.3 – 2.8	3
Parylene C	2.35	2.2
Parylene N	2.65	2.8
SiO_2	4 – 6	4.9
Polymide	1.2 – 2.4	3.2 – 3.6
Ta_2O_5	14	
Si_3N_4	7.5	100
BST	50 – 220	
PDMS	1.4 – 1.8	0.14
Water	81	65 – 70

The Lippmann equation indicates that the insulation layer should be as thin as possible and have a high dielectric constant for maximum effect on the contact angle reduction. There are however limitations on the minimal thickness of this insulation layer. The achievable thickness will depend on the processing technique and the requirements on the conformality of the processed layer. Furthermore, the combination of thickness and breakdown strength limits the maximum allowed electric field, and as a consequence the applied voltage. A thicker layer allows a higher voltage, but will result in a lower actuation force compared to a thinner layer with the same applied voltage. This means an optimal insulation thickness

can be found, which will require the lowest possible voltage to generate the necessary force for actuation. The effect of the insulation layer will be studied in detail in Section 3.4.4.

Liquids

The actuation liquid used for electrostatic manipulation must be either polarisable or conductive. An example of a polarisable liquid is de-ionised water. When an external electric field is applied, the dipoles in the liquid will rearrange, causing a net force acting on the droplet. In the case of a conductive liquid the force is caused by the rearrangement of ions in the droplet. Liquids that have been successfully used in electrowetting devices are KCl (Pollack *et al.* 2002) and NaCl (Klingner *et al.* 2003), salt solutions of varying concentrations, ionic liquids (Ricks-Laskoski *et al.* 2006) and various biofluids including DNA-containing fluids (Chang *et al.* 2006). An overview of suitable liquids for electrowetting is given by Chatterjee *et al.* (2006).

In this work, DI-water and a water-salt-glycerine mixture were tested. The DI-water used in the experiments was water for High Performance Liquid Chromatography (HPLC), with a molecular weight of 18.02 g, and thus only consists of dipoles. In an electric field the dipoles will orientate along the field lines, but no free charge carriers are positioned on the liquid-solid contact line. The water-salt-glycerine mixture is a conductive liquid. The free charge carriers are brought in liquid by dissolving NaCl in the water. As discussed in Section 3.2.1, water has the property to evaporate very quickly, even at room temperature. To prevent evaporation, glycerol is added to the salt water. Glycerol has the beneficial effect of keeping the water molecules in the liquid phase, but the poor solubility of salt in glycerol is an obvious disadvantage. Adding too much salt to the water will lead to sedimentation of the salt in the glycerol-water mixture.

3.2 Stationary droplet deformation

To understand the effect of an externally applied voltage on the droplet shape and its behaviour, first the impact on a stationary droplet is investigated experimentally. In this section, the deformation of a droplet on both a smooth and a rough surface is studied. To correlate the behaviour of the droplet on a rough surface to theoretical considerations, the roughness needs to be known and controllable. Therefore an artificial roughness is used; an array of microchannels etched in the substrate mimics the roughness of the substrate. By applying the voltage, the wetting of the droplet on the substrate will increase. However, the droplet as a whole will not move. In the next section, the electrostatic induced droplet motion will be discussed.

The test samples for the investigation of the droplet behaviour are processed from an arsenic-doped silicon wafer. This electrical conductive part will act as the bottom electrode to create a voltage difference across the droplet and insulation layer (Figure 3.1). The liquid droplet is positioned on top of the sample. For the experiments on the 'rough' surface microchannels of 100 μm x 100 μm cross-section are produced using anisotropic ion etching. At the end of the etching process, the insulating silicon oxide layer was thermally grown up to a thickness D of 1 μm. In order to create a hydrophobic surface, resulting in contact angles θ larger than 90°, an additional monolayer (approx. 2 nm) of Octadecyl-

TrichloroSilane (OTS) was deposited on top of the oxide layer, following Sagiv's protocol (Sagiv 1980).

The liquid used in the experiments was either purified water, referred to as '*water*', or a mixture of glycerol (74.8% in weight), water (18.7%) and salt (6.5%), referred to as '*mix'*. In the latter, glycerol is used in order to reduce evaporation and salt (NaCl) is added to increase the conductivity of the liquid. The main difference between the two tested liquids is the electrical conductivity. The purified water acts as a dielectric liquid where the mixture is electrically conductive; the electrical conductivity of the mixture is measured to be 0.14 mS/cm. The viscosity μ of the solution was measured with a stress controlled rheometer (Rheometric Scientific SR-5000) and amounts to μ = 80 N/m²-s at 20 °C and μ = 25 N/m²-s at 60 °C. The surface tension γ_{LV} of the mixture is experimentally characterised and amounts to 65 mN/m. For the experimental measurements the AC voltage V ranges from 0 to 65 V (RMS value) at a frequency of 10 kHz, with a modulation of 0.1 Hz. This voltage is applied between the substrate and an electrode immersed in the drop, as schematically represented in Figure 3.1.

3.2.1 Electrostatically induced droplet deformation on flat substrates

The electrowetting effect for droplets positioned on flat areas of the sample is evaluated by measuring the contact angle between the liquid droplet and the substrate as a function of the applied voltage. Figure 3.2 shows pictures of an undeformed droplet and a droplet deformed using a voltage of 50 V respectively. In Figure 3.3 the experimental contact angle measurement results are shown for pure water and for a mixture of water, salt and glycerol. Droplet volumes of 5 and 10 µl have been used.

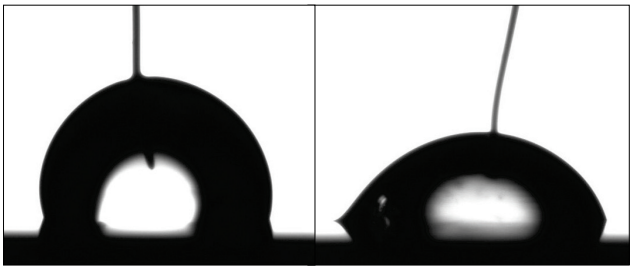

Figure 3.2. (a) Droplet shape with no voltage applied. (b) Deformed droplet shape under an applied voltage of 50 V.

Figure 3.3 shows that the curves satisfy well Lippmann's equation (3.1) up to 50 V. Above 50 V, a saturation regime is detected. The measurements with water show a significant higher static contact-angle compared to the mixtures. However, the contact angle change (i.e. the electrowetting effect) is the same for the mixture as for water. For both, the same voltage is required to result in a certain contact angle reduction. Both the mixture and the purified water can be considered conductive liquids. The maximum voltage difference that can be applied is limited by the breakthrough characteristics of the SiO_2 layer. Results of

thickness measurements, using a spectrometer, reveal that the thickness for the layer ranges from 760 nm to 912 nm. Combined with an estimated breakdown strength of 100 V/µm for the silicon oxide, this results in a maximal voltage difference over the droplet of 75 V.

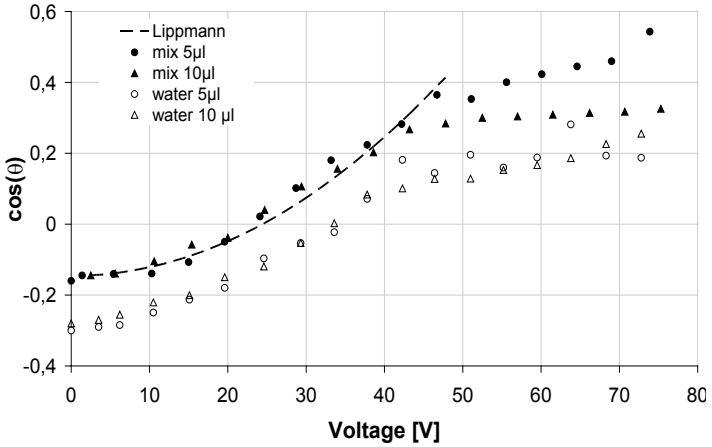

Figure 3.3. Lippmann curves for the experimental set-up in use for pure water and a water-glycerol-salt mixture. Both liquid behave as a conductive liquid.

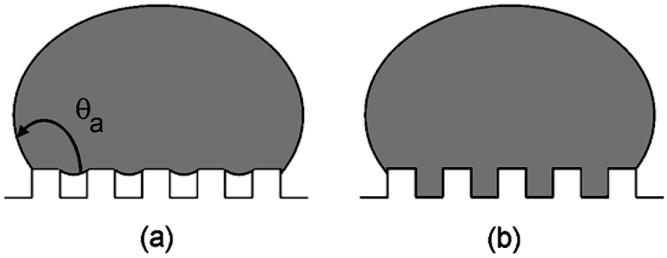

Figure 3.4. Droplet morphologies on microchannels: (a) a droplet sits on top of the channels, (b) a drop fills the channels.

3.2.2 Electrostatically induced droplet deformation on rough substrates

A droplet deposited on open microchannels with rectangular cross-section has multiple equilibrium states. Typically, there are two prominent states in which the drop can reside on the channels (Patankar 2003): the drop either sits on top of the channels or wets the channels, as shown in Figure 3.4 (a) and (b) respectively. The morphology referring to the minimal energy state depends on the dimensions of the channel and the wettability of the liquid. According to Seemann *et al.* (2005), the morphology can be expressed as a function of two parameters : the contact angle of the drop on the planar substrate and the aspect ratio of the channel.

These morphological states can be detected by evaluating the apparent contact angle θ_a (see Figure 3.4). Indeed, on the one hand θ_a for a droplet that wets the channels is given by Wenzel's formula (Wenzel 1936)

$$\cos\ \theta_{a,w} = r_w \cos\theta_e \tag{3.2}$$

where r_w is the ratio of the actual area of liquid-solid contact to the projected area on the horizontal plane and θ_e is the equilibrium contact angle on a planar substrate. On the other hand, θ_r for a drop that sits on the channels is given by Cassie's formula (Cassie 1944):

$$\cos\ \theta_{a,c} = r_c \phi \cos\theta_e + \phi - 1 \tag{3.3}$$

where ϕ is the area fraction on the horizontal projected plane of the liquid-solid contact and r_c is the ratio of the actual area to the projected area of liquid-solid contact. For the conducted experiments with the water-salt-glycerol mixture (contact angle $\theta_e \cong 100°$) in microchannels with a square cross section of 100 µm x 100 µm, the apparent contact angles without a voltage applied, are expected to be $\cos\theta_{a,w}$= -0.34 and $\cos\theta_{a,c}$= -0.58 (r_w=2, r_c=1 and ϕ=0.5) for the Wenzel and Cassie case respectively. The experiment is now performed as follows: a drop of the solution is deposited on an array of microchannels and the voltage U between the drop and the substrate is gradually increased. Figure 3.5 shows the evolution of the apparent contact angle as a function of the applied voltage for a 5 µl droplet of the water-salt-glycerol mixture. Further, point 1 on the figure indicates the moment the liquid starts wetting the channels, while at point 2 the liquid wets all channels.

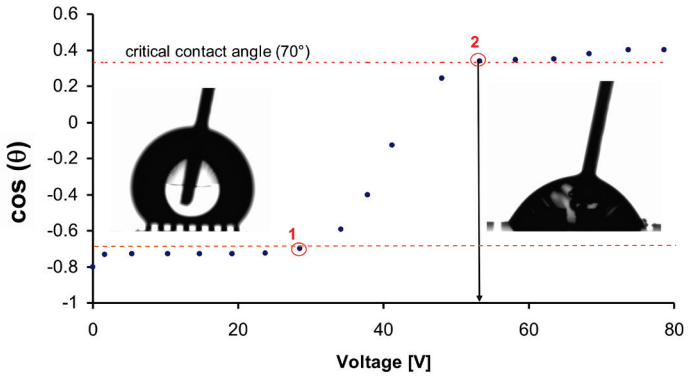

Figure 3.5. Apparent contact angle of a 5 µl drop deposited on the microchannels as a function of the applied voltage.

From Figure 3.5, it can be concluded that for the dimensions in use a drop deposited on the channels will not wet the microchannels without applying a voltage. However, by changing the contact angle by applying a voltage, the morphological transition occurs. Moreover, in the latter case the liquid wets the microchannels over a certain length when a critical voltage value is applied. From that point on, the liquid filament grows with increased voltage. The criterion for the observed capillary transition from drop-to-groove wetting is described by Patankar *et al.* (2002):

$$\cos\theta_a > \frac{-1}{1+2(d/w)}; \tag{3.4}$$

with $A=d/w$ the aspect ratio of the channel. Following a 2D approach, this formula can readily be understood by describing the energy contents E_d of the drop state and the one of

the groove wetting state (E_g). Indeed, writing the energy change in between these states, one obtains

$$E_g - E_d = (w+2d)\gamma_{LS} - w\gamma_{LV} - (w+2d)\gamma_{VS}\,; \tag{3.5}$$

with γ_{LS}, γ_{LV}, γ_{VS} the surface tension between the liquid-solid, liquid-vapour and vapour-solid interface respectively. As grooves will be wetted for $E_g<E_d$, and as $\cos\theta=(\gamma_{SV}-\gamma_{SL})/\gamma_{LV}$, equation (3.4) is obtained. Evaluation of this formula for the squared microchannels leads to a wetting angle of 109°. On the other hand, the transition for further wetting the channels can be similarly derived. For this case, the energy change while filling the channel over a length Δx is examined:

$$\Delta E = \gamma_{LS}(w+2d)\Delta x + \gamma_{LV} w\Delta x - \gamma_{SV}(w+2d)\Delta x\,. \tag{3.6}$$

Again looking for a decrease in energy results now in

$$\cos\theta_a > \frac{1}{1+2(d/w)}\,; \tag{3.7}$$

leading to an apparent contact angle for filling of 70° for the squared channels. From Figure 3.5, it can be concluded that the experimental results correspond well with the theoretical values obtained from equations (3.4) and (3.7). Furthermore, for 5 µl drops of the water-salt-glycerol mixture, the transition is observed at 51 V ± 4 V. This is the threshold voltage for the filling of the microchannels; if the applied voltage is higher than the threshold voltage, the liquid will fill the channels. When the voltage is switched off, the liquid will pull back and the channels will be emptied. By applying a voltage oscillation between 0 V and a voltage higher than the threshold voltage, a periodical filling and emptying of the channels can be achieved. This pulsating motion of the liquid in the microchannels can be applied as an active heat spreader. In Chapter 6, a thermal analysis of such a system is performed.

3.3 Methodology for the calculation of the actuation force for electrostatically induced droplet motion

Introduction

In the previous section, the electrode was centred below the droplet. Under the application of the voltage the droplet will deform but not move. In this section on the other hand, an asymmetric voltage application on the droplet is considered. Due to the voltage difference at the left and right side of the droplet, the droplet will move towards the activated electrode. The principle for this actuation mechanism is explained in the next session. When a voltage is applied, the droplet will deform under the electrostatic force, but only after a certain threshold voltage is exceeded the droplet will start moving. This deformation is characterised by the contact angle hysteresis between the advancing angle θ_A and the receding angle θ_R. In order to slide the droplet, this electrostatic force needs to overcome a critical force due to the contact angle hysteresis. Figure 3.6 shows an example (Hectors and Huybrechts 2003) of the deformation and subsequent motion of the droplet between two parallel plates with integrated electrodes on the bottom side. The electrodes are coated with a 2 µm thick insulating layer of BCB and a hydrophobic layer of Teflon AF 1600.

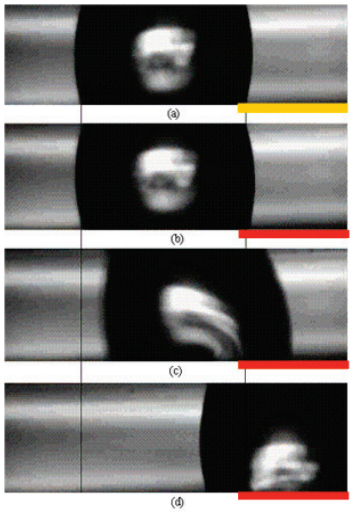

Figure 3.6. Motion and deformation of the droplet in the channel (Hectors and Huybrechts 2003).

In this section, the actuation force acting on a droplet during its transition through a channel is calculated numerically. First, different formulations for the electrostatic force calculation are compared. Next, the influence of geometrical and material properties of the system on the resulting force is studied for both systems introduced in Chapter 1; (1) the planar electrode system and (2) the cylindrical channel with integrated annular electrodes. In the next chapter, the actuation force is combined with the results of Chapter 2 on the opposing forces to estimate the transient behaviour of the droplet. The ultimate objective is the modelling of the droplet motion, the internal fluid circulation inside the droplet as well as the heat transfer between chip and droplet. The first part in this modelling process is the calculation of the electrostatic force, responsible for the droplet actuation. The purpose of the electrical simulations is to characterise the actuation force and assess the impact of the system parameters on this force. With this information, the electric actuation strategy and electrode design can be optimised.

3.3.1 Principle of electrostatic droplet actuation

As shown in the previous section, electrowetting (changing the wetting properties of a liquid on a solid substrate) is an interesting technique to manipulate small discrete amounts of liquid in the nanolitre to millilitre scale. This is of special interest for channels in the sub-millimetre range, where pressure driven systems require a high pressure gradient. One means of droplet movement (Pollack *et al.* 2002) using electrostatic actuation is shown in Figure 3.7. This set-up is referred to as a confined EWOD (electrowetting on dielectric) system. Here the pump is integrated in the channel and consists of electrodes along the channel. In this way the pressure gradient is avoided.

The device consists of two flat parallel plates separated by a spacer creating a small gap between the two plates. In a practical case, the top and bottom plate could be a chip and a substrate respectively. On the bottom plate an array of individual addressable control electrodes separated by an insulator is fabricated. The top plate consists of a single

grounded electrode. The electrodes on both top and bottom plate are covered with an insulating dielectric layer. This dielectric layer prevents electric current flowing from the activated electrode to the liquid droplet which would cause chemical reactions such as electrolysis. Both top and bottom plate are coated with a thin hydrophobic layer. This layer is not essential for the operation of the droplet actuation, but reduces the friction between the droplet and the walls and allows larger changes in contact angles as reaction to the application of an electric field and therefore possibly a larger effect. When a voltage is applied to a control electrode at the bottom plate close to the droplet, the droplet will feel a force and as a result the droplet will move towards the activated electrode until the droplet is centred symmetrically above the electrode. At this position, no electrostatic force will act on the droplet. In the previous section, the stationary droplet deformation was studied for an applied AC voltage. The application of the numerical study for the droplet transport in this section is applicable for well shielded electric fields. This is the case with DC and low frequency (up to several kHz) signals AC for the voltage application.

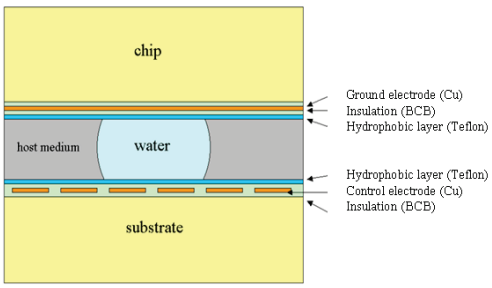

Figure 3.7. Schematic representation of a droplet actuation system.

This force can be studied from two points of view. In the first method, the force acting on the droplet is considered to be an electromechanical force pulling the droplet. In case of a conductive liquid, charges are induced in the solid-liquid and liquid-vapour interface when a voltage is applied on an electrode and consequently an electric field is generated. Due to this distribution of ions on the interface of the water an electrostatic force originating from the attraction between induced charges and charged electrodes is acting on the droplet. In case of a dielectric polar liquid, the force is not created by ions on the interface but by the alignment of the dipoles in the liquid to the electric field caused by the activated electrode. This behaviour is similar to a dielectric material being pulled in a charged parallel plate capacitor. Capacitors are associated with dielectric losses, which cause a reduction of the effective permittivity (real part of the complex permittivity) of the dielectric material as a function of the frequency. In this work, a unit step considered for the voltage application. By transforming the step function to the frequency domain, the effect of the dielectric losses of the capacitors can be taken into account. In this work, however, the effect of the dielectric losses is not taken into account.

The second method to study the actuation force is the energy-minimisation-based approach. When a voltage is applied at an electrode, the solid-liquid interfacial tension at the side of the droplet close to the electrode decreases. To minimise the total surface energy, the droplet moves to the activated electrode and equilibrium is reached when the droplet is at the centre of the activated electrode. In this view the reduction in solid-liquid interfacial tension leads to a reduced contact angle, the electrowetting effect, and makes the droplet

spread out. This change in contact angle between both sides of the droplet leads to a pressure gradient across the droplet towards the activated electrode. If the actuation force is sufficiently high, the droplet will move towards the activated electrode. In order for the droplet to start moving, the actuation force must overcome the retentive force by the surface tension, discussed in Chapter 2. The presence of this retentive force leads to a threshold value for the actuation force and the applied voltage. For voltages lower than this threshold, the droplet will only deform but not move. By switching the electrodes sequentially, the droplet can be transported along the electrode path. With a good choice of the powering frequency for the different succeeding pads, the droplets can have a continuous movement through the channel between the two plates. It is important to note that the electrostatic actuation is possible for both conductive and polar dielectric liquids. However, the actuation effect is much more pronounced is the case of conductive liquids for the same application voltage. To reduce the required voltage for droplet actuation the droplet can be surrounded by a low viscosity non-evaporating liquid.

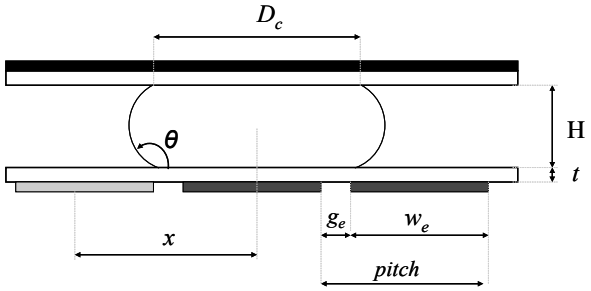

Figure 3.8. Schematic diagram of the geometrical parameters for droplet actuation.

Table 3.1. Parameters for the electrostatic force calculation.

Parameter	
D_c	Contact line diameter
w_e	Control electrode width
g_e	Gap between two control electrodes
θ	Contact angle of the liquid on the hydrophobic coating (this angle can be different at top and bottom side)
t	Thickness of the insulating layer
x	Relative droplet position. This is the distance between the centre of the droplet and the centre of the activated electrode. The convention used is that the relative position is negative when the droplet is at the left side of the activated electrode for a droplet moving from left to right.

In this section, the actuation force acting on a droplet during its transition through a channel is calculated. The parameters investigated in this study on the actuation force are shown in Figure 3.8 and explained in Table 3.2.

3.3.2 Electrostatic force formulations

The electrostatical modelling involves the computation of two coupled phenomena: the electric field distribution in the channel and the shape of the droplet. The first is evaluated by finite element simulations. The latter by a total energy minimisation with a constant liquid volume constraint. Because of their mutual influence, the two phenomena should be solved iteratively until a converged solution for forces and shape is achieved. For a certain fixed droplet shape the electrostatic force can be calculated based on the distribution of the electric field. The influence of the droplet shape, and the assumed decoupling, on the force profile is discussed in Section 3.4.3. For each position of the droplet in the channel the electrostatic force can be calculated in a quasi static way for an assumed shape of the droplet. In this section, two approaches for the formulation for the electrostatic force on a fixed shape are derived. The first method is based on the force acting on a dielectric in an electric field ('Maxwell stresses'). The second method is based on the principle of virtual work.

A. Maxwell stresses

An electric field $\vec{E}$ induces a body force $\vec{f}$ in a dielectric fluid (Stratton 1941):

$$\vec{f} = \underbrace{\rho_f \vec{E}}_{\text{Coulomb force}} - \underbrace{\frac{1}{2}E^2\nabla(\varepsilon)}_{\text{dielectrophoretic force}} + \underbrace{\frac{1}{2}\nabla(E^2\rho\frac{\partial\varepsilon}{\partial\rho})}_{\text{electrostriction force}} \tag{3.8}$$

where ρ is the charge density (per unit volume), ρ_f the charge density of the free charges distributed in the dielectric material and ε is the permittivity. The dielectrophorectic force can also be used to manipulate small amounts of liquids (Jones 2002). However this is only possible for very small masses and at very high frequencies. This type of actuation is therefore out of the scope of this work. Equation (3.8) could have been formulated as a dynamic equation. However, the electrodynamic transients are much faster than the hydrodynamic transient effects in the liquid. Therefore, in the steady state analysis approach of the droplet motion, it is sufficient to study the electrostatic phenomena in steady state.

This last contribution to the body force is caused by the inhomogeneity of the electric field. By applying the divergence theorem, a volume integration of $\vec{f}$ can be reformulated into a surface integral over the droplet surface *S* of a surface force $\vec{t}$ (Verplaetsen 1999) :

$$\vec{t} = \varepsilon\vec{E}(\vec{E}\cdot\vec{n}) - \frac{1}{2}\left(\varepsilon - \rho\frac{\partial\varepsilon}{\partial\rho}\right)E^2\vec{n} \tag{3.9}$$

where $\vec{n}$ is the unit outward normal on surface *S*. Therefore, the net force acting on a unit area of the interface between 2 fluids in the direction from medium 1 towards medium 2 as the thickness of the layer approaches zero equals :

$$\vec{t} = \left[\varepsilon\vec{E}\left(\vec{E}\cdot\vec{n}\right)\right]_2 + \left[\varepsilon\vec{E}\left(\vec{E}\cdot\vec{n}\right)\right]_1 - \frac{1}{2}\left[\left(\varepsilon - \rho\frac{\partial\varepsilon}{\partial\rho}\right)E^2\vec{n}\right]_2 - \frac{1}{2}\left[\left(\varepsilon - \rho\frac{\partial\varepsilon}{\partial\rho}\right)E^2\vec{n}\right]_1 . \tag{3.10}$$

Electrostriction is the deformation of a dielectric under the application of an electric field. This deformation induces stresses in the material, which partly compensate the traction exerted by the electric field on the interface. To find the net force acting on the interface,

the electrostriction term should be removed from (3.10). This leads to the following expression for the net surface force :

$$\vec{t} = \left[\varepsilon\vec{E}\left(\vec{E}\cdot\vec{n}\right)\right]_2 + \left[\varepsilon\vec{E}\left(\vec{E}\cdot\vec{n}\right)\right]_1 - \frac{1}{2}\left(\varepsilon E^2\vec{n}\right)_2 - \frac{1}{2}\left(\varepsilon E^2\vec{n}\right)_1; \tag{3.11}$$

where index 1 refers to the liquid of the droplet and index 2 refers to the fluid surrounding the droplet. Using the boundary conditions of the electric field at the interface for the normal and tangential components of the electric field and electric displacement vectors

$$\begin{aligned} D_{n,1} &= D_{n,2} \\ E_{t,1} &= E_{t,2}; \end{aligned} \tag{3.12}$$

the electric field in material 2 can be expressed as a function of components of the electric field in material 1:

$$E_2^2 = E_{n,2}^2 + E_{t,2}^2 = \frac{\varepsilon_1^2}{\varepsilon_2^2}E_{n,1}^2 + E_{t,1}^2 . \tag{3.13}$$

Using this relation, equation (3.11) can be rewritten as a function of components of the electric field in material 1 only:

$$\vec{t} = \frac{\varepsilon_1 - \varepsilon_2}{2}\left(\frac{\varepsilon_1}{\varepsilon_2}E_{n1}^2 + E_{t1}^2\right)\vec{n}_2 . \tag{3.14}$$

The total force exerted by the electric field on the liquid-vapour interface is referred to as the Maxwell stress. In the case of a conductive liquid (material 1), there is no electric field inside the material, $E_1=0$, and the net force on the interface of the droplet can be described as a function of the electric field in the surrounding material:

$$\vec{t} = \frac{1}{2}\varepsilon_2 E_2^2\vec{n}_2 . \tag{3.15}$$

The net electrostatic force acting on the droplet is calculated by integrating equation (3.14) over the surface S_1 of the droplet:

$$\vec{F} = \int_{S_1}\vec{t}dS . \tag{3.16}$$

The horizontal component of this electrostatic force is the actuation force which will pull the droplet through the channel.

B. Virtual work method

The second method is based upon the principal of virtual work. The total electrostatic energy U_{el} in the system, with a volume *Vol*, is given by

$$U_{el} = \frac{1}{2}\int_{Vol}\vec{E}\cdot\vec{D}dVol . \tag{3.17}$$

The electrostatic force can be calculated as the negative gradient of the energy variation. The system tends to move towards a situation of minimal energy. In the case where only the contribution of the electric energy to the total energy is considered, the change in total energy can be written as follows:

$$dW = -dU_{el} . \tag{3.18}$$

Because only the horizontal component of the electrostatic force contributes to the moving of the droplet, the net actuation force is given by

$$F = \frac{dU_{el}}{dx}. \tag{3.19}$$

Both approaches will lead to the same result for the electrostatic actuation force. The main advantage of the Maxwell stresses method is that this method provides information of the spatial distribution of the electrostatic force acting on the surface of the droplet. On each point of the interface the Maxwell stress is known. This information is lost in the virtual work method. A drawback of the Maxwell stresses method is that it is more difficult to implement in the post processing of the finite element simulation. Not only the value of the electric field should be extracted from the simulation but also its orientation and the location and orientation of the discretised part of the interface considered. On the other hand, the implementation of the virtual work method is much more straight forward since only the value of electric field and the size the element considered need to be extracted. The drawback of this method is that two simulations at slightly different positions are required to estimate the force at one position.

3.3.3 Electrostatic finite element modelling

For the evaluation of the electrostatic force, the normal and tangential components of the electric field on the interface of the liquid droplet are required. To calculate and visualise the electric field distribution steady state electrostatic simulations in 2D and 3D with the general purpose finite element software MSC.MARC are performed. For these simulations the Poisson equation for a scalar potential Φ is solved:

$$\nabla^2\Phi = -\frac{\rho}{\varepsilon}. \tag{3.20}$$

where ρ is the charge density and ε the dielectric constant. The Poisson equation (3.20) is solved together with the boundary conditions (3.12) on the interface between two materials 1 and 2, while Φ is continuous over the interface between the materials. Input for the electrostatic simulations are the geometry of the droplet, electrodes and insulating layer, the material properties, for steady state electrostatic simulation is this only the dielectric constant of the material ε_R, and the applied voltages at the electrodes as boundary conditions. The voltage at the activated control electrode will be put at the applied voltage V. The voltages at the other control electrodes in the bottom layer and at the ground electrode are set to 0V. The simulations are performed for conductive and dielectric liquids. In the case of a conductive droplet, the dielectric constant of the liquid is set to infinity since there is no electrical field inside a conductor. The results of the simulations are the distribution of the potential Φ, the electric field $\vec{E}$ and the electric displacement $\vec{D}$. The values for the components of the electric field on the interface of the droplet are extracted during the post-processing of the simulation. From these values, the electrostatic force can be calculated according to equations (3.16) and (3.19).

The electrostatic simulations are performed using 2D and 3D finite element models. For all simulations, a grid sensitivity analysis is performed to ensure a grid independent solution (see Section 3.3.3 C). The result of the grid sensitivity analysis indicates the number of cells and the required dimension of the cells. For the 2D case, the number of cells is typically in the order of 30,000 cells. In the case of a 3D simulation, the grid consists of around 250,000 elements for the planar structure and 150,000 for the annular system. In

Figure 3.9 an example of a grid for a 2D electrostatic simulation is shown. High electric field intensity values are expected at the interface of the liquid droplet close to the activated electrode. A fine mesh is required in this area to capture the gradients of the electric field. The right hand side of Figure 3.9 shows an example of the mesh in this region of interest. This three phase point is a singular point in the simulation. It is on the border of three materials with each different material properties. The scalar potential is continuous over the interface of different materials, however the normal component of the electric field is not. Since this component is used in the calculation of the force care should be taken to extract the value of the electric field at this point. Depending on which interface is looked at (solid-liquid, solid-vapour or liquid-vapour), different values for the Maxwell stress are found. For this study the force is calculated on the interface of the droplet. Therefore the value extrapolated from the liquid-vapour interface is chosen.

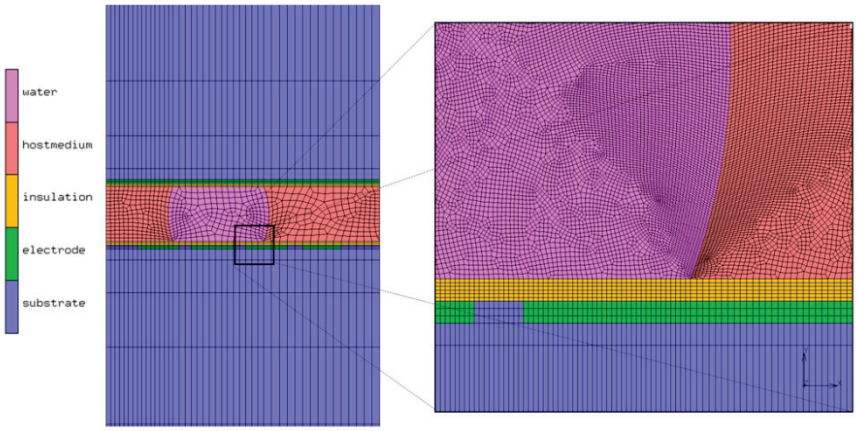

Figure 3.9. Example of a grid used in a 2D electrostatic simulation (left). Detail of the refined mesh around the three phase line where high gradients in the electric field are expected (right).

A. Calculation for a dielectric liquid

In case of a polar dielectric liquid, the force acting on the droplet is the result of the alignment of the dipoles in the polar liquid. To calculate the force on the droplet, equation (3.14) will be used for the Maxwell stresses method and equation (3.19) for the energy method. For a dielectric liquid drop, the voltage difference between 0 V at the grounded electrodes and the applied voltage V at the activated electrodes is divided over the insulating layers and over the liquid. Since the liquid is much thicker than the insulating coating, most of the potential drop will occur over the dielectric droplet. An overview of the electrical properties of commonly used materials is given in Table 3.1. The voltage distribution in the droplet for an applied voltage of 150 V at the energised electrode is shown on the left hand side of Figure 3.10. The right hand side shows the electric field vectors at the interface of the droplet. The electric field is non zero in the entire droplet, but is only visualised on the interface of the droplet for clarity. The highest values of the electric field will occur in the region closest to the activated electrode. Since the force scales with the second power of the electric field (3.14), the highest forces will also be localised in the area close to the electrode.

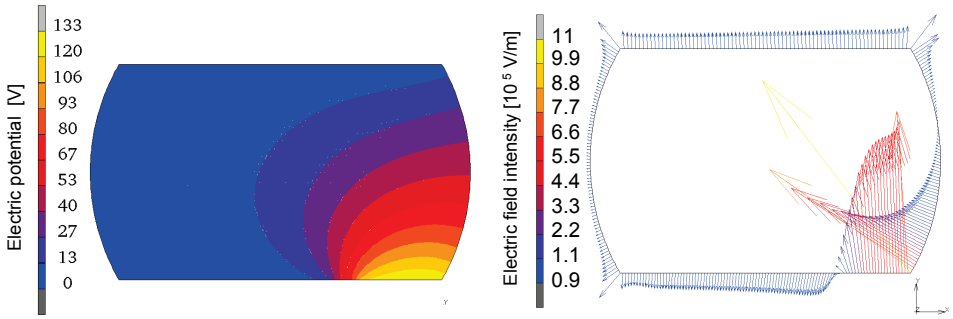

Figure 3.10. 2D simulation results in a dielectric droplet (ε_r=81) for an applied voltage of 150 V: Potential distribution in the drop (left). Electric field on the interface of the droplet (only shown on the interface of the droplet for clarity) (right).

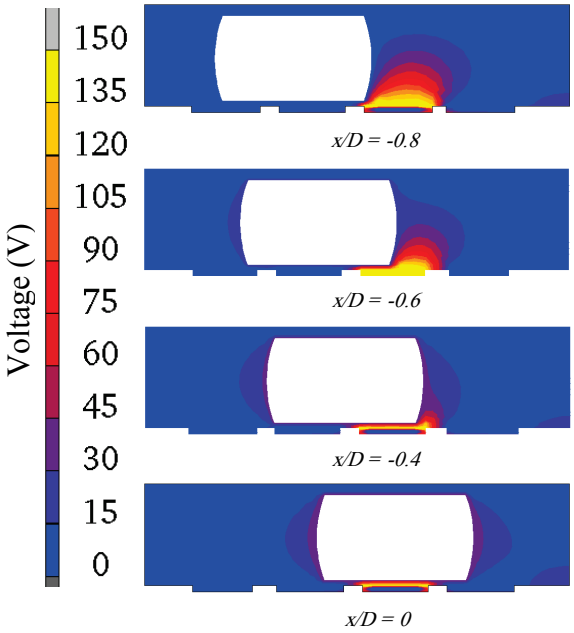

Figure 3.11. Distribution of the electric potential for different positions of the droplet. The normalised droplet positions are -0.8, -0.6, -0.4 and 0 respectively.

B. Calculation for a conductive liquid

In the case of a conductive droplet, the force acting on the droplet is the result of the attraction between the induced charges on the droplet interface and the activated electrode. For the simulation of the conductive liquid, the dielectric constant is set to infinity. This means that there is no electric field inside the droplet, but the normal component of the electric displacement is continuous over the interface. Indeed, in a conductive droplet all

charges are concentrated on the outside of the droplet. Additionally no electric field exists inside the droplet and the electric field in the surrounding area is perpendicular to the droplet interface. As a conductor in an electric field, the droplet is an equipotential body. Assuming that the electric double layer is much thinner than the insulating layer, the voltage drop, between the applied voltage on the activated electrode and 0 V at the grounded electrodes, mainly occurs over the insulating dielectric coatings. The potential in the droplet will be the result of the voltage division between the insulating layer at the activated electrode, the insulating layer at the grounded electrode and the insulation at the top electrode. The potential distribution in the channel is shown in for different positions of the droplet. Compared to the case of the dielectric droplet, the same voltage drop is realised over a much smaller distance leading to higher values of the electric field and consequently to higher actuation forces.

C. Accuracy and truncation error estimation of the electrostatic force

The truncation error of the simulation due to the discretising of the solution domain can be assessed by the Richardson extrapolation (Ferziger and Peric 1997). The error can be estimated from the difference between solutions obtained on systematically refined grids. In this way, the sensitivity of the solution ϕ_h on grid refinements with cell width h can be assessed. Three subsequent grids are tested with a cell width of $4h$, $2h$ and h respectively. The order p of the method may be estimated as follows:

$$p = \frac{\log\left(\frac{\phi_{2h} - \phi_{4h}}{\phi_h - \phi_{2h}}\right)}{\log 2} \tag{3.21}$$

The discretisation error on grid h, the finest grid, can be approximated by

$$\varepsilon_h^d \approx \frac{\phi_h - \phi_{2h}}{2^p - 1} \tag{3.22}$$

Using the Richardson extrapolation, an approximation of the quantity being more accurate than the solution on the finest grid, can be obtained by adding the error estimate:

$$\Phi = \phi_h + \varepsilon_h^d \tag{3.23}$$

The accuracy analysis can be performed for the different quantities that are used in the electrostatic modelling: the potential Φ, the electric field intensity $\vec{E}$, the electrostatic force F and the electrostatic energy W_{el}. Using the electric field as a parameter for the grid convergence analysis causes a problem. The node at the location of the three-phase point between the liquid, the substrate and the air is a singular point for the calculation. For further refining of the mesh, the value of the electric field will diverge. There is no problem however for the analysis of the quantity of the energy. For this case an integral approach around the singular point is used. Refining of the mesh leads to a convergence of a single value, in this case the exact solution. This grid sensitivity analysis is performed on both the 2D and 3D simulations, discussed in the next sections. The element sizes of the subsequently refined grid are typically 20 µm ($4h$), 10 µm ($2h$) and 5 µm (h). For the calculation of the electrostatic energy of the case in Figure 3.10, with a normalised droplet position of -0.6, the Richardson extrapolation shows that the discretisation error ε_h^d on the electrostatic energy smaller than 0.1% is for cell size h (5 µm). As a result of the grid

sensitivity analysis can be concluded that the solution can be considered grid independent and that solution is sufficiently close to the exact solution.

The Richarson extrapolation is a technique to estimate the truncation error that is usually used in fluid dynamics. Similar techniques are available for the error estimation for finite element simulations (Zienkiewicz and Taylor 1987).

3.4 Actuation force calculation for the planar electrode system

3.4.1 Calculation of the actuation force for a nominal case

Both formulations for the electrostatic actuation force are now applied to a nominal case which will serve as reference case for later parameter variations. A broad range of liquids can be used for the application of electrowetting. Chatterjee *et al.* (2006) provide an extensive list of suitable liquids. In this section, both conductive and dielectric liquids are considered. The parameters used in this nominal case are shown in Table 3.2. For this quasi static analysis the electrostatic force is calculated for each droplet position with respect to the powered electrode for a given shape of the droplet. In order to calculate the forces during motion, the droplet shape should be known. The evolution of the static actuation force as a function of the droplet position can be considered to be an approximation of the dynamic case. As a first approximation, a constant droplet shape is considered.

Table 3.2. Parameter values used in the simulation of the nominal case.

Simulation parameters		Value
Insulator thickness	t_{ins}	2 μm
Droplet diameter	D_c	1.5 mm
Substrate thickness	t_{sub}	5 mm
Electrode width	w_e	0.9 mm
Electrode spacing	g_e	0.1 mm
Channel height	H	1 mm
Voltage	V	150 V
Dielectric constant liquid	ε_L	81
Dielectric constant insulation	ε_{ins}	2.3

A. Dielectric liquid

Figure 3.12 shows the results of the calculation of the electrostatic energy and actuation force based on a 2D simulation of the nominal case. The graphs are plotted as a function of the normalised relative droplet position with respect to the droplet diameter. This dimensionless distance is the ratio between the relative droplet position, as defined in Table 3.2, divided by the droplet diameter. The left hand side of the figure shows the evolution of electrostatic energy in the system calculated using equation (3.17). It can be seen that the electrical energy reaches a maximum, when the droplet is located symmetrically above the

powered electrode. As a result the droplet will feel a force towards the powered electrode until the equilibrium position is reached. On the right hand side of the figure, the evolution of the actuation force is shown calculated with both the virtual work method and the Maxwell stresses method. The discretisation error ε_h^d, calculated using the Richardson extrapolation (3.22) is added to the graph in the form of error bars. From the graph, it can be seen that the droplet starts feeling a force shortly before the contact line reaches the edge of the powered electrode. In the graph, the point where the contact line reaches the edge of the powered electrode is at position $x/D_c = 0.8$. At that location, a sharp peak in the force profile can be observed. A second peak, corresponding with a sudden change in slope of the energy profile can be seen at position $x/D_c = 0.167$. The first peak corresponds to the location where the front of the droplet contact line reaches the edge of the activated electrode. Similarly, the second peak corresponds to the location where the front of the droplet contact line reaches the edge of the next electrode, which is kept at 0 V. The appearance of the peaks and the profile of the force evolution are discussed in detail in the next section. Furthermore, from the graphs it can be seen that the force becomes zero when the droplet is symmetrically above the charged electrode; this means that the droplet will move until it is aligned with that electrode, when no inertial forces are available in the system. This position corresponds with the location of minimal total energy as discussed above.

The method of the Maxwell stresses and the method of the virtual energy are equivalent descriptions for the same phenomenon. Therefore, the result should be the same using both approaches. The agreement between the two methods for the force calculation is very good in the central part of the transition and for the position close to the centre. However, a large difference can be observed at the peaks of the force profile. As discussed in the section above, the 2D simulation results for these positions are not mesh independent and have a large truncation error. Therefore the values of the forces at this peak are not significant. Further refinement of the mesh leads locally to very high forces close to the singular point and even no overlap of the error bars representing the truncation error estimation for both methods is observed. A possible reason could be that for the three subsequently refined meshes used, the simulation results are not yet in the region to allow the Richardson extrapolation to predict the truncation error and a further refinement is required. This is an obvious limitation of the computational method used here: a very fine mesh is required to accurately calculate the electrostatic force at those droplet locations.

Figure 3.13 shows the grid, used for the 3D electrostatic simulations. For this 3D case, only the method of the virtual work is used to calculate the actuation force on the droplet. The left hand side of Figure 3.14 shows the calculated electrostatic energy and actuation force as a function of the droplet position for the nominal case of Table 3.2. To compare this result, the previously obtained force from the 2D simulations is multiplied with the width of the droplet. The graphs of these forces are plotted on the right hand side of Figure 3.14. The overall agreement between the force calculated from the 3D simulation and those from the 2D simulation is rather good. The main difference is that the force profile does not decrease as fast for the 3D model after the first peak as it does for the 2D model. This can be explained by the fact that in the 3D case, the contact line is a curved line that gradually crosses the edge of the activated electrode whereas in the 2D case the contact line is assumed to be a straight line that passes the location of the edge of the contact line at one droplet position leading to a high and narrow peak in the force curve.

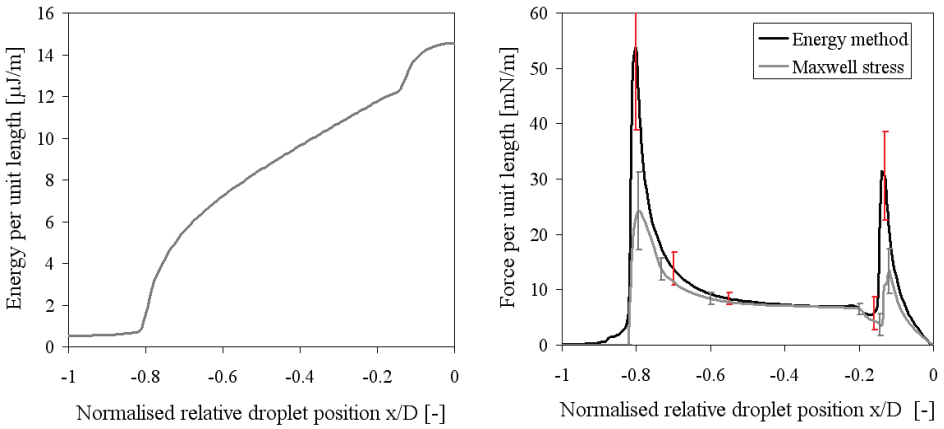

Figure 3.12. Left: Evolution of the 2D electrostatic energy in the whole system for a dielectric droplet as a function of the normalised relative droplet position. Right: Evolution of the 2D actuation force as a function of the normalised relative droplet position calculated with the virtual work method and the Maxwell stress method.

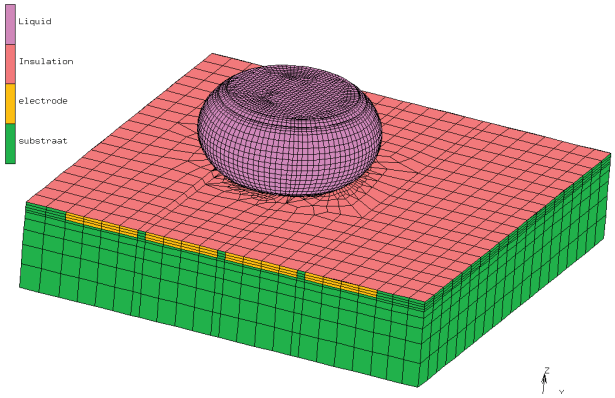

Figure 3.13. Mesh for the 3D electrostatic simulation of the droplet transition. Top plate and filler medium are removed for clarity.

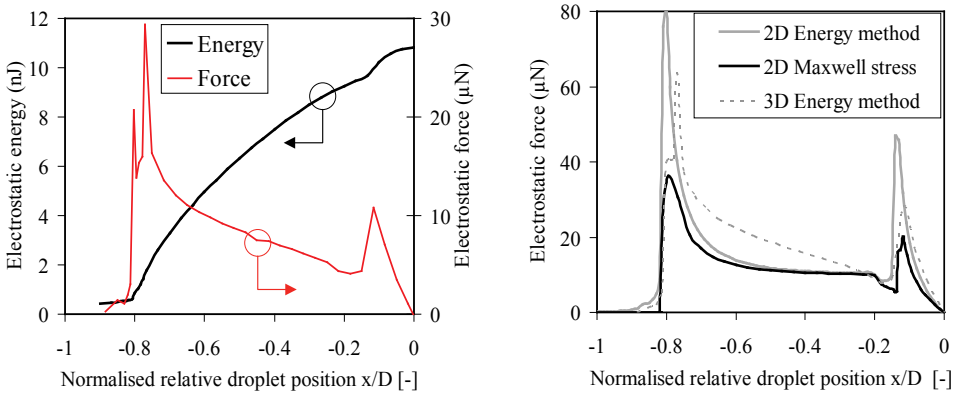

Figure 3.14. Evolution of the electrostatic energy (left vertical axis) and actuation force (right vertical axis) for a dielectric liquid droplet as a function of the droplet position for an applied voltage of 150 V (left). Comparison of the evolution of the electrostatic force calculated with the method of virtual work and the Maxwell stress method for the 2D simulation and with the method of virtual work for the 3D simulation (right).

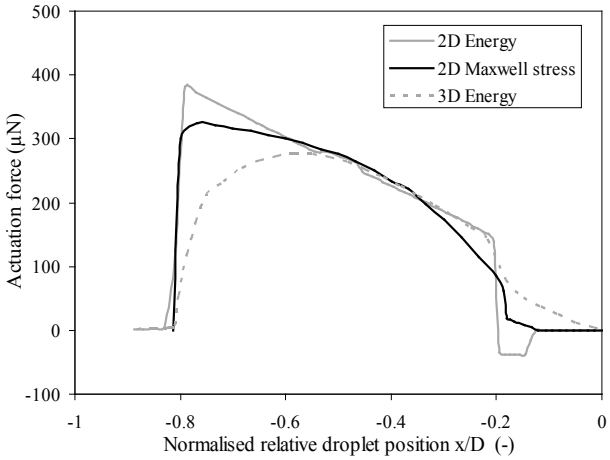

Figure 3.15. Comparison of the evolution of the electrostatic force calculated with the method of virtual work and the Maxwell stress method for the 2D simulation and with the method of virtual work for the 3D simulation for the case of a conductive droplet with an applied voltage of 150 V.

B. Conductive liquid

The same analysis is performed for a conductive liquid droplet for the same parameter values specified in Table 3.2. Only the value for the dielectric constant ε_R is set to infinity to mimic the behaviour of a conductive liquid. The comparison between the different calculated forces is shown in Figure 3.15. In comparison with the dielectric liquid are the peaks in the force profile less pronounced. The force calculations for the 2D and the 3D cases show a good agreement in the middle of the droplet transition. At the location at the edges of the electrode, the difference is larger. In the 3D case no peaks are observed in the force profile. In the 2D case however a sudden increase in force occurs at the location of

the edge of the electrode. After this position, the force gradually decreases towards the point where the advancing front reaches the end of the activated electrode. The 2D virtual work method predicts a sudden drop at that point and even a negative force, whereas both other methods show a positive force.

C. Conclusion for the electrostatic force calculation of the nominal case

Simulations have been performed for both dielectric and conductive liquid droplets to calculate the actuation force with different methodologies for 2D and 3D cases. The force in case of a conductive droplet is around 10 times higher compared to dielectric liquids with a permittivity ε_R of 81. From the simulations, it can be seen that the 2D methods are in good agreement with the 3D method for the central part of the droplet transition. However, at positions close to the edges of the activated electrode, the 2D simulations suffer from the singular point in the calculations and the results are mesh dependent. Therefore the large values of the force on these peaks cannot be trusted. To investigate trends and parameter sensitivity of the actuation force, the average force during the transition is most important. Therefore, less time consuming 2D simulations can be used for a first coarse optimisation to reduce the range of parameters considered and to investigate the trend of the parameter sensitivities. For a final detail optimisation, the 3D method can be used with the reduced design space of parameters.

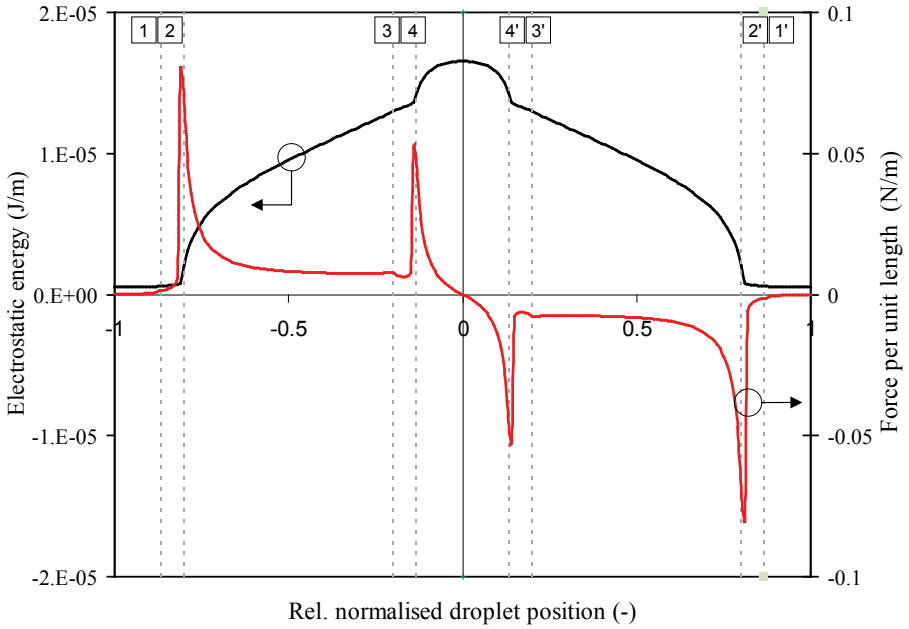

Figure 3.16. Evolution of the electrostatic energy (left vertical axis) and actuation force (right vertical axis) calculated using the method of virtual work based on 2D simulations for a long dielectric droplet.

3.4.2 Discussion on force during transition

In this section, the force profile in the 2D case is studied in detail and the appearance of the peaks and locations is discussed. First, a dielectric droplet sufficiently longer than the electrodes is considered. Figure 3.16 shows the evolution of the energy and actuation force during the transition of the dielectric droplet over an activated electrode for the parameters specified in Table 3.1. From the graph, the positions where the contact line of the droplet crosses the edge of an electrode and the associated peaks can be identified. These locations are shown graphically in Figure 3.17.

For a droplet moving form right to left with a contact line diameter D_c, an electrode width w_e and a spacing g_e between the electrodes, the positions x_1 to x_4 can be read from the graph for the advancing front of the droplet, and the positions x_1' to x_4' for the receding front of the droplet. These locations can be defined as follows as a function of the droplet and electrode geometries:

$$x_1 = -\frac{D_c + w_e + 2g_e}{2}; \tag{3.24}$$

$$x_2 = -\frac{D_c + w_e}{2}; \tag{3.25}$$

$$x_3 = -\frac{D_c - w_e}{2}; \tag{3.26}$$

$$x_4 = -\frac{D_c - w_e - 2g_e}{2}; \tag{3.27}$$

for the advancing side and:

$$x_1' = \frac{D_c + w_e + 2g_e}{2}; \tag{3.28}$$

$$x_2' = \frac{D_c + w_e}{2}; \tag{3.29}$$

$$x_3' = \frac{D_c - w_e}{2}; \tag{3.30}$$

$$x_4' = \frac{D_c - w_e - 2g_e}{2}; \tag{3.31}$$

for the receding side respectively. Now the case of a long droplet compared to the width of the electrodes is considered:

$$D_c > w_e + 2g_e. \tag{3.32}$$

This is the most relevant case since overlap between the droplet and the next electrode to be activated is desired to ensure a continuous droplet motion over the electrodes. Before the advancing front of the droplet reaches position x_1, the whole droplet is in contact with the grounded electrode at the bottom plate and no force is acting on the droplet. In between positions x_1 and x_2, the droplet front is in the space between the grounded electrode at a voltage 0 and the activated electrode at voltage V, at a floating potential. In this region the droplet starts feeling an attractive force from the electrode. This force reaches a peak value at the position x_2 where the location of the advancing front of the droplet coincides with the

edge of the activated electrode. Between positions x_2 and x_3, the front of the droplet is above the activated electrode. In this region the force decreases from the peak at x_2 to position x_3.

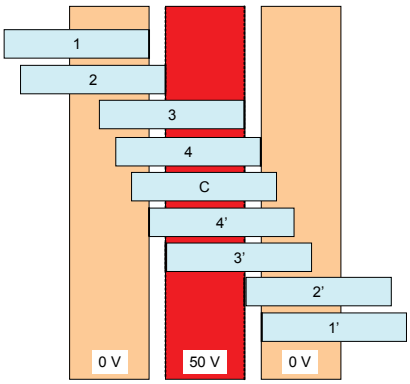

Figure 3.17. Schematic representation of the positions where the droplet contact line crosses the edge of an electrode in the 2D simulations.

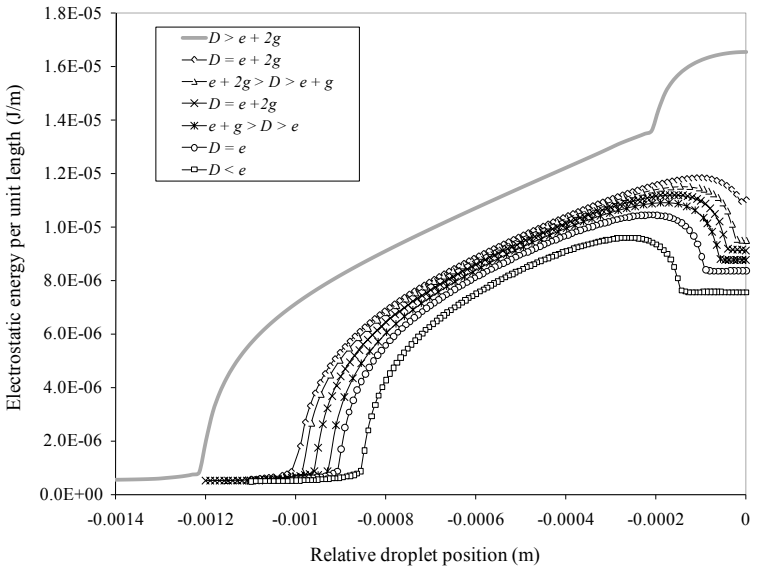

Figure 3.18. Influence of droplet diameter on the 2D electrostatic energy profile during the transition of a dielectric droplet on an activated electrode of 900 µm and an electrode spacing of 100 µm.

The behaviour in the region between x_3 and x_4 is similar to that between locations x_1 and x_2. The force profile shows a steep increase towards a new positive force peak at x_4. Here the front of the droplet touches the edge of the next grounded electrode while the backside of the droplet is still above the previous grounded electrode. After this position, the force reduces gradually until the droplet is symmetrically above the powered electrode, at

position *x=0*. At this point, there is no net force acting on the droplet. As can be seen from the energy evolution during the droplet transition, this position corresponds to the equilibrium situation of minimal total energy. From the force curve it is clear that it is a stable equilibrium for a more positive position, i.e. more to the right of the powered electrode a negative force acts on the droplet and will pull the droplet back to its equilibrium position. The energy profile is symmetric at both sides of the centre of the activated electrode. This leads consequently to an attractive force towards the centre of the electrode for droplet positions at the left side of the electrode, showing negative peaks at positions x_4' and x_2' corresponding to the location of the receding front of the droplet as shown in Figure 3.17.

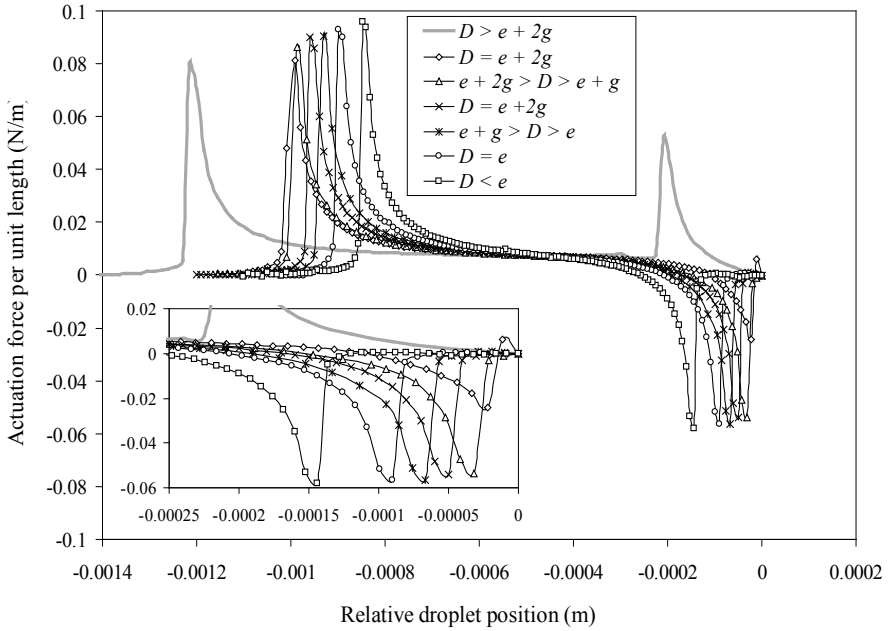

Figure 3.19. Influence of droplet diameter on the 2D force profile during the transition of a dielectric droplet on an activated electrode of 900 µm and an electrode spacing of 100 µm. Inset: Detail of the force profile close to the equilibrium point.

For the case of a long droplet, the force is positive in the whole transition towards the centre of the activated electrode. In case shorter droplets are used and condition (3.32) is not fulfilled, negative values of the forces can occur in the transition. In literature negative force values are found in those cases and are attributed to numerical inaccuracies (Torkkeli 2003) or 'capacitance behaviour' (Hectors and Huybrechts 2003). But from equations (3.24) to (3.31) and their locations in Figure 3.16 can be seen that the value of the locations x_4' and x_3' of the negative force peaks can become zero for certain values of the droplet diameter and electrode width. This means that the negative force peaks appear in the part of the droplet transition before the equilibrium point has been reached and where positive forces are expected. For the case where

$$D_c = w_e + 2g_e, \tag{3.33}$$

both the positive peak position x_4 and the negative peak position x_4' coincide at the point *x=0* where the net force should be zero due to the symmetric nature of the actuation force.

Since a steep increase to a positive peak from x_3 to x_4 and a steep decrease to a negative peak are expected this leads to a small positive peak close to $x=0$ and a larger negative peak a bit further from the centre between x_3 and zero. For shorter droplet diameters x_4 and even x_3 can become positive. Figure 3.19 shows the force profile for different sizes of droplet compared to the electrode size and spacing. For droplet diameters smaller than the criterion in equation (3.32) a negative force peak is observed at location x_4'. All the force curves intersect at the location

$$x = -\frac{w_e}{2}. \tag{3.34}$$

At this location the centre of the droplet is located above the edge of the activated electrode. This means that half of the droplet is located above the activated electrode and the other is located before the electrode. At this point the 2D force is the same for all droplet sizes.

3.4.3 Validation of the decoupling approach

In the force calculation approach, a fixed droplet shape during the motion of the droplet through the channels is assumed. However, in reality, the droplet deforms due to the electrowetting effect and the forces acting on the droplet during the motion. When a voltage is applied on an electrode, the contact angle of a droplet reduces at the location where the contact line is above the activated electrode. In this section, the effect of the droplet shape on the force profile of the droplet transition through the channel is studied.

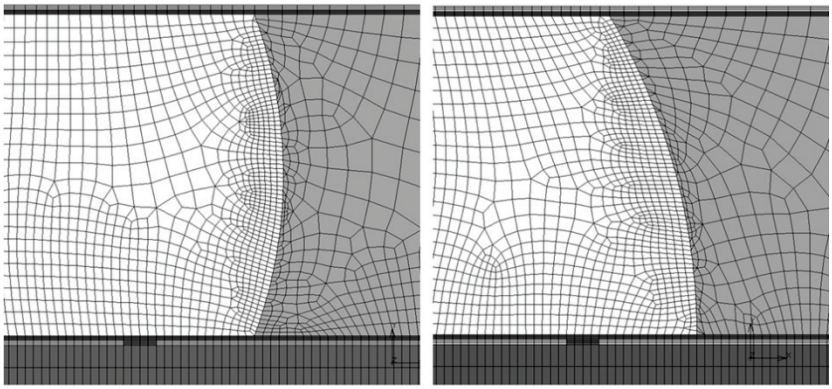

Figure 3.20. Example of the grid used for the finite element simulations for the electrostatic force calculation in case of an underformed droplet (θ=135°) and a deformed droplet (θ=95°).

The effect of the droplet shape is illustrated by considering two extreme droplet shapes for the system parameters listed in Table 3.2. For the first situation, an undeformed droplet shape on a highly hydrophobic surface is considered. A static contact angle of the liquid droplet on this surface of 135° is chosen. For the deformed droplet, an electrowetting induced contact angle reduction of 40° is considered for the applied voltage. In this case the contact angle above the activated electrode is 95°. Figure 3.20 shows an example of the grid used for the finite element simulations for both droplet shapes.

In Figure 3.21, the effect of the droplet shape on the actuation force is shown. The left graph shows the force profile for both droplet shapes. The right graph shows the absolute and relative difference between the force profiles. The maximum force during the droplet motion is 20 μN for the system parameters listed in Table 3.2. The largest force difference between the two droplet shapes is around 1 μN at the droplet position *x=-1.3 mm*. The locations at the left side of this position show a larger relative difference. However, the absolute force in this region is not sufficiently high to overcome the threshold force. As a result, deviation in this part of the force profile will not affect the dynamic modelling in Chapter 4 for which the calculated force profile is used as input. This corresponds to a relative difference of 10%. In the largest part of the droplet motion, between the location -1.2 mm and the central position, the absolute difference is around 0.2 μN, which corresponds to a relative difference between 1% and 3%.

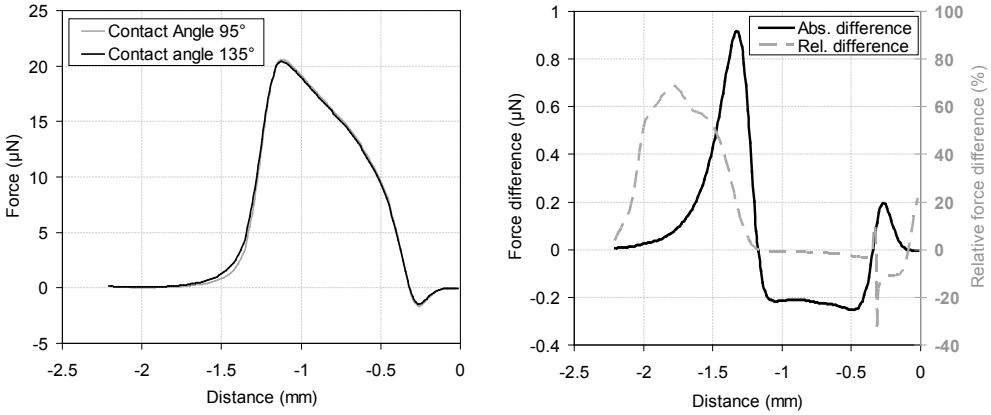

Figure 3.21. Evolution of the actuation force during the droplet transition over an electrode for the system parameters in Table 3.2 for an underformed and a deformed droplet (left). Absolute and relative force difference between the deformed and underformed droplet (right).

For the generation of the electrostatic force, the region between the droplet and the electrode, in the insulating layer, is the most important. Most of the electric field intensity will be localised in this area. As a result, the electrostatic actuation force is generated in a region very close to the contact line. Consequently, the macroscopic shape of the droplet (and consequently the macroscopic contact angle) only has a small impact of the actuation force acting on the droplet. The result of the integration of the Maxwell stress over the droplet surface will be changed significantly. The largest force deviation observed between two extreme droplet shapes is only 10%. Therefore, the assumption to use a fixed droplet shape in the analysis of the evolution of the actuation during the droplet transport over an activated electrode is justified.

3.4.4 Comparison with models from literature

The results of the calculations can be compared to data available in literature. Bahadur and Garimella (2006) propose an analytical energy-based model for the actuation force calculation in confined electrowetting-induced actuation systems. The analytical model

presented, calculates the force by derivation of the electrostatic energy content in the insulation, below the droplet contact area in the bottom plate and above the droplet contact area in the upper plate respectively. In their study a 0.6 µl droplet in a channel with a height of 0.3 mm actuated with a voltage of 50 V is considered. The parameters used in the calculations are shown on the right hand side of Figure 3.22. The left hand side of the figure shows the comparison between the calculated actuation force using the method of virtual work in 3D presented here and the results from literature (Bahadur and Garimella 2006). Overall, the agreement is rather good. Both curves show a similar evolution of the force as a function of the position. Main differences are a lower peak force value, 41 µN compared to 46 µN, and a smaller peak close to the equilibrium point at $x = -0.25\ mm$. The simulation of the same configuration using a dielectric water droplet instead of a conductive droplet results in a maximal actuation force of 4.77 µN.

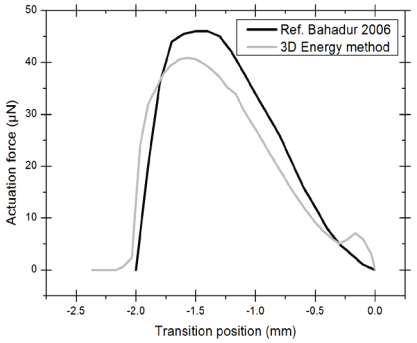

Parameters used in [Bahadur2006]

Parameter	Value
Droplet radius (r) = half the electrode width	1 mm
Plate separation (d)	0.3 mm
Dielectric constant: lower plate dielectric (k_1)	3
Dielectric constant: upper plate dielectric (k_2)	3
Thickness: lower plate dielectric (d_1)	1 μm
Thickness: upper plate dielectric (d_2)	1 μm
Actuation voltage (V)	0–50 V

Figure 3.22. Comparison of the actuation force using the method of virtual work in 3D to data from literature(left). Overview of the parameters used for the comparison (right).

Comparison between the analytical models and the numerical techniques show that the simplified analytical models are capable to predict the force profile very well. In the electrowetting system, the capacitive energy in the region between the liquid and the electrode is the most important aspect. Simple analytical formulations are sufficient to describe this capacitive energy as a function of the droplet position to achieve a good estimation of the actuation force. To achieve a similar result with the computational technique a very fine mesh is required. The advantage of the computational technique is that the method can be applied for complex geometries whereas the analytical method is limited to simple geometries.

3.4.5 Parameter sensitivity analysis

In this section the influence of the parameters on the actuation force is investigated by means of finite element simulations.

3.4.5.1 Insulation layer

The importance of the insulation layer is already pointed out in Section 3.1.2. Theoretical considerations indicate that a material with a high dielectric constant should be chosen and the layer should be as thin as possible without exceeding the breakdown strength of the

material. Table 3.1 gives an overview of the dielectric strength and dielectric constant of commonly used insulation materials. In this section the influence of the insulation layer on the electrostatic actuation force is studied in detail both for a dielectric and conductive droplet.

A. Dielectric liquid

In the case of a dielectric liquid, the voltage drop between the activated electrode and the grounded electrode is realised over the liquid droplet and the insulation layers. Due to the voltage drop in the insulation layer only a reduced voltage will act on the dielectric droplet. The insulation layers are thin compared to the dimensions of the droplet and the dielectric constant of the insulating material is low compared to the one of water. Therefore the major part of the voltage drop will occur across the liquid. To estimate the voltage drop over the dielectric liquid, a simplified 1D situation of three materials is considered. In this simple model a voltage difference is applied over three layers. These are the bottom insulation, the dielectric droplet and the top insulation. Based on the thickness and the dielectric constant of each layer the voltage drop across each of the layers can be estimated. Based on the voltage division over the layers as a function of the capacitance the reduced voltage at the dielectric liquid can be estimated as follows:

$$V_{eff} = \frac{\frac{1}{C_{liq}}}{\frac{1}{C_{ins,top}} + \frac{1}{C_{liq}} + \frac{1}{C_{ins,bottom}}} \cdot V_{app} = \frac{\frac{t_{liq}}{\varepsilon_{lid}}}{\frac{t_{liq}}{\varepsilon_{liq}} + 2\frac{t_{ins}}{\varepsilon_{ins}}} \cdot V_{app} = f \cdot V_{app} \,. \qquad (3.35)$$

Here, the effective voltage is expressed as a function of the applied voltage V_{app} at the electrode and the thickness t_{liq} and t_{ins} and dielectric constant ε_R of the liquid and insulating material respectively. The voltage is reduced by a voltage factor f that depends on the thickness and dielectric constant of the insulating layer and the liquid. For the geometry and material properties of the nominal case, as defined as in Table 3.1, the actuation force is calculated for different values of the insulation thickness. The thickness of the insulation is assumed to be the same at the top and bottom side. The force profile during the droplet transition for an insulation thickness of 1, 2, 5, 10 and 20 µm respectively is shown on the left hand side of Figure 3.23. For thinner layers, the force peaks are more pronounced. The right hand side of the figure shows the influence of the thickness on the actuation force at the normalised relative droplet position *x/D = -0.5*. This data is represented by the markers in the graph. On the right vertical axis the second power of the voltage factor defined in equation (3.35) is drawn. The electrostatic force is expected to scale to the second power of this factor. From the graph can be seen that there is a good agreement between the predicted trend (solid line) and the simulations at different values of the insulation thickness. Therefore, in the case of a dielectric liquid droplet, following trend can be found for the actuation force:

$$F \sim \left(\frac{\frac{t_{liq}}{\varepsilon_{lid}}}{\frac{t_{liq}}{\varepsilon_{liq}} + 2\frac{t_{ins}}{\varepsilon_{ins}}} \cdot V_{app} \right)^2 . \qquad (3.36)$$

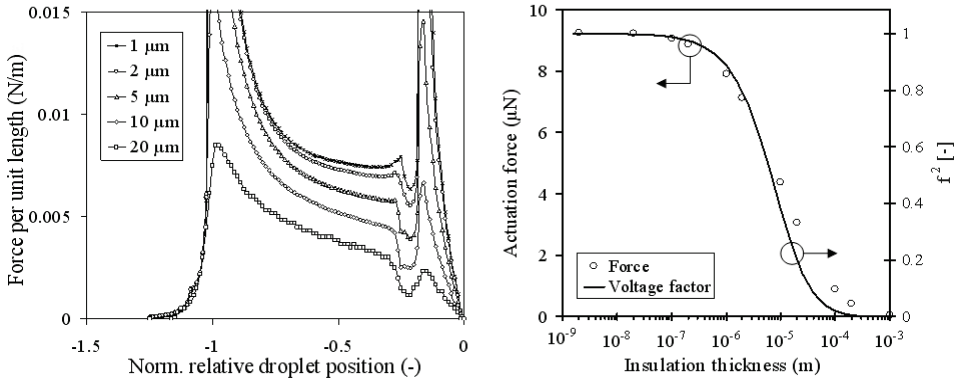

Figure 3.23. 2D force evolution during the droplet transition for different values of the insulation thickness for a dielectric droplet (left). Variation of the electrostatic force at location x/D=-0.5 as a function of the insulation thickness (right).

In the case of a dielectric droplet, the value of the dielectric constant and the thickness of the droplet are much higher than those of the insulation. This means most of the voltage drop will occur over the liquid. The thickness of the water droplet will be in the order of 100 µm to 1 mm. As a result, no problem is expected for dielectric breakdown in the insulation layer as long as no excessively high voltage is used.

B. Conductive liquid

In the case of an electrically conductive liquid, the voltage drop between the applied voltage *V* at the activated electrode and 0 Volt at the grounded electrode is realised in the insulating layers only. No voltage appears across the conductive liquid, which acts as an equipotential body. The voltage is divided at three locations; at the insulation layer on top of the activated electrode, at the insulation layer at the bottom side, on top of the grounded electrode and at the insulation at the top electrode. If a constant voltage is assumed the electric field increases inversely with the thickness of the insulation. From Table 3.1 can be seen that the dielectric strength of BCB 3 MV/cm is. For the nominal simulation case of 150 V this value of the electric field is reached for insulation layers thinner than 0.5 µm. In these cases the electric field will cause defects in the insulation and electric currents can occur through the insulation towards the liquid conductive droplet. This means that lower voltages should be used in that case to prevent the dielectric breakdown of the insulation. The left hand side of Figure 3.24 shows the actuation force on a conductive droplet at the normalised relative droplet position *x/D = -0.5* in the nominal case of Table 3.1 for different values of the insulation thickness and dielectric constant. Since the applied voltage is 150 V, the breakdown strength of the material will be reached for a thickness of 0.5 µm in the case of BCB. Thinner layers should not be used for the given voltage but are shown to visualise the trend of the parameter sensitivity. From the graph can be seen that the actuation force is proportional to the dielectric constant of the insulating material and inverse proportional to the thickness of the insulation layer. Therefore, the influence of the properties of the insulation on the actuation force of a conductive droplet is described by following equation:

$$F \sim \frac{\varepsilon_{ins}}{d_{ins}} V^2 . \tag{3.37}$$

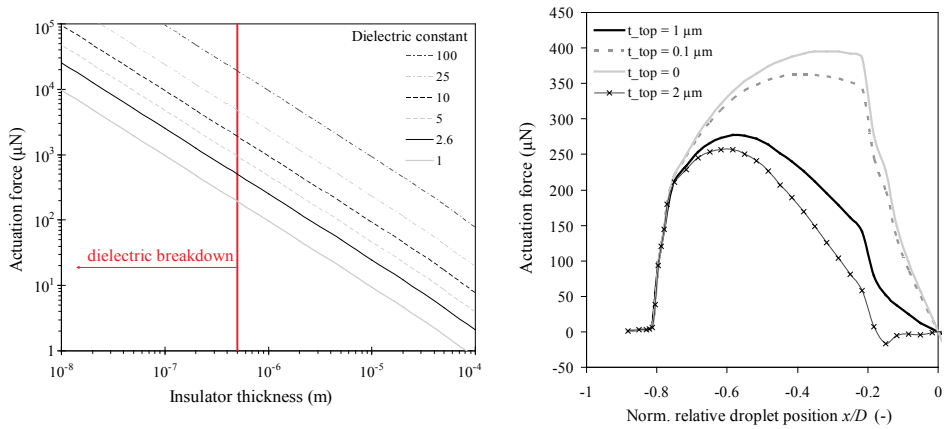

Figure 3.24. Influence of the insulation properties on the actuation force on a dielectric droplet at position x/D = -0.5 for an applied voltage of 150 V (left). Actuation force during the droplet transition for different values of the thickness of the top insulation for a constant bottom insulation of 1 µm (right).

Most of the voltage drop is realised over the insulation layer on top of the activated electrode and only a small part of the voltage drop is realised across the insulation layer at the top. Since the electrode at the top plate is grounded, the insulation layer is not essential for the operation of the droplet actuation. The electrode at ground potential however is essential for the droplet actuation to generate a positive force during the droplet transition. The graph on the right hand side shows the actuation force on the conductive droplet during the transition. The solid black line represents the case of top and bottom insulation of equal thickness. By reducing the thickness of the top insulation relative to the bottom insulation, the force can be increased until the limiting case of no top insulation. In this case a maximum force of 400 µN is reached compared to 250 µN in the case of equally thick top and bottom insulation. In the case where the top insulation is thicker than the bottom insulation, a negative force will be observed during the droplet transition. Therefore, the insulation at the top plate should be chosen at thin as possible. A sufficiently thick insulation at the bottom plate is required to prevent dielectric breakdown. As a result an optimal thickness of the bottom insulation can be found for which the required voltage to generate the desired actuation force is minimised and no breakdown will occur.

The described methodology for the calculation of the actuation force and the knowledge on the influence of the major parameters now allows optimising the structure for a maximum actuation force and a minimal applied voltage required.

Optimal insulation thickness

As described above the electrostatic actuation force is strongly dependent on the properties of the insulation layer. Optimising the thickness of this layer reduces the required voltage and ensures no breakdown occurs in the insulation. *Figure 3.*25 shows the required voltage to generate a certain actuation force on a conductive droplet as a function of the insulation thickness. On the same graph the requirement for dielectric breakdown can be drawn. In a voltage versus thickness graph this relation is a straight line with the dielectric breakdown strength as slope. Points above this line will lead to breakdown since the electric field is larger than the dielectric strength of the material. The optimal thickness of the insulation can be found on the intersection between the curve of dielectric breakdown and the curve of the required voltage. This thickness is the minimal thickness for which the requested force can be generated with a minimal voltage. To compensate for variations due to processing and other external factors, a safety factor should be taken in to account.

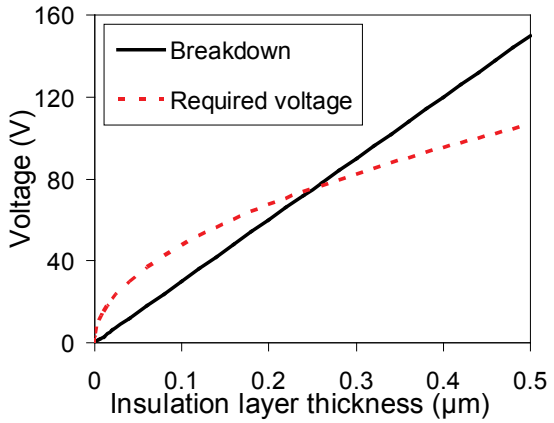

Figure 3.25. Actuation force as a function of the thickness of the insulation layer and applied voltage. In this example, BCB is considered as an insulating material(ε_R =2.3).

3.4.5.2 Droplet geometry

In this section the influence of the droplet size on the actuation force is investigated. These trends are compared with the scaling of the retentive force as described in Chapter 2. The operating voltage should be chosen sufficiently high for the resulting actuation force to overcome the retentive force caused by the surface tension. Parameters studied here are the droplet volume and the droplet diameter.

For a droplet as presented in Figure 3.8, the volume of a droplet can be estimated as a function of the contact angle θ, the droplet contact line radius R_c and the height of the channel H (see Appendix A.2):

$$Vol = \pi R_c^2 H + \frac{\pi R_c H^2}{\cos^2\theta}\left(\alpha + \frac{\sin 2\alpha}{2}\right), \tag{3.38}$$

where α is defined as follows:

$$\alpha = \theta - \frac{\pi}{2}. \tag{3.39}$$

Here the contact angles at top and bottom plate are assumed to be the same. A similar relation can be written for different contact angles at top and bottom side. This means for a given value of the contact angle only two of the three parameters, droplet contact line radius R_c, height of the channel H and droplet volume Vol, can be chosen independently. Depending on which of the parameters are controllable, different situations are considered.

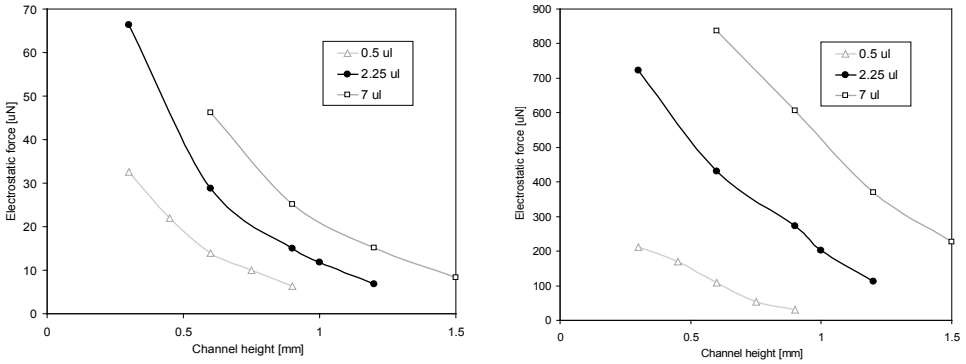

Figure 3.26. Influence of the channel height and droplet volume on the actuation force at position x/D = -0.5 for an applied voltage of 150 V for a dielectric liquid (left) and conductive liquid (right).

Constant volume

First, the situation of a given droplet volume and a fixed channel height is studied. In this case the droplet contact line diameter will be determined by equation (3.38). The electrostatic actuation force is calculated for droplet volumes of 0.5, 2.25 and 7 µl as a function of the channel height for both a dielectric droplet and a conductive droplet. The results are shown in Figure 3.26. From the graph can be seen that the actuation force increases with increasing droplet volume and decreasing channel height. Both effects lead to an increase in droplet diameter; for a fixed droplet volume increases the droplet diameter for decreasing channel height as can be seen for equation (3.38). Similarly for a constant channel height an increasing droplet volume will lead to an increase of the droplet diameter. The graphs of the actuation force as a function of the droplet volume and channel height should be compared with similar graphs of the retentive force to estimate the required voltage for droplet actuation.

Influence of droplet diameter and channel height

Figure 3.26 shows an increase in actuation force for a decreasing channel height and increasing droplet contact line diameter. To assess the influence of those contributions, both are studied separately. First the influence of the droplet diameter is studied for a fixed channel height. Since both droplet diameter and channel height are chosen here, the droplet volume cannot be chosen freely but is calculated by equation (3.38) and will change

accordingly to the droplet diameter. Figure 3.27 shows the influence of the droplet diameter on the actuation force on a conductive droplet for four different values of the channel height. The graph is plotted as a function of ratio of the droplet diameter divided by the channel height. An almost linear relation between the actuation force and the droplet diameter can be observed. Similarly, a droplet diameter can be chosen to study the influence of the channel height. Figure 3.28 shows the influence of the channel height on the actuation force on a conductive droplet activated by 150 V for four different droplet diameters. It can be seen that the actuation force is nearly independent of the channel height. This can be explained by the fact that the force is generated in a small region close to liquid – solid interface at the bottom of the droplet. Increasing or decreasing the channel height for a fixed droplet diameter will therefore not change the actuation force on the droplet even though the droplet volume changes accordingly to the channel height. As a result the increase in actuation force observed in Figure 3.27 can be attributed to the increase in droplet diameter and not to the decrease in channel height.

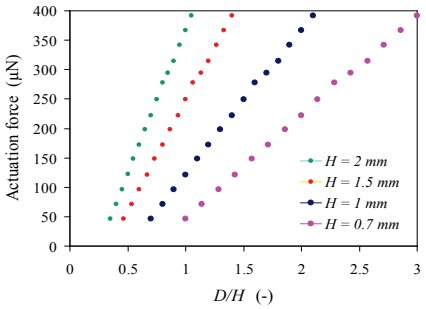

Figure 3.27. Influence of the droplet diameter on the actuation force for different channel heights.

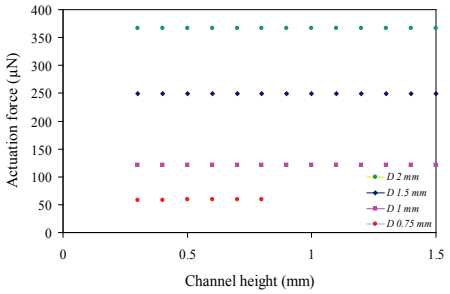

Figure 3.28. Influence of the channel height on the actuation force on a conductive droplet.

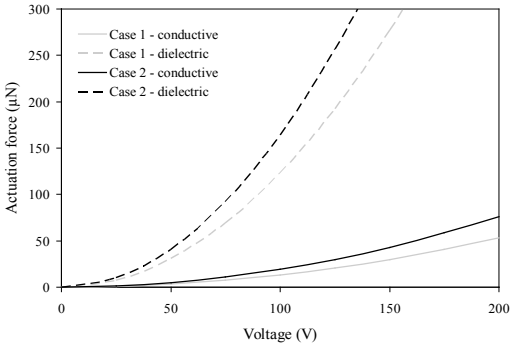

Figure 3.29. Influence of the applied voltage on the actuation force on a dielectric and conductive droplet.

3.4.5.3 Actuation voltage

The most important parameter for the droplet actuation is the applied voltage. The actuation force depends heavily on the applied voltage. Both the method of the Maxwell stresses, equation (3.14), and the method of the virtual work (3.17) indicate that the actuation force scales with the second power of the electric field strength and consequently also with the second power of the application voltage. Figure 3.29 shows the influence of the applied voltage on the electrostatic actuation force for the nominal case *'Case 1'* defined in Table 3.1 and the comparison case *'Case 2'* as described in Figure 3.22 for both a dielectric and conductive liquid droplet. It can be seen from the graph that the force in case of a conductive droplet is roughly 10 times higher compared to the dielectric droplet for the same applied voltage and droplet and electrode geometry. This means that in the case of a dielectric droplet three times the voltage should be applied to realise the same electrostatic actuation force compared to the conductive droplet.

3.5 Actuation force calculation for the annular electrode system

In this section, the methodology for the calculation of the electrostatic actuation (see Section 3.3.1) is applied to the annular electrode system. The principle and application of this system is described in Section 1.4. The relevant part for the droplet actuation of this system consists of a cylindrical channel with embedded annular electrodes at the inside of the channel. Similar to the case of the planar electrode system, the electrodes in this case are covered with an electrical insulating layer to prevent electric currents in the liquid. During the actuation, one electrode is activated while the other electrodes are kept at 0 V. In Figure 3.30 a schematic representation is shown for a cylindrical channel with integrated annular electrodes. The range of channel diameters investigated is from 150 µm to 500 µm, whereas the range of droplet length is 150 µm to 750 µm. When centred on top of an electrode, the droplet needs to at least overlap at little bit with the next electrode in order to be actuated by this next electrode. Therefore, the length of the droplet must be at least as long as the width of the electrode.

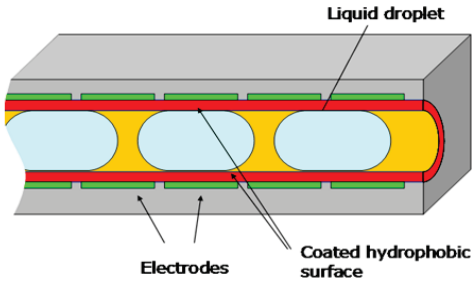

Figure 3.30: Schematic cross section of a channel in the annular electrode system.

To calculate the electrostatic actuation force in this case, the method of the virtual work is used (Section 3.3.2). First, a parameterised finite element model of the liquid droplet and the channel is built to perform the electrostatic simulation. Typically, the grid used for the electrostatic simulations consists of 150,000 cells. The grid of this model used for the electrostatic simulations is shown in Figure 3.31. In this figure, the air inside the channel and the top part of the channel, the insulation layer and the electrodes are not shown to reveal the inside of the channel. With the method of the virtual work, the force is calculated as the derivative of the electrostatic energy with respect to the position. This means that the energy has to be extracted from the simulation at two positions near the position of interest to approximate the local force. The closer the two evaluation points are set to each other the better the approximation. To get an accurate representation of the electrostatic force during droplet motion over the electrode, the simulations need to be performed for many droplet positions. In this work, the transition distance of the droplet moving over an electrode is divided in 200 steps. At each droplet position the electrostatic, finite element simulations are performed to extract the value of the electric energy stored in the system using equation (3.17). The local electrostatic force can be found as the derivative of this energy according to equation (3.19).

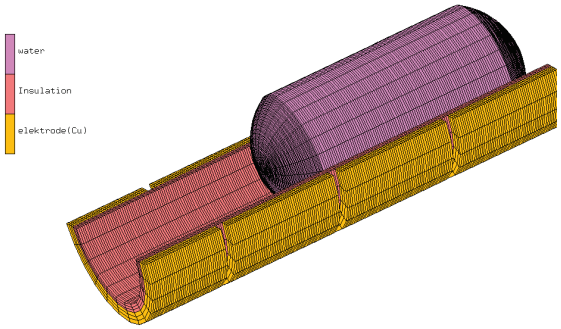

Figure 3.31: Grid of the finite element model of the liquid droplet in the cylindrical channel (top side of the channel, electrodes and insulation layer and the air in the channel are removed for clarity).

3.5.1 Force calculation of a nominal case

First, the study of the electrostatic force is performed for a nominal case. This will be the reference case to compare the results and effects of parameter study to. For the reference case, an electrode pitch of 150 µm and a gap of 10 µm between subsequent electrodes is assumed. The length of the droplet is considered to be 250 µm, the channel diameter 150 µm and the thickness of the insulation layer 1 µm. Figure 3.32 shows the electrostatic energy in this system as a function of the droplet position for an actuation voltage of 20 V. The magnitude of the electrostatic energy can be read from the left vertical axis. The droplet position is defined as the distance between the centre of the droplet and the centre of the powered electrode. In the same graph, the evolution of the electrostatic actuation force as a function of the droplet position is shown. The force is the derivative of the energy with respect to distance. The magnitude of the electrostatic force can be read from the right vertical axis. For this case a maximum actuation force of 12 µN is generated by the system. Several peaks can be observed in the force profile at the following locations:

- *x = 200 µm*
  At this location, the advancing edge of the moving droplet reaches the beginning of the activated electrode. Since the contact line is a circle perpendicular to the face of the electrode, the whole contact line crosses the edge of the electrode at once. This leads to a sudden increase in the actuation force.
- x = 100 µm
  The receding edge of the droplet leaves the grounded electrode 2 positions before the activated electrode.
- x = 90 µm
  The receding edge of the droplet reaches the grounded electrode in front of the activated electrode. Between the 2 positions a small positive peak is observed.
- *x = 50 µm*
  At this location the advancing edge of the moving droplet crosses the edge of the activated electrode. From this position on, the edge of the droplet is the region between the two electrodes. At this point the droplet feels a repulsive force trying to push the droplet away from the droplet centre. This leads to a negative peak in the force profile.
- *x = 40 µm*
  The advancing edge of the droplet reaches the beginning of the next electrode that is kept at 0 V. From here on, no actuation force is acting on the droplet since both the receding and advancing edge of the droplet are above a grounded electrode. Therefore the net force on the droplet is zero.

A similar analysis can be made from the energy profile, where a sudden rise or drop corresponds with the location where the droplet crosses an electrode. In the next section, the effect of parameter variations on the actuation force and the profile of the actuation force is studied.

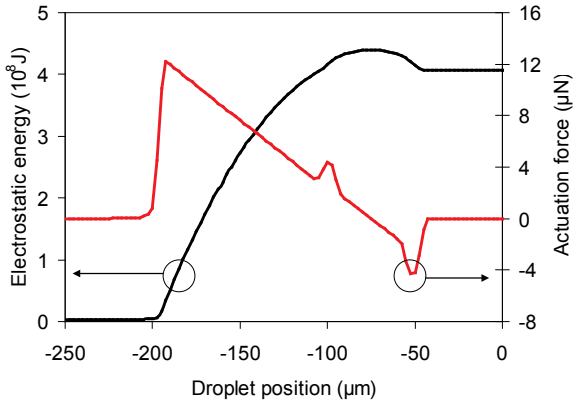

Figure 3.32: Electrostatic energy and electrostatic actuation force as a function of the droplet position for an actuation voltage of 20 V in the annular electrode system.

3.5.2 Influence of the channel diameter

In the nominal case, the channel diameter is 150 µm. In this section, the effect of a larger or smaller channel diameter on the actuation force is studied. The range of the diameter is varied from 50 µm to 250 µm while the other parameters are kept constant. This means that by changing the channel diameter and keeping the droplet length constant, the droplet volume is also changed. Figure 3.33 and Figure 3.34 show respectively the energy and forces profiles for the different diameter values in the range of 50 to 250 µm. From the graphs, it can be observed that the actuation force scales linearly with the channel diameter. The opposing force caused by the contact line friction also scales linearly, whereas the mass and therefore also the inertial forces scale with the second power of the diameter.

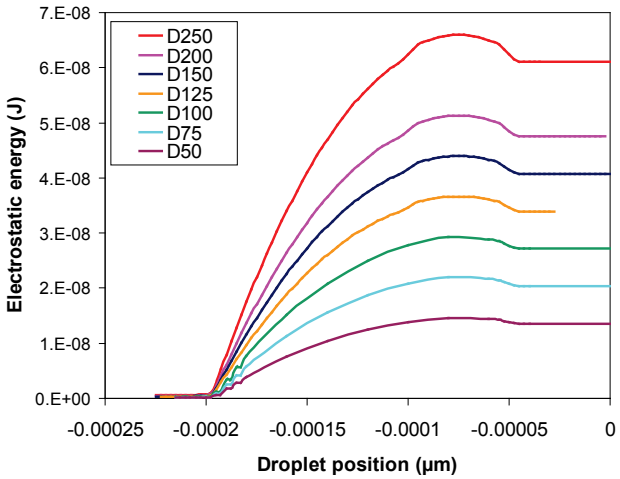

Figure 3.33: Profile of the electrostatic energy as a function of the droplet position for different values of the channel diameter.

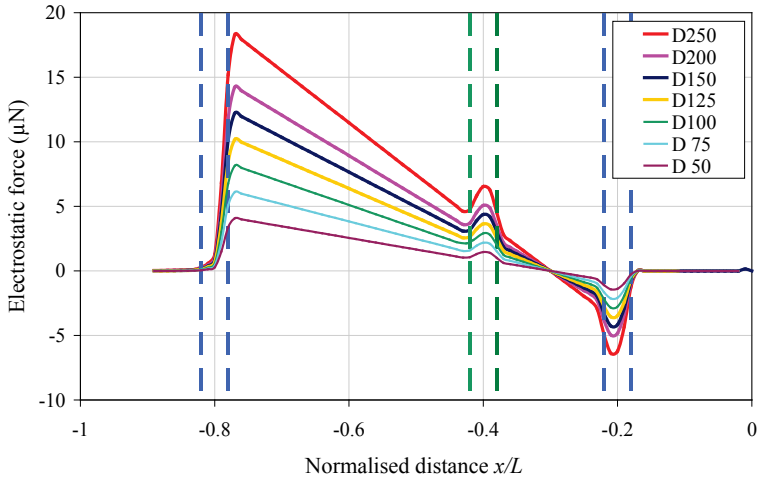

Figure 3.34: Profile of the actuation force as a function of the droplet position for different values of the channel diameter.

3.5.3 Influence of the droplet length

In this section, the effect of variations in droplet length on the actuation force is studied. The values of the droplet length are varied in a range of 140 to 300 µm while the other parameters are kept constant. Figure 3.35 and Figure 3.36 show the energy and the force profile respectively for an actuation voltage of 20 V. From Figure 3.36, it can be seen that the maximum actuation force is not affected by the droplet length. The force profile on the other hand shows a large dependence on the droplet length. For shorter droplets, the negative peak becomes more pronounced. In the case where the droplet has the same length as the electrode both the negative and positive peaks have the same magnitude due to the symmetry of the situation. This can also be seen from the energy profile; for the case with a droplet length of 150 µm, the energy at the centre of the electrode is the same as the energy at a position before the droplet reaches the electrode. For longer droplets, the negative peak decreases. This means there could be a droplet length found for which no negative peak is observed. On the other hand, the size of the region with zero force close to the centre of the electrode increases. In this region, the droplet will not be actuated. From the force profile can be observed, that for all the cases the force is zero for the location where the centre of the droplet is located above the edge of the activated electrode. In the graph, this occurs at location $x=75\ \mu m$. At this position, the left half of the droplet is above a grounded electrode and the right half above the activated electrode. In this case, no force is acting on the droplet. Figure 3.37 shows the force profiles as a function of the normalised droplet position. The droplet position is normalised with respect to the droplet length. From this figure, it can be seen that the slope of the profile versus the normalised position is the same for all droplet lengths. It can also be seen that the maximum force does not depend on the length of the droplet. Since the opposing force scales with the length of the droplet, the droplet should be chosen as short as possible. The shortest droplet, which can be actuated continuously over an array of electrodes, always needs to be in contact with two electrodes,

to be attracted by the next electrode when the voltage is switched. An additional argument for shorter droplets is length of the region of zero force close to the zero position. If this region is too long, the region where the droplet will stop is too large and the droplet might not be actuated by the next electrode.

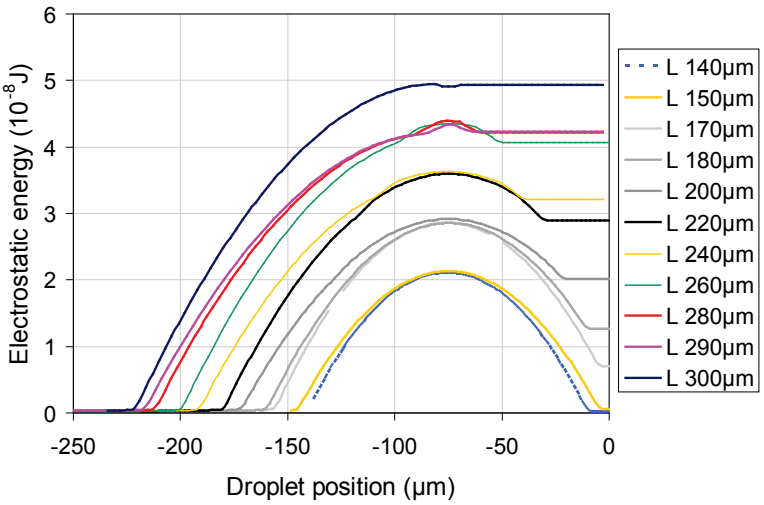

Figure 3.35: Profile of the electrostatic energy as a function of the droplet position for different values of the droplet length.

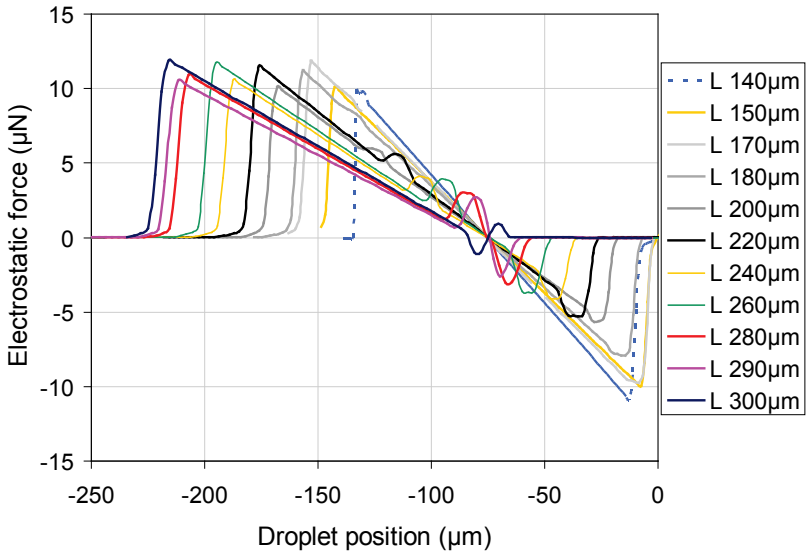

Figure 3.36: Profile of the electrostatic actuation force as a function of the droplet position for different values of the droplet length.

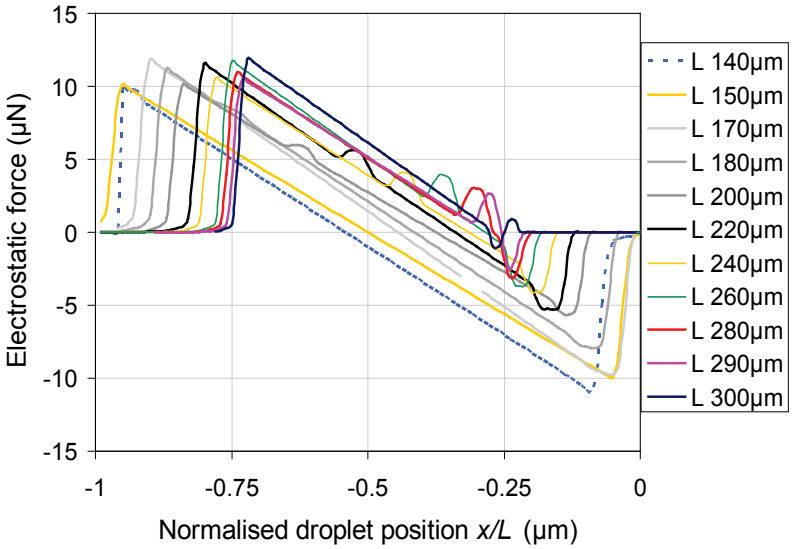

Figure 3.37: Profile of the electrostatic actuation force as a function of the normalised droplet position for different values of the droplet length. The droplet position is normalised by the length of the droplet.

3.6 Conclusions

In this chapter, the droplet deformation and motion in the presence of an external electric field is investigated. First, the effect is studied experimentally for a stationary droplet on either a flat or a rough surface. For the droplet on a flat surface, the relation between the contact angle and the applied voltage was studied for both a conductive and a dielectric, polarisable liquid. The rough surface is mimicked by 100 x 100 µm² microchannels. For a droplet on a rough surface two meta-stable morphological states exist: the Cassie state (the droplet sits on top of the peaks of the surface) and the Wenzel state (the droplet wets the complete surface). It was found that the droplet is in the Cassie state for the geometry considered. A morphological transition to the Wenzel state occurs when the applied voltage exceeds a threshold of 51 V. Theoretical transition criteria for the contact angle are derived from energy considerations. These contact angle predictions correspond well to the measured contact angle before and after the morphological transition.

Next, the electrostatic induced droplet flow in a channel is studied numerically. Formulations for the actuation force are derived both from a force perspective (method of Maxwell stresses) and an energy approach (method of virtual work). These formulations are applied on the results of electrostatic finite element simulations. Results from these force calculations based on 2D finite element simulations (both force and energy formulation) are compared to the force calculation based on 3D simulations (only the energy method). The advantage of the force approach, is the ability to visualise the force distribution over the interface of the droplet. The more complex implementation is a drawback of this method. This is also the reason why this method is not applied on the 3D simulation. The energy

approach on the other hand, provides one average value for the force acting on the droplet. The advantage of this method is the ease of implementation. The agreement between the 2D and 3D calculations is good for the central part of the droplet trajectory over the electrode. Large differences are found at positions, where the contact line of the droplet crosses the edge of an electrode. At this position the results of the 2D simulation are not accurate. However, for design exploration through parameter studies interested in the average droplet force, the 2D methods can be used to reduce the range of parameters before starting time consuming 3D simulations.

The methodology of the force calculation as a function of the droplet location is applied both to the planar electrode system and the cylindrical channel with annular electrodes. For both systems, the shape of the force and energy profile are explained by the droplet position and the overlap with the activated electrodes. Next, a parameter study is performed to study the effect of both material parameters and geometrical parameters. The influence of the properties of the insulation layer is explained by a simple analytical capacitance model in the case of both conductive and dielectric liquids in the planar electrode system. Finally, the force calculation for the planar electrode system is compared to analytical models available in literature (Bahadur and Garimella 2006). The comparison shows that the simplified analytical models are capable to predict the force profile very well due to the dominance of the capacitive energy. To achieve a similar result with the computational technique a very high mesh density is required in the region of the contact line. The advantage of the computational methods is the application for complex geometries, material properties and voltage signals. Furthermore, the numerical force simulations could be coupled to the numerical tools for the fluid flow and analysis to allow an optimisation of the whole process.

Furthermore, in this chapter, the decoupling approach has been validated by assessing the influence of the droplet shape on the actuation force profile. It was found that for two extreme droplet shapes – an undeformed droplet with a contact angle of 135° and a deformed droplet with a locally reduced contact angle of 95° – the maximum difference in the force profile during the transition over an activated electrode is 10%.

From the performed parameter studies using the force calculation methodology, several consequences for the design and use of the actuation system can be observed. In the case of a conductive liquid, the actuation force acting on the droplet is much higher compared to a dielectric droplet; for a dielectric droplet with a permittivity ε_R of 81, the difference is a factor of 10. As a result, in the case of conductive droplets, a voltage of roughly a factor 3 lower can be used compared to a dielectric liquid with $\varepsilon_R = 81$ to realise the same force. Furthermore, the parameter study reveals the thickness of the insulation should be as low as possible and the dielectric constant as high as possible to achieve a maximum actuation force. The minimum thickness of the insulation is however limited by dielectric breakdown which results in an optimum thickness and corresponding optimum operation voltage.

Chapter 4

Dynamic modelling of electrostatically induced droplet motion

Abstract

In this chapter, a general methodology for the dynamic study of electrostatically actuated droplets is presented. A simplified 1D transient model is developed to investigate the transient response of a droplet to an actuation voltage and to study the effect of geometrical and fluid-thermal properties and electrical parameters on this behaviour. First, the general approach for the dynamic droplet motion model is described. All forces acting on the droplet are introduced and presented in a simplified algebraic expression. For the retentive force, the empirical models from Chapter 2 are used and for the electrostatic actuation force, the numerical results of Chapter 3 are used. Next, the approach is applied for the planar electrode system and for the annular electrode system. Further, the model is solved and the parameter sensitivity is studied for the case of a single electrode and an array of electrodes. Using this methodology, the influence of the threshold force, switching frequency and voltage on the droplet trajectory is studied. Finally, the modelling methodology is validated using experimental data, available in literature.

Introduction

In the droplet based microfluidic systems studied in this work, also referred to as digital microfluidics, small discrete amounts of liquid (nanolitres to microlitres) are manipulated by means of electrostatic forces. The electrostatic forces are generated by an array of individually addressable electrodes. The actuation of the separate electrodes requires an efficient control algorithm to ensure a successful continuous flow of droplets. To develop such an algorithm for the electrode actuation, a detailed understanding of the dynamic droplet response to a voltage pulse is necessary. The study of the individual control of droplets is important to be able to predict the droplet motion, to optimise the voltage application and to precisely control the droplet manipulations such as droplet generation, splitting, merging and mixing.

In this chapter, a generic simplified macroscopic model is described to predict the dynamics of droplet motion as a reaction to the application of a voltage at a single electrode or subsequently at an array of electrodes. In literature, several dynamic models are reported (Ren *et al.* 2002; Bahadur and Garimella 2006) that successfully predict the steady state velocity of the droplet flow under certain actuation conditions. The model developed in this chapter describes both the steady state condition and the transient droplet behaviour before reaching this steady state condition. The required result from such a transient model is the position of the droplet at each time step and the required voltage to actuate the droplet. From these data, the time the droplet needs to reach a certain position, the time dependent velocity, the possible overshoot and oscillations and the settling time can be extracted. If this information is known, an efficient algorithm for the voltage application can be developed to optimise the flow rate, ensuring a continuous droplet flow through the channel and to minimise the power consumption. Based on the transient behaviour of an individual droplet a suitable frequency can be chosen to switch the voltage between the subsequent electrodes.

The accuracy of the prediction of the dynamic droplet response depends on the accuracy of modelled forces. These includes both the electrostatic actuation force as well as the opposing forces that are acting on the droplet while moving through the channel. The nature and dynamics of these forces and the complex interfacial phenomena behind them are not completely understood. Many aspects of the dynamics of moving contact lines are subjects of research at many international research groups. It is not the intention of the present work to resolve all the challenges regarding droplet motion prediction and moving contact line complications. The objective here, is to study the influence of the different opposing forces on the droplet, the influence of the geometrical, electrical properties of the structure, the thermo-physical properties of the liquid and the interfacial properties and to identify the dominant forces and parameters. In this work a macroscopic model is presented where the droplet is considered as a single discrete mass moving through the channel. This leads to a 1D model using simplified algebraic equations for the opposing forces. Input for this model are the experimentally derived material characterisation properties discussed in Chapter 2 and the electrostatic actuation force derived in Chapter 3.

Several experimental techniques exist that can be used to experimentally validate the modelling results. A first technique is optical sensing of the droplet position by a camera using a transparent electrode and substrate (Gong and Kim 2006). Another technique is the measurement of electrical signals (capacitance, impedance) (Armani *et al.* 2005) to detect the location of the droplet position. These sensors could be used for a dedicated closed-loop

control and feedback system (Ahmadi *et al.* 2009, Bhatthacharjee 2009). In this work no additional experiments are carried out. However, the modelling results are validated using experimental and modelling results published in literature.

4.1 General description of the dynamic droplet model

A simplified one-dimensional model is presented to describe the dynamic response of a single droplet based on the forces acting on the droplet. The droplet is considered as a single mass moving through the channel as a result of the electrostatic actuation force. Since the droplet is simplified to a single mass, the droplet is assumed to be moving with average droplet velocity U_{av}, which is the volume-averaged velocity of the droplet. The internal motion inside the droplet and the consequent relative velocities are not considered here. They will be discussed in Chapter 5. The opposing forces are represented by algebraic expressions based on modelling results of the electrostatic force (Chapter 3) and semi-empirical models (Chapter 2). For the structures considered in this work, the droplet is moving in air. However, in literature (Pollack *et al.* 2000) systems are described where the channel is filled with a host medium, mostly a low viscosity silicone oil. This oil reduces resistive force, prevents droplet evaporation and reduces contact angle hysteresis. As a result, lower actuation voltages are required. To make the model as general as possible, the influence of the host medium or filler liquid (whether it is oil or air) is included in the model. Based on all the forces acting on the droplet, the model describes the droplet response to a voltage applied at one of the electrodes in the system. Furthermore, it allows to study the influence of the different forces as well as the effect of the electrical, geometrical, physical parameters and interfacial properties. The electrical parameters include the permittivity of the dielectric layer, the voltage applied, the switching frequency and the electrical conductivity of the liquid. The physical parameters include the viscosity of the liquid and the filler liquid, the droplet density. The interfacial properties include the surface tension parameters between droplet, substrate and host medium, the contact line friction and the retentive force. Geometrical parameters include electrode pitch and spacing, droplet volume and channel spacing.

4.1.1 Dynamic model formulation

The driving force for the droplet motion is the electrostatic actuation force, discussed in Chapter 3. Important opposing forces acting on the droplet (Ren *et al.* 2004; Bahadur and Garimella 2006) are the shear force between the droplet and channel F_w, the contact line friction force F_{CL} and the viscous drag F_D due to the droplet moving through the filler liquid. The contact line friction force includes the threshold effect that is observed for droplet movement. The droplet will deform under the electrostatic force and lead to contact angle hysteresis between the advancing angle θ_A and the receding angle θ_R (Berthier 2007). In order to move the droplet, this electrostatic force needs to overcome a critical force due to the contact angle hysteresis.

Since the droplet is considered as a single discrete mass moving through the channel, a one-dimensional force balance of the forces acting on the droplet, projected on the actuation direction, can be written as follows:

$$M\frac{dU_{av}}{dt} = F_{el} - F_W - F_{CL} - F_D, \tag{4.1}$$

with:
- M : mass of the droplet;
- U_{av} : average velocity of the droplet;
- F_{el} : electrostatic driving force;
- F_w : shear force between the droplet and the channel;
- F_{CL} : contact-line friction force;
- $F_{D:}$ drag force on filler liquid.

The differential equation (4.1) describes the dynamic behaviour of the droplet as function of the driving force and the opposing forces. The formulation of the different forces acting on the droplet will be discussed more in detail in the next Sections 4.1.2 to 4.1.5. In Section 4.1.6, these formulations will be combined in (4.1), to present the complete dynamic model including all parameters.

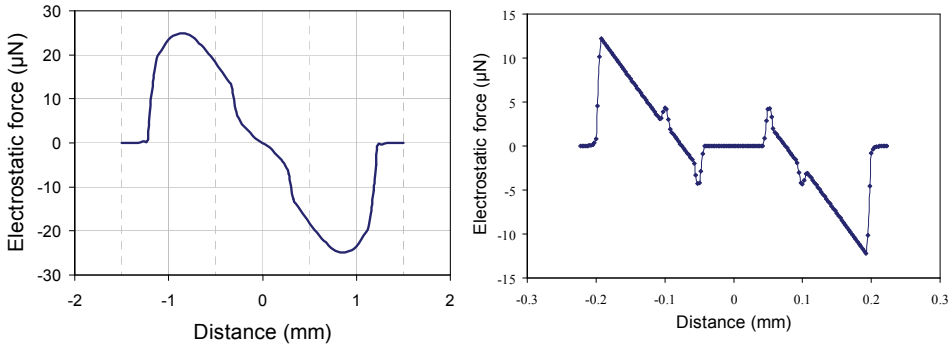

Figure 4.1. Electrostatic actuation force acting on a droplet as a function of the droplet position for both electrode configuration systems: Force profile for a planar system for an actuation voltage of 45 V (left). Force profile for the annular electrode system (right).

4.1.1.1 Formulation for the electrostatic force F_{el}

The electrostatic force is the driving force for the droplet actuation. From the results of the quasi-static electrostatic finite element modelling in Chapter 3, this force is known at each droplet position and as a function of the following parameters: droplet volume, channel height, liquid material properties, insulation thickness, dielectric constant of the insulation and the applied actuation voltage. Figure 4.1 shows the force profile as a function of the droplet position for both the parallel electrode system (left) as the annular electrode device (right). These profiles are calculated in Chapter 3 using the energy method for a three dimensional finite element model. These force profiles as a function of the droplet position are used as an input for the transient dynamic model. The electrostatic force attracts the droplet towards the centre of the electrode. Using the convention on the location as introduced in Chapter 3 (see Figure 3.8), the force is positive for negative x_d locations and

the force is negative for positive locations. When the droplet is centred above the powered electrode, the actuation force is zero. In the absence of opposing forces, the droplet would oscillate around the centre of the electrode, which is the equilibrium position. Due to the opposing dissipative forces the oscillation will be damped and the droplet will stop at a certain position depending on the level of the opposing forces and the applied voltage. If the voltage is not sufficiently high to overcome the opposing forces, the droplet will not start moving.

4.1.1.2 Formulation for the shear force F_w

The shear force between the droplet and channel can be estimated when the velocity profile in the channel is known. A velocity profile can be assumed in the droplet with zero slip boundary conditions on top and bottom walls. In Chapter 5, it will be shown by detailed simulations of the fluid flow inside the droplet, that a parabolic velocity profile is observed across the height of the channel if a no-slip boundary condition at the top and bottom wall is assumed.

A. General Formulation

Based on the average droplet velocity U_{av}, the vertical velocity profile in the channel can be determined. For a known velocity profile the viscous dissipation force can be estimated as follows:

$$F_W = \mu A \frac{\partial v}{\partial y} \tag{4.2}$$

where μ is the droplet viscosity and A is the contact area between the droplet and the wall, v is the velocity profile parallel to the wall and y is the distance perpendicular to the wall. Based on the average droplet velocity, the vertical velocity profile in the channel can be determined. The constraint for the average droplet velocity can be expressed as follows:

$$\frac{1}{S}\int_S U \cdot dS = U_{av} \tag{4.3}$$

where S is the cross sectional area of the channel. A parabolic velocity profile leads to higher shear forces compared to a linear velocity profile for the same average velocity. However, the shear force will only account for a small part of the resistive forces.

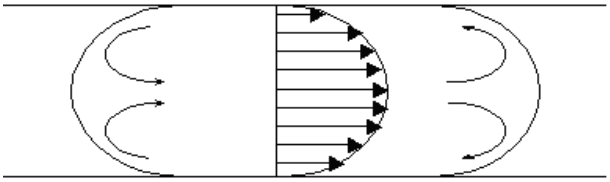

Figure 4.2. Assumed velocity profile in the droplet.

B. Formulation for the planar electrode configuration

In the planar system, the geometry of the droplet is assumed to be a truncated sphere with a circular contact line between the droplet and the top and bottom wall. The shape of the droplet is assumed not to change during the motion through the channel. The geometrical properties of the system are as follows: R_c is the radius of the contact line circle and H is the gap between the top and bottom wall. The opposing forces can now be expressed as a function of the geometry of the droplet in the considered system. Assuming the parabolic velocity profile (4.3) in the channel, the velocity across the height of the channel can be expressed as a function of the height as follows:

$$U(y) = \frac{3}{2} U_{av} \left(1 - \left(\frac{y}{H/2} \right)^2 \right). \tag{4.4}$$

Using equation (4.2) the total shear force exerted by the top and bottom can be written as follows:

$$F_W = 6\mu \frac{U_{av}}{H} \pi R_c^2 . \tag{4.5}$$

C. Formulation for the annular electrode configuration

In the annular electrode system, the droplet moves through a cylindrical channel. For the droplet in such a channel, the contact line between the droplet and the walls is a circle at both the receding and advancing side of the droplet. Consider D the diameter of the cylindrical channel and L the length of the droplet.

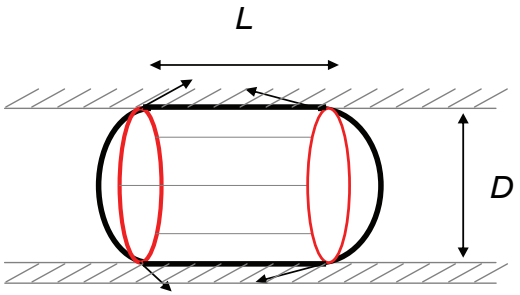

Figure 4.3. Schematic representation of a droplet in a cylindrical channel.

Assuming the parabolic velocity profile in the channel, the velocity $U(r)$ as a function of the radial direction r of the channel can be related to the average velocity U_{av} and the channel diameter as follows :

$$U_{av} \cdot \frac{\pi D^2}{4} = \int_S U(r) dS , \tag{4.6}$$

leading to following formulation for the velocity profile :

$$U(r) = 2U_{av} \left(1 - \left(\frac{r}{D/2} \right)^2 \right) \tag{4.7}$$

Using equation (4.2), the total shear force exerted by the top and bottom can be written as follows:

$$F_W = 4\mu \frac{U_{av}}{D} \pi DL \tag{4.8}$$

4.1.1.3 Formulation for the drag force of the filler fluid

Assuming that a droplet is moving through the filler fluid as a rigid body, the viscous drag on the droplet can be estimated by:

$$F_D = \frac{1}{2}\left(C_D \rho_f U^2\right) A_c \tag{4.9}$$

where, C_D is the drag coefficient and ρ_f is the density of filler fluid and A_c is the cross section area.

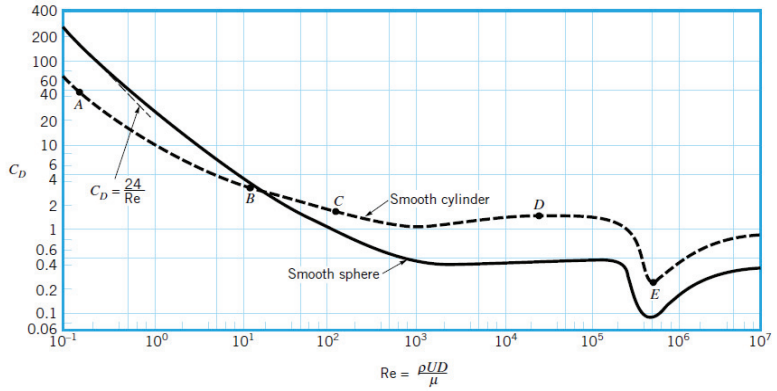

Figure 4.4. Drag coefficient as a function of Reynolds number for a smooth circular cylinder and a smooth sphere (taken from Munson et al. 2002)

The situation of a droplet moving through the filler fluid can be approximated by a cylinder in cross flow for the calculation of the drag coefficient. The drag coefficient C_D depends on the Reynolds number of the flow. This dependency is shown in Figure 4.4 for a cylinder and a sphere as function of the Reynolds number based on the cylinder or sphere diameter. For the electrowetting induced droplet flow, velocities up to 10 cm/s are expected. For a droplet with a diameter of 1 mm, this corresponds to a Reynolds number of 5. For a low R_e number, the drag coefficient C_D is inverse proportional with the Reynolds number for the filler liquid. Therefore, the drag coefficient C_D can be written as

$$C_D = \frac{a}{Re} \tag{4.10}$$

where a is a constant depending on the geometry of the object. In the case of a sphere, a is 24. For a cylinder, a can be assumed to be 12. To estimate the drag coefficient on the droplet, a value between the sphere and cylinder case is choosen. As a result, the viscous drag force F_D will scale linearly with the droplet velocity. Since the Reynolds number is defined as

$$Re = \frac{\rho_{filler} DU}{\mu_{filler}}, \tag{4.11}$$

the drag force (4.9) can be written as follows:

$$F_D = \mu_{filler} \cdot \frac{a}{2} \cdot \frac{A_c}{D} \cdot U \tag{4.12}$$

In the case of the planar electrode system, the cross-sectional area of the droplet can be approximated by the product of the droplet diameter and the channel height *H*. Therefore, the viscous drag force acting on the droplet as the droplet is moving through the filler liquid, can be written as follows using equation (4.9):

$$F_D = \mu_{filler} \cdot \frac{a}{2} \cdot H \cdot U \,. \tag{4.13}$$

In the case of air as a filler medium, the drag force is negligible compared to the dynamic contact line friction force and the viscous force as will be illustrated in the test case.

In the annular electrode system, the droplet moves through a cylindrical channel. Therefore no drag force of any filler liquid is acting on the droplet. There might be a pressure difference to overcome while being transported through the channel, however this effect is not taken into account in this simplified model since the channel is considered to be connected to a much larger reservoir and the length of the channel is considered to be short (only several times the length of a droplet).

4.1.1.4 Formulation for the contact line force

Contact line friction is a complex phenomenon and is very difficult to model. The friction originates from intermolecular attraction forces near the contact line which is not yet completely understood. Many different approaches exist to account for this effect ranging from experimental empirical correlations (Shapiro *et al.* 2003; Mohseni *et al.* 2007; Ren *et al.* 2004) to complex molecular-kinetics modelling (Blake 2006). An excellent review of recent theoretical, experimental, and numerical progress in the description of moving contact line dynamics can be found in (Bonn *et al.* 2009). In this work, an approximation for the static and the dynamic contact line friction force is used.

The **static** contact line friction force can be expressed as a function of the contact angle hysteresis of the droplet at the moment movement will start. This static contact angle hysteresis corresponds with the threshold, the actuation force needs to overcome before motion is initiated. The expression for this friction force is (Extrand and Kumagi 1995):

$$F_{CL} \cong 2.k\gamma_{LV} \left[\cos(\theta_R) - \cos(\theta_A)\right] w \tag{4.14}$$

where *w* is the width of the drop in the direction perpendicular to the droplet motion and θ_A and θ_R are the advancing angle and the receding angle respectively.

In the **dynamic** case, these contact angles are function of the velocity of the moving contact line U_{CL}. The left hand side of Figure 2.20 shows the evolution of the contact angles θ_A and

θ_R as a function of the velocity. Since the contact line friction force depends on θ_A and θ_R, the friction force will also be a function of the velocity. This dynamic contact angles and relation with droplet velocity is characterised in Chapter 2. Those results will be used in this chapter as an approximation of the complex contact line friction force. Different algebraic expressions are presented in literature to approximate this dynamic behaviour of the friction force. A commonly used expression based on the molecular interaction theory from Blake (2006) describes the dynamic part of the friction force as a power law function of the velocity:

$$F_{CL,dyn} = \zeta U^n L \tag{4.15}$$

where L is the length of the contact line and ζ is the coefficient of contact line friction defined in molecular kinetics and the exponent n varies between 0 and 2 (Chen and Hsieh 2006). Ren *et al.* (2002) and Chen *et al.* (2004) assume a linear relation between the friction and the velocity (i.e. n=1) and extract the value of the coefficient of contact line friction ζ from a fitting of simulations of steady state velocities as a function of the applied voltage to experiments. In this chapter, the exponent n will be assumed 1. For droplet actuation in silicone oil, Ren found a value of 0.04 Pa·s for the coefficient of contact line friction ζ. In this work, the coefficient ζ is extracted from tilt tests where droplets slide from a tilted surface while the contact angles and droplet velocity are measured (see Section 2.3.2 and Figure 2.20).

Summarised, the contact line friction force shows a threshold behaviour. For actuation forces smaller than the threshold force caused by the static contact line friction, the droplet will not move and only deform. The constitutive relation for the droplet deformation is shown in Figure 2.17(c) for a sessile droplet and in Figure 2.22 for a confined droplet. For actuation forces larger than the static contact line friction (4.14), the droplet will start moving. This threshold behaviour can be mathematically described using a 'minimum' function. The total expression for the contact line friction force can be written as follows:

$$F_{CL} = \min\left(2.k\gamma_{LV}\left[\cos(\theta_R) - \cos(\theta_A)_{\max}\right]w,\ F_{el}\right) + \zeta UL\,. \tag{4.16}$$

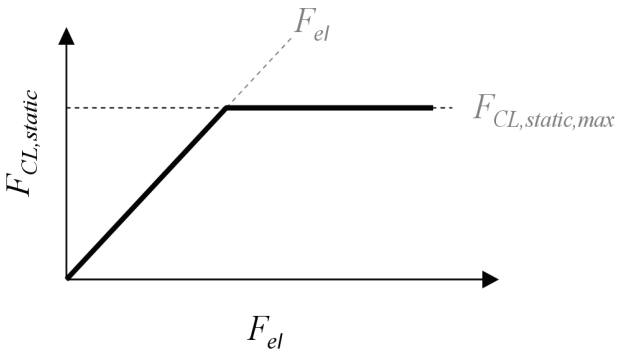

Figure 4.5. Schematic representation of the static part of the contact line friction force as a function of the actuation force.

For an actuation force smaller than the threshold force, the actuation force is compensated for by static contact line friction force, due to the droplet deformation. Using equation (4.14) the droplet deformation can be related to the actuation force as follows:

$$\cos(\theta_R) - \cos(\theta_A) = \frac{F_{el}}{2.k\gamma_{LV} w} \tag{4.17}$$

where θ_A and θ_R are a function of the actuation force. When the actuation force is high enough to overcome the threshold value of the static contact line friction force

$$F_{el} > 2.k\gamma_{LV} w\left[\cos(\theta_R) - \cos(\theta_A)\right]_{\max,static} \tag{4.18}$$

the droplet will start moving. Even for an increasing actuation force, the static contact line friction force is assumed to remain equal to the threshold force. This is schematically represented in Figure 4.5.

For the global model, the assumption is made that shape of the contact line does not change during the electrostatic actuation and motion through the channel. The effect of small changes in contact line shape are not expected to have a significant impact on the friction force. As a result, the first term of (4.16) can be obtained from a static contact angle analysis.

A. Formulation for the planar electrode configuration

The static contact line friction force for a confined droplet between parallel plates is experimentally characterised in Chapter 2. In these contact angle measurements, the tilt angle required to initiate droplet movement between two parallel Teflon coated surfaces was studied. These experiments are summarised in Figure 2.20. The gravitational force for this tilt angle corresponds to the static contact line friction. This also corresponds to the maximal static contact angle hysteresis. For a higher force, the contact angle hysteresis will not increase anymore and the droplet will start moving. From the experimental results, the maximum static contact angle hysteresis factor $\left[\cos(\theta_R) - \cos(\theta_A)\right]_{\max}$ can be experimentally determined. From the dynamic measurements as a function of the droplet velocity, it is found that the coefficient of contact line friction ζ is 0.08±0.03 Pa s.

The total contact line friction force for a droplet between two parallel surfaces can be written as a function of the droplet velocity:

$$F_{CL} = min\left(F_{el}, 2.k\gamma_{LV} w\left[\cos(\theta_R) - \cos(\theta_A)\right]_{\max,static}\right) + (0.08 \pm 0.03 \text{ Pa.s}) \cdot U_{av} 4\pi R_c \tag{4.19}$$

with R_c the radius of the contact line and the droplet width $w=2R_c$.

B. Formulation for the annular electrode configuration

A droplet in a cylindrical channel has contact lines with the solid, both at the receding and at the advancing side. This geometry is schematically represented in Figure 4.3. The length of these circular contact lines is πD. For this geometry, the static part of the contact line friction can be written as follows :

$$F_{CL,static} = min\left(F_{el}, \gamma_{LV}\left[\cos(\theta_R) - \cos(\theta_A)\right]_{\max,static} \pi D\right). \quad (4.20)$$

For this case, no experimental data are available. Therefore, the same values as for the planar configuration are used. The dynamic part can be written as follows :

$$F_{CL,dynamic} = \zeta U 2\pi D . \quad (4.21)$$

4.1.1.5 Summary for the model formulation

In case of a **static** droplet, the droplet deformation is related to the actuation force by equation (4.17). For actuation forces higher than the threshold force, the droplet will move. For this **dynamic** case, the droplet motion can be described by equation (4.1). The formulation of the opposing forces, as a function of the average droplet velocity can be substituted in the dynamic model for the droplet motion (4.1). For slow and moderate droplet velocities, the net force acting on the moving droplet can be approximated by the difference between the actuation force and the static contact line friction. In this work, the transition between the static and dynamic case is not studied in detail. For an actuation force higher than the threshold force, a rigid body motion of the droplet is assumed. For this droplet motion, velocities up to 10 cm/s are expected which correspond with a Reynolds number with respect to the filler medium of 5 for a droplet with a radius of 1 mm.

The electrostatic actuation force is calculated in Chapter 3 using finite element simulations. This force is calculated as a function of the applied voltage, the droplet volume, the electrode geometry (pitch and gap), the height of the channel or channel diameter, the dielectric constant and thickness of the insulation layer and the contact angle. As mentioned above, w and R_c in the case of the planar system, and L in the case of the annular electrode system are not independent parameters, but can be calculated from a combination of other parameters. Table 4.1 provides an overview of the independent parameters that are included in the dynamic model.

Table 4.1. Overview of the dynamic model parameters and the reference values used in the test cases.

Category	Description	Symbol	Planar	Annular
Geometrical	Droplet volume	Vol	*2.7 µl*	*4.5 nl*
	Channel height / diameter	H / D	*1 mm*	*150 µm*
	Electrode pitch	w_e+g_e	*1 mm*	*150 µm*
	Electrode gap	g_e	*100 µm*	*10 µm*
	Drag coefficient	C_d	*30*	*30*
	Insulation thickness	t	*1 µm*	*300 nm*
Material properties	Droplet viscosity	μ_d	*1.005 Pa s*	*1.005 Pa s*
	Droplet density	ρ	*1000 kg/m³*	*1000 kg/m³*
	Surface tension	γ	*72 mN/m*	*72 mN/m*
	Contact line friction (static)	$\left[\cos(\theta_R) - \cos(\theta_A)\right]_{\max,st.}$	*~8 µN*	*~6µN*
	Contact line friction coeff.	ς	*0.08 Ns/m²*	*0.08 Ns/m²*
	Contact angle	θ	*110°*	*110°*
	Dielectric const. insulation	ε_r	*3*	*4*
Application	Voltage	V	*45 V*	*35 V*
	Start position	x_0	*-1 mm*	*-150 µm*
	Switching frequency	f	*25 Hz*	

In the case of the **planar electrode configuration**, the dynamic droplet motion model can be written as follows:

$$\rho \cdot Vol \cdot \frac{dU_{av}}{dt} = F_{el}(x,t) - min\left(F_{el}(x,t), 2.k\gamma_{LV} w\left[\cos(\theta_R) - \cos(\theta_A)\right]_{\max,static}\right) - 12\mu \frac{U_{av}}{H}\pi R_c^{\,2} - \mu \cdot \frac{a}{2} \cdot H \cdot U_{av} - \zeta U_{av} L \tag{4.22}$$

In case the actuation force is smaller than the threshold force, the static contact line friction force is equal to the actuation force and as a result (Figure 4.5), the droplet will not move. The contact line force, created by the droplet deformation will compensate for the actuation force on the droplet. Below the threshold force, the relation between the droplet deformation and the actuation force is given by following relation:

$$\cos(\theta_R) - \cos(\theta_A) = \frac{F_{el}}{2.k\gamma_{LV} w} \tag{4.23}$$

In the expression of the dynamic case, the terms with a dependence on the droplet velocity can be grouped. In the equation for a moving droplet, the values for the planar test case from Table 4.1 are substituted in the equation, assuming air as a filler medium to reveal the contribution of the different forces after reordering the terms in the dynamic equations:

$$\rho \cdot Vol \cdot \frac{dU_{av}}{dt} = F_{el}(x,t) - \underbrace{2.k\gamma_{LV} w\left[\cos(\theta_R) - \cos(\theta_A)\right]_{\max,static}}_{8\mu N} - U_{av} \cdot \left[\underbrace{12\mu \frac{\pi R_c^{\,2}}{H}}_{2.1\times10^{-5}\,\frac{Ns}{m}} + \underbrace{\mu \cdot \frac{a}{2} \cdot H}_{5\times10^{-8}\,\frac{Ns}{m}} + \underbrace{\zeta L}_{4\times10^{-4}\,\frac{Ns}{m}} \right] \tag{4.24}$$

From the values of the different contributions to the opposing damping force, can be seen that the dynamic contact line friction is the dominant force compared to the viscous dissipation and the drag force.

In case of the **annular electrode configuration**, the dynamic formulation for the droplet motion can be written as follows :

$$\rho \cdot Vol \cdot \frac{dU_{av}}{dt} = F_{el}(x,t) - min\left(F_{el}(x,t), \gamma_{LV}\pi D\left[\cos(\theta_R) - \cos(\theta_A)\right]_{\max,static}\right) + \ldots - 4\mu \frac{U_{av}}{H}\pi DL - \zeta U_{av} 2\pi D \tag{4.25}$$

where the droplet length L is a function of the droplet volume, the channel diameter and the contact angle.

4.1.1.6 Equivalent damped mass-spring system

The behaviour of a moving droplet towards an activated electrode in the case of a sufficiently high actuation force $F_{el} > F_{CL,static}$ can be described as a damped mass-spring system. This simplified model can be used to develop a control strategy for the switching of the electrodes. The dynamic contact line friction, the drag force and the viscous dissipation

force are proportional to the droplet velocity and can be described with an equivalent viscous damping coefficient c_{eq} (Ns/m). The actuation force F_{el} can be linearised in the region of the centre of the activated electrode and therefore be represented by an equivalent spring constant k_{eq} (N/m).

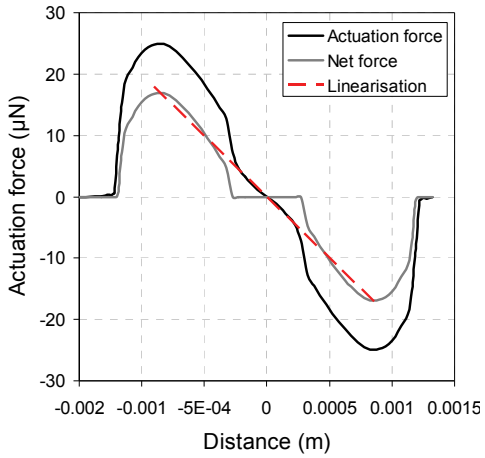

Figure 4.6. Force profile as function of the droplet position for an actuation voltage of 45 V: actual calculated profile (solid black line), difference between the actuation force and the static contact line friction (solid grey line) and the linearised force profile (dashed line).

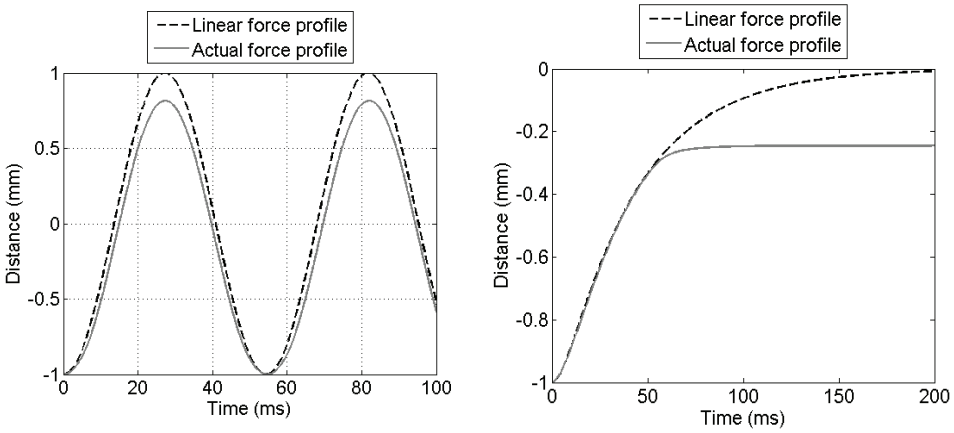

Figure 4.7. (a)Transient undamped droplet response for the actual force profile (45 V) and the linearised force profile. (b) Transient droplet position for the actual force profile and the linearised force profile.

Figure 4.6 shows the actuation force as function of the droplet position for the parameters in Table 4.1 and an actuation voltage of 45 V. The net force acting on a moving droplet is approximated by the difference of the actuation force and the static contact line friction force. For droplet positions with an actuation force lower than the threshold force, the net actuation force is considered to be 0. In the region around the electrode centre, the net force

can be linearised using an equivalent spring constant. The linearisation is shown in Figure 4.6 as a dashed line. Figure 4.7(a) shows the comparison of the droplet motion in a hypothetical case without damping force for the actual force profile and the linearised equivalent spring model. From this graph can be seen that the oscillatory behaviour (frequency and period) is similar for the actual force profile and the linearisation. In the actual force profile, the net force is zero close to the electrode centre. In the linear approximation, this effect is not present. As a result the equivalent model overestimates the forces close to the electrode centre. The droplet will stop earlier than the equivalent model predicts and will exhibit less oscillations than the equivalent mass spring damper model predicts. Figure 4.7(b) shows the comparison of the droplet motion calculated with the actual force profile and the equivalent linearised force profile. The equivalent damping coefficient is

$$c_{eq} = 12\mu\frac{\pi R_c^{\,2}}{H} + \mu\cdot\frac{a}{2}\cdot H + \zeta L \tag{4.26}$$

for the parallel electrode configuration, and

$$c_{eq} = 4\mu\frac{\pi DL}{H} + \zeta 2\pi D \tag{4.27}$$

for the annular electrode configuration.

After linearisation of the force profile, the droplet motion equations for a moving droplet, (4.24) and (4.25) can be written as an equivalent equation of a damped spring-mass system:

$$M\frac{d^2x}{dt^2} = -k_{eq}x - c_{eq}\frac{dx}{dt}. \tag{4.28}$$

Based on the nature of the motion equation, the droplet motion can exhibit oscillatory behaviour. The linearised equation allows analysis of the droplet motion by calculation of an equivalent natural angular frequency ω_0 and an equivalent damping ratio ζ_{eq}. In this way the possible oscillatory behaviour can be predicted and an optimal switching frequency for droplet motion over several subsequent electrodes can be obtained. The undamped angular frequency ω_0 and the damping ratio are defined as:

$$\omega_0 = \sqrt{\frac{k_{eq}}{M}}, \tag{4.29}$$

and

$$\zeta_{eq} = \frac{c_{eq}}{2M\omega_0}. \tag{4.30}$$

The value of the equivalent damping ratio ζ_{eq} determines the behaviour of the droplet motion. For $\zeta_{eq} > 1$, the system is overdamped and the droplet moves towards the electrode centre without oscillations. For $\zeta_{eq} = 1$, the system is critically damped. For $\zeta_{eq} < 1$, the system is underdamped, and the system oscillates with a damped natural frequency ω_d

$$\omega_d = \omega_0\sqrt{1-\zeta_{eq}^2} \tag{4.31}$$

In the case of the electrostatically actuated droplet, the natural frequency and damping ratio depend on the actuation voltage for a certain configuration (system and material parameters). A certain voltage corresponds to a critical damped droplet behaviour $\zeta_{eq} = 1$.

For lower voltages, the droplet motion will exhibit an overdamped behaviour and for higher voltages oscillations will occur.

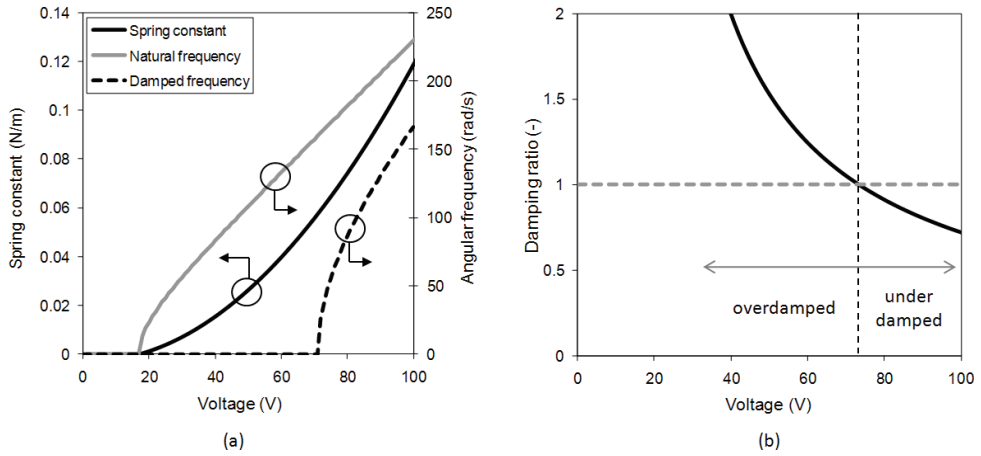

Figure 4.8. (a) Voltage dependency of the linearised spring constant (left vertical axis) and the natural angular frequency and the damped angular frequency (right vertical axis) for the planar electrode configuration with system parameters listed in Table 4.1.
(b) Voltage dependency of the damping ratio.

4.1.1.7 Limitations of the dynamic model

The validity of the dynamic model is limited to a certain range of the system parameters. For parameter values outside this range, the dynamic model can no longer be used to accurately predict the droplet motion. In this section, the limited range of the droplet size, application voltage and droplet velocity are discussed.

Droplet dimensions

The application of the dynamic model is only valid for sufficiently small droplet volumes. The force calculations are performed for a certain droplet shape, assuming the effect of surface tension dominates the effect of the gravity. For large droplet volumes, the droplet shape is flattened due to the increased importance of the gravity. The characteristic length to assess the relative impact of the surface tension and the gravity is the capillary length λ_c. The capillary length is defined as follows:

$$\lambda_c = \sqrt{\frac{\gamma_L}{\rho g}} \tag{4.32}$$

In the case of a water droplet at 20 °C in air, the capillary length is around 2.7 mm. For droplets with dimensions smaller than the capillary length, the surface tension dominates. For dimensions larger than the capillary length, the gravity will have an impact on the droplet shape and the dynamic model cannot be used anymore to predict the transient droplet motion.

Voltage range

The dynamic model cannot be used for very high actuation voltages. The first reason is the effect of voltage **saturation** of the electrowetting effect. From a certain voltage on, an increase in voltage will not result in a further contact angle decrease and consequently a higher actuation force acting on the droplet. The saturation limit of the voltage depends on the material properties of the solid surface and the liquid (Quinn *et al*. 2005). An example of this voltage saturation can be seen in Figure 3.3. The dynamic model should be used below this saturation limit. The second voltage related limitation is caused the required **rise time** of the voltage signal. In the model, a step function of the voltage application is assumed. In reality, a finite rise time is required to reach the desired voltage. This rise time is not included in the dynamic model. As a result the very fast transient (in the order of ms) predicted by the model will deviate from the actual droplet response. To realise a very fast build-up of the voltage, a high supply current is required. For typical power supplies (Agilent 2009, Keithley 2006), a rise time of 0.1 ms/V should be considered. To improve the model, a linear voltage increase to the desired voltage could be included.

Drag coefficient C_d correlations

The correlation for the drag coefficient C_d as function of the Reynolds number (4.10) is only valid for low Re number flow up to a Reynolds number with respect to the host medium of 5. For higher droplet velocities, this correlation is not valid and other correlations for low to intermediate Re numbers should be used (White 2003).

4.1.2 Solution of the dynamic model

The electrostatic actuation force is known as a function of the droplet position *x(t)*, whereas the shear force, drag force and contact line friction force are a function of the velocity *U(t)*. Since the velocity is the derivative of the position

$$U(t) = \frac{dx(t)}{dt}, \tag{4.33}$$

the differential equation (4.24) or (4.25) of the force balance of a moving droplet can be solved numerically by integrating with respect to time to find the position *x(t)* and velocity *U(t)* of the droplet.

4.1.2.1 Time dependent actuation force

By introducing the switching scheme of the electrodes, time dependent information is added to the electrostatic force. From the finite element simulations in Chapter 3, this force is known as a function of the droplet position with respect to the activated electrode. The switching scheme describes which electrode is activated at which time, with which voltage applied. This is schematically shown in Figure 4.9. On the left hand side, the force profile is shown as a function of the droplet position for three consecutive electrodes. On the right hand side, the time dependent voltage application at the different electrodes is shown for a switching frequency *f*. This means each of the electrodes is powered for a time *1/f*. As a result, the actuation force acting on the droplet is not only function of the droplet position but also of time. Indeed, in the time interval [0, *1/f*] the first electrode is powered. In this time interval, the force profile of electrode '1' is used. At time *1/f* the power is switched to the second electrode and for the period [*1/f, 2/f*] the force profile of electrode '2' should be

used as a function of the droplet position with respect to electrode '1'. As such, a time dependent formulation of the electrostatic force is created. For the droplet position, the centre of electrode '1' is used as a reference. As an example, the time dependent force $F_{el}(x,t)$ for three consecutive power electrodes with frequency f, can be written as follows :

$$F_{el}(x,t) = \begin{cases} F_{el,1}(x) & \text{for } t \in [0,1/f] \\ F_{el,2}(x-(w_e+g_e)) & \text{for } t \in [1/f,2/f] \\ F_{el,3}(x-2\cdot(w_e+g_e)) & \text{for } t \in [2/f,3/f] \end{cases} \quad (4.34)$$

where $F_{el,i}(x)$ is the actuation force as a function of the distance from the centre of activated electrode 'i'. Using a similar method, the time dependent force can be described for any switching pattern, including multiple electrodes activated at the same time using superposition of the different force profiles.

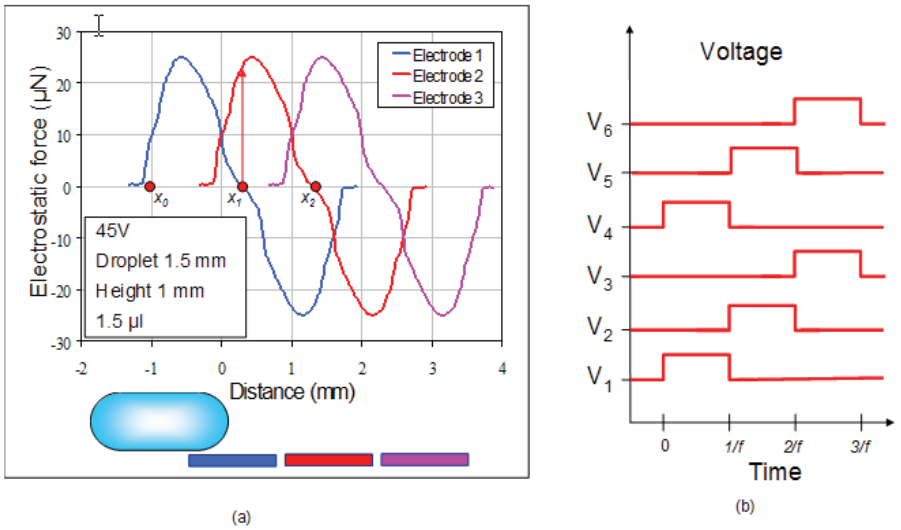

Figure 4.9. (a) Electrostatic actuation force profile as a function of the droplet position at three subsequent electrodes. (b) Schematic representation of the switching of the voltage in the actuation electrodes.

4.1.2.2 Solution strategy

The dynamic model (4.24) or (4.25) for a moving droplet can be solved for a certain switching pattern and a start position x_0 using a time-stepping approach with a time step Δt .

Time step t_0

At time step 0, the droplet is position x_0. The initial velocity of the droplet can be zero or a specified value u_0. For this position, the actuation force can be found as $F_{el}(x_0, t_0)$. At this position, the opposing forces $F_{CL,dyn}$, F_D and F_w can be evaluated as function of u_0. The instantaneous acceleration a_0 of the droplet at this time step can be found from the force balance as:

$$a_0 = \frac{\left[F_{el}\left(x_0,t_0\right) - min\left(F_{el}\left(x_0,t_0\right), F_{CL,stat,max}\right)\right] - F_{CL,dyn}(u_0) - F_D(u_0) - F_w(u_0)}{M} \tag{4.35}$$

In case the actuation force is smaller than the threshold force $F_{CL,stat,max}$, the static contact line friction force is equal to the actuation force and the expression for the acceleration reduces to:

$$a_0 = \frac{-F_{CL,dyn}(u_0) - F_D(u_0) - F_w(u_0)}{M}. \tag{4.36}$$

Time step t_1

At the next time step $t_1 = \Delta t$, the new droplet position x_1 and droplet velocity u_1 can be found as follows:

$$\begin{aligned} x_1 &= x_0 + u_o \cdot \Delta t + \frac{a_0 \left(\Delta t\right)^2}{2} \\ u_1 &= u_0 + a_0 \cdot \Delta t \end{aligned} \tag{4.37}$$

At this time step, the opposing forces $F_w(u_1)$, $F_{CL,dyn}(u_1)$, $F_D(u_1)$ could be evaluated using the velocity u_1, and the electrostatic force can be evaluated for position x_1 and time t_1. The acceleration for this time step can be found from the force balance:

$$a_1 = \frac{\left[F_{el}\left(x_1,t_1\right) - min\left(F_{el}\left(x_1,t_1\right), F_{CL,stat,max}\right)\right] - F_{CL,dyn}(u_1) - F_D(u_1) - F_w(u_1)}{M}. \tag{4.38}$$

Time step t_{n+1}

Generally, to calculate the variables at time step $n+1$ from the known time step n, the acceleration a_n is used to find the position x_{n+1} and velocity v_{n+1}. With these values, all the forces can be evaluated at time step $n+1$. Depending on the value of the actuation force at this time and position, the acceleration a_{n+1} can be found analogously to (4.38). This procedure can be repeated for all time steps until the final time step is reached. As a result, the droplet position and velocity are found at all time steps.

The parameterised transient droplet response to a voltage application at the electrodes can be used to optimise the droplet flow rate, to minimise the applied voltage and therefore power consumption and to study the influence of the system parameters. In the next sections, this approach is applied on the planar electrode system and the annular electrode system.

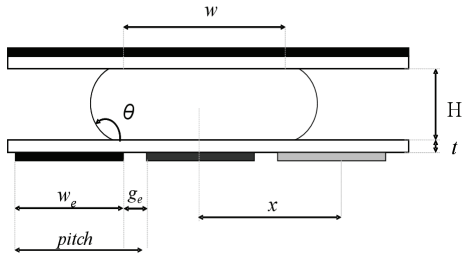

Figure 4.10. Schematic of the planar electrode system.

4.2 Dynamic model for the planar parallel plate system

In this section, the dynamic model (4.22) for the transient modelling of the droplet motion is applied on the planar parallel plate system (see Section 1.3.1). This system consists of a planar array of electrodes at the bottom side and a parallel control electrode at the top side. A typical force profile of the electrostatic force as a function of the droplet position with respect to the activated electrode is shown on the left hand side of Figure 4.1. For this particular case, the electrode pitch is 1 mm, the electrode gap is 100 μm, the height of the channel is 1 mm, the droplet volume of 2.7 μl and the applied voltage is 45 V. For this geometry, the width of the droplet w in Figure 4.10, is 1.5 mm. The starting position of the droplet is -1 mm. The reference parameters for this system are listed in Table 4.1 in the column 'planar'. The static contact line friction force for this test case amounts to 8 μN. For other droplet geometries, this force is scaled according to (4.19). From the Figure 4.1, it can be observed that the maximum actuation force is 25 μN for these parameters.

4.2.1 Single electrode response

Reference case

First, the dynamic droplet motion of an individual droplet is calculated for a single activated electrode. A constant voltage is assumed to be applied to an electrode close to the droplet. This will be first illustrated for a voltage of 45 V and 75 V. This can be considered an infinitely long voltage pulse. Even if the voltage is kept switched on, the droplet will stop at a position where the actuation force is lower than the opposing forces and the droplet does not have enough inertia to move on. The position after actuation depends on the applied voltage and the opposing forces. In the next section, a finite pulse will be applied at different electrodes at different points in time. The starting position of the droplet is chosen to be x=-1 mm. Since the electrode pitch is 1 mm, this means the droplet is positioned above the electrode at the left side of the activated electrode. For this position, the advancing edge overlaps the activated electrode with 150 μm. From the left hand side of Figure 4.1, the actuation force at this position can be extracted. If the force at the starting position is sufficiently high to overcome the threshold force, the droplet will start to move. In this case, the force at the starting point is 22 μN. This is higher than the threshold force of 8 μN and therefore the droplet will start moving. As long as the net actuation force, as defined in Section 4.1.2.2, is higher than the opposing forces, the droplet will accelerate. When the opposing forces are higher than the actuation force the droplet will slow down and eventually stop. Depending on the opposing forces and applied voltage, this can mean that the droplet could stop before reaching the centre of the powered electrode if the voltage is too low (in the case of 45 V), or on the other hand that the droplet will overshoot the centre (in the case of 75 V). When the droplet overshoots the centre of the electrode, the droplet is pulled back towards the centre by the reverse electrostatic force. As a result, the droplet will perform an oscillation around the centre until its inertia is too small to overcome the opposing forces. The result is a damped oscillation around the centre of the powered electrode. The point where the droplet stops is important to ensure actuation by the next electrode in an array of subsequent electrodes.

Figure 4.11 shows the first 50 ms of the results of the dynamic model for an applied voltage of 45 and 75 V. The graph in the top left of the figure shows the droplet position as a

function of time. For the given system parameters and a voltage of 75 V, a small overshoot beyond the centre and a damped oscillating motion around the centre can be observed. A settling of the droplet motion is observed after 50 ms. The graph in the top right corner of the figure shows the evolution of the droplet velocity as a function of time. The graph in the bottom left corner shows the droplet trajectory in the velocity versus position plane. Here, the decay of the peaks of the oscillations can be clearly observed. Figure (d) shows both the evolution of the actuation force and the dynamic contact line friction force as a function of time. From equation (4.24) can be seen, that this dynamic contact line friction force is the dominant force. In case of a voltage of 75 V, the actuation force is larger than the opposing forces during the first 8 ms of the droplet motion and as a result the droplet will accelerate as can be seen from graph (b). In the interval between 8 and 20 ms the opposing forces dominate the actuation force. In this interval, the droplet will slow down. However, due to the inertia of the moving droplet, the droplet already overshoots the centre of the electrode at 20 ms. Between 8 and 30 ms the electrode feels a negative actuation force, pulling it back towards the centre of the electrode, hence the oscillating motion. At 30 ms it overshoots the centre back again in the direction of the starting point and will be again pulled back towards the centre. For this actuation voltage, the motion is damped after this cycle.

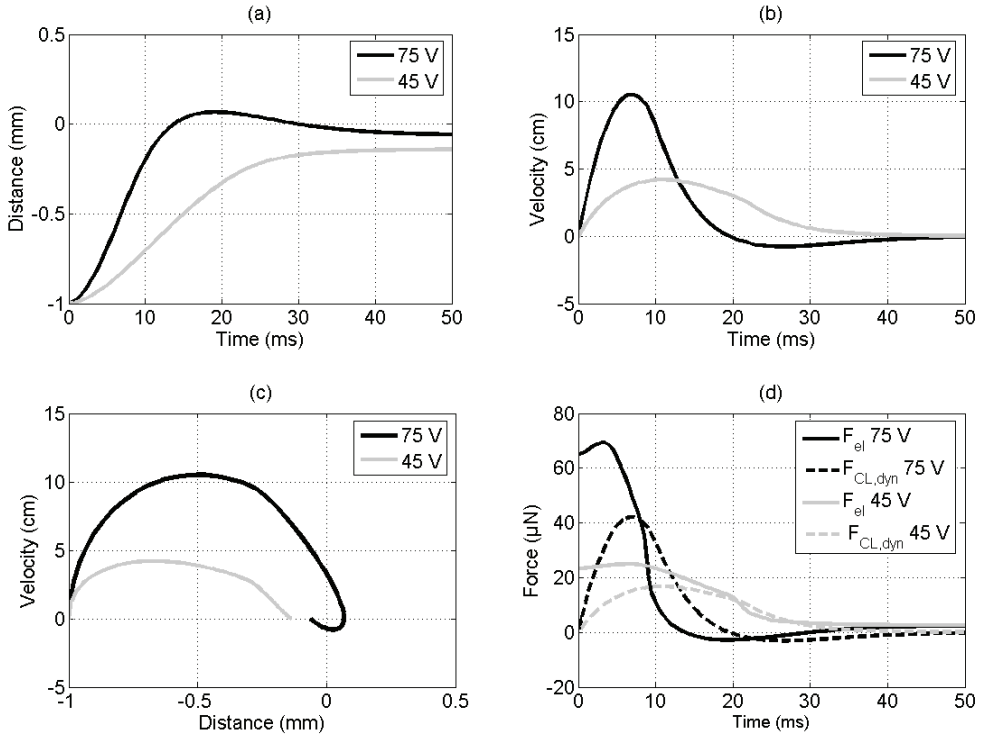

Figure 4.11. Results of the dynamic droplet position model for the parameters listed in Table 4.1 for the 'planar' test case for an actuation voltage of 45 V and 75 V.

Parameter study

The dynamic model can be used to study the influence of the parameters listed in Table 4.1. In this section the effect of the voltage and the influence of the properties of the filler liquid are discussed. A similar study can be performed for the effect of the other parameters such as the droplet volume, channel height and geometry of the electrodes.

For higher voltages, a more pronounced oscillating behaviour is observed as predicted by the equivalent damped spring-mass model (Figure 4.8). A higher voltage will lead to a higher actuation force and consequently a higher velocity in the initial stage of the droplet motion. Therefore, the overshoot is expected to be higher for higher voltages. Figure 4.12 shows the transient droplet position for different actuation voltages. It can be observed that a minimal voltage, required to actuate the droplet, exists. At 18 V, the resulting electrostatic force is large enough to overcome the opposing force, however the net force is not sufficient to accelerate the droplet in such a way that the centre of the electrode is reached in a short time. In this case, after 100 ms only one quarter of the distance has been covered. This will have an influence on the switching frequency that can be achieved. To achieve a high flow rate, a switching frequency should be sufficiently high. Therefore a higher actuation voltage might be required. This will be discussed in Section 4.2.2. From the linearised mass-spring-damper analysis (Figure 4.8), the critically damped situation corresponds to an actuation voltage of 71 V. For higher voltages, oscillations will occur and the droplet motion is underdamped. For lower voltages, the droplet motion is overdamped. In practise, only the droplet motion in the overdamped regime will occur. In the model, the rise time of the voltage has not been included. It is not possible to create a very high voltage difference in a very short period, unless very high currents are required. As an approximation, an average rise time of 0.1 ms/V of the power supply can be considered during which the voltage is built up linearly

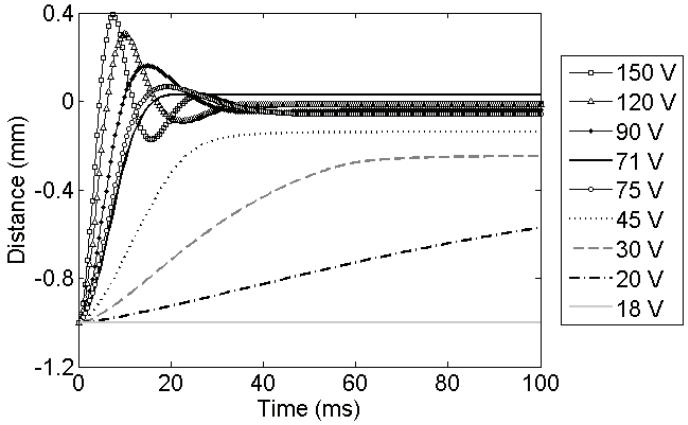

Figure 4.12. Transient droplet position for different actuation voltages.

For the results presented above, the filler liquid in the channel was assumed to be air. In literature, several alternative immiscible liquids are presented that benefit the droplet actuation. Most commonly used is a low viscosity silicone oil (Pollack *et al*. 2002). The oil prevents the evaporation of the liquid droplets and lowers the static and dynamic contact

line friction force. As a result, the minimum required voltage to actuate the droplet will be lower when the channel is filled with the silicon oil compared to air. On the other hand, the drag forces acting on the droplet while moving through the oil are higher compared to the case where the droplet moves through air due to the much higher viscosity of the oil. The viscosity of the oil is $\mu_{oil} = 1.7 \cdot 10^{-3} Pa\ s$ (Ren *et al.* 2002) compared to $\mu_{air} = 18 \cdot 10^{-6} Pa\ s$ for the viscosity of air. These increase in drag force will lead to a higher damping of the oscillating motion and as a result to a shorter settling time. In literature, following properties for the static and dynamic contact line friction in silicone oil can be found (Ren *et al.* 2004): the threshold force is 2.5μN and the coefficient of contact line friction ζ is 0.04 Pa s. In , the comparison for the dynamic droplet motion is made between the effect of air and the silicone oil as a filler liquid for an actuation voltage of 25 V and 75 V respectively. Since the friction force is lower in the case of oil, for the same voltage the droplet will feel a higher net force. This leads to a higher velocity in the initial phase of the droplet motion and a faster dynamic response. In the case of oil, the drag force is higher. Since this force scales linearly with the droplet velocity,, the damping effect of this force will be more pronounced on the droplet motion as the droplet velocity increases. This additional damping results in less overshoot past the centre of the electrode and a shorter settling time of the droplet motion. An actuation voltage of 75 V leads to an overshoot of the droplet beyond the electrode centre in the case of air as a filler liquid. In the case of a silicone oil filler liquid, no oscillatory behaviour is observed and the droplet position stabilises after 25 ms whereas the settling time for the droplet motion in air is 120 ms. This faster stabilisation allows faster switching to the next electrode in the case of an array of electrodes.

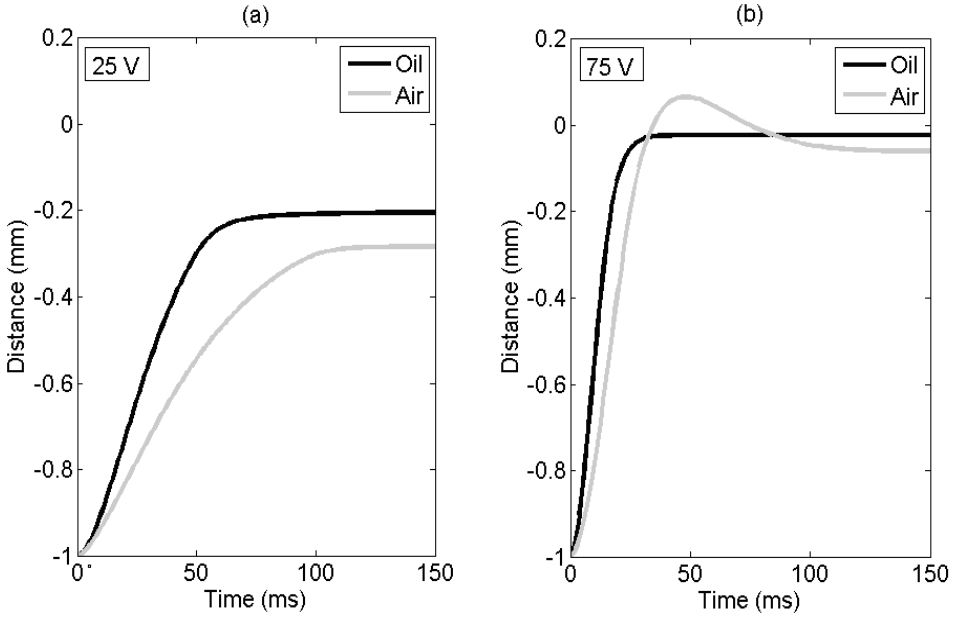

Figure 4.13. Dynamic droplet response of droplet for an actuation voltage of 25 V (a) and 75 V (b). The filler liquid in the channel is either air or a low viscosity oil.

Contribution of the opposing forces

As mentioned above, the total opposing force consists of three components: the contact line friction force, the shear force and the drag force. Bhattacharjee (2010) discusses the relative contribution of the different opposing forces. A similar approach can be followed for the system studied in this work. In Figure 4.14, the relative contribution of the different opposing forces is shown as a function of time. The forces are calculated for the dynamic response using an actuation voltage of 45 V and with silicon oil as a filler liquid. The transient droplet position for a voltage of 45 V is shown by the dashed line in Figure 4.12.

The dynamic part of the contact line friction, the shear force between the droplet and the wall and the drag force of the filler medium scale linearly with the droplet velocity. In the initial stage of the droplet motion, at very low droplet velocities, the static contact line friction force is the dominant opposing force. For higher droplet velocities, the importance of the velocity dependent forces increases. The maximum droplet velocity is reached after 15 ms. At this position, the dynamic contact line friction force is the dominant opposing force (50%). The contribution of the viscous flow force, drag force and static contact line friction force at this time step amounts to 20%, 15% and 15% respectively. After this point, the opposing forces are larger than the actuation force and as a result the droplet slows down. At 25 ms, the actuation force is smaller than the threshold force. From this point on, the value of the static contact line friction force is equal to the actuation force. At 40 ms, the droplet stops. At this point, there is still an actuation force acting on the droplet. The force is however not sufficiently large to overcome the threshold force. At this position, the only opposing force acting on the droplet is the static contact line friction force that compensates the actuation force.

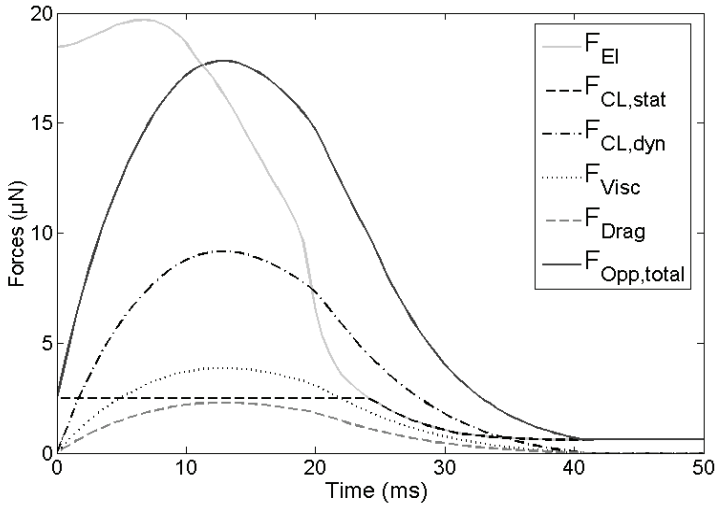

Figure 4.14. Contribution of the different opposing forces during the droplet motion for an actuation voltage of 45 V and silicone oil as a filler medium.

4.2.2 Droplet trajectory over an array of electrodes

The purpose of the array of electrodes in the microfluidic system is to generate a continuous flow of discrete liquid droplets. As a result, a flow rate is generated through the channel. The flow of droplets will remove the heat from the heat dissipating component and transport the heat away. In the section above, the dynamic droplet motion towards a powered electrode is described. To generate a continuous motion of the droplet through the channel, the droplet should be attracted from one electrode to the next by subsequently applying a voltage to the array of electrodes. This means that analysis for a single electrode can be repeated for all the electrodes in the array. What the droplet motion through the channel looks like, depends on the actuation voltage, the switching frequency, the starting position of the droplet and the opposing forces. The end position of the droplet motion for the first activated electrode is the starting position of the motion for the second actuated electrode. The droplet motion from one electrode to the next will be successful if the actuation force of the next electrode acting on the droplet is sufficiently high for the position the droplet is in at the moment, the voltage is switched off in the first electrode and switched on in the second. As discussed above, the transient droplet motion can show an oscillating behaviour and as a result the droplet could be in a wrong position at the moment the voltage is switched. When this happens the droplet will be stuck.

It is important to carefully control the switching frequency. If the frequency is set too high the electrodes will switch before the droplet reaches the region of attraction of the next electrode and the droplet will stop. The safest option is to wait to switch until the droplet has stabilised. However, a successful droplet motion can be achieved by switching before this time at the right side of the oscillation. On the other hand, if the velocity is too low, the flow rate is suboptimal and the droplet will be waiting before the being switched to the next electrode. In this case, the power consumption will be unnecessarily high. To develop an efficient control of the voltage and frequency of the droplet actuation, the transient droplet motion across multiple electrodes is studied more in detail.

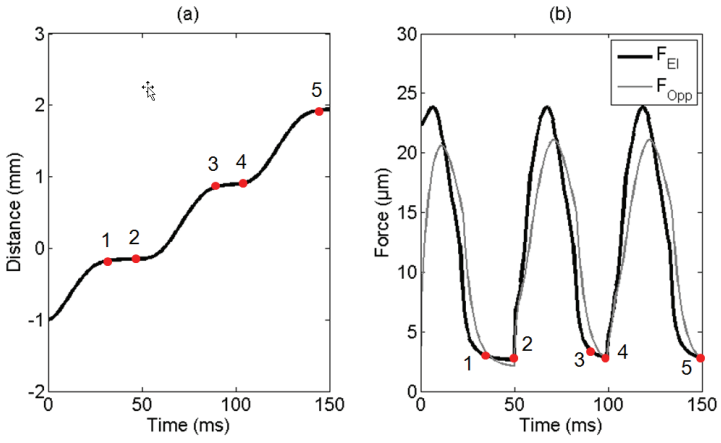

Figure 4.15. (a) Dynamic droplet response for the actuation over three subsequent electrodes for an actuation voltage of 40 V. (b) Evolution of the actuation and opposing force on the droplet as a function of time.

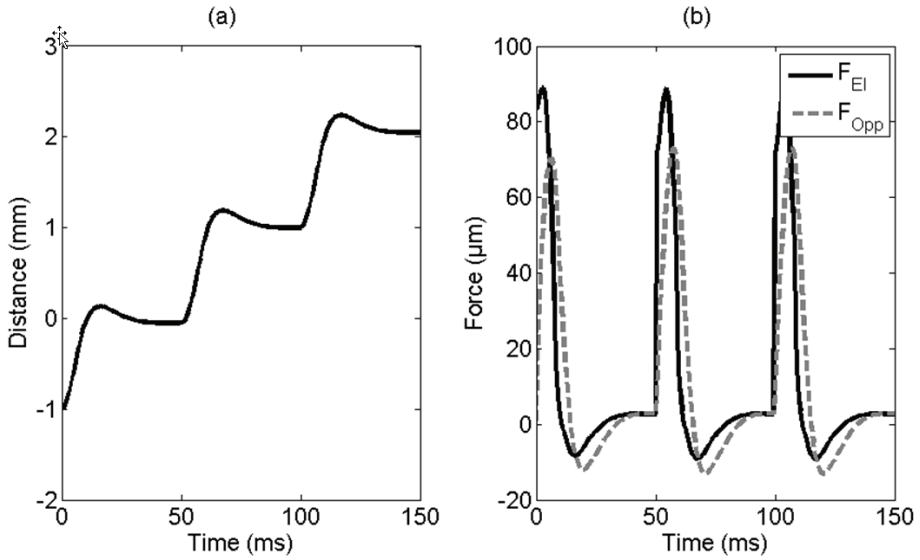

Figure 4.16. (a) Dynamic droplet response for the actuation over three subsequent electrodes in case of an oscillating motion of the droplet for an actuation voltage of 95 V. (b) Evolution of the actuation and opposing force on the droplet as a function of time.

Using the time dependent formulation for the electrostatic force (4.34), the droplet response over multiple electrodes can be calculated using the dynamic model (4.1). Figure 4.15 shows the transient droplet motion for the reference parameters (Table 4.1) during the actuation over three electrodes using a switching frequency of 20 Hz. In this case, a voltage of 40 V and a starting position of -1.1 mm are used. The voltage is chosen in such a way not to have an oscillating motion in the droplet trajectory. Position '1' in the graph indicates the position where the droplet stabilises. At position '2', the voltage is switched to the next electrode. As can be seen on the graph, the droplet stabilises well before the voltage is switched to the next electrode. This means the chosen frequency is a conservative choice to actuate the droplet in this case. The same reasoning can be repeated for the next electrodes. The right hand side of Figure 4.15 shows the time and position dependence of the actuation force. At time '2', when the voltage is switched, the actuation force changes from the attraction force towards the centre of electrode 1, hence the negative force, to the attraction towards the centre of electrode 2. This jump can be clearly observed in graph (b). The same applies for time '4' where the voltage is switched from electrode 2 to 3.

It is illustrated in Figure 4.16, that the same approach can be used in the case of heavily oscillating droplet behaviour. In this case, an unrealistically low level of dissipative forces, an actuation voltage of 95 V and a frequency of 10 Hz were chosen for the purpose of illustration. On the right hand side, the evolution of the forces as a function of time can be seen. The profile of the forces reflects the oscillation of the droplet motion where during subsequent cycles of the oscillation the distance from the centre of the electrode decreases. As a result also the level of the force decreases as the force is zero at the centre and higher in absolute magnitude further away.

Influence of the switching frequency

From the previous graphs could be observed that the chosen frequency is safe to actuate the droplet over that particular array of electrodes. However, it is also clear that there is still room for improvement to increase the flow rate for the same voltage by increasing the frequency. The effect of the frequency is studied for the case discussed in Figure 4.15, i.e. an actuation voltage of 40 V to limit the effects of the oscillation. shows the effect of frequency on the droplet motion for a range of the frequency of 5 to 35 Hz. In the graph, the first 200 ms of the motion is shown. This corresponds to one cycle for a frequency of 5 Hz. The droplet can follow the voltage switches up to a frequency of 35 Hz. For the case of 40 Hz, the droplet is too far away from the second electrode at the moment of switching and the droplet is stuck close to the centre of the first electrode. Further study learns that the maximum switching frequency for this case with an actuation voltage of 40 V is 36 Hz. A maximum frequency can be determined for each actuation voltage. In the case of an actuation voltage of 60 V, the maximum switching frequency is 62 Hz. This is important information to develop an efficient and robust control for the droplet actuation. For each value of the actuation voltage, a maximum frequency can be found. Figure 4.18 shows the maximum frequency that can be used for a successful droplet transportation over multiple electrodes for a voltage range of 0 to 80 V. As was shown in Figure 4.12, the minimal voltage that is required to move the droplet is 18 V. The voltage region below this threshold is indicated with region '1' in the graph. However, for this actuation voltage the droplet does not reach the centre of the powered electrode.

Simulations show that the minimal voltage for which droplet motion over multiple electrodes can be achieved is 28 V. For the range in between 18 and 28 V, the droplet will move but will not move far enough to be close enough to the second electrode. This corresponds to region '2' in the graph. For voltages higher than 28 V, increasing frequencies can be reached for increasing actuation voltages. The voltage however is limited by the dielectric breakdown in the insulating material. Moreover, for higher voltages more pronounced oscillating behaviour will be observed. Therefore a trade off needs to be made between the voltage and frequency, considering the limitations of the insulating material, the specifications of the power supply and the complexity of control.

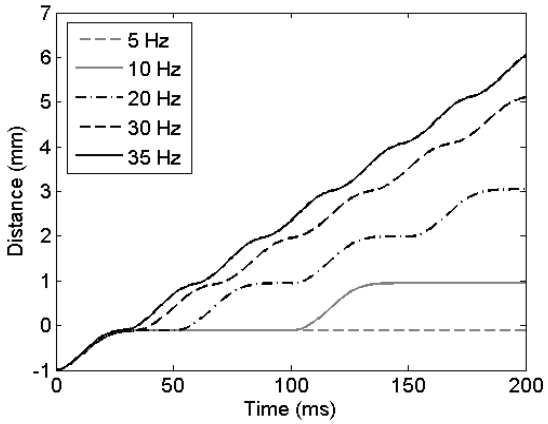

Figure 4.17. Dynamic droplet motion over an array of electrodes for different switching voltages (5-35 Hz) for a voltage of 40 V.

In Figure 4.18, the maximum switching frequency is compared to the double of the natural frequency of the linearised damped mass-spring model. In the linearised model, the mass moves from one extreme point to the opposite (Figure 4.7a). After one half of the period, the opposite position is reached. At this moment, the voltage can be switched to the next electrode to move the droplet forward towards this next electrode. Therefore, the optimal switching frequency, extracted from the linearised model can be written as follows:

$$f_{opt} = 2 \cdot f_{nat} = \frac{\omega_0}{\pi} \tag{4.39}$$

where ω_0 is the angular natural frequency of the damped mass-spring system (4.29). By comparing the switching frequency to the maximum frequency obtained from the simulations with the actual force profile, two differences can be observed. The first difference is that the damped mass-spring system predicts a continuous droplet motion from one electrode to the next for a lower voltage than the actual force profile. For voltages higher than 18 V, a droplet motion is realised. For this moving droplet, using the linearised model a natural frequency and consequently a switching frequency can be found. In reality however, the droplet will not move far enough to be actuated by the next electrode. Only for a voltage of minimum 25 V, a continuous droplet motion can be achieved. The second deviation between the linearised model and the actual force profile is that the linearised model underpredicts the value of the switching frequency. This can be explained by the fact that the actuation force on the droplet already starts acting before the droplet reaches the centre of the previous electrode. As a result, the voltage can be switched slightly before this position is reached, leading to a slightly higher achievable switching frequency. Despite those two deviations, the linearised model provides an useful approximation of the optimal switching frequency within 10% of the results obtained by the dynamic model using the actual force profile. Therefore, the linearised model can be used as a fast tool to develop a control strategy for the activation of the electrodes in order to optimise the droplet flow.

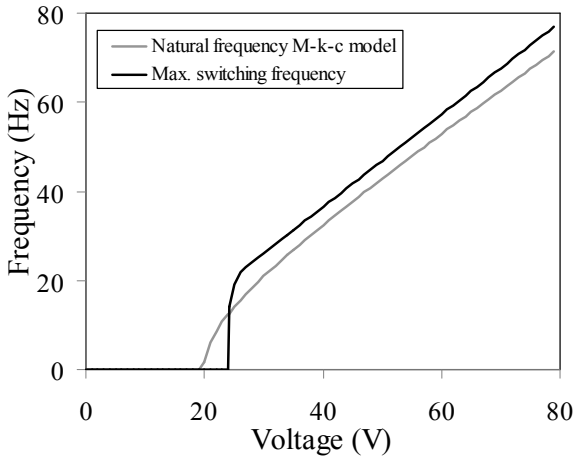

Figure 4.18. Maximum switching frequency as a function of the actuation voltage for the planar electrode configuration with air as filler liquid and with the system parameters listed in Table 4.1. The switching frequency is compared for the results of the dynamic model using the actual force profile and the results of the linearised damped spring-mass model (two times the natural frequency).

4.2.3 Validation of the dynamic modelling of the planar system

The modelling results of the electrostatic induced droplet motion can be validated using experimental results on droplet motion published in literature. Ren *et al.* (2002) described a dynamic model to predict the steady state average droplet velocity for electrowetting droplet transport. These experimental results are represented in Figure 4.19 by the markers. In this graph, the linear average droplet speed is shown as a function of the actuation voltage. The average droplet speed is defined as the ratio of the distance travelled by the droplet through the channel to the time taken by the droplet to do this. These measurements will be used to validate the dynamic model presented in this work.

The measurements in the paper of Ren *et al.* (2002) are performed for the case of a droplet with a 1 mm contact line radius in a channel with a height of 0.3 mm. The channel is filled with oil as a filler liquid. The comparison between the average droplet velocity calculated from the dynamic model and the experimental data (Ren *et al.* 2002) is shown in Figure 4.19. From these graph can be seen that the agreement between the simulations and the experimental data is within 20%. Considering the number of assumptions made to achieve a workable model the modelling agrees reasonably well with the experimental data.

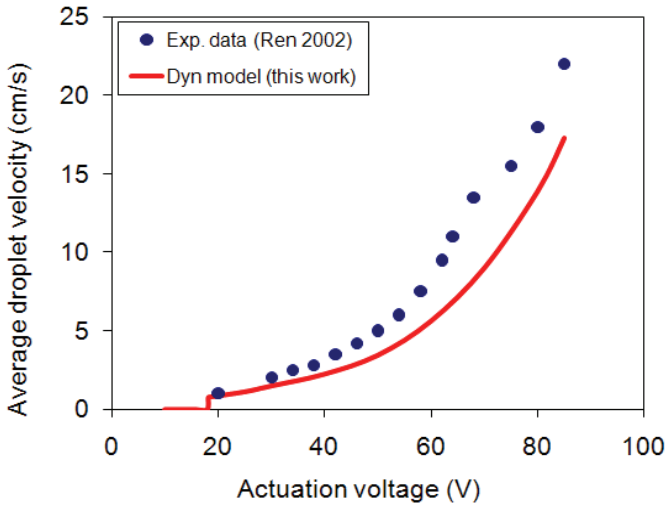

Figure 4.19. Validation of the dynamic droplet motion model by experimental data from literature.

4.3 Dynamic model for the annular electrode system

In this section, the approach for the dynamic droplet motion model is applied to the annular electrode system. The structure and application of this system is described in Section 1.5. In this system, the droplets are actuated through a cylindrical channel with integrated annular electrodes in the wall. In Chapter 3, the electrostatic actuation force is modelled for this type of structure for a range of channel diameters between 150 and 500 µm and a range of droplet lengths from 150 to 750 µm.

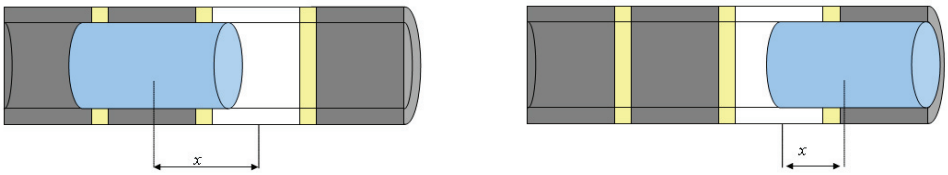

Figure 4.20. Schematic of the annular electrode system and the droplet position. Left : start position (x = -150 µm). Right: end position of voltage application on white electrode (x = 80 µm).

The parameters of the reference case for this system are listed in Table 4.1 in the column 'annular'. The channel diameter is 150 µm and the droplet volume is 4.5 nl. This leads to a droplet length of 250 µm. For the reference starting position, x=-150 µm, the droplet is centred above the electrode next to the activated electrode. For this position, the overlap between the droplet and the activated electrode is 30 µm. The force profile for this system is shown in Figure 4.1. For this case, the maximum force amounts to 6 µN for a droplet volume of 4.5 nl. The profile shows a steep increase when the interface of the droplet passes the activated electrode. Due to the shape of the contact line, the whole interface crosses the beginning of the electrode at once. After this peak, a linear decrease, of the force with respect to the droplet position can be observed. The other peaks in the profile correspond to locations where either the advancing or receding front of the droplet crosses the edge of one of the electrodes. For the case of a long droplet compared to the electrode pitch the negative peaks are relatively small. The profile during the transition over one electrode shows several local peaks and a relative large region of the trajectory where the force is very small or nearly zero. During the transportation over the electrode, the droplet is very likely to get stuck is this area. In Figure 4.1 this region corresponds to the interval of locations between -80 and 80 µm from the centre of the electrode. This region is indicated in Figure 4.25.

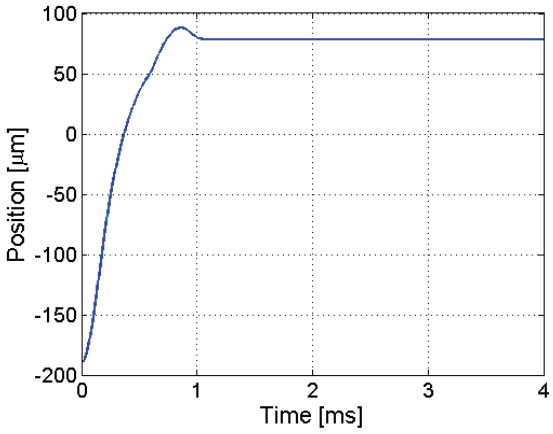

Figure 4.21. Transient droplet motion in the annular electrode system for the reference case (droplet length 250 µm, voltage 35 V).

If the droplet stops at a location too far from the next electrode it will not be attracted by the next electrode after the switching of the voltage. In the case of this system the position where the droplet will stop is difficult to predict. Basically, the droplet can stop moving anywhere in the indicated region depending on the actuation voltage, the starting position of the droplet and the opposing forces. For small variations in one of those parameters, the end point of the droplet might be different as will be illustrated in the next section. Therefore, the control of such a system will be very difficult to ensure a continuous droplet motion over multiple electrodes.

4.3.1 Single electrode response

The dynamic model (4.25) is solved for the parameters listed in Table 4.1. Figure 4.22 shows the result of the dynamic droplet motion model for this case. The droplet reacts very fast to the applied voltage. The settling time of the droplet motion is in the range of 1 ms. This is mainly due to the very small size and mass of the droplet considered; in this case the volume of the droplet is only 4.5 nl. In this case the end point of the droplet motion is at position 80 µm. As expected, this is in the region with nearly zero force, as discussed before. This indicates the droplet is too long for the size of the electrodes. In Chapter 3 (Figure 3.34) it was shown that the length of the region increases with increasing droplet length. To ensure droplet actuation by the next electrode, one should aim for the end position to be close to zero. Therefore a shorter droplet should be used. In Figure 4.22, the results are shown for a droplet length of 180 µm and a voltage of 70 V. This voltage should be sufficiently high to overcome the point of zero force at the position -40 µm. For these parameters, the end point of the droplet transition is close to the central position zero.

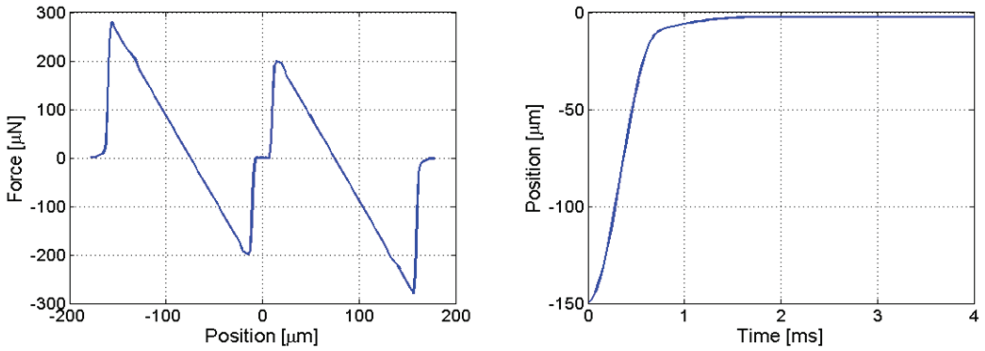

Figure 4.22. Force profile and transient droplet motion in the annular electrode system for a shorter droplet (droplet length 250 µm, voltage 35 V).

Due to the complex force profile of the actuation, the final droplet position after the actuation by one electrode can differ greatly for small changes in the input parameters. To illustrate this, the droplet motion is studied for 4 cases with slightly different input parameters, such as the actuation voltage and the assumed starting point of the droplet motion. These 4 cases are:

1. voltage 50 V; start position: -190 µm;
2. voltage 60 V; start position: -190 µm;
3. voltage 50 V; start position: -150 µm;
4. voltage 60 V; start position: -150 µm.

Figure 4.23 shows the droplet motion for those 4 cases. In the case of the planar electrode system the droplet response showed a damped oscillation around the centre of the activated electrode, which is the only equilibrium location in the system. For the system discussed here, the response is more complex due to the multiple peaks and locations with zero force in the force profile. From an energy perspective, this means there are multiple local minima (zero force) which are all potential positions where the droplet motion might stop. The droplet will therefore not oscillate around one location but show an oscillating motion around these multiple points. In this case, three of these points can be identified from the force profile in Figure 4.1(b); (1) the first location with zero force at position -80 µm and (2) the region around the centre of the electrode at position 0; (3) the next location with zero force at position 80 µm. As a result, small variation in the input parameters might make the difference between convergence to one of this local optima, or moving on the next one due to a slightly higher momentum of the droplet.

An example of this can be seen from the first two cases in Figure 4.23. The convergence of the damped oscillation can be best visualised in the velocity vs. position plane. For the first case with an actuation voltage of 50 V the droplet starts an oscillation around position ‘3’, has to much momentum and moves back before being stuck at the region around the centre of the electrode. If the voltage is increased to 60 V, the droplet will have more momentum after returning from position ‘3’ to bypass region ‘2’ and convergence with an oscillation around position ‘1’. In cases 3 and 4, for a starting position closer to the centre of the electrode, for both 50 and 60 V actuation voltage, the droplet does not have enough momentum and will converge around position ‘3’.

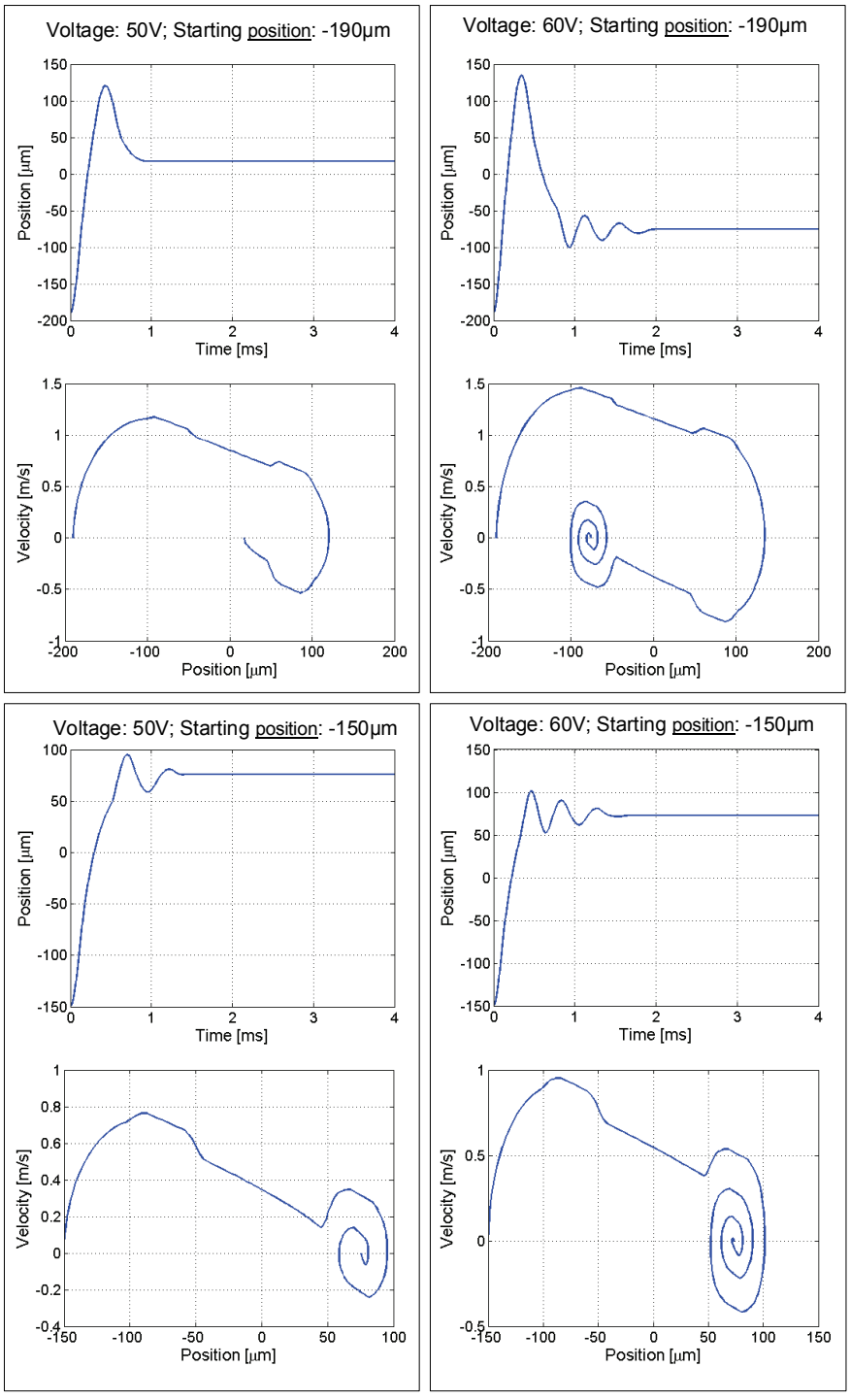

Figure 4.23. Overview of the dynamic response of a droplet to a voltage pulse for 4 different cases.

4.3.2 Multiple electrodes

In this section, the actuation over several subsequent electrodes is discussed. For the droplet transportation, the end point of the motion on an electrode is the starting point for the next. In the previous section, it is shown that a slight variation of the starting might lead to a large difference droplet position after the actuation. This makes it very difficult to predict the droplet position after several electrodes. This is first illustrated for the parameters of the reference case. The start position is -180 µm, and the electrode pitch is 150 µm. In Figure 4.24, the result of the dynamic modelling of a droplet over 3 electrodes with an actuation voltage of 40 V is shown. For this set of parameters, the end point after the first electrode is close to zero (20 µm), which means close to the centre of the powered electrode. The voltage is switched to the second electrode at 2 ms. For the second step, the relative starting position with respect to the second electrode is therefore -130 µm. The absolute position after the second step is 140 µm, which translates to a relative position of -10 µm with respect to the second electrode. At 4 ms the voltage is switched to the third electrode. For this step the relative starting point is -160 µm. After the third step, the relative position is +180 µm. This means a relative starting point of -30 µm for the fourth step. This position falls in the region with zero force which means the droplet will not be actuated by the next electrode.

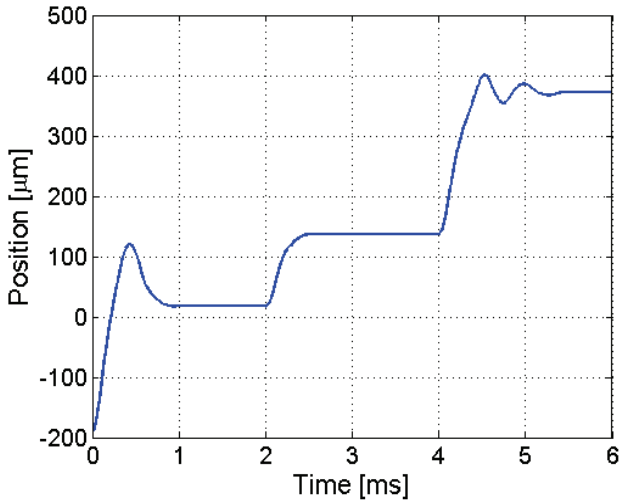

Figure 4.24. Transient droplet motion over 3 electrodes for an actuation voltage of 35 V.

From this example, it can be observed that the relative starting position for all 3 steps is different. As a result, the transient profile will be different for the 3 dynamic responses to the respective electrodes. Another complication is the fact that the region in which the actuation force is sufficiently larger than the opposing force is rather limited. In Figure 4.1(b), this region is from -200 to 100 µm. This means that the droplet should be in this range of locations after actuation by the previous electrode, to be successfully actuated by the current electrode. This puts a constraint on the location of the end position of the dynamic response. In Figure 4.25, the area where the droplet is expected to stop is indicated with an arrow. The area, which corresponds to the region of high electrostatic force of the

next electrode, is indicated by the shaded area in the same graph ('safe area'). It can be seen that the range of likely end-position is larger than the 'safe zone'. For the end positions that fall out of the 'safe zone', the droplet will not move when actuated by the next electrode.

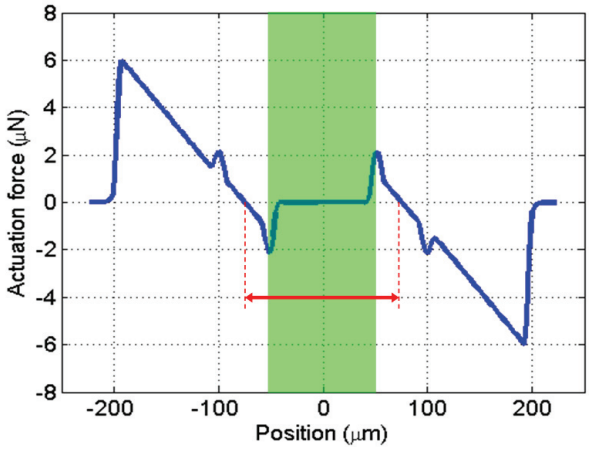

Figure 4.25. Indication of the region where the droplet most likely will stop moving (arrow) and the region of the end position in which actuation by the next electrode will be successful (shaded area).

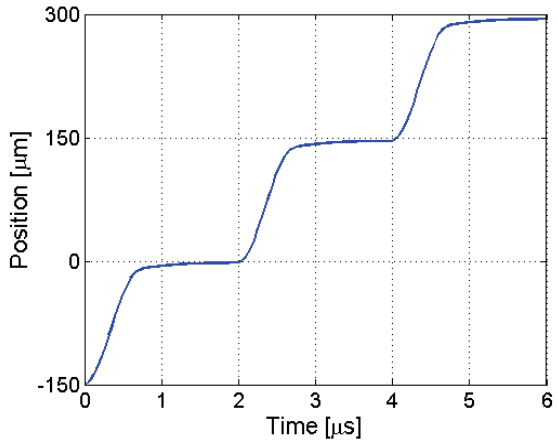

Figure 4. 26.Transient droplet motion over 3 electrodes for a droplet length of 180 μm and a voltage of 70 V.

To achieve a continuous droplet flow over multiple electrodes, it is important that the droplet is transported from one electrode to the other, without getting stuck. To achieve this, the parameters of the system should be optimised that the relative starting position for each electrode is more or less the same as for the previous one. In this way a repetitive droplet transport from electrode to electrode can be ensured. The narrow the range of potential end points, the region indicated by the red arrow in Figure 4.25 should be as small as possible. Therefore, a droplet length should be used. This is illustrated for the case already shown in Figure 4.22. For a droplet length of 180 μm and a voltage of 70 V, a robust switching scheme is found, for which the droplet start and ends at the same relative

distance for each electrode. In Figure 4.24, this is illustrated for a droplet transported over 3 electrodes with a switching frequency of 500 Hz. For each electrode, the droplet response is the same, and a distance of 150 μm is covered. This is the same distance as the electrode pitch.

4.4 Conclusions

In this chapter, a general methodology for the dynamic modelling of electro-actuated droplets is presented to predict the transient droplet motion. In this simplified geometry, the droplet is dealt with as a single mass. The dynamic model predicts the macroscopic droplet motion, based on a force balance of all forces acting on the droplet. The opposing forces on the droplet are as described algebraic expressions as a function of the average droplet velocity. For the electrostatic force, the simulation results from Chapter 3 are used. The empirical models from Chapter 2, are used to describe the static and dynamic contact line friction force. The dynamic model is solved using a time stepping approach to find the transient droplet position. The resulting reached droplet velocity will be used in Chapter 5 to study the internal fluid motion and heat transfer inside a droplet moving with this velocity. Furthermore, a linearised equivalent damped mass – spring model has been derived to approximate the dynamic droplet motion. This linearised model can be used to develop control strategies for the switching of the electrodes.

Next, the methodology is applied to an array of electrodes. The voltage is switched subsequently from one electrode to the next. For each actuation voltage, a maximum switching frequency is found that the droplet will be able to follow. For higher frequencies, the droplet will not reach the next electrode before the voltage is switched. The maximal switching frequency can be approximated by twice the natural frequency of the linearised damped mass – spring system. Therefore, the linearised model can be used for the development of control strategies to optimise the switching of the electrodes. Using an optimised switching frequency, the dynamic model predicts droplet velocities in the range of 5 to 10 cm/s for a voltage range from 30 to 80 V. For this velocity, a switching frequency of 75 Hz is required. This is a feasible frequency considering the required time for the voltage build-up. For the parallel plate electrode configuration, the methodology of the dynamic model is successfully validated using experimental data on average droplet velocities in literature (Ren *et al.* 2002).

In the case of the annular electrode system, the force profile is complicated with multiple instances with zero forces. As a result, droplet position after actuation over an electrode is difficult to predict. Indeed, small changes in input parameters can lead to a large variation in the prediction of the position after the application of the voltage. For this case, a robust switching scheme is derived to ensure continuous droplet motion from one electrode to the next.

Chapter 5

Flow patterns and heat transfer in moving droplets

Abstract

In this chapter, the internal flow and heat transfer inside electrostatic actuated droplets is studied for different droplet velocities by means of detailed flow computations. It is shown that the internal droplet flow exhibits a parabolic characteristic and that the presence of two convection cells decreases the heat transfer to the lower part of the droplet, thereby limiting the overall heat transfer. A typical enhancement of the heat transfer with a factor 2 is achieved with respect to the minimal value that would be obtained assuming heat conduction in the liquid only. Further, an analytic lumped model is presented to estimate the transient average droplet temperature with an accuracy of 5% compared to the full transient CFD modelling.

5.1 Introduction

In Chapter 4, the dynamic droplet motion over a series of electrodes is studied. The dynamic model predicts average droplet velocities up to 10 cm/s. If the voltage is switched appropriately from electrode to electrode a continuous droplet transport over the array of electrodes can be realised. The dynamic model predicts average droplet velocities up to 10 cm/s. Figure 5.1 shows an example of the evolution of the droplet position over the array of electrodes. This droplet motion can be approximated by a droplet moving with a constant droplet velocity through the channel, indicated by the dashed line in Figure 5.1. In this chapter, the internal flow inside the droplet and the heat transfer through such a moving droplet are studied numerically. This numerical modelling will provide insight in the internal motion and its influence on the heat transfer. Part of the simulations presented in this chapter were performed by Johan Danneels and Brecht Van Ham in the framework of their MSc dissertation assisted by Herman Oprins and supervised by prof. Martine Baelmans (Danneels and Van Ham 2006). That work resulted in a conference publication (Oprins *et al.* 2007) and an extended journal publication (Oprins *et al.* 2008). The extended journal publication served as basis for this chapter.

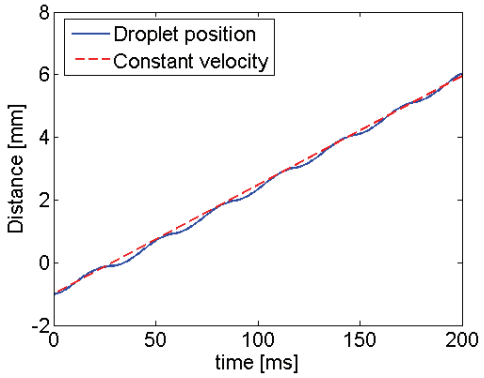

Figure 5.1. Example of the transient droplet position (solid line) and the constant velocity approximation (dashed line).

5.1.1 Flow and thermal modelling introduction

In the proposed cooling system, the heat is removed from the chip by individual droplets moving through a channel close to the chip (see Section 1.3). During their motion through the channel, the droplets will heat up. To estimate the amount of heat that such a droplet flow can extract from the chip, the thermal behaviour of a single droplet is studied. First, the internal circulation flow inside the droplet is investigated. This circulation flow is expected to have a beneficial effect on the convective heat transfer inside the droplet. Using detailed modelling, the effect can be quantified and a parameter study and optimisation can be performed. Moreover, the knowledge of the flow pattern in the droplet can be used to formulate approximate expressions for the forces acting on the droplet. This chapter focuses on the internal flow and the heat transfer inside the droplet. The flow and temperature distribution inside the droplet are described by the Navier Stokes equations. This set of equations includes the continuity equation, the momentum equations and the

energy equation. For the simulation of the flow field, the first two equations are solved. For the thermal analysis, the third equation is included. These equations are solved numerically using Computational Fluid Dynamics (CFD). The software packages used, are Gambit (preprocessor) and Fluent (solver and post processor). First, the fluid flow inside the droplet is studied. Next, the steady state heat transfer is investigated. Finally, the transient heat transfer is studied.

5.1.2 Approach and assumptions

The electrostatic actuation of liquid droplets is a very complex system to model. Many coupled and not completely understood phenomena are involved. As discussed in Section 1.3, a decoupled approach is used in this work to model the several aspects of the droplet actuation. To be able to model the droplet flow, several assumptions are made. These assumptions are listed below.

Fixed droplet shape
The droplet shape is a result of all forces acting on the droplet such as the surface tension, the electrostatic actuation force and the internal pressure due to the fluid motion. On the other hand, the shape of the droplet will influence the electric field and consequently the electrostatic force. This coupled effect complicates the simulations. To simplify the procedure, a decoupling between the electric and the flow field is made. In the case of an electrical conductive liquid, the electric field is only present at the interface of the droplet. As a consequence, no body force is assumed to be exerted on the liquid inside the droplet. As such, the flow inside the droplet is modelled using the shape of the moving droplet as an input for the model. This shape is extracted from contact angle measurements of a moving droplet. In the simulations, this shape is assumed not to change during the motion of the droplet through the channel. Numerically, this means the interface of the droplet is treated as the symmetry boundary condition. If the droplet shape is chosen correctly, this assumption does not influence the simulation results of the internal flow. However, if the assumed shape does not correspond to the real shape, this fixed artificial shape will create an additional pressure in the flow. Therefore, the validity of the assumption on the shape for the moving droplet should be tested by verifying the pressure balance at each point of the interface. Neglecting the friction force from the surrounding air, the pressure balance can be written as follows:

$$P_{in} + P_{hydr} = P_{\gamma} + P_{amb} \tag{5.1}$$

where P_{in} is the static pressure inside the droplet, P_{hydr} is the hydrostatic pressure, P_{γ} is the pressure due to the surface tension and the local curvature of the droplet interface, and P_{amb} is the pressure of the environment acting on the droplet.

Viscous drag forces neglected
The viscous drag forces from the air surrounding the moving droplet are neglected. Since the droplet shape is considered to be fixed, the effect of these viscous friction forces on the droplet interface can not be included. However, the effect of the viscous friction forces is expected to be small in the case of air as a filler liquid. The kinematic viscosity of air is nearly two orders of magnitude smaller than the one of water.

Constant droplet velocity
The next assumption is that only the steady state droplet motion is considered, decoupled from its actuation force. This corresponds to the steady state motion of the droplet. For a constant macroscopic droplet velocity, the response of the liquid is simulated both in the steady state and transient regime. Furthermore, the variation of the electric field along the path is neglected.

No-slip boundary condition
For the droplet moving through the channel, a no-slip boundary condition between the droplet and the walls of the channel is assumed. This means that the velocity of the liquid is zero at the interface with the walls. In literature, several models for droplet motion over surface are discussed using different modelling approaches for the interface between the liquid and the solid: no-slip, stick slip, ... In this work, the objective is to quantify the effect of the droplet motion on the internal heat transfer. It is not the intention to predict the local internal velocities very accurately. Therefore, for this application, the assumption of a no-slip boundary condition is sufficient.

Moving coordinate system
For the simulation of the moving droplet with no-slip boundary conditions, a moving coordinate system fixed with the overall droplet motion is used. As such, for an average droplet velocity U, the boundary conditions on the upper and lower wall have no-slip boundary conditions with a fixed velocity of $-U$. Thus, the simulation will compute relative droplet velocities within this moving reference frame. The absolute velocity can be found by adding the average droplet velocity to the relative velocity.

2D simulation
Though 3D effects might further alter the overall heat transfer to the droplet in comparison to the 2D results, it is expected that the forward traction on the droplet in combination with the presence of a top and bottom wall as well as a free surface at the droplets sides will predominantly induce internal flows in the vertical streamwise direction of the droplet. Thus, it is assumed that a 2D simulation in a vertical streamwise plane covers the main issues with respect to internal flow and convection heat transfer. Only the parts of the droplet without contact to the top or bottom wall are expected to exhibit a slightly deviating out of plane velocity profile.

Laminar flow
The Reynolds number Re_H is defined as

$$\mathrm{Re}_H = \frac{UH}{\mu} \tag{5.2}$$

For typical droplet velocities up to 10 cm/s Re_H varies between 0.1 and 150.

The critical Reynolds number in case of a droplet flow is 1000 (Ren *et al.* 2004) or in the order of magnitude of 2000 in the case of a continuous flow between two parallel plates (Kakaç 1987). Both critical numbers are clearly higher than the Reynolds numbers encountered here. Therefore, the flow in the droplet can be considered laminar.

Constant material properties
The liquid properties are assessed at the average droplet temperature. This means that in this study the temperature dependency of the thermophysical material properties and the surface tension is not taken into account.

5.2 Internal flow in moving droplets

First, the internal flow inside a droplet moving between two parallel plates is studied numerically, using the above mentioned assumptions. These detailed simulations reveal the internal flow.

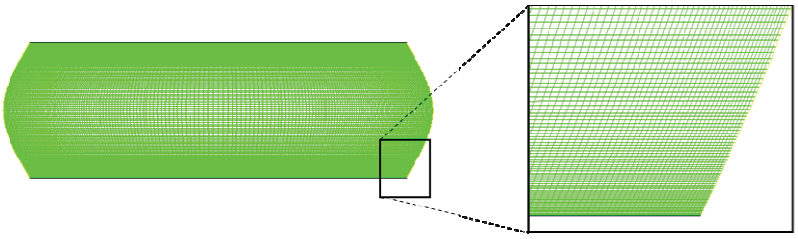

Figure 5.2. Grid for the Computational Fluid Dynamics (CFD) simulations of the internal flow inside the droplet moving between two parallel plates.

5.2.1 Model description for numerical steady state flow simulations

2D laminar Computational Fluid Dynamics (CFD) simulations are performed on this fixed shape. The dimensions of the droplet are set to a length of 2.8 mm, a width of 2.8 mm and a height of 1 mm. This amounts to a droplet volume of 20 µl. The velocity profile inside the droplet is calculated for average droplet velocities up to 15 cm/s. Deionised water with the characteristics taken at 20 °C is used as coolant. Figure 5.2 shows the grid of 40000 cells used for this 2D simulations. The curved sides at the left and right of the droplet in Figure 5.2 represent the interface between the liquid droplet and the surrounding air. At these sides a symmetry boundary condition is assumed. This is a consequence of the choice of a fixed droplet shape. At the top and bottom wall, a no-slip boundary with a constant velocity $-U$ is chosen. For the numerical simulations, the following solver settings are used:

- double accuracy (order of magnitude of the numerical accuracy $\sim 10^{-15}$);
- segregated solver scheme;
- laminar flow;
- second order discretisation scheme for the pressure, power law discretisation scheme for the momentum.

5.2.2 Grid sensitivity analysis

Before discussing the results of the simulations, the numerical convergence, grid sensitivity and the validity of the assumptions need to be verified. When all of these are successfully checked, the results of the simulations can be considered accurate.

Table 5.1. Convergence analysis of the total residuals.

	Fluent Residuals	Overall residual estimation
Continuity (kg/s)	$3 \cdot 10^{-16}$	$2 \cdot 10^{-15}$
Momentum X (kg m /s)	$5 \cdot 10^{-16}$	$2 \cdot 10^{-17}$
Momentum Y (kg m /s)	$3 \cdot 10^{-16}$	$2 \cdot 10^{-17}$

Convergence analysis

First, the convergence of the simulation is verified. The software provides residuals for the continuity and momentum equations for each iteration. These residuals are compared with an estimate for the overall residual for all cells that could be achieved. This estimate for the continuity equation and x and y component of the momentum equations is based on the accuracy of the solver. The overall residual for the continuity equation can be estimated as follows

$$\mathrm{Res}_{tot,cont} = \dot{m}_{avg} \cdot N_{cells} \cdot 10^{-15}. \tag{5.3}$$

An estimation for the overall residual for a component of the momentum equation is

$$\mathrm{Res}_{tot,mom,x} = \dot{m}_{avg} \cdot U_{x,avg} \cdot N_{cells} \cdot 10^{-15}, \tag{5.4}$$

where $\dot{m}_{avg}$ is the average droplet flow rate in a cell, N_{cells} is the number of cells in the model, $U_{x,avg}$ is the average droplet velocity in the x direction and 10^{-15} is the factor for the accuracy for the double precision setting of the solver. Table 5.1 gives an overview of the residuals provided by the software for the current simulation and the target of the overall residual. From this table, one can conclude that the simulation can be considered converged.

Boundary conditions

For the simulations, a fixed droplet shape is assumed. This droplet shape is extracted from pictures of a droplet moving between parallel plates. Through the surface tension and the curvature, internal pressure exists in the droplet. This pressure is described by the Young-Laplace equation:

$$p = \gamma_{LV} \left(\frac{1}{R_1} + \frac{1}{R_2} \right) \tag{5.5}$$

where R_1 and R_2 are the radii of curvature of the droplet interface. For the 2D simulations, only one radius of curvature is considered. If the assumed shape deviates too much from the real profile, the internal pressure inside the droplet is not correct. Therefore, to validate the assumption, the force balance (5.1) needs to be verified at the points of the interface. This radius is estimated by a curve fitting of the droplet interface at the point of interest.

Grid sensitivity analysis

To check the grid sensitivity of the numerical solution, a similar approach as used for the electrostatic actuation force in Section 3.3.3 can be used. Using the Richardson extrapolation, the truncation error and an estimate for the exact solution can be calculated. Table 5.2 shows the results for the calculation of the friction force at the bottom wall for three consequently refined grids of 10000, 40000 and 160000 cells respectively. Using the Richardson extrapolation, the truncation error is found to be 2% for the friction force for the grid with 40000 cells. The estimation for the exact solution is 0.228 μN/mm. From this

analysis can be concluded that a grid of 40000 is sufficiently fine to be used for the calculation of the velocity profile and resulting viscous friction forces.

Table 5.2. Grid sensitivity analysis.

Grid	Number of grid cells	Friction force (μN/mm)
1	10000	0.21160069
2	40000	0.22267698
3	160000	0.22674923

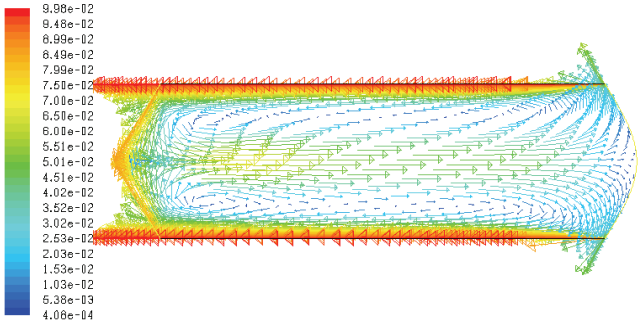

Figure 5.3. Relative velocity profile of the flow inside a moving droplet with a velocity of 10 cm/s from left to right.

5.2.3 Discussion of the simulation results for the internal flow

Steady state flow simulation

Figure 5.3 shows a vector plot of the relative velocity inside a droplet moving at 10 cm/s from left to right. In this graph, the arrows indicate the direction of the local flow and the colour and length of the arrow indicate the magnitude. This flow pattern is schematically represented in Figure 5.5(a). From this figure it can be seen that the flow inside the droplet consists of two independent rolling motions. They divide the droplet into two separate compartments. This division will influence the nature of the heat flow through the droplet. In the relative coordinate frame, the top and bottom wall are moving to the left side. This motion of the top and bottom wall creates a pressure increase (see Figure 5.4). This leads to a highest pressure in the top and bottom left corner of the droplet. Due to the fixed boundaries assumed at left and right side of the droplet, a fluid motion from left to right is created at the horizontal midplane.

In Figure 5.5(b), the vertical velocity profile across the height of the droplet is shown at a position in the middle of the droplet. The vertical solid line indicates the average droplet velocity. This velocity is used as a no-slip boundary condition at the top and bottom boundary of the droplet. As a result, the relative velocity field with respect to the average droplet velocity is calculated in the simulations. This relative velocity is represented by the

left curve in Figure 5.5(b). The absolute velocity is the sum of the relative and the droplet velocity. At a position in the middle of the droplet, the vertical velocity profile approximately matches the parabolic velocity profile of a continuous flow between two parallel plates:

$$u(y) = \frac{3}{2} U_{av} \left(1 - \left(\frac{2y'}{H} \right)^2 \right) \tag{5.6}$$

where U_{av} is the average droplet velocity, H is the droplet height and y' is the vertical coordinate starting from the midplane of the droplet. At other positions, the profile is slightly different. Figure 5.6 shows the vertical profile of the absolute velocity at different positions in the droplet. The profile is shown at the left interface of the droplet, at a position *H/2* from the left interface, the position in the middle, at a position *H/2* from the right interface and finally at the right interface. From this graph can be concluded that for the larger part of the droplet, a parabolic profile can be assumed.

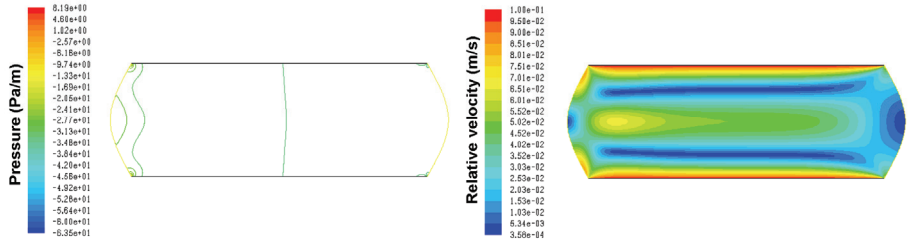

Figure 5.4. Contour plots of the pressure (left) and the relative velocity (right) inside a moving droplet with a velocity of 10 cm/s.

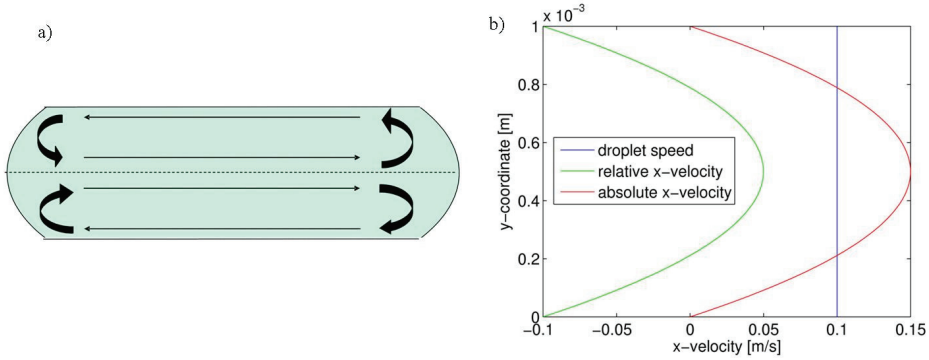

Figure 5.5. Representation of the principle flow and the vertical velocity profile in the middle of the droplet; (a) Principle representation of the relative internal flow field;(b) The velocity profile in the middle of the droplet at a droplet speed of 10 cm/s.

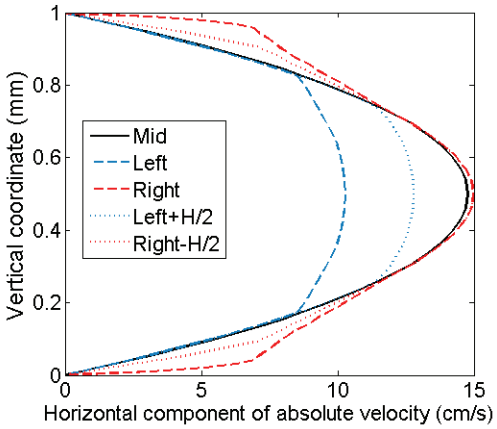

Figure 5.6. Absolute velocity profile over the height of the droplet at different positions. The profile is evaluated shown at the left interface of the droplet, at a position H/2 from the left interface, the position in the middle, at a position H/2 from the right interface and at the right droplet interface.

The presence of two symmetric circulation cells within a moving electrostatic actuated droplet was demonstrated experimentally by Lu *et al.* (2008). They confirmed this flow pattern experimentally using micro particle image velocimetry (µPIV) in electrostatic actuated liquid droplets, however local deviations from the parabolic profile are found. Figure 5.7 shows the velocity field measured inside the droplet using 2 µm large beads. A strong downward flow due to the electrostatic actuation from the bottom substrate is observed near the advancing side of the droplet. The fluid near the substrates circulates back into the droplet near the receding side of the droplet. They concluded that the flow is asymmetric across the height of the droplet due to corresponding asymmetry. However, this asymmetric effect is only observed near the interface of the droplet. Therefore, the parabolic profile could be used to describe the droplet flow in the central part of the droplet.

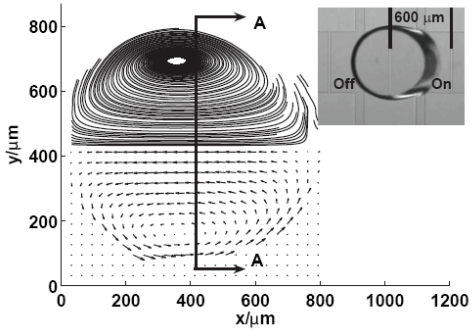

Figure 5.7. Micro particle image velocimetry (µPIV) measurement of an electrostatic actuated liquid droplet: Two-dimensional velocity field (bottom half) and the streamlines (top half) (taken from Lu et al. 2008).

The parabolic profile can be used to estimate the viscous friction force between the droplet and the walls, as discussed in Section 4.1. For a droplet, moving with an average velocity of 10 cm/s, this friction force amounts to 2.4 μN/mm.

Transient flow simulation

For a transient simulation, a stationary droplet is considered as initial condition. At the start of the simulation, a velocity $-U$ is applied on both the top and bottom wall. To check the response of the internal fluid flow, the velocity at the horizontal midplane of the droplet is monitored. For an applied macroscopic velocity of 1 cm/s, 88% of the total velocity increase is reached after 0.05 s. After 0.1 s, 98% of this value is reached. Even for an applied velocity of 10 cm/s, 95% of the velocity is reached after 0.1 s. During this time, the boundary layer at the top and bottom wall are developing. Even for high velocities this time is relatively low, especially compared to the time constant of the thermal behaviour. Therefore, it is sufficient to study the internal flow field in steady state conditions.

5.3 Steady state heat transfer

Based on the fluid flow calculations of the previous section, the droplet velocity is expected to have a beneficial effect on the total heat transfer. To quantify this effect, the heat transfer trough a 2D droplet is studied in detail. First, the steady state regime is studied. From these simulation results, a lumped model for transient heat transfer to the droplet is proposed. The coefficients of this model are extracted from the steady state results of the detailed simulations. Subsequently, the results of this lumped model are compared to the results of a 2D transient CFD simulation. In addition, the effect of natural convection is assessed. Finally, the consequences of the internal heat transfer in the droplet on the performance of the cooling application are discussed.

5.3.1 Model description

To numerically solve the temperature distribution in the droplet, the energy equation is added to the continuity and momentum equations. The numerical set-up for the flow simulation and geometry are set identical to those used for the flow simulation. The related parameters are described in Section 5.2.1. Two separate configurations for the boundary conditions are considered. In the first configuration, a temperature difference is applied between the top and the bottom side of the droplet and respectively set at 350 and 300 K. Therefore in steady state conditions, a heat flux will flow through the droplet. This heat flow is studied for different droplet velocities. In the second case, a constant heat flux is applied at the top surface of the droplet. For this situation, the maximum temperature in the droplet will be monitored as function of the droplet velocity.

Since the friction with the air surrounding the droplet can be neglected, the left and right side can be considered thermally insulated. Vaporisation of the liquid will not be considered. Further, constant material properties of water at 20 °C are used in the study

(specific heat capacity c = 4182 J/kg-K; thermal conductivity k = 0,556 W/m-K; thermal diffusivity α = 1.33e-7 m^2/s).

5.3.2 Grid sensitivity analysis

Convergence analysis

Before discussing the results of the simulations, the truncation error and the convergence of the numerical modelling is assessed. The same approach as discussed in Section 5.2.2 can be used. The additional estimation for the overall residual for the energy equation is as follows:

$$\mathrm{Res}_{tot,en} = \dot{m}_{avg} \cdot h \cdot T_{avg} \cdot N_{cells} \cdot 10^{-15} \tag{5.7}$$

where h is the specific enthalpy of water, and T_{avg} is the average droplet temperature. The analysis is performed for a steady state simulation of a droplet moving with a velocity of 1 cm/s. Table 5.3 gives an overview of the provided values by the software and the target estimations.

Table 5.3. Convergence check for the flow and temperature simulation of a moving droplet with a velocity of 1 cm/s.

	Fluent residuals	Overall residual estimation
Continuity (kg/s)	$3 \cdot 10^{-16}$	$2 \cdot 10^{-15}$
Momentum X (kg m /s)	$5 \cdot 10^{-16}$	$2 \cdot 10^{-17}$
Momentum Y (kg m /s)	$3 \cdot 10^{-16}$	$2 \cdot 10^{-17}$
Energy (J/s)	$6 \cdot 10^{-9}$	$3 \cdot 10^{-9}$

Truncation error

Using the Richardson extrapolation, the truncation error is estimated for 3 grid refinements; 2500, 10000 and 40000 cells respectively. For each grid the heat flow through the droplet is calculated for the case with two fixed temperatures set as boundary conditions. Table 5.4 gives an overview of the solution for these refined grids.

Table 5.4. Grid sensitivity analysis of the heat flow through a moving droplet with a velocity of 1 cm/s.

Grid	Number of grid cells	Heat flow (W/m)
1	10000	0.35935729
2	40000	0.36063336
3	160000	0.36099336

The truncation error is 0.00014 W/m for the grid of 40000 cells. This error is smaller than 0.1%. Therefore, the solution of the simulation can be considered grid independent. Using the Richardson extrapolation, the estimate for the exact solution is 0.36113 W/m.

5.3.3 Discussion of the simulation of the temperature profile

Figure 5.8 shows the temperature contour lines inside a moving droplet, for different droplet velocities, ranging from a stationary droplet to an average velocity of 10 cm/s. The wall temperatures are considered to be 350 K at the top wall and 300 K at the bottom wall respectively. In Figure 5.9 the vertical temperature profile in the middle of the droplet is presented for three different droplet velocities: 0, 5 and 10 cm/s. In the stationary droplet, the heat transfer only occurs by conduction from the top to the bottom side. The vertical temperature profile is linear between the imposed temperatures at the top and bottom sides. In the moving droplet, the temperature contour lines are governed by the flow pattern from Figure 5.3. The contour lines of the temperature are entrained by the flow inside the droplet. For low droplet velocities, this effect is rather small. The temperature contour lines remain more or less horizontal. The effect is more pronounced for higher velocities as can be seen from Figure 5.8 and Figure 5.9.

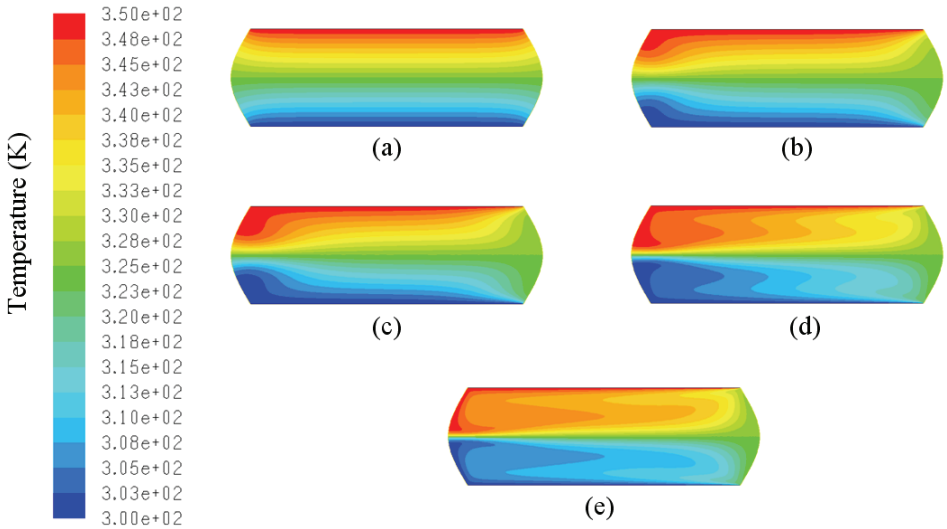

Figure 5.8. Temperature distribution (K) in a moving droplet for a fixed temperature of 350 K at the top wall and 300 K at the bottom wall. Different droplet velocities: (a) Stationary droplet, (b) 6 mm/s, (c) 1 cm/s, (d) 5 cm/s, (e) 10 cm/s.

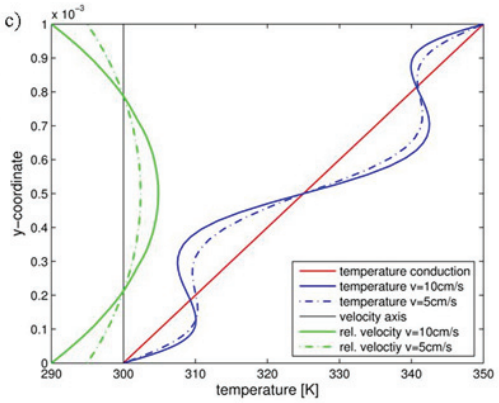

Figure 5.9. Vertical temperature profile in the middle of the droplet.

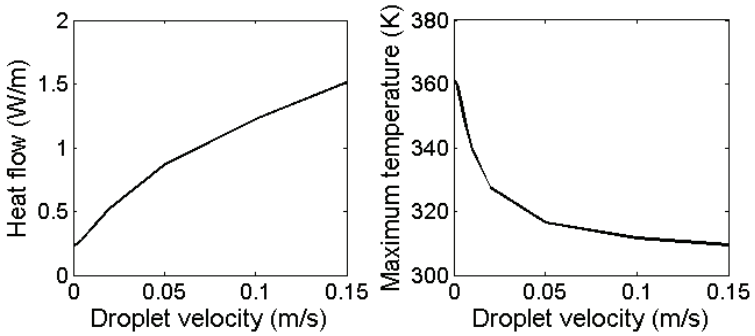

Figure 5.10. Effect of the droplet velocity on the heat transfer in a moving droplet: heat flow through the droplet for fixed temperature boundary conditions (left), maximum temperature at the top plate for a fixed heat flux boundary condition (right).

At the droplet horizontal midplane, a high concentration of contour lines can be observed. This indicates the presence of a high thermal resistance at this location. It can be considered to be a thermal barrier between the convection cell at the top of the droplet and the one at the bottom. No liquid flows through this imaginary barrier. Therefore, only conduction heat transfer occurs across this thermal barrier even at higher velocities. This effect limits the overall heat transfer. For higher droplet velocities, the temperature gradients at the walls will increase. This increase leads to a locally higher heat transfer coefficient and consequently to a higher heat flux at the wall. As a result, the total heat flux through the droplet will increase for higher velocities. This is caused by an enhanced heat transport in both convection cells. This leads to a steepening of the temperature gradients at these locations where heat conduction is the only mean for heat transfer. This is at the top and bottom plane and in the horizontal midplane. As expected, internal droplet motion has a beneficial effect on the heat transfer in the droplet. For a stationary droplet, the heat flow by conduction through the droplet can be estimated based on the geometry, the temperature

difference and the material properties. For the parameters considered here, this amounts to 0.23 W/m. For higher velocities, the heat flow through the top and bottom wall can be extracted. The evolution of this heat flow through the droplet is shown in Figure 5.10 as a function of the droplet velocity. The increase in heat flow is less than linear because the beneficial effect of the internal droplet motion is limited by the barrier at the horizontal midplane.

A similar analysis can be performed for the case with a fixed heat flux at the top side. In this case, the maximum temperature at the top side is monitored. Here, an enhanced heat transfer will lead to a lower temperature in the droplet for the same applied heat flux. This trend is shown on the right hand side of Figure 5.10. Both graphs contain the same information; the equivalent thermal resistance decreases for an increasing droplet velocity.

5.3.4 Lumped model for the temperature distribution

The numerical simulation of the combined flow and temperature distribution in the moving droplet is time consuming, especially in the case of transient simulations. Therefore, an analytic lumped model is developed to estimate the temperature profile and to assess the influence of the velocity on the heat transfer coefficients. In the study presented here, the lumped model will be used to predict the average droplet temperature for different velocities during the stay in the channel. In this section, a lumped model is developed to describe the steady state situation. In the next section, the model is expanded to predict the transient temperature evolution.

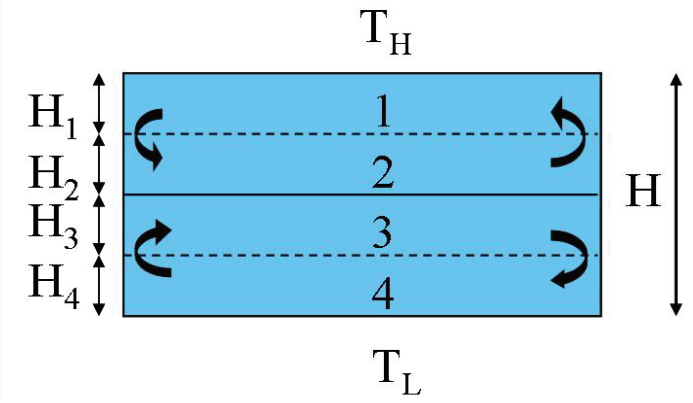

Figure 5.11. Schematic representation of the lumped model with 4 cells.

Based on the temperature profile (Figure 5.8) and the flow pattern (Figure 5.4) resulting from the 2D numerical simulations, a lumped model of 4 cells is chosen. The choice of 4 cells allows taking into account the heat transport at the top and bottom wall, but also the heat transport from one convection cell to the other. A schematic representation of this 4 cell model is shown in Figure 5.11. In each cell, a cell-averaged temperature is monitored. The division of the cells over the height of the droplet is based on the parabolic velocity profile as deduced in Section 5.2.3. This means that the location of the border between the cells corresponds to the locations on the vertical profile where the relative velocity is zero

to guarantee the same flow rate in each cell. Using this 4 cell lumped model, the heat flow from the top plate through the four cells to the bottom plate can be described, taking into account the convective and the conductive heat transfer in the droplet. The transport phenomena involved for the different cells differ as follows: cell 1 receives the heat flow from the top plate through convection heat transfer in the boundary layer; cell 1 passes heat on to cell 2 through conduction heat transfer through the liquid and heat is also transferred to cell 1 by large scale convection heat transfer because of the liquid flow from cell 1 to 2 and vice versa; a thermal barrier exists between cell 2 and 3, leading at this place predominantly to conduction heat transfer; the heat transfer in cells 4 and 3 is analogous to the heat transfer in cell 1 and 2. Based on these assumptions, a characteristic heat transfer equation can be written for each cell:

$$\begin{aligned}
&cell\ 1\text{:}\ \left(T_H - T_1\right)h_{top}A_{H1} - \left(T_1 - T_2\right)\frac{kA_{12}}{d_{12}} + \dot{m}c_p\left(T_2 - T_1\right) = 0;\\
&cell\ 2\text{:}\ \left(T_1 - T_2\right)\frac{kA_{12}}{d_{12}} - \left(T_2 - T_3\right)h_{mid}A_{23} + \dot{m}c_p\left(T_1 - T_2\right) = 0;\\
&cell\ 3\text{:}\ \left(T_2 - T_3\right)h_{mid}A_{23} - \left(T_3 - T_4\right)\frac{kA_{34}}{d_{34}} + \dot{m}c_p\left(T_4 - T_3\right) = 0;\\
&cell\ 4\text{:}\ \left(T_3 - T_4\right)\frac{kA_{34}}{d_{34}} - \left(T_4 - T_L\right)h_{bottom}A_{4L} + \dot{m}c_p\left(T_3 - T_4\right) = 0.
\end{aligned} \tag{5.8}$$

where T_i is the averaged temperature in cell i, h the local convective heat transfer coefficient, A_{ij} the contact area between the cell i and j, d_{ij} the characteristic distance between temperature T_i and T_j and $\dot{m}$ the mass flow rate from cell i to cell j. The local heat transfer coefficients are defined for each cell individually. The average temperature of the cell is used as bulk temperature in calculation of the heat transfer coefficients. E.g. for cell 1, the heat transfer coefficient h_{top} is defined by following equation:

$$Q_{top} = h_{top}A\left(T_{top} - T_{1,ave}\right) \tag{5.9}$$

where Q_{top} is the heat flow through the top plate into cell 1, T_{top} is the fixed temperature of the top plate and $T_{1,ave}$ is the average temperature of cell 1. The values for the heat transfer coefficients are extracted from the results of the numerical simulations. Figure 5.12 shows these extracted *Nu* numbers and calculated heat transfer coefficients based on the averaged heat transfer coefficient and characteristic dimension of each cell. At the transition between cell 1 and 2 and between cell 3 and 4, a large influence of the velocity on the coefficient is noticed. The coefficient for the conduction both at the top and bottom plates as well as across the midpoint plane is less sensitive to the velocity. This is due to the fact that the heat transfer is caused by conduction only. It can be clearly concluded that the droplet transport favours an enhanced heat transfer in comparison with continuous liquid flow through microchannels. In a continuous bulk flow, the Nusselt number is constant and independent of the Reynolds number for a fully developed laminar flow. However, in the case of the droplet flow, the flow is not thermally developed. The flow in the droplet can be considered to remain in the thermal entrance region since the thermal boundary layer needs

to be established for each new position of the moving droplet. Based on the theory for convective heat transfer in short ducts an increase of the Nusselt number is expected for increasing Reynolds numbers for thermally developing flow in the entrance region (Kakaç 1987).

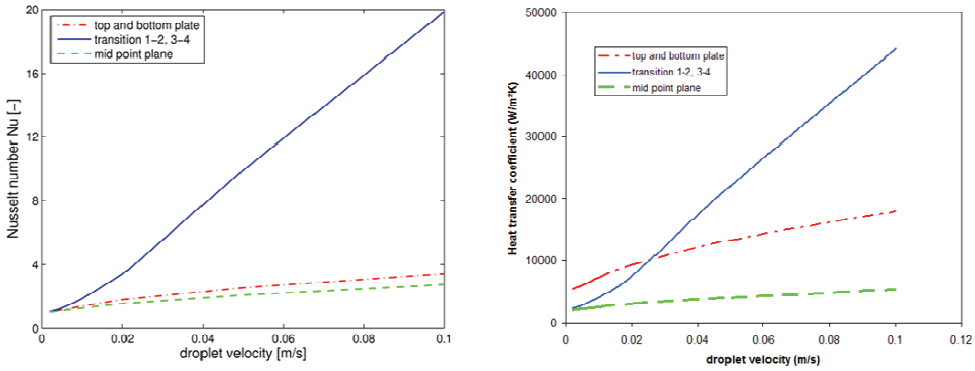

Figure 5.12. Nu numbers (left) and heat transfer coefficients (right) in the different cells extracted from CFD simulations at different droplet velocities.

5.4 Transient heat transfer

In this section, the transient heat transfer in a droplet moving between two parallel plates is studied. The transient behaviour will be studied using both CFD simulations and an analytic lumped model.

5.4.1 Transient heat transfer simulations

For the transient CFD model, the same boundary conditions are used as for the steady state modelling. An initial condition of the average droplet temperatures of 300 K is introduced. A time step of 0.05 s is used and for the time integration a first order implicit scheme is chosen. Figure 5.13 shows the evolution of the temperature contour lines for a droplet with a velocity of 10 cm/s. The internal motion in the droplet causes the temperature contour lines to be entrained with the liquid. At the initial stage (0.1 s) the temperature is highest at the top left corner since the liquid sticks to the heat source while the latter moves from the right to the left. At later time steps, the thermal barrier at the midpoint plane can be clearly observed.

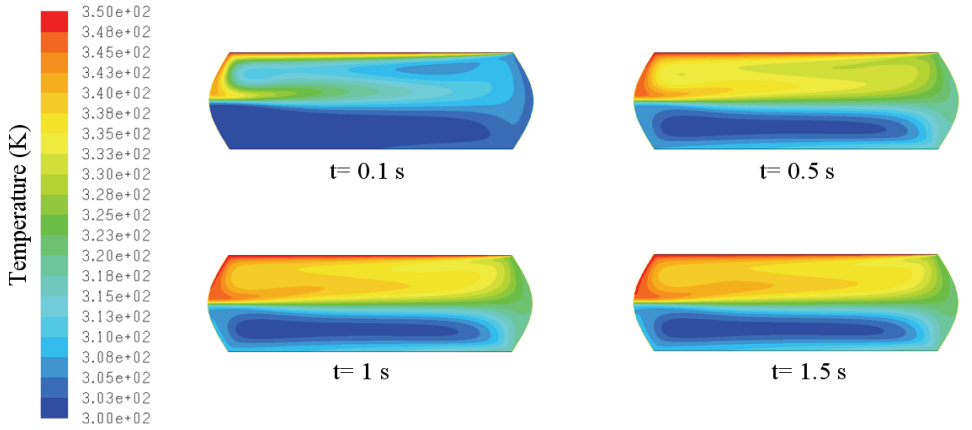

Figure 5.13. Transient temperature contour lines in a moving droplet with velocity of 10 cm/s.

Figure 5.14 (left) shows the evolution of the average droplet temperature for different velocities as a function of time. As expected, the faster the droplet moves through the channel, the steeper its temperature rise. This is due to the increased convection heat transfer in the droplet. Indeed, the Nusselt number at the top varies between 1.0 and 3.1 for the speed between 0 and 10 cm/s (Figure 5.12). From the graph of the transient droplet velocity can be seen that the time constant for the temperature response is in the order of seconds. This is much longer compared to the other time scales in the coupled phenomena involved in the electrostatic actuation. The time scale of the rearrangement of the ions or dipoles is a few hundred μs, the macroscopic droplet motion has a time scale of a few tens of ms and the time scale of the flow response inside the droplet is around 0.1 s. This difference in time scales is a justification for the decoupling.

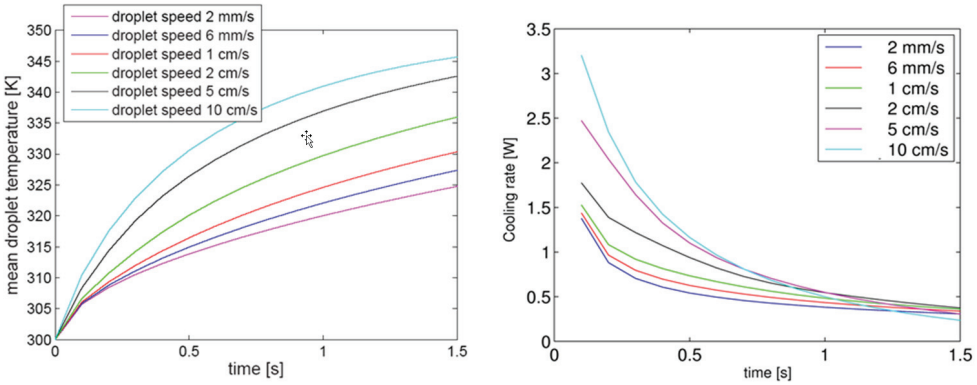

Figure 5.14. Simulation results (CFD) for the transient average droplet temperature (left) and the transient cooling rate (right) as function of time for different droplet velocities.

5.4.2 Transient lumped model

The analytical lumped 4 cell model discussed in Section 3.1.2. can be expanded with time dependent terms to describe the transient heating of the droplet :

$$\begin{aligned}
&cell\ 1: \quad m_1 c_p \frac{dT_1}{dt} = \left(T_H - T_1\right) h_{top} A_{H1} - \left(T_1 - T_2\right) \frac{k}{d_{12}} A_{12};\\
&cell\ 2: \quad m_2 c_p \frac{dT_2}{dt} = \left(T_1 - T_2\right) \frac{k}{d_{12}} A_{12} - \left(T_2 - T_3\right) h_{mid} A_{23};\\
&cell\ 3: \quad m_3 c_p \frac{dT_3}{dt} = \left(T_2 - T_3\right) h_{mid} A_{23} - \left(T_3 - T_4\right) \frac{k}{d_{34}} A_{34};\\
&cell\ 4: \quad m_4 c_p \frac{dT_4}{dt} = \left(T_3 - T_4\right) \frac{k}{d_{34}} A_{34} - \left(T_4 - T_L\right) h_{bottom} A_{4L}.
\end{aligned} \tag{5.10}$$

where T_i is the average temperature in cell i. The values of h_{ij} can be obtained from the transient numerical simulations for each time step using the same approach as discussed in Section 5.3.4. As a result, the heat transfer coefficients will be time dependent. This will complicate the use of the lumped model. Figure 5.15 shows the evolution of these coefficients with respect to time, for different droplet velocities. It can be observed that the curves exhibit a short transitional behaviour before reaching the asymptotic steady state value. The time interval for this transitional behaviour is relatively short. Therefore, using the transient lumped model with the constant steady state values would only lead to small errors in the region of small time steps.

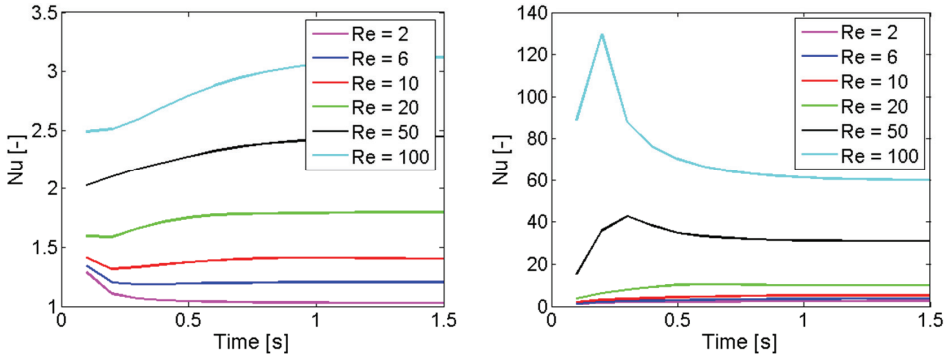

Figure 5.15. Time dependent heat transfer coefficients for the lumped model, extracted from the transient CFD simulations; at the top wall (left), at the border between cell 1 and 2 (right).

This lumped model (5.10) is numerically solved for the temperatures T_i using a backward Euler algorithm with the values obtained from the steady state CFD simulations, which are shown in Figure 5.12. The left hand side of Figure 5.16 shows the evolution of the average temperature of the four cells for a droplet velocity of 1 cm/s. A large difference between the

temperatures in cell 1 and 2 on the one hand, and the temperatures in cell 3 and 4 on the other hand can be observed. This difference is caused by the thermal barrier at the horizontal midplane of the droplet. The graph at the right hand side shows the evolution of the average droplet temperature. The results from the lumped model with constant heat transfer coefficients are compared to the results from the CFD simulation, for several droplet velocities.

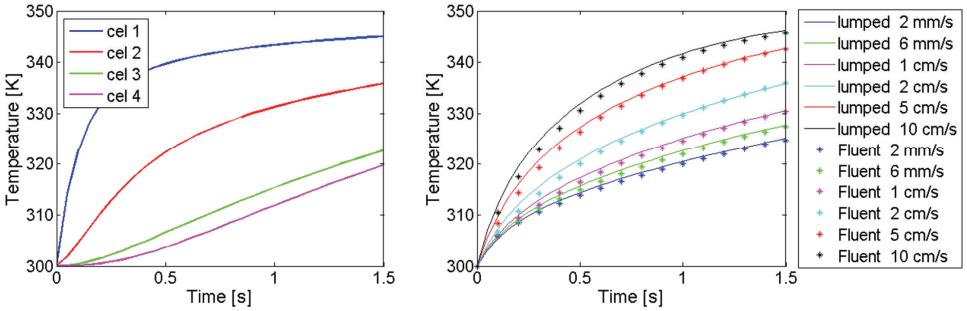

Figure 5.16. Transient temperature profiles from the lumped 4 cell model; temperature in the 4 cells for a droplet velocity of 1 cm/s (left), comparison between the lumped model and the CFD simulations for the average droplet temperature (right).

A good overall agreement is achieved between the results of the lumped model with constant coefficient and the full transient numerical simulations. Only at the initial stage, the lumped model seems to overestimate the temperature rise. This is a result of the use of the constant heat transfer coefficient. With the constant coefficients, the build-up of the heat transfer coefficients is not taken into account. For small velocities, the *Nu* number at the wall decreases with time, whereas for high velocities the *Nu* increases with time. Nevertheless, overall the maximal error of the lumped model compared to the full transient numerical simulations is less than 5%. Since the error of the lumped model is this small compared to the time consuming transient numerical simulations, the transient lumped model will be used for a fast and parameterised evaluation of the transient behaviour of the liquid droplet cooling. To extract the model, only one time consuming simulation is required. This is the simulation for the steady state regime. In the case of the full transient detailed simulation, the flow and temperature distribution are calculated in every time step. The use of the lumped model results in a dramatic reduction in computational time to assess the transient droplet temperature, without loosing too much accuracy.

5.4.3 Cooling rate of moving droplets

As the droplet moves through the channel, it will accumulate heat and the average temperature will rise. As a result, the temperature difference between the droplet of the coolant and the hot chip decreases. This leads to a decreased cooling rate with respect to time. The total heat removed by the droplet can be found by integration of the cooling rate for the time during which the droplet is in the channel.

In the next step, the transient lumped model can be used to assess the cooling performance of a cooling device based on discrete liquid droplets. The time a droplet stays in the channel

depends on the droplet velocity. A fast moving droplet will have a higher heat transfer coefficient but spends a shorter time in the channel than a slower moving droplet. For this analysis, a chip with typical droplet paths of approximately 15 mm is considered. From the transient droplet temperatures shown in Figure 5.16, the cooling rate per droplet is calculated. Figure 5.17 shows the average cooling rate of a droplet as a function of the contact time between the droplet and the chip for the different droplet velocities. The marker on each curve indicates the time the droplet needs to cross the chip at this velocity. From the graph, the corresponding average cooling rate per droplet during the stay of the droplet in the channel can be read. The cooling rate between the chip and the droplet decreases with time since the droplet temperature raises and consequently the temperature difference between the average droplet temperature and the fixed temperature at the top side decreases. For higher velocities the cooling rate is higher at the beginning.

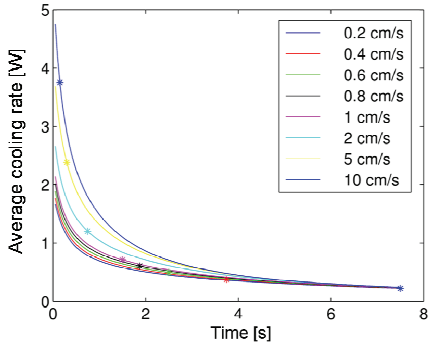

Figure 5.17. Transient cooling rate per droplet of a moving droplet as function of time for different droplet velocities.

5.5 Influence of natural convection

For the simulations above, the heat source was considered to be at the top side of the channel. However, when the heat source is at the bottom of the channel, natural convection cells might appear. These cells could have a beneficial effect on the heat transfer in the droplet. Natural convection is caused by the temperature dependence of the density. As a result, a volume with a hot liquid below a cold volume will feel a buoyancy force. This body force can move the liquid and as such, create convection flows in the liquid. When the heat source in the configuration considered here, is switched from the top to the bottom, Raleigh-Bénard convection cells may be created. Natural convection is characterised by the dimensionless Rayleigh number *Ra*. The Raleigh number, based on the height *H* of the droplet is defined as follows:

$$\begin{aligned} Ra_H &= Pr \cdot Gr_H \\ &= \frac{\upsilon}{\alpha} \cdot \left(\frac{g\ \beta\ \Delta T\ H^3}{\upsilon^2} \right) \end{aligned} \tag{5.11}$$

where Gr_H is the Grashoff number, α is the thermal diffusivity, β is the thermal expansion coefficient and υ is the kinematic viscosity. The critical Raleigh number for convection cells in enclosures is 1800 (Soong *et al.* 1996; Wang and Hamed 2006). The Raleigh

number in the droplet under consideration is 1982. This means natural convection could appear in this situation. The presence and effect of these cells on the heat transfer is studied with CFD simulations for the same geometry discussed before. For water, a thermal expansion coefficient of 0.00054 K^{-1} is used.

Stationary droplet

First, natural convection is studied numerically for a stationary droplet. The top side of the droplet is kept at a constant temperature of 300 K, while the temperature of the bottom wall is 350 K. Figure 5.18 shows the temperature and velocity distribution in the droplet. In the case where the heat source is on top, a linear temperature profile is found (Figure 5.8). When the heat source is placed at the bottom, three convection cells can be observed (Figure 5.18). The maximum velocity in the convection cells is 0.8 mm/s. These convection cells have an influence on the heat flow through the droplet. In this case the heat flow is 30% higher compared to the case with the heat source on top.

Moving droplet: steady state analysis

First, the effect of natural convection is studied for steady state conditions. In the case of moving droplets, both forced convection and natural convection occur. Both convection phenomena exhibit a completely different flow pattern. The overall pattern will depend on the relative contribution of both types of convection. For droplet velocities higher than the maximum velocity of the convection cells, the forced convection is dominant. Figure 5.19 shows the influence of natural convection on the heat flow through the droplet. For smaller velocities, a beneficial effect can be observed. For higher velocities, the effect is small. Figure 5.20 shows the flow pattern for both heat source configurations for a low droplet velocity. For this case, the natural convection cells can 'break' the thermal barrier of the two forced convection cells and enhance the heat transfer. For higher velocities, the influences of the forced convection is too dominant.

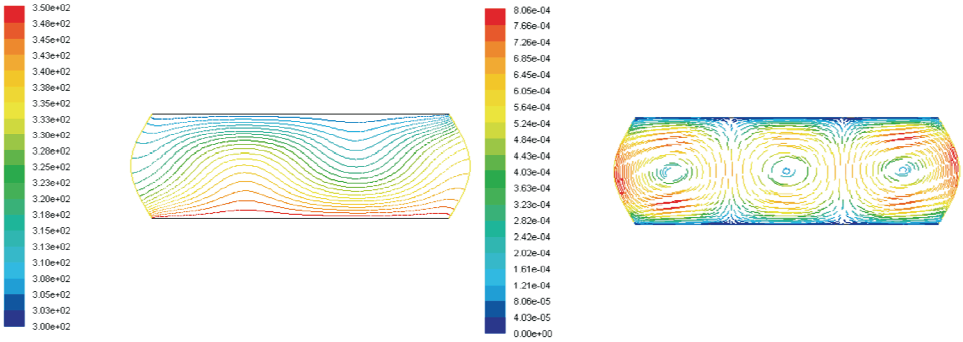

Figure 5.18. Simulation result for the natural convection in a stationary droplet with a fixed temperature of 300 K at the top, and a fixed temperature of 350 K at the bottom; temperature contour lines (K) (left), stream lines (m/s) (right).

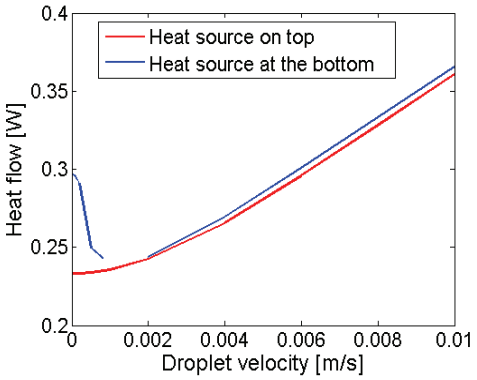

Figure 5.19. Influence of the location of the heat source on the heat flow through the droplet.

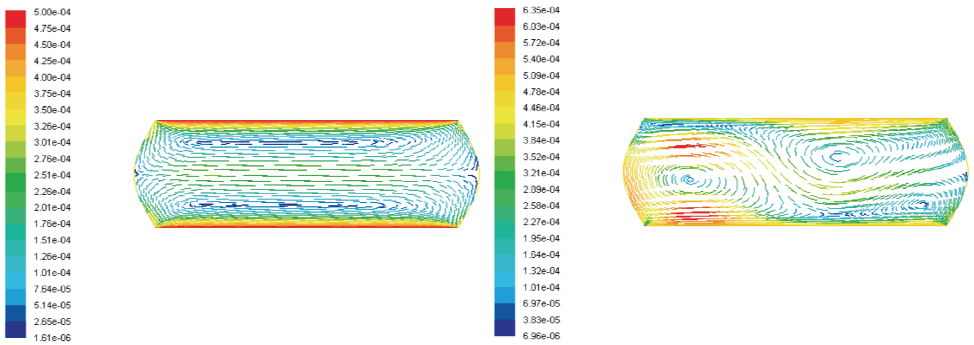

Figure 5.20. Stream lines (m/s) for a moving droplet with a velocity of 0.5 cm/s; heat source on top (left), heat source below (right).

Conclusion natural convection analysis

When the hot heat source is placed at the bottom wall instead of the top wall, Raleigh-Bénard convection cells may be created. In this case, natural convection could have a beneficial influence on the total heat transfer in the droplet. The critical Raleigh number for convection cells in enclosures is 1800 (Soong *et al*. 1996; Wang and Hamed 2006). The Raleigh number in the droplet under consideration is 1982. CFD simulations indeed show these convection cells. In a stationary droplet, this temperature induced convection flow enhances the total heat transfer by 30%. The maximum fluid velocity in these natural convection cells is 0.8 mm/s. In moving droplets, both forced convection and natural convection are present. However, at droplet speeds above 1 mm/s, the forced convection is dominant and the natural convection is not able to alter the flow pattern and to break the thermal barrier. This is confirmed by transient CFD simulations which show that the influence of natural convection is negligible at droplet speeds above 1 mm/s. As such, natural convection will not play a crucial role for realistic velocities.

5.6 Conclusions

In the previous chapter, the macroscopic droplet motion was predicted over an array of subsequently activated electrodes. For an optimal switching frequency, the droplet motion can be approximated by a constant velocity motion. In this chapter, the flow patterns and heat transfer in such a moving droplet are assessed by means of detailed 2D numerical flow calculations.

It is shown that the flow pattern inside the droplet consists of two separate circulation zones. Furthermore, it is shown that the internal droplet flow exhibits a parabolic characteristic. This facilitates the prediction of viscous flow forces. However, the heat transfer shows a much more complicated behaviour. On the one hand, the heat transfer is enhanced at the top plate by forced convection. On the other hand, the presence of two convection cells decreases the heat transfer to the lower part of the droplet. As a result, the overall heat transfer does not increase as much as expected by the increased internal convection. Nevertheless, at a velocity of 10 cm/s, a typical enhancement of the heat transfer in steady state conditions with a factor 5 is achieved with respect to the minimal value that would be obtained assuming heat conduction in the liquid only. For short channels, the temperature distribution in the droplet will not reach the steady state condition. For a very short channel of 15 mm, the heat transfer is enhanced by a factor 2 at a velocity of 10 cm/s.

Furthermore, in this chapter, an analytic lumped model with four cells is developed to predict the droplet temperature. The parameters for the lumped model are extracted from steady state numerical simulations (CFD). Using these parameters, the transient average droplet temperature can be estimated with the lumped model. The difference between the results of the lumped model and the full transient CFD modelling is less than 5%.

Chapter 6

Towards an integrated droplet based cooling system

Abstract

In this chapter, the cooling performance of an integrated cooling system, based on droplet flows is assessed. First, the requirements for such an integrated cooling system are stated and the strengths of the droplet based system are evaluated. Next, the thermal performance of the planar parallel electrode system is studied using the results of the detailed flow and thermal simulations, discussed in Chapter 5. For this system, the influence of the droplet velocity on the cooling rate is studied. Finally, the thermal performance and the required power consumption are compared for a droplet based cooling system and a continuous flow cooling system. In the first part of the comparison, both cooling systems are compared in a fundamental way in terms of the Nu number and friction factor as a function of the Reynolds number. In the second part, a practical example of a heat sink based on the droplet flow and continuous flow are compared.

6.1 Droplet based cooling systems

In this chapter, the thermal performance of a droplet based cooling system is evaluated. The main part of this cooling system is the cooler, attached to the heat generating component. In this cooler, a flow of droplets is generated, which will remove the heat from the chip. At the entrance of the cooler, the droplets are dispensed from a reservoir. After moving through the channel, the droplets are collected again in a reservoir. The cooling system should be able to work autonomous, without the need to be refilled when the reservoir is empty. This is especially important for mobile applications. Therefore, the system should be closed-loop. The reason for the closed-loop is twofold. Not only to recirculate the liquid but the coolant should also be cooled before entering the cooling channel again. An option to create such a closed-loop system, is the use of a single reservoir, surrounding the cooler. The droplets are extracted from this reservoir, and after transport through the cooler, fed back into this reservoir. This option is possible if the reservoir can be externally cooled to allow the liquid to cool down sufficiently before entering the cooler again. For higher power applications, where the coolant will heat up too much for this option, an external heat exchanger needs to be foreseen to cool the coolant. A closed-loop system, including this external heat exchanger is schematically shown in Figure 6.1. The loop with this secondary heat exchanger links the reservoir where the droplets are collected to the reservoir from which the droplets are extracted. In this heat exchanger, the liquid is cooled by a secondary cooler using a secondary coolant. This could be the ambient air, in the case of a liquid-air heat exchanger.

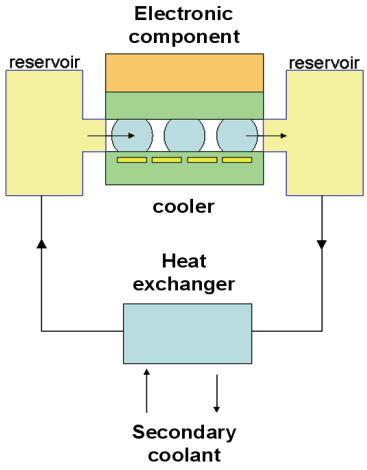

Figure 6.1. Schematic representation of the closed-loop cooling system including the electrostatic droplet actuation in the cooler.

Inside the cooler, the droplets are transported over a two dimensional array of individual addressable control electrodes. The droplets are guided from electrode to electrode. As a result, the droplets can be moved along any arbitrary path over the chip surface. Using the array of electrodes, the droplets can be directed to a location of interest. In this way, a targeted cooling of hot spots on the chip can be provided. This offers the flexibility to choose a cooling strategy to match the actual thermal load of the chip. This means the channel is reconfigurable and no walls or valves are used to define parallel droplet flows.

The droplet paths can be easily changed to match the changing heat generating areas on the chip. This reconfigurable concept allows a large flexibility for different cooling strategies. Depending on the spatial and temporal distribution of the heat load on the chip, an optimal cooling strategy can be defined. This is an important advantage compared to continuous flow microchannel heat sinks. In these heat sinks, the channels are etched or micromachined in the cooler. Therefore, the location of the channels, through which the coolant flows, is fixed. Moreover, to control the flow in the different parallel channels of a microchannel heat sink, a complex system of valves would be needed. An additional advantage of the droplet based cooler is the absence of a pump to transport the coolant through the channel. In the case of the microchannel heat sink, a large pressure difference needs to be overcome by an external pump. For the droplet based cooler, the 'pump' is integrated in the channel and there is no need for an external pump. Therefore, the droplet based cooling system can be fabricated as a compact and light construction that can fit into a small space. Due to the planar nature of the cooler, the system can easily be integrated in the microsystem to cool using microelectronic fabrication technologies. Furthermore, no mechanical valves or pumps are required to actuate and control the droplets in the cooler. This has a beneficial effect on the reliability of the cooling system.

The above highlighted advantages illustrate the potential of a droplet based cooler. In the next section, the thermal performance of the electrowetting based cooling systems is studied. In the third section, the thermal performance of the droplet based cooling is compared to the performance of a continuous flow cooling system, which is the reference for liquid cooling.

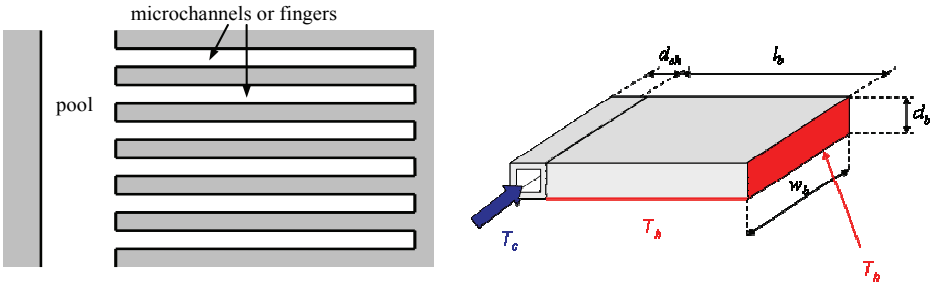

Figure 6.2. Sketch of principle of the electrowetted system (left), Schematic of the reference cooling system (right) (Van der Veken 2005).

Alternative electrowetting based cooling system

In this work, the electrowetting principle is applied to generate a continuous droplet flow either between parallel planar electrodes or in cylindrical channels. However, other electrowetting based implementations of integrated coolers are possible. Van der Veken (2005) studied the application of electrowetting induced pulsation of liquid fingers in microchannels in a silicon block as a cooling technique. In this cooling system, 100 µm x 100 µm microchannels are connected perpendicular to a feeding channel. By forced convection, the coolant is pumped through the main channel. By applying a voltage to the silicon, a pulsating liquid flow can be generated in the microchannels using the electrowetting phenomenon.

A theoretical study (Oprins *et al.* 2007) of the heat transfer reveals that this implementation will induce enhanced heat transfer, due to the pulsating flow in the microchannels, above a critical frequency of the pulsation in the microchannels. This frequency amounts to about 0.25 Hz for the 100 μm square microchannels. Based on experimental filling data, an enhancement in cooling capacity of 55% is estimated without increasing the pressure requirements of the external pump. The thermal resistance of the reference case is 56 K/W. At the optimal frequency, the thermal resistance of the electrowetting assisted filling is 31.9 K/W. This is an increase in thermal performance of 55%.

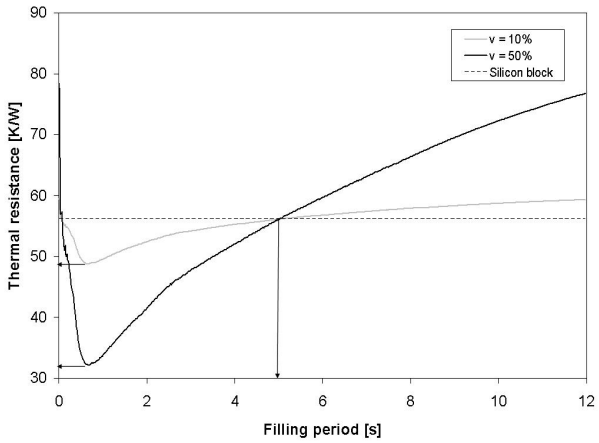

Figure 6.3. Comparison of the thermal resistance of the silicon block and the electrowetting assisted pulsating microchannel flow.

6.2 Cooling performance of the planar system

In this section, the cooling performance of the planar system is estimated. In this planar system, droplets are actuated between two parallel plates, as introduced in Section 1.3.1. The control electrodes on the bottom plate of the structure actuate the droplets through the channel formed between the top and bottom plate. In Figure 6.4 an example of an array of control electrodes is shown. By moving through the channel, the droplets will heat up and remove the heat from the heat generating top side. By studying the temperature evolution of the liquid droplets and the flow rate, the cooling performance of the proposed cooling technique can be estimated. Both the flow rate and the droplet temperature response depend on the droplet velocity. For a higher droplet velocity, a higher flow rate is achieved. Moreover, a higher droplet velocity leads to a higher internal circulation and thus a higher heat transfer. As a result, from the thermal point of view, the droplet velocity should be as high as possible. However, to achieve high velocities, a higher actuation voltage and faster switching are required. This leads to a higher power consumption and a more complex control system.

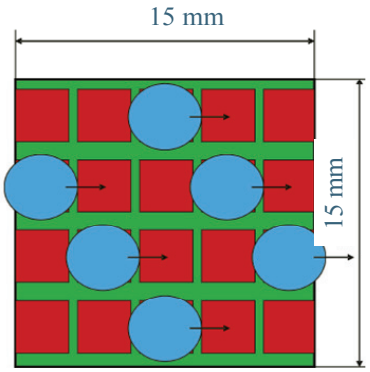

Figure 6.4. Matrix of control electrodes at the bottom plate of the planar droplet actuation system.

Table 6.1. Parameters used in the thermal performance feasibility calculations.

Droplet diameter	1.5 mm
Droplet volume	2.5 µl
Channel height	1 mm
Electrode pitch	1 mm
Chip size	15 x 15 mm²
Channel length	15 mm
Droplet speed	10 cm/s (*)
Droplet temperature at inlet	20 °C
Chip temperature	70 °C

(* Washizu 1998, Pollack 2002, Cho 2003)

To study the thermal performance and the effect of the droplet velocity on this performance, a test case is considered. In this test case, the top plate consists of a 15 mm x 15 mm heat generating chip. The droplets are transported over a 2D array of electrodes on the bottom plate, which has the same size as the top plate. Table 6.1 gives an overview of the parameters used in this thermal analysis. The assumed droplet velocity is 10 cm/s. This is a high, but realistic droplet velocity (Pamula and Chakrabarty 2003). Using the parameters given in Table 6.1, five parallel arrays fit in the chip area, keeping a safe distance of one droplet diameter between the arrays to avoid coalescence of the droplets. Assuming a pitch of 1.5 mm between subsequent droplets, the flow rate through the channel amounts to 100 µl/s per row. In literature, flow rates up to 170 µl/s per row of 1.5 x 1.5 mm² electrodes have been reported (Paik *et al.* 2005). For five parallel rows in the matrix of electrodes, this leads to a total flow rate of 500 µl/s or 30 ml/min over the chip. Fitting five rows of electrodes on the available area is a conservative choice for the droplet spacing. The use of denser packed arrays of electrodes, and a staggered pattern of moving droplets on the parallel rows can lead to significantly even higher flow rates.

6.2.1 First order calculation of the cooling performance range

A first order estimation of the cooling capacity of the system is carried out to check the feasibility of the proposed technique. To this end an upper and lower limit for the heat transfer are calculated. The actual value of the cooling will be in between those extreme values, and depends on the effect of the internal circulation flow on the heat transfer. For slowly moving droplets, the beneficial effect of the internal convection is limited and the cooling performance will be close to the lower limit.

Lower limit

In the case of the lower limit only transient heat conduction in the water droplet is taken into account, during the period the droplet moves through the channel. Using the transient heat equation, the increase of the average temperature can be estimated for a single droplet. For the analysis, a temperature difference between the liquid and the heat source of 50 °C is assumed. With an average droplet velocity of 10 cm/s, the droplet will spend 0.15 s inside the channel. At the moment the droplet leaves the channel, the average temperature rise in the water droplet amounts to 8.4 °C. Considering the flow rate of 500 µl/s, this result for one droplet can be extrapolated to the cooling performance of a continuous flow of droplets through the channel. This results in a cooling capacity of 3.5 W per array of electrodes or 17.5 W for the total chip. Therefore, the lower limit of the cooling performance of the test case is 7.8 W/cm².

Upper limit

To compute the upper limit, for the heat transfer we assume an infinite heat transfer coefficient between the droplet and the chip as well as an ideal mixing inside the droplet. Here, the assumption is made that the droplet will reach the temperature of the hot top surface by the end of the channel. As such, the average droplet temperature at the outlet will rise by 50 °C, leading to a cooling power of 20 W per electrode array. Leaving also a pitch of 1.5 mm between droplets in the lateral direction, giving rise to 5 parallel droplet arrays, an upper limit of 100 W for the 15x15 mm^2 chip is estimated. Therefore, the upper limit of the cooling performance of the test case is 44.4 W/cm².

6.2.2 Detailed calculation of the cooling performance

The actual value of the cooling will be in between the estimations for the lower and upper limit. To study the effect of the droplet velocity on the cooling performance, the transient lumped model can be used. For this analysis, the same chip with typical droplet paths of approximately 15 mm is considered. The time a droplet stays in the channel depends on the droplet velocity. A fast moving droplet will have a higher heat transfer coefficient but spends a shorter time in the channel than a slower moving droplet. Slower individual droplets will remove more energy due to the longer stay in the channel for a single droplet. However, as the liquid droplet flow can be enhanced proportional to the droplet velocity, the cooling capacity of the high speed droplets will be highest when the continuous flow of droplets is considered. Figure 6.5 shows the average cooling rate of a droplet as a function of the contact time between the droplet and the chip for the different droplet velocities. The marker on each curve indicates the time the droplet needs to cross the chip at this velocity.

From the graph, the corresponding average cooling rate per droplet during the stay of the droplet in the channel can be observed. The cooling rate between the chip and the droplet decreases with time since the droplet temperature raises and consequently the temperature difference between the average droplet temperature and the fixed temperature at the top side decreases. For higher velocities, the cooling rate is higher at the beginning.

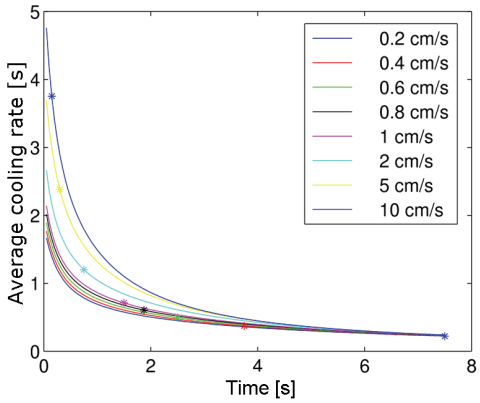

Figure 6.5. Average cooling rate per droplet as a function of the time for a temperature difference of 50 K.

Using the lumped model to calculate the transient average droplet temperatures, it is found that the average cooling rate per droplet is 3.8 W. To reach a flow rate of 500 µl/s, on average 8 droplets are simultaneously in the cooling channel. Therefore, a total cooling capacity of 15 W/cm² is achieved for an average droplet velocity of 10 cm/s and a flow rate of 500 µl/s. This value of the cooling performance is roughly twice the value of the lower limit of the heat transfer, achieved by pure conduction (7.8 W/cm² for a difference in temperature of 50 K and a volume flow rate of 500 µl/s). When the chip is operating at a higher temperature, even higher cooling rates can be achieved. If a temperature difference of 90 K is considered between the chip and the coolant at the entrance, an average cooling rate per droplet of 6 W is found using the lumped model for a droplet velocity of 10 cm/s. This results in a total cooling performance of 23 W/cm². The cooling rate scales linearly with the number of droplets simultaneously in the channel. Assuming 8 droplets in the channel is a conservative choice. Therefore the cooling rate can increased by allowing more droplets at the same time in the cooling channel.

The cooling performance of the proposed technique can be expressed as an equivalent thermal resistance. This thermal resistance is defined as follows:

$$R_{th} = \frac{\Delta T}{Q_{flow}} \tag{6.1}$$

where ΔT is the temperature difference between the heat source and the coolant, and Q_{flow} is the average cooling rate for the droplet flow during the stay in the channel. This corresponds to the markers in Figure 6.5. This formulation of the average cooling rate includes the effect of increasing flow rate for higher droplet velocities (i.e. more droplets) and the effect of enhanced cooling for every droplet. Figure 6.6 shows this equivalent

thermal resistance for different droplet velocities based on an initial temperature difference of 50 K. The internal convection inside the droplet causes an enhancement of the heat transfer (i.e. reduction of the thermal resistance) typically of a factor of 2. The rest of the drop in thermal resistance is caused by the increased flow rate for higher droplet velocities. This concept of equivalent thermal resistance allows comparing the thermal performance of the droplet based cooling system with a continuous single-phase flow cooling technique.

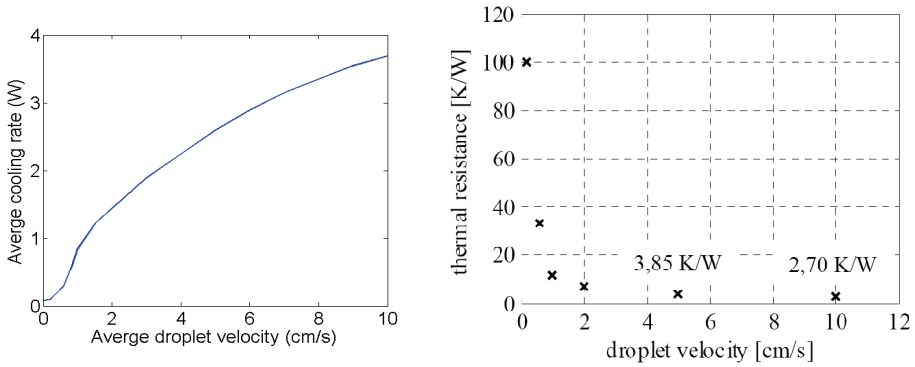

Figure 6.6. Average cooling rate of a continuous flow of droplets as a function of the average droplet velocity (top). Equivalent thermal resistance of the droplet based cooling system for different droplet velocities (right).

6.3 Thermal performance analysis of the droplet based cooling system

In this section, the thermal performance of the droplet based cooling system is compared to the heat transfer and friction forces of a continuous liquid flow cooling system. First, the thermal performance is compared in terms of fundamental non-dimensional numbers. Next, the comparison is applied to a practical test case of a droplet based and continuous flow based heat sink. Finally, the achievable thermal performance of the droplet based cooling system and potential applications are discussed.

6.3.1 Fundamental comparison with continuous flow

The heat transfer in the droplet flow is characterised in terms of dimensionless numbers. The dimensionless number for the droplet velocity is the Reynolds number, using the height of the channel as characteristic length:

$$Re = \frac{UH}{\upsilon} \tag{6.2}$$

where U is the average droplet velocity, H is the channel height and υ is the kinematic viscosity. The dimensionless number for the heat transfer is the Nusselt number, with the height of the channel as characteristic length:

$$Nu = \frac{hH}{k} \tag{6.3}$$

where h is the total heat transfer coefficient in the droplet, and k is the thermal conductivity of the fluid. The heat transfer coefficient h is defined as follows:

$$h = \frac{Q}{A \cdot \Delta T} \tag{6.4}$$

where Q is the heat transfer through the droplet and A is the contact area between the droplet and the wall. Using equations (6.2) and (6.3), the computational results from Chapter 5 can be represented as a function of the dimensionless numbers *Re* and *Nu* and can be compared with continuous flow in a similar configuration. Figure 6.7 shows the dimensionless representation of the steady state heat transfer through a moving droplet (Figure 5.9).

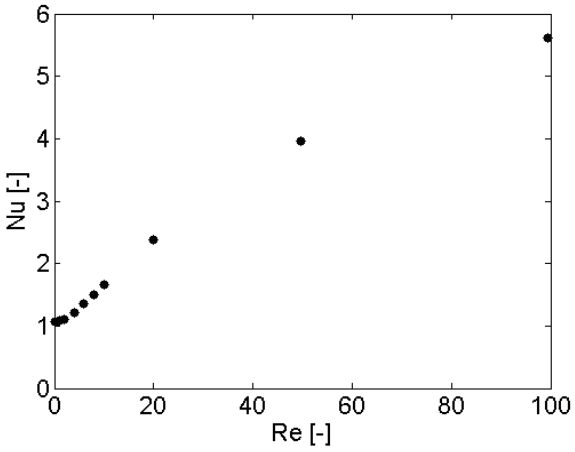

Figure 6.7 Simulation results of the dimensionless steady state heat transfer in the moving droplet as function of the dimensionless droplet velocity.

The considered channel is not sufficiently long to reach steady state conditions. Therefore, a transient analysis is required. In Figure 6.8 and Figure 6.9, the actual dimensionless heat transfer *Nu* and average dimensionless heat transfer $Nu_{0\text{-}t}$ are shown respectively as a function of time for different dimensionless droplet velocities. These figures are the dimensionless representations of the numerical results, presented in Figures 5.13 and 5.16 respectively. From the graph of the average heat transfer $Nu_{0\text{-}t}$ as a function of time, the channel-averaged heat transfer during the stay of the droplet in the channel can be obtained for the different droplet velocities. Figure 6.10 shows the results of the lumped model for the normalised average heat transfer $Nu_{0\text{-}t}$. The lumped model is used to extrapolate the results to 8 s to include the time slowest moving droplet (0.2 cm/s) requires to reach the end of the channel. This is the dimensionless representation of Figure 6.5. The markers on each curve indicate the required time to reach the end of the channel (15 mm).

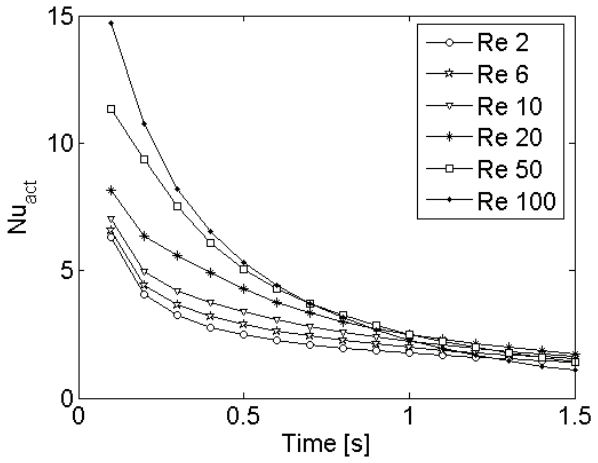

Figure 6.8. Simulation results of the actual Nu number for the heat transfer in the droplets as a function of time, for different values of the Reynolds number.

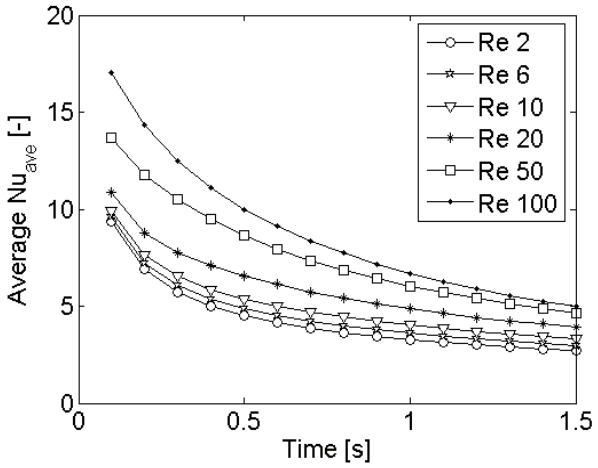

Figure 6.9. Simulation results of the average $Nu_{0\text{-}t}$ number for the heat transfer in the droplets as a function of time, for different values of the Reynolds number.

The heat transfer characteristic of a thermally developing flow is generally shown in terms of the evolution of the Nu number as a function of a normalised distance. To allow comparison of the heat transfer in the droplet flow with the heat transfer for thermally developing continuous flow, the evolution of the average Nu number $Nu_{0\text{-}t}$ in the droplet flow is plotted as function of a dimensionless distance x^*. This dimensionless distance, based on the height of the channel, is defined as follows:

$$x^* = \sqrt{\frac{x / H}{Re_H Pr}} \tag{6.5}$$

where *Pr* is the Prandtl number, which is defined as follows:

$$Pr = \frac{\upsilon}{\alpha} \tag{6.6}$$

where υ is the kinematic viscosity and α is the thermal diffusivity. To convert the transient evolution of the average Nu number $Nu_{0\text{-}t}$ (Figure 6.10), the dimensionless distance x^* can be expressed as a function of time. Using the relation between the droplet velocity *U*, droplet position *x* and the time *t*:

$$x = U \cdot t \tag{6.7}$$

the dimensionless distance can be written as follows:

$$x^* = \sqrt{\frac{\upsilon}{H^2 Pr}}\, t \tag{6.8}$$

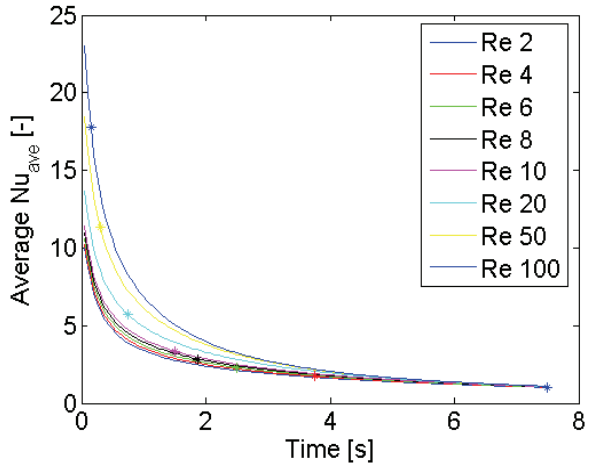

Figure 6.10. Results of the lumped model for the average $Nu_{0\text{-}x^*}$ number for the heat transfer in the droplets as a function of time, for different values of the Reynolds number.

The evolution of the average Nu number $Nu_{0\text{-}x^*}$ as a function of x* is shown in Figure 6.11. This evolution can be compared with the thermal characteristics of thermally developing flow in case of continuous flow. In the cooling channel considered here, the height is 1 mm and the width of the channel is 15 mm, leading to an aspect ratio of 15. The reference flow for comparison can either be approximated by the flow between two parallel plates or by a rectangular channel with an aspect ratio of 15. In both cases, constant temperatures are assumed as boundary conditions. For a parallel plate duct with constant temperature boundary conditions, the Nu number for thermally developed flow is 7.54. For the rectangular channel with a high aspect ratio, correlations can be used (Shah and London 1978) to find the Nu number as a function of the aspect ratio. Since the aspect ratio in this case is high, the difference of the Nu number between the parallel plate duct and rectangular duct is expected to be smaller than 10%. Therefore, in the following

comparison, the thermal performance of the droplet flow will be compared with the thermal behaviour of a continuous flow between parallel plates.

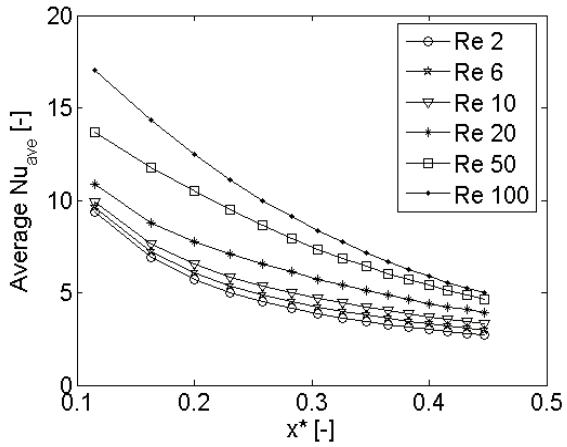

Figure 6.11. Simulation results of the average $Nu_{0\text{-}x^*}$ number for the heat transfer in the droplets as a function of the nondimensional distance x, for different values of the Reynolds number.*

Figure 6.12 shows the thermal characteristics of thermally developing continuous flow in a parallel plate duct (Bejan 2004) in a log-log plot as function of the dimensionless distance x^*. On this graph, the curves of the droplet heat transfer for different droplet velocities are added. From this graph can be seen, that for high droplet velocities, the droplet heat transfer exceeds the continuous flow heat transfer in a parallel plate duct in the case of short channels ($x^* < 0.2$). The vertical lines in Figure 6.12 (bottom) represent the values of x^* corresponding to the end of the channel for different flow velocities. At the intersection of the vertical lines with the respective curves of the Nu number $Nu_{0\text{-}x^*}$, the channel-averaged Nu numbers can be extracted both for the continuous and droplet flow as a function of the flow velocity. Figure 6.13 shows the channel-averaged Nu_L number over the length of the channel for both the continuous flow and the droplet flow. From this graph can be seen, that the dimensionless heat transfer in a droplet exceeds the heat transfer in the continuous flow for Re numbers higher than 30. However, this is the heat transfer in a single droplet. For an actual comparison, the droplet heat transfer needs to be corrected for the number of droplets in the channel and relative droplet size. To include this in the analysis, the droplet filling ratio is introduced.

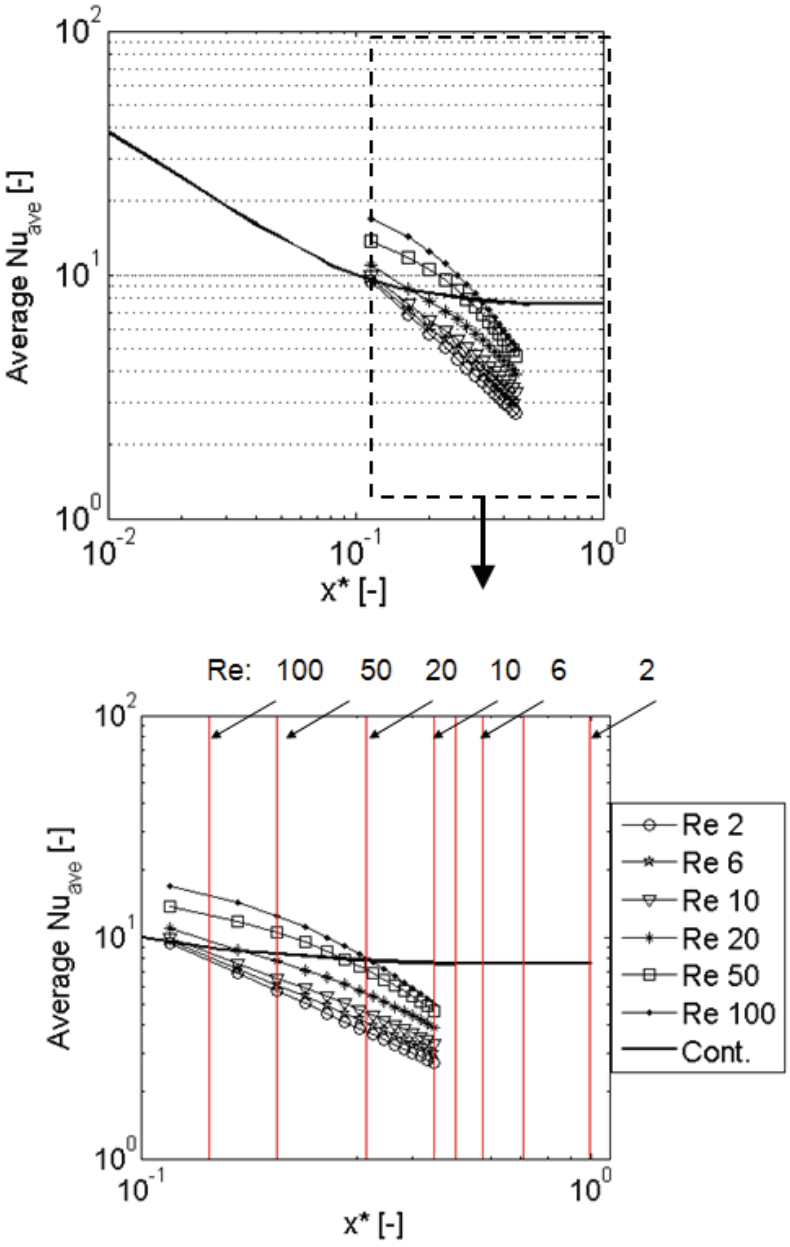

Figure 6.12. Comparison of the average $Nu_{0\text{-}x^*}$ number as function of the dimensionless channel distance for a continuous flow in a parallel plate duct with the heat transfer in a droplet for different droplet velocities (top). Detail of the range of interest for the channel of 15 mm. The vertical lines indicate the dimensionless location of the end of the channel as function of the respective dimensionless flow velocity (bottom).

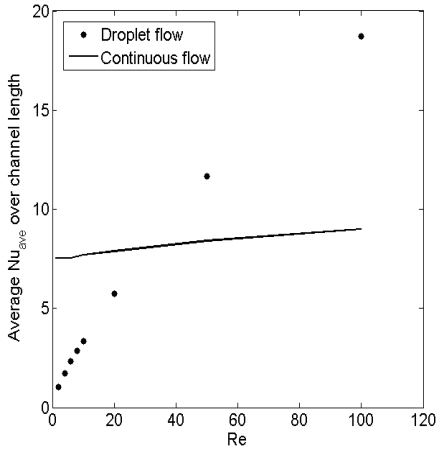

Figure 6.13. Average Nu_L number over the length of the channel (15 mm) for the droplet flow (in a single droplet) and a continuous flow in a parallel plate duct as a function of the dimensionless flow velocity.

Droplet filling ratio

To compare the thermal performance of the droplet based cooling system to the performance of continuous flow, the number and size of the droplets simultanuously present in the channel, need to be taken into account. Consider a channel with an area $A_{channel}$ and N droplets with a contact area $A_{droplet}$. The droplet filling ratio χ can be written as follows:

$$\chi = \frac{N \cdot A_{droplet}}{A_{channel}} \tag{6.9}$$

This ratio will be used to estimate an channel-averaged value of the heat transfer and the friction forces for the droplet flow. In the practical example above, a channel of 15 x15 mm² and droplets with a contact area of 1.78 mm² are considered. The presence of 16 droplets at the same time in the cooling channel corresponds to a droplet filling factor of 12.5%. For 25 droplets, the filling factor is 20%. A conservative estimation of the maximum number of droplets by assuming at least one droplet length between different droplets in both directions leads to of maximum of 25% for the filling fraction. Higher values could be obtained for droplets transported in a staggered checkers board pattern. In the following analysis, the channel-averaged values will be shown for filling ratios of 5, 10 and 20%.

Nu number

Using the filling ratio, the channel-averaged value of the Nu number can be calculated. Consider $Nu_{droplet}$, the average Nu number for a single droplet over the length of the channel, as shown in Figure 6.13. At the regions of the channel where no droplets are

present at a certain time, locally no heat is being removed. The channel-averaged value of the Nu number $Nu_{channel}$ can be expressed as follows:

$$Nu_{Channel} = N \cdot Nu_{droplet} \cdot \frac{A_{droplet}}{A_{channel}} = \chi \cdot Nu_{droplet} \tag{6.10}$$

In Figure 6.14, the channel-average Nu number is shown for droplet filling ratios of 5, 10 and 20% respectively.

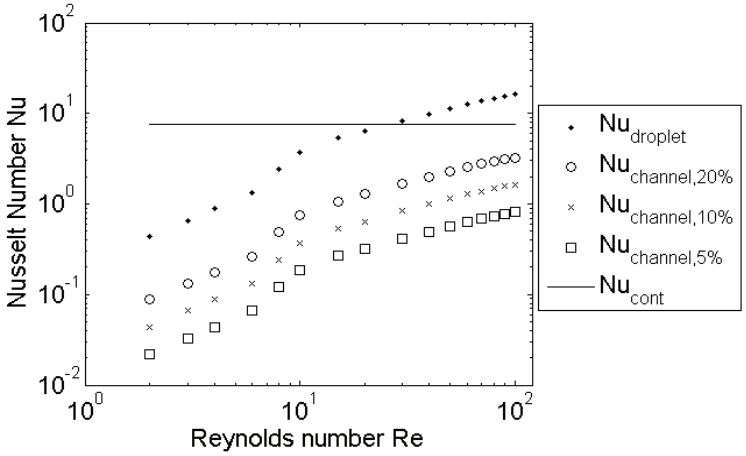

Figure 6.14. Comparison of the channel-averaged $Nu_{channel}$ number of the droplet flow for filling ratios of 5,10 and 20% with the Nu number of a continuous flow in a parallel plate duct as a function of the dimensionless flow velocity.

Friction factor

The friction losses of a flow in a channel can be described dimensionlessly using the Fanning friction factor *f*. The Fanning friction factor *f* is defined as follows

$$f = \frac{F_{tot}}{\frac{1}{2}\rho U^2 A_{contact}} \tag{6.11}$$

where F_{tot} is the total opposing force acting on the liquid and $A_{contact}$ is the contact area between the liquid and the channel. The friction factor should not be confused with the Darcy friction factor which is four times the Fanning factor. In this work when the term 'friction factor' is used, reference is made to the Fanning friction factor. The friction factor can be expressed for a single droplet as follows:

$$f_{droplet} = \frac{F_{tot,droplet}}{\frac{1}{2}\rho U^2 A_{droplet}}. \tag{6.12}$$

The friction factor with respect to the channel with area $A_{channel}$, filled with *N* droplets, can be written as follows:

$$f_{Channel} = \frac{N \cdot F_{tot,droplet}}{\frac{1}{2}\rho U^2 A_{channel}} \tag{6.13}$$

Using the relation between the droplet and channel area from the definition of the filling ratio (6.9)

$$\frac{N}{A_{channel}} = \frac{\chi}{A_{droplet}} \tag{6.14}$$

the expression of the friction factor for the channel (6.13) can be rewritten as follows:

$$f_{Channel} = \frac{N \cdot F_{tot,droplet}}{\frac{1}{2}\rho U^2 A_{channel}} = \chi \cdot f_{droplet} \tag{6.15}$$

The channel-averaged friction factor scales linearly with the droplet filling ratio. The friction factor for a single droplet can be expressed as function of the opposing forces, discussed in Chapter 4. As a result, the friction factor can be written as follows:

$$f_{droplet} = \frac{1}{\frac{1}{2}\rho U^2 A_{contact}} \cdot \left(F_{CL,stat} + F_{CL,dyn} + F_{visc} + F_{drag} \right) \tag{6.16}$$

After substitution of the expressions of the different forces, the friction factor can be written as follows:

$$f_{droplet} = \frac{1}{\frac{1}{2}\rho U^2 A_{contact}} \cdot \left(F_{CL,stat} + 12\mu \frac{U_{av}}{H} \pi R_c^{\,2} + \mu \cdot \frac{a}{2} \cdot H \cdot U_{av} + \zeta U_{av} L \right) \tag{6.17}$$

The contribution of the static contact line friction force to the friction factor scales inversely proportional with the droplet velocity. Plotted in a *log f* versus *log Re* graph, this term will show a *1/Re* behaviour. The contributions of the dynamic contact line friction, the drag force and the viscous flow force to the friction factor scale with the inverse of the second power of the droplet velocity. In the log f versus log Re graph, these term will have a $1/Re^2$ behaviour. Using (6.15), the droplet based friction factor can be converted to a channel based friction factor.

The friction factor of the droplet flow is compared to the factor of a continuous laminar flow in a parallel plate duct with constant temperature boundary conditions. For this case the friction factor is *24/Re*. In Figure 6.15, Fanning friction factor of the droplet based flow is compared to the friction factor of the continuous flow. In the case of the droplet flow, for low Re numbers, the $1/Re^2$ behaviour caused by the constant static contact line friction force can be observed, while for higher Re numbers, the 1/Re behaviour dominates. As illustrated in Chapter 4, the contribution of the contact line forces is larger than the contribution of the viscous flow forces in case of the droplet flow. As a result, the friction factor of the droplet flow is higher than the friction factor of the continuous flow where the friction is only caused by the viscous forces.

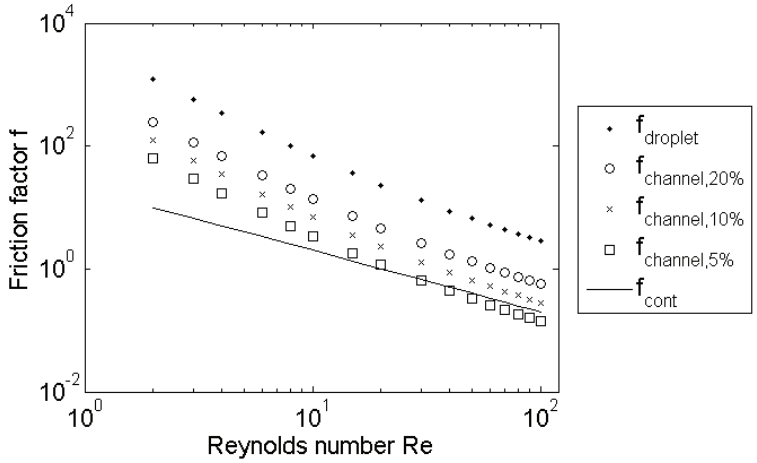

Figure 6.15. Comparison of the channel-averaged Fanning friction factor of the droplet flow for filling ratios of 5, 10 and 20% with the Nu number in a parallel plate duct as a function of the dimensionless flow velocity.

Comparions

Figure 6.14 and Figure 6.15 provide the fundamental comparison between the droplet flow and the continuous flow in a parallel plate duct in terms of heat transfer and friction forces respectively. For a single droplet, the Nu number exceeds the Nu number of the continuous flow for droplet Reynolds numbers higher than 30. At Reynolds number 100, the Nu number of the droplet is twice the Nu number of the continuous flow. The increase in heat transfer in the droplet flow as a function of droplet velocity is caused by the increased convection in the two convection cells in the droplet. At a realistic droplet filling ratio of 20 %, the Nu number of the droplet flow is 50% of the one of the continuous flow for a Reynolds number of 100. For higher droplet velocities, the Nu number of the droplet flow is in the same order as the continuous flow.

The opposing forces in the droplet flow are dominated by the contact line friction force. The contribution of the viscous friction forces is limited to around 30%. In the case of continuous flow, only viscous friction forces are present. As a result, the friction factor of the droplet flow is larger than the one of the continuous flow. Assuming a realistic filling factor of 20%, the channel-averaged friction factor of the droplet flow is twice as high as the friction factor of the continuous flow for a Reynolds number of 100. In the case of the droplet flow, the higher friction forces do not result in a high pressure that needs to be generated by a feeding pump, since the pumping mechanism is integrated in the channel by means of electrodes.

Summarised, can be stated that the cooling and friction forces of the droplet based cooling system are in the same order of magnitude as those of the continuous flow.

6.3.2 Practical comparison with continuous flow

In this section, the droplet flow is compared to continuous flow for a practical test case of a 15x15 mm² cooling channel. The reference case for liquid cooling of electronic components is continuous single-phase liquid flow. The continuous liquid flow is circulated through a microchannel cooler by means of a separate feed pump. Optimisation algorithms are derived for this continuous liquid cooling case (Stevens *et al.* 2006, 2007). Using that approach, the overall thermal performance of the system can be assessed by estimating the total thermal resistance and the required pumping power. In this way, the thermal performance can be compared to the droplet based cooling system.

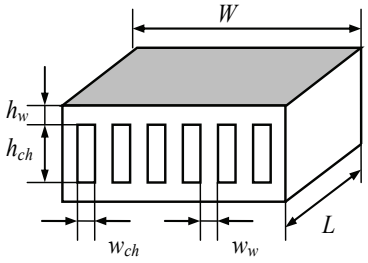

Figure 6.16. Heat sink geometrical design parameters (Stevens et al. 2006).

Thermal performance analysis of a continuous flow

The thermal performance of a single-flow microchannel heat sink is described by Stevens *et al.* (2006, 2007) in terms of the thermal resistance and the required pumping power. For the analysis a microchannel heat sink is considered for the cooling of a 15 mm x 15 mm chip that dissipates a heat flux of 100 W. This heat sink is schematically shown in Figure 6.16. The analysis is reproduced in Appendix D and applied to the range of flow rates typically achieved in droplet based channels.

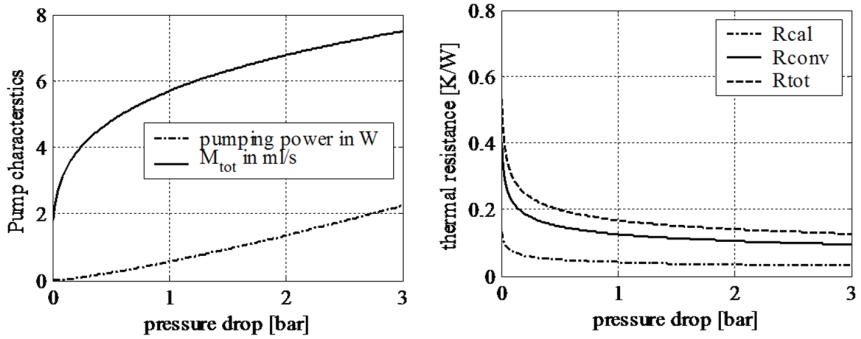

Figure 6.17. Pumping power and total mass flow through the cooler as a function of pressure. Total thermal resistance as a function of pressure drop for square channels (right).

In the analysis, the heat sink parameters are optimised to minimise the overall thermal resistance. This total thermal resistance of the heat sink is the series connection of the caloric and convective thermal resistances. The thermal resistance can be evaluated as a function of the pressure drop. An increase in flow rate leads to a decrease of the thermal resistance, and hence an enhancement of the cooling performance. To increase this flow rate, the pressure needs to be increased. This requires a pumping power W_p.

The left hand side of Figure 6.17 shows the evolution of the flow rate and the required pumping power as a function of the pressure drop. This high power consumption and relatively high pressure drops remain critical issues especially with respect to reliability and control of the cooling system, despite the promise of achieving very low thermal resistances.

Thermal performance comparison

The cooling performance and required pumping power to deliver this cooling are compared for the continuous flow and the droplet based flow. From the analysis above, the pumping power and thermal resistance are known as a function of the pressure drop. Both graphs of Figure 6.17 can be combined, by plotting the pumping power as a function of the equivalent thermal resistance, using the pressure drop or the flow rate as a parameter. This cooling characteristic shows which cooling can be achieved and how much power this requires. In this way, the comparison with the droplet based flow can be made. In that case no external pressure is applied, but the driving power is delivered by the electrodes. This equivalent pumping power can be estimated based on the opposing forces and the droplet velocity. Figure 6.18 shows the cooling characteristic of both systems. The required pumping power is plotted as a function of the inverse of the thermal resistance, i.e. the enhancement of the cooling. From this graph, the additional required pumping power to achieve a desired increase in cooling performance can be read. The solid line indicates the thermal performance of the continuous flow through a 15 x 15 mm² microchannel heat sink with square channels. To compare to the droplet based system, a similar range for the flow rate of several hundreds µl/s is studied.

In the case of the droplet based flow, the mass flow rate depends on the droplet velocity U_{av} and the number of droplets simultaneously present in the cooler, N. The mass flow rate can be written as follows:

$$\dot{M} = N\rho\frac{U_{av}}{L}\cdot Vol \tag{6.18}$$

where L is the length of the channel, and Vol is the droplet volume. The mass flow rate scales linearly with both the droplet velocity and the number of droplets. Using the formulation for the opposing forces, described in Chapter 4, the required pumping power can be expressed as a function of the number of droplets and the average droplet velocity as follows:

$$\begin{aligned} W_p &= N\left(F_{visc}+F_{CL}+F_D\right)\cdot U_{av} \\ &= N\cdot U_{av}\cdot\left(12\mu\frac{U_{av}}{H}\pi R_c^{\,2} - 2.k\gamma_{LV}\,w\left[\cos\left(\theta_R\right)-\cos\left(\theta_A\right)\right]_{\max,static} - \zeta U_{av}L\right) \end{aligned} \tag{6.19}$$

The inverse of the thermal resistance, the thermal conductance G, is a measure for the performance of the cooling system. A higher value of the conductance indicates a better cooling performance. This conductance is also a function of the number of droplets and the droplet velocity:

$$G = \frac{1}{R} = N \cdot \frac{Q_{droplet}}{\Delta T} \tag{6.20}$$

where ΔT is the difference between the inlet temperature of the coolant and the temperature of the hot surface and $Q_{droplet}$ is average cooling for a continuous flow with only a single droplet at the same time in the channel. The relationship between $Q_{droplet}$ and the droplet velocity can be extracted from Figure 6.5 at the position of the markers. The evolution of the average cooling rate with respect to the average droplet velocity is less than linear. This behaviour is plotted in Figure 6.6. From the equations (6.19) and (6.20), it can be seen that both the pumping power and the conductance scale linearly with the number of droplets. Furthermore, the pumping power scales with the second power of the average droplet velocity, whereas the conductance scales less than linearly with the average droplet velocity. The thermal performance characteristics can be plotted in the pumping power versus conductance diagram in Figure 6.18 for different number of droplets (4, 8, 12 and 16 respectively) that are at the same time in the channel. The markers are plotted for droplet velocities ranging from 1 cm/s to 10 cm/s.

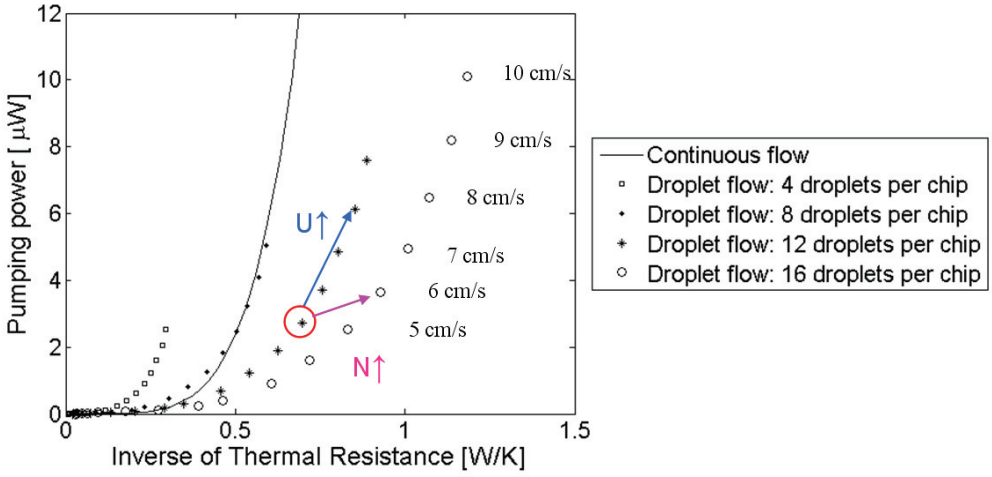

Figure 6.18. Cooling characteristic of the continuous liquid flow and the droplet based flow for several filling rates.

Electrowetting is generally accepted to be a low power consuming actuation technique with reported powers in the order of several µW. This is stated as one of the major advantages compared to other liquid pumping techniques. However, the pumping power for the continuous flow is from the same order of magnitude as the power required for the droplet flow to achieve the same level of cooling. This is illustrated in Figure 6.18. In the case of the continuous flow, the flow rate can only be altered, by changing the velocity of the flow.

However, for the droplet flow, the flow rate depends on the velocity and the number of droplets. Increasing the velocity corresponds to moving upwards on one of the curves for a certain number of droplets on the chip. Increasing the number of droplets, corresponds to moving towards another curve. As an example, to increase the flow rate by 30%, either the velocity or the number of droplets can be increased by 30%. Both changes are indicated in the graph. It is clear that it is better to increase the number of droplets to limit the increase in pumping power. Realising the flow rate increase by increasing the droplet velocity results in a increase in power consumption of 70%. In the case the number of droplets is increased, the power consumption rises by 30%. The number of droplets in the cooler is however limited. Sufficient space between the droplets should be foreseen to avoid coalescence of the droplets.

6.3.3 Cooling performance discussion

Current CPUs typically have an average power dissipation density of 100 W/cm² and this is expected to increase by 70% over the next 8 years (ITRS 2009). For high end applications, the projections for the power dissipation are even twice as high. These power values are much higher than the calculated thermal performance of the droplet based cooler. For the calculation, a conservative estimate is used for the number of droplets at the same time in the cooler, and consequently for the flow rate. By assuming a higher droplet throughput, higher cooling rates can be achieved. Currently, the droplet velocities are limited by the voltage that can be applied. For voltages above a certain value, saturation will occur, and increasing the voltage even more will not lead to higher actuation forces. New developments for electrical insulation materials, might remove this limitation. Nevertheless, the droplet based cooling system will not be suitable to cool these high power applications, mainly due to the low flow rate compared to continuous flow.

Therefore, the targeted applications for the droplet based cooling technique will be low to medium power applications. The droplet based cooling system is capable of cooling several to tens of W, with a power consumption in the order of µW. Due to higher achievable flow rates, the continuous liquid microchannel cooling clearly outperforms the droplet based cooling system with respect to global thermal resistances. Nevertheless, the low energy consumption and the flexibility as a reconfigurable cooling system, make the electro-actuated cooling systems attractive in these applications where the advantages of the droplet based system can be exploited. This is the case for applications with strong non-uniform heat dissipation for which the hot spots vary both in time and space. The droplet cooling allows adaptive cooling of these hot spots by directing droplets towards the locations with a high local power generation.

6.4 Conclusions

In the previous chapters, the electrical, mechanical and thermal aspects have been studied for a single droplet: the electrostatic actuation force to move the droplet (Chapter 3), the opposing contact angle hysteresis related friction force (Chapter 2), the macroscopic droplet motion (Chapter 4) and the internal circulation flow and heat transfer inside the droplet

(Chapter 5). In this chapter a continuous flow of droplets is considered to assess the overall cooling performance of the droplet based cooling system.

The cooling performance of the droplet flow is assessed using the transient lumped model developed in Chapter 5. For the cooling calculation, a channel of 15 x15 mm² is considered. Using the dynamic model from Chapter 4, it is found that droplet velocities up to 10 cm/s can be reached, requiring a realistic switching frequency to allow the voltage generation. Assuming a realistic droplet filling ratio in the channel of less than 20%, a flow rate in the order of 500 µl/s can be achieved, requiring a pumping power in the range of tens of µW. The cooling performance of this droplet flow is 52 W of 23 W/cm². It is found that this is roughly twice as high as the calculated lower limit of the cooling, based on conduction heat transfer only.

Furthermore, the heat transfer and friction forces in the droplet flow have been compared to those of continuous flow in a parallel plate duct in terms of the Nusselt number and Fanning friction factor *f* as function of the Reynolds number. Unlike the continuous flow, the droplet shows a large increase in the Nu number for increasing Reynolds number. For Reynolds numbers higher than 30, the Nu number of the flow in a single droplet exceeds the Nusselt number of the continuous parallel plate flow. For a droplet filling ratio of 20% at a Reynolds number of 100, the channel-averaged Nu number of the droplet flow is around half of the one of the continuous flow. For this droplet flow conditions, the Fanning friction force of the droplet flow is twice as high compared to the continuous flow. This shows that the heat transfer and friction forces for the droplet flow are in the same order as those of the continuous flow.

The droplet cooling allows adaptive cooling of hot spots by directing droplets towards the locations with a high local power generation. Moreover, the required power consumption to actuate the droplets to achieve the flow rates of 500 µl/s amounts to several µW to several tens of µW. Since the flow rate of the droplet based cooling is limited to several hundreds µl/min, the technique will not be suitable to cool high power applications. Nevertheless, the low power consumption and the capability of adaptive hot spot cooling make the droplet based cooling system attractive for low to medium power applications with highly non-uniform power dissipation of several tens of W.

Chapter 7

General conclusions and perspectives

The need for new cooling techniques is driven by the current trends in microelectronics. The continuous miniaturisation and increase in component integration lead to a continuing increase in power dissipation of electronic components. For many applications, the limits of the conventional cooling techniques are nearly reached. Furthermore, the increase in functionality and integration of components leads to strong non-uniform power dissipation. Therefore, there is a need for the development of new cooling techniques, capable of cooling these ever increasing heat fluxes and capable to efficiently deal with hot spots. In this work, a novel cooling technique based on electrostatically actuated liquid droplets is presented. In this system, individual liquid droplets are transported over an array of electrodes. The major advantages of this system over conventional cooling systems are the ability for selective cooling of hot spots and the low power consumption. The main objective of this PhD study is to develop a modelling framework to characterise the droplet motion in a droplet based cooling system and to assess the cooling performance of such a system. The first part of this final chapter summarises the main conclusions and achievements of the work. In the second part, the future perspectives of this research are discussed.

7.1 Conclusions

In this work, a simplified modelling approach to approximate the droplet motion and heat transfer in droplet based cooling systems is presented. The modelling of the electrostatically actuated droplets is decoupled into three separate parts. The first part consists of the electrical analysis. In this part, the actuation force acting on the droplet is determined for a certain application voltage. In the second part – the mechanical analysis – the macroscopic droplet motion is predicted based on the forces acting on the droplet. Finally, the third part describes the internal flow and heat transfer inside the moving droplet and provides an estimate for the thermal performance of an integrated droplet based cooling system.

7.1.1 Conclusions for the electrical analysis

In **Chapter 3**, the application of an external electric field in order to deform or move a liquid droplet has been investigated. The droplet deformation under a symmetric electric field has been studied experimentally, both on a flat surface as well on a rough surface. For a droplet on a surface with structured roughness, a morphological transition between two meta-stable states occurs when a voltage is applied. Theoretical transition criteria, derived from energy considerations, correspond well to the experimental contact angle data before and after the transition. For the case of a non-symmetric application of the voltage, the electrostatic actuation force has been studied numerically (FEM) using a quasi static approach. A methodology has been developed to calculate the actuation force from these quasi static electrostatic simulations, both for dielectric and conductive liquids. Formulations for the actuation force are derived both from a force approach (method of Maxwell stresses) as well as an energy approach (method of virtual work). The results of both methods for a 2D finite element simulation are compared to the energy method for 3D simulations. It is shown that the 2D approach can be used to predict the average force during the droplet motion instead of the 3D time consuming simulation. However, both the Maxwell stress method and the energy method in 2D lead to large overestimates of the force calculations, at the positions where the liquid interface crosses an edge of the electrode.

The force calculation methodology has been applied to perform a parameter study for both the planar electrode system as well as the cylindrical channel with annular electrodes to assess the impact of material properties and geometrical parameters on the actuation force. In the case of a conductive liquid, the actuation force acting on the droplet is much higher compared to a dielectric droplet; for a dielectric droplet with a permittivity ε_R of 81, the difference is a factor of 10. As a result, in the case of conductive droplets, a voltage of roughly a factor 3 lower can be used compared to a dielectric liquid with $\varepsilon_R = 81$ to realise the same force. Furthermore, the parameter study reveals the thickness of the insulation should be as low as possible and the dielectric constant as high as possible to achieve a maximum actuation force. The minimum thickness of the insulation is however limited by dielectric breakdown which results in an optimum thickness and corresponding optimum operation voltage. For a constant droplet volume, the actuation force increases with decreasing channel height. However, the increase in actuation force can be attributed to the increase in droplet diameter (due to the constant volume constraint) and not to the decrease in channel height.

7.1.2 Conclusions for the mechanical analysis

In the mechanical analysis, the droplet motion has been modelled based on the force balance of all the forces acting on the droplet. The actuation force investigated in Chapter 3 is the driving force for this droplet motion. The opposing forces include the contact line friction force, the shear force and the drag force from the host medium. In **Chapter 2**, empirical models have been derived for the static and dynamic contact line friction force. This contact line force acts as a threshold for droplet motion. When an external force is

applied on a droplet, this force needs to be sufficiently high to overcome this threshold, caused by the contact angle hysteresis. This force has been studied experimentally by performing contact angle measurements during the droplet deformation and motion in tilt tests. These experiments provide insight in both the static and the dynamic droplet behaviour on the surface of interest. For this purpose, a dedicated test fixture is developed to study confined droplets between two parallel surfaces. Empirical correlations are derived for sessile and confined droplets sliding on Teflon coated surfaces. These correlations relate the maximum retentive force to the droplet volume, the equilibrium contact angle, the height of the channel and the maximum contact angle hysteresis. The tilt tests can only be performed for droplet volumes larger than 3 µl. Smaller droplets remain attached to the Teflon coated surfaces, even when placed vertically. For these droplets, the retentive force exceeds the gravitational force. The derived empirical correlations allow extrapolating the measurement data of the retentive force for droplets in the range of 3 to 25 µl, to an equivalent threshold force for droplet volumes in the range used in microfluidic applications.

Furthermore, the effect of roughness on the retentive force is investigated. The analytic 1D roughness model of Johnson & Dettre (1964) predicts an increase of both the static contact angle and the contact angle hysteresis for increasing surface roughness. The increased static contact angle leads to a reduction of the retentive force, whereas an increasing hysteresis results in a higher retentive force. The relative importance of both effects will determine whether the increasing roughness reduces or increases the retentive force. First, the effect of the surface roughness on Teflon coated mechanically roughened surfaces was investigated. For these samples, increasing roughness leads to a higher retentive force due to the dominant increase in hysteresis. However, no conclusive empirical relation could be determined for the roughness effect due to the large variation of the contact angle measurements. The most important factor to reduce the retentive force is to reduce the contact angle hysteresis. A very static contact angle is not sufficient. In the case of silanised structured surfaces high static contact angles in the range of 150° to 160° were observed. Nevertheless, a drastically increased hysteresis resulted in an increased retentive force. A very low hysteresis (below the limits of detection) was observed in the case of a black silicon surface. On this surface, a very low retentive force was observed.

A general methodology for the dynamic modelling of the macroscopic electro-actuated droplet motion has been presented in **Chapter 4**. In this simplified model, the droplet is considered to be a single mass. Algebraic formulations are provided for the opposing forces acting on the droplet. This model uses the simulation results from Chapter 3 for the electrostatic force, and the derived empirical models of Chapter 2 for the contact line friction force as input. Using the information of the voltage switching on the electrodes, the static results for the electrostatic force are converted to time dependent data. A time stepping approach has been implemented to find the transient droplet position and velocity as a solution of the dynamic model. This dynamic model has been applied to the planar electrode system and the annular electrode system. First, the dynamic droplet response to the activation of a single electrode is calculated. Depending on the level of the opposing forces and the actuation voltage, oscillating behaviour might be observed. For higher voltages, more pronounced oscillations are observed. Next, the methodology is applied to an array of electrodes. The voltage is switched subsequently from one electrode to the next. For each actuation voltage, a maximum switching frequency is found that the droplet will be able to follow. For higher frequencies, the droplet will not reach the next electrode

before the voltage is switched. The maximal switching frequency can be approximated by twice the natural frequency of the linearised damped mass – spring system. Therefore, the linearised model can be used for the development of control strategies to optimise the switching of the electrodes. Using an optimised switching frequency, the dynamic model predicts droplet velocities in the range of 5 to 10 cm/s for a voltage range from 30 to 80 V. For this velocity, a switching frequency of 75 Hz is required. This is a feasible frequency considering the required time for the voltage build-up. For the parallel plate electrode configuration, the methodology of the dynamic model is successfully validated using experimental data on average droplet velocities in literature (Ren *et al.* 2002).

In the case of the annular electrode system, the force profile is complicated with multiple instances with zero forces. As a result, droplet position after actuation over an electrode is difficult to predict. Indeed, small changes in input parameters can lead to a large variation in the prediction of the position after the application of the voltage. For this case, a robust switching scheme is derived to ensure continuous droplet motion from one electrode to the next.

7.1.3 Conclusions for the thermal and flow analysis

Based on the achieved macroscopic droplet velocities in Chapter 4, the flow patterns and heat transfer inside a moving droplet between two parallel plates have been assessed in **Chapter 5** by means of detailed two dimensional numerical flow calculations (CFD). The simulations reveal the parabolic characteristic of the internal flow. Furthermore, two convection cells can be observed in the moving droplet. The presence of these cells has a large impact on the heat transfer in the droplet. Inside these cells, the heat is transferred by means of convection. This part of the heat transfer clearly benefits from an increased droplet velocity. However, the heat transfer from one cell to the other is limited by conduction. This limits the gain in total heat transfer. As a result, the overall heat transfer does not increase as much as expected by the increased internal convection. Nevertheless, at a velocity of 10 cm/s, a typical enhancement of the heat transfer in steady state conditions with a factor 5 is achieved with respect to the minimal value that would be obtained assuming heat conduction in the liquid only. For short channels, the temperature distribution in the droplet will not reach the steady state condition. For a very short channel of 15 mm, the heat transfer is enhanced by a factor 2 at a velocity of 10 cm/s.

Furthermore, an analytic four cell lumped model has been developed to predict the droplet temperature. The parameters for the lumped model are extracted from steady state numerical simulations (CFD). Using these parameters, the transient average droplet temperature can be estimated with the lumped model. The difference between the results of the lumped model and the full transient CFD modelling is less than 5%. In this way, only one time-consuming detailed simulation is required instead of performing these simulations at each time step of the transient droplet motion.

In **Chapter 6**, the thermal performance of droplet based cooling systems has been assessed. The thermal performance of the parallel electrode system is studied using the transient lumped droplet temperature model, derived in Chapter 5. For the cooling calculation, a channel of 15 x15 mm² is considered. Using the dynamic model from Chapter 4, it is found that droplet velocities up to 10 cm/s can be reached, requiring a realistic switching

frequency to allow the voltage generation. Assuming a realistic droplet filling ratio in the channel of less than 20%, a flow rate in the order of 500 µl/s can be achieved, requiring a pumping power in the range of tens of µW. The cooling performance of this droplet flow is 52 W of 23 W/cm². It is found that this is roughly twice as high as the calculated lower limit of the cooling, based on conduction heat transfer only. Next, the pumping power and equivalent thermal resistance of the electro-actuated system are compared to those of a continuous flow microchannel cooler. High pressure drops are often stated to be the main drawback pressure driven microchannel flow. However, this is for much higher flow rates than those achieved in the droplet based system. When extrapolated to the flow rate range of the droplet based system, it is shown that the pumping power for the continuous flow, delivered by the external pump, is comparable to the power required to transport the droplets. In both cases this power amounts to several µW. For a fundamental comparison, the heat transfer and friction forces in the droplet flow have been compared to those of continuous flow in a parallel plate duct in terms of the Nusselt number and Fanning friction factor *f* as function of the Reynolds number. Unlike the continuous flow, the droplet shows a large increase in the Nu number for increasing Reynolds number. For Reynolds numbers higher than 30, the Nu number of the flow in a droplet single droplet exceeds the Nusselt number of the continuous parallel plate flow. For a droplet filling ratio of 20% at a Reynolds number of 100, the channel-averaged Nu number of the droplet flow is around half of the one of the continuous flow. For this droplet flow conditions, the Fanning friction force of the droplet flow is twice as high compared to the continuous flow. This shows that the heat transfer and friction forces for the droplet flow are in the same order as those of the continuous flow.

The results of the thermal analysis of the planar droplet based cooling system indicate that the droplet based cooling system is not suitable to cool high power applications. This is mainly due to the low flow rate in the cooler: the flow rate of the droplet based cooling is limited to several hundreds µl/min. New developments in the material research of the insulation coating might result in higher droplet velocities and a higher flow rate. However, this still will not allow this planar droplet based cooling system to compete with the continuous liquid microchannel cooling in terms of heat removal rates. Therefore, the technique will not be suitable to cool high power applications. Nevertheless, the low energy consumption and the flexibility for reconfigurable hot spot cooling, make the droplet based cooling system an attractive cooling option. The cooling performance is in the range of several to tens of W/cm², while the power consumption is only in the order of µW. Therefore, the targeted applications for the proposed cooling technique are low to medium power systems with a highly non-uniform power dissipation of several tens of W.

7.2 Future perspectives

In this work the thermal performance of a droplet based cooling has been assessed using several assumptions and simplifications. This allows providing an estimate of the droplet motion and thermal behaviour. However, to be able to accurately predict the cooling performance and the droplet motion, further research is needed. In following paragraphs some recommendations for future research for both the modelling of the cooling system as well as the development and integration of the actual system are presented.

Numerical analysis

The numerical approach, presented in this work, includes many assumptions, including the decoupling and the assumption of a fixed droplet shape. However, the electrowetting principle is based on droplet deformation and the induced contact angle change. For a more accurate prediction of the droplet behaviour, the droplet deformation should be considered under the influence of the external electrical field, the interfacial tension and pressure of the internal fluid motion. All these phenomena should be included to accurately track the moving boundary of the droplet using a free surface flow approach. To implement the free surface flow, several methods could be used including the Volume-of-Fluid (VOF) method (Walker and Shapiro 2006; Mohseni and Baird 2007) and the level-set method (Cahill *et al.* 2008). This should be combined with a description of the pinning force on each point of the contact line to accurately predict the actual threshold behaviour.

To improve the results of the dynamic and thermal modelling, the temperature dependency of the material properties can be included. These dependencies can either facilitate or deteriorate the droplet motion and thermal performance, compared to the case with constant material properties. As an example, both the surface tension and the viscosity of the liquid decrease with increasing temperature. Due to the change in surface tension properties, a droplet on a hydrophobic surface is attracted to a hot region (thermo-capillary effect). This has a beneficial effect on the cooling of hot spots, since the droplets will be assisted to move into the direction of the hot spot by the capillary effect. The decrease in viscosity at elevated temperatures will result in higher droplet velocities for the same actuation voltage.

The detailed 2D thermal analysis in this work is limited to the boundaries of the droplet, with fixed temperature or heat flux boundary conditions imposed on these boundaries. Although, the 2D approach captures the most important internal flow features, the thermal effect of everything outside the droplet is not taken into account. For a more integrated thermal analysis, the rest of the cooling channel, the chip and the packaging should be included, considering the actual power dissipation in the chip. A conjugated heat transfer analysis in 3D will reveal more information on the lateral and vertical heat spreading in the chip and the package and the effect of the droplet cooling on the chip temperature.

Development of the cooling system

First, the thermal modelling results need to be experimentally validated. This could be realised using a test chip with integrated heaters and multiple temperature sensors. The integrated heaters mimic the heat dissipation in an actual electronic component device. With the temperature sensors, the effect of the droplet flow on the temperature distribution of the heat generating component can be assessed. Alternatively, the temperature of the liquid droplets leaving the cooler can be measured to estimate the average cooling performance of the droplet flow.

To implement the different cooling strategies for efficient hot spot cooling, a feedback control needs to be defined. This control can partially rely on passive actions, such as the thermo-capillary effect to induce more droplet flow towards the hot regions. The active feed back control will be based on temperature measurements in sensors integrated in the cooling system. Based on the temperature difference between the targeted operation

temperature and the actual temperature measurement, the control of the electrodes will be adapted to change the trajectory of the droplet flow(s).

The heat removal rate of the droplet based cooling system is mainly limited by the achievable flow rates in the system. The droplet velocities are limited by the voltage that can be applied to induce the contact angle change. For voltages above a certain value, saturation will occur, and increasing the voltage even more will not lead to higher actuation forces. New developments for electrical insulation materials, might remove this limitation or at least increase the droplet velocities. Research is currently ongoing for insulating materials with higher dielectric constants and materials that could be processed in very thin layers, such as mono-layer coatings. Both trends will result in a decrease of the required voltage to induce a certain contact angle change.

To increase the thermal performance of the cooling system, evaporation in the cooling channel can be considered. By allowing the liquid droplets to evaporate, advantage could be taken of the high latent heat during the phase transition. However, the vacuum could not be actuated by the external electric field to be removed from the channel. This would require a pressure difference to evacuate the vapour from the channel. This pressure difference can be induced by the evaporation or it can be externally applied.

Appendix A: Analytical droplet shape formulations

In this appendix, analytical formulae are provided to describe the droplet shape. In the first section, the droplet volume of a spherical sessile droplet is described as function of the radius and contact angle. The second section describes the volume of a droplet confined between two parallel plates. In the final section, correlations available in literature are listed to estimate the contact angle of a droplet based on the surface tension γ_{LV} of the liquid and the critical surface tension γ_C .

Appendix A.1: Calculation of the droplet volume of a sessile droplet

In this appendix the volume of a sessile droplet is estimated. For the calculation, the droplet is assumed to be a spherical cap. Therefore the droplet can be described as a truncated sphere.

Definition of the parameters

R	radius of the spherical cap
R_c	radius of the contact line
θ	contact angle
h	height of the centre of the sphere
h_2	height of the spherical segment 'below the surface'

Schematic

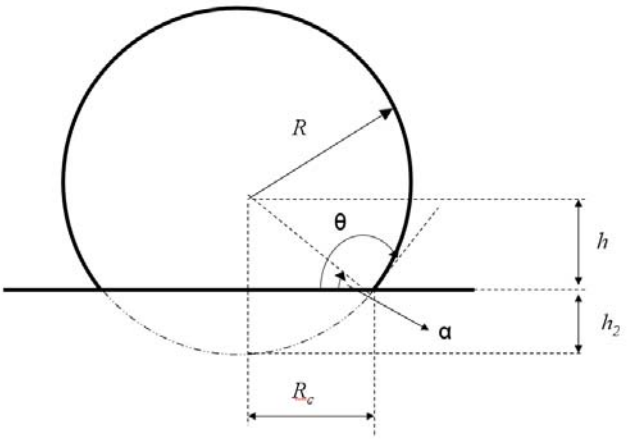

Figure A.1 Schematic cross section of the sessile droplet.

Volume calculation

The volume of the truncated sphere is found by subtracting the volume of the spherical segment V_{segm} from the volume of the sphere :

$$V_{droplet} = V_{sphere} - V_{segment} . \tag{A.1}$$

The volume of the sphere can be expressed as function of the radius :

$$V_{sphere} = \frac{4}{3}\pi R^3 . \tag{A.2}$$

The volume of the segment can be expressed as function of the radius R and the height h_2 :

$$V_{segment} = \pi h_2^2 \left(R - \frac{1}{3} h_2 \right). \tag{A.3}$$

The height h can be written as function of the radius and the contact angle :

$$h_2 = R\left(1 + \cos\theta\right) \tag{A.4}$$

Substitution of (A.4) in (A.3) leads to following expression for the volume of the segment :

$$\begin{aligned} V_{segment} &= \pi R^3 \left(1+\cos\theta\right)^2 \left(1 - 1/3 \cdot \left(1+\cos\theta\right)\right); \\ V_{segment} &= \frac{1}{3}\pi R^3 \left(3\cos\theta - \cos^3\theta - 2\right). \end{aligned} \tag{A.5}$$

The volume of the droplet can be found by combining (A.5) and (A.2) into (A.1) :

$$V_{droplet} = \frac{\pi R^3}{3}\left(\cos^3\theta - 3\cos\theta + 2\right). \tag{A.6}$$

Contact line radius

For a certain droplet with a given volume Vol and a specified contact angle, the droplet radius can be calculated as follows :

$$R = \sqrt[3]{\frac{3 \cdot Vol}{\pi\left(\cos^3\theta - 3\cos\theta + 2\right)}} . \tag{A.7}$$

The radius of the contact line can be expressed as follows :

$$R_c = R\cos\left(\theta - \pi/2\right), \tag{A.8}$$

and the length of the contact line is

$$L = 2\pi R\cos\left(\theta - \pi/2\right). \tag{A.9}$$

Appendix A.2: Volume of a confined droplet

In this appendix two approximations are discussed to calculate the volume of a confined droplet. For the volume calculation, the droplet is assumed to be a revolution body created by the revolution of a circular arc around a central axis. For this simplified geometry, the volume can be expressed as function of the height of the channel, radius of the contact line and the contact angle.

Schematic

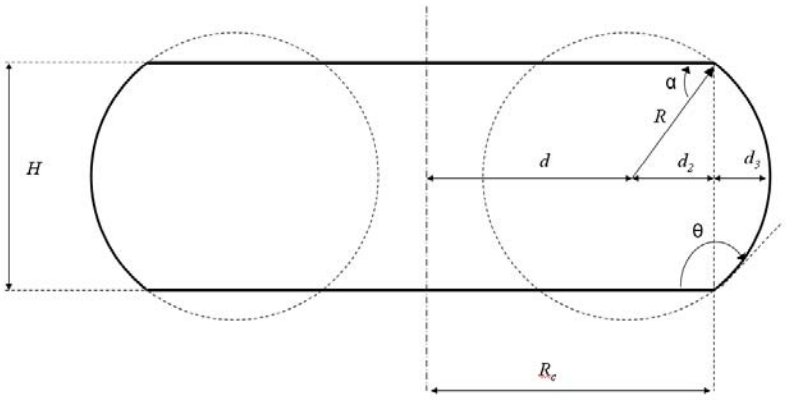

Figure A.2. Schematic cross section of the confined droplet.

Definition of the parameters

R	radius of the circular profile
R_c	radius of the contact line
θ	contact angle
H	height of the channel
d_1	distance between the centre of the circular profile and the revolution axis
d_2	distance
d_3	distance
α	$\theta - \pi/2$

Method 1: Volume of revolution body

The volume is described in the coordinate system (r, z, θ). The height of the channel H and the distance d_2 can be related to the radius of the droplet profile and the contact angle:

$$H = 2R\cos\theta \tag{A.10}$$

$$d_2 = -R\sin\theta \tag{A.11}$$

The position of the centre of circular profile can be written as follows:

$$\begin{aligned} d &= R_c + R\sin\theta \\ d &= R_c + \frac{H}{2}\tan\theta \end{aligned} \quad . \tag{A.12}$$

This circular profile can be expressed as function of the height *z:*

$$(r-d)^2 = R^2 - z^2 \tag{A.13}$$

$$r = \pm\sqrt{R^2 - z^2} + d \ . \tag{A.14}$$

The volume of the droplet can be obtained by integration of an infinitesimal volume *dVol*

$$dVol = r \cdot dr \cdot dz \cdot d\theta \tag{A.15}$$

using following boundaries :

$$\begin{aligned} \theta: &\quad 0 \to 2\pi \\ r: &\quad 0 \to \sqrt{R^2 - z^2} + d \\ z: &\quad -H/2 \to H/2 \end{aligned} \tag{A.16}$$

This leads to following integral for the volume:

$$Vol = \int_0^{2\pi} \int_0^{\sqrt{R^2-z^2}+d} \int_{-H/2}^{H/2} r \cdot dz \cdot dr \cdot d\theta \tag{A.17}$$

As a result, the droplet volume can be described as function of the height of the channel, radius of the contact line and the contact angle:

$$Vol = \pi\left(HR_c^{\,2} + \frac{R_c H^2}{2\cos^2\theta} + \frac{H^3}{4\cos^2\theta}(1+\alpha) \right) \tag{A.18}$$

A similar formulation can be derived for different contact angles at the top and bottom wall of the channel.

Method 2: Volume approximation

The volume of the droplet can be approximated by the summation of the volume of a cylinder with radius R_c and the revolution body of an additional circle segment. The area of this circle segment in the cross section is the difference between the area of the circle sector and the area of the enclosed triangle :

$$A_{segment} = A_{\text{sector}} - A_{\Delta} \tag{A.19}$$

with

$$A_{\text{sec}tor} = \left(\frac{\alpha}{2} \right) R^2 \tag{A.20}$$

$$A_{\Delta} = \frac{1}{2} d_2 H = -\frac{R^2}{2} \sin 2\alpha \,. \tag{A.21}$$

This leads to the expression of the area of the circle segment:

$$A_{segment} = A_{\text{sector}} - A_{\Delta} = \frac{R^2}{2} \left(2\alpha + \sin 2\alpha \right). \tag{A.22}$$

The additional volume is found by revolving this segment around the central axis. The radius of revolution is the distance between the central axis and the centre of gravity of the segment. For confined droplets where the length of the droplet is much longer than the height of the channel, this distance can be approximated by the contact line radius R_c:

$$Vol = \pi R_c^2 H + A_{segment} \cdot 2\pi R_c \tag{A.23}$$

By substitution of the expression of the profile radius:

$$R = \frac{H}{2\cos\theta}, \tag{A.24}$$

the volume can be expressed as function of the height of the channel, radius of the contact line and the contact angle

$$Vol = \pi R_c^2 H + \left(\frac{H}{2\cos\theta} \right)^2 \left(2\alpha + \sin 2\alpha \right) \cdot 2\pi R_c \tag{A.25}$$

$$Vol = \pi R_c^2 H + \frac{\pi R_c H^2}{\cos^2\theta} \left(\alpha + \frac{\sin 2\alpha}{2} \right) \tag{A.26}$$

Appendix A.3: Contact angle correlations

Important information about the surface tension and forces acting on a droplet can be extracted from the shape of the droplet. On a flat surface the droplet shape is described by the contact angle and the droplet volume. The contact angle is dependent on the surface tension γ_{LV} of the liquid , the critical surface tension γ_C of the solid and the surface roughness of the solid. The shape of the droplet, characterised by its contact angle represents the situation of minimal free energy.

A droplet on a flat ideal surface can be considered axisymmetric. Therefore, the shape of the droplet is described by the volume and the contact angle. The contact angle of a droplet on a flat substrate can be predicted based on the thermodynamical properties of the liquid and the solid. Both from the mechanical equilibrium of the components of the surface tensional forces and from the minimisation of total free energy, can the contact angle be found as follows:

$$\gamma_{LV}\cos\theta = \gamma_{SV} - \gamma_{SL}. \tag{A.27}$$

From this parameters, the surface tension γ_{LV} and contact angle θ can be measured but the surface tensional components γ_{SL} and γ_{SV} are unknown. They can be estimated using correlations in function of known material properties. The contact angle is assumed to depend on the surface tension of the liquid and on the critical surface tension of the solid:

$$\cos(\theta) = f(\gamma_L, \gamma_S) \tag{A.28}$$

where γ_{L} is the surface tension of liquid and γ_{S} the critical surface tension of solid. Here the assumptions are made that the equilibrium pressure can be neglected. This means that the adsorption at solid-vapour or liquid-vapour interface is negligible or:

$$\begin{aligned} \gamma_{\mathrm{SV}} &\simeq \gamma_{\mathrm{S}} \\ \gamma_{\mathrm{LV}} &\simeq \gamma_{\mathrm{L}} \end{aligned} \tag{A.29}$$

Therefore, the equation of the contact angle can be written as follows:

$$\gamma_L\cos\theta = \gamma_S - \gamma_{SL} \tag{A.30}$$

To evaluate the contact angle, knowledge of $\gamma_{\mathrm{SL\ is}}$ needed. Different correlations can be found in literature.

a) Zisman approach

Based on his definition of the critical surface tension of solids, Zisman proposed a linear relation for a series of homologous series of liquids on the same solid:

$$\cos(\theta) = 1 - b(\gamma_L - \gamma_S) \tag{A.31}$$

b) Equation of state

Through the thermodynamic equation of state, the unknown property γ_{SL} is assumed to be a function of the known properties γ_S and γ_L:

$$\gamma_{SL} = f(\gamma_S, \gamma_L) \tag{A.32}$$

This function is found to be (Sharma and Hanumantha 2002)

$$\gamma_{SL} = \gamma_L + \gamma_S - 2\sqrt{\gamma_S\gamma_L}\cdot\exp\left[-\beta(\gamma_L - \gamma_S)^2\right] \tag{A.33}$$

with

$$\beta = 0{,}0001247\left[\frac{m^2}{mJ}\right]^2 \tag{A.34}$$

as a parameter. Using equation (A.27) the state equation (A.33) can be rewritten into a contact angle as follows:

$$\cos(\theta) = -1 + 2\sqrt{\frac{\gamma_S}{\gamma_L}} \cdot \exp\left[-\beta\left(\gamma_L - \gamma_S\right)^2\right] \tag{A.35}$$

c) Good-Girifalco equation

Using the free energy of adhesion and the free energy of cohesion Good and Girifalco obtained following relation for the contact angle (Sharma and Hanumantha 2002) :

$$\cos(\theta) = -1 + 2\phi\sqrt{\frac{\gamma_S}{\gamma_L}} \tag{A.36}$$

where ϕ is the interaction parameter. This parameter is 1 for 'regular' interfaces, i.e. systems for which the cohesive forces of the two phases and the adhesive forces across the interface are of the same type. ϕ is lower than 1 when the predominant forces within the separate phases are unlike, e.g. London-van der Waals vs. metallic or ionic or dipolar.

Applied for a water droplet on a Teflon coated substrate with following properties:

Water: γ_L = 72.8 mN/m

Teflon: γ_S = 18 mN/m

The contact angle for a water droplet on a Teflon surface is 108°.

Appendix B: Surface roughness model for an idealised rough surface

To study the effect of the roughness on both the apparent contact angle and the contact angle hysteresis, Johnson and Dettre (1964) presented an analytical axisymmetric model for contact angle hysteresis on a idealised surface; the profile of the rough solid is assumed to be sinusoidal. The idealised surface is schematically represented in Figure B.1. In this graph, θ is the Young's contact angle: this is the intrinsic contact angle between the liquid droplet and the horizontal flat surface on which the droplet is placed. ϕ is the apparent contact angle and α is the slope of surface locally at the contact line. With this formulation the apparent contact angle and the range of the contact angle can be predicted as function of the normalised roughness z_0/x_0, where z_0 is the height of the ridge of the rough surface and x_0 is the period of the sinusoidal surface.

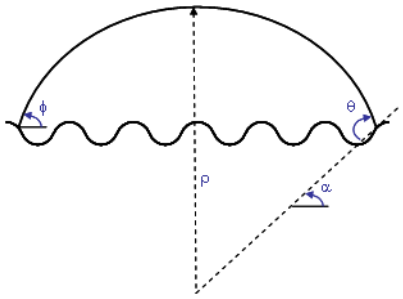

Figure B.1. Schematic representation of the 1D model of a droplet on a rough surface (Johnson and Dettre 1964).

Appendix B.1 Johnson and Dettre model description

The profile *z(x)* can be described as follows:

$$z = z_0\left(1+\cos\frac{2\pi x}{x_0}\right). \tag{B.37}$$

The relation between the intrinsic contact angle, apparent contact angle and slope of surface can be written as:

$$\phi = \theta + \alpha\,. \tag{B.38}$$

The slope of the rough surface is the derivative of the profile of the surface:

$$\tan\alpha = -\frac{dz}{dx}\,. \tag{B.39}$$

By taking the arc tan of the slope the angle of the surface can be found:

$$\alpha = \tan^{-1}\left(\frac{2\pi z_0}{x_0}\sin\frac{2\pi x}{x_0}\right). \tag{B.40}$$

A minimum and maximum value for this slope angle are:

$$\alpha_{\max} = \alpha_{\min} = \tan^{-1}\frac{2\pi z_0}{x_0}. \tag{B.41}$$

The ratio z_0/x_0 is a normalised measure of the surface roughness. The apparent contact angle is related to the slope of the surface by equation (B.38). This leads to following expression for the contact angle hysteresis:

$$\begin{aligned}\phi_{\min} &= \theta - \alpha_{\min}\\ \phi_{\max} &= \theta + \alpha_{\max}\end{aligned}. \tag{B.42}$$

The apparent contact angle ϕ of the droplet on the rough surface will be in the interval $[\phi_{\min}, \phi_{\max}]$. From equations (B.41) and (B.42), it can be seen that the range of potential contact angles increases with increasing surface roughness z_0/x_0. The calculation of the equilibrium contact angle is based on the minimisation of the total free energy of the surfaces. The total free energy of the surfaces can be written as follows :

$$E_{rel} = \Omega_{LV} - \Omega_{SL}\cos\theta \tag{B.43}$$

where Ω_{LV} and Ω_{SL} are the area of the liquid-vapour and solid-vapour interface respectively. If the shape of the droplet is assumed to be a spherical cap, the area of the liquid-vapour interface Ω_{LV} can be written as follows:

$$\Omega_{lv} = \frac{2\pi\rho^2}{1+\cos\phi} \tag{B.44}$$

where ρ is the radius of the spherical cap. Let A_{SL} be the projection of the profile of the solid surface on the horizontal plane. The ratio r between the surface area of the droplet and the projection A of the solid surface on horizontal plane can be written as follows :

$$r = \frac{\Omega_{sl}}{A_{sl}}. \tag{B.45}$$

Therefore the surface area can be written as :

$$\Omega_{sl} = rA_{sl} = r\pi\rho^2. \tag{B.46}$$

Substitution of equation (B.46) into equation (B.43) leads to following expression for the free surface area E_{rel}:

$$E_{rel} = \frac{2\pi\rho^2}{1+\cos\phi} - \pi r\rho^2\cos\theta \tag{B.47}$$

For a droplet with a given volume Vol, an intrinsic contact angle θ, and a roughness z_0/x_0, the relative surface free energy can be calculated for the range of potential apparent contact

angles ϕ. The apparent contact angle that corresponds to the lowest relative surface free energy, is the most likely contact angle to appear.

Appendix B.2 Solution strategy

To find the apparent contact angle ϕ in the interval $[\phi_{\min}, \phi_{\max}]$, which corresponds to the lowest energy state, equation (B.47) has to be evaluated. First, the radius of the spherical cap is calculated. The volume *Vol* of the sessile droplet between the spherical cap and the rough surface can be expressed as function of the radius ρ and the normalised surface roughness z_0/x_0 as follows:

$$Vol = 1/3\pi\rho^2\left(\frac{\cos^3\phi - 3\cos\phi + 2}{\sin^3\phi}\right) + z_0\left(\pi\rho^2 - \frac{x_0^2}{\pi}\right)\cos\frac{2\pi\rho}{x_0} - x_0 z_0\rho\left(\sin\frac{2\pi\rho}{x_0}\right) + \frac{x_0^2 z_0}{2\pi} \quad \text{(B.48)}$$

This equation can be solved numerically for ρ. An iterative procedure is used to find the value of ρ. An appropriate starting point for the iteration is the radius of the droplet with the same volume on a flat surface (see Appendix A).

Once the radius ρ is found, the surface ratio *r* (B.45) can be calculated. The area of the solid-liquid interface can be expressed as follows :

$$\Omega_{sl} = \int_0^{\rho} 2\pi x\left[1 + \left(\frac{\partial z}{\partial x}\right)^2\right]^{1/2} dx \,. \quad \text{(B.49)}$$

This leads to following expression for the area radius *r*, using expression (B.37) for the surface :

$$r = \frac{1}{\pi\rho^2}\int_0^{\rho} 2\pi x\left[1 + \left(\frac{\partial z}{\partial x}\right)^2\right]^{1/2} dx = \frac{4\pi z_0}{x_0\rho^2}\int_0^{\rho}\sqrt{\frac{x_0^2 x^2}{4\pi^2 z_0^2} + x^2\sin^2\left(\frac{2\pi x}{x_0}\right)}dx \quad \text{(B.50)}$$

Solving (B.50) directly using a quadrature formulation for the numerical integration, is numerically instable. Therefore, the non-dimensional droplet diameter κ is introduced :

$$\kappa = \frac{\rho}{x_0} \,. \quad \text{(B.51)}$$

Using following transformation :

$$y = x \Big/ x_0 \,, \quad \text{(B.52)}$$

the expression for the area ratio is transformed to :

$$r = \frac{4\pi\left(z_0/x_0\right)}{\kappa^2}\int_0^{\kappa}\sqrt{\frac{y^2}{4\pi^2\left(z_0/x_0\right)^2} + y^2\sin^2\left(2\pi y\right)}dy \quad \text{(B.53)}$$

During the integration, κ is limited to a certain number (e.g. 10) to improve the numerical stability. This prevents the integration aborting early due to excessive function evaluations.

Now, for each value of ϕ in the interval $[\phi_{\min}, \phi_{\max}]$, the surface energy (B.47) can be evaluated using the expressions (B.48) and (B.53).

In Figure B.2 and Figure B.3, the effect of the limitation on the non-dimensional droplet diameter is illustrated. When the original formulation (B.50) is used, the solution of the area ratio does not converge. As a result, the random number, obtained at the last iteration of the specified number of allowed iteration, will be reported by the algorithm. These results are shown in Figure B.2. In Figure B.3 the converged solution is shown, using the reformulated expression for the area ratio *r*.

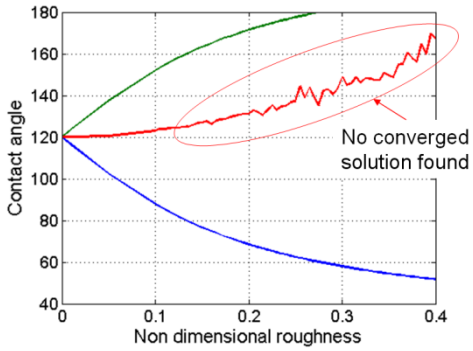

Figure B.2. Solution of the surface roughness model using the original formulation.

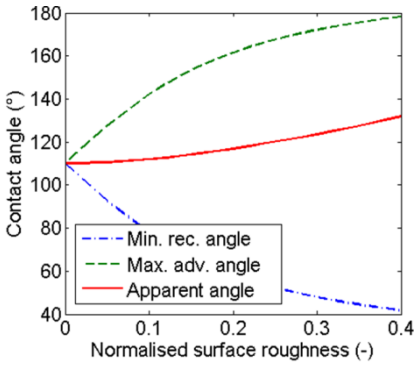

Figure B.3. Solution of the surface roughness model using the limitation of the non-dimensional droplet radius.

Appendix C: Teflon coating procedure

This appendix describes the procedure to apply a Teflon AF1600 coating on a sample. First, the initial cleaning of the tools and substrate is specified. Next, the surface preparation of the sample to improve adhesion is discussed in Step 3. In Step 4, the spinning parameters for the spin coating are listed. And finally in Step 5, the programming of the vacuum oven to cure the Teflon and evaporate the solvent is listed.

1) Wafer Case and Tweezers Clean

a. Solvent clean
   i. Place the wafer cases and tweezers in an acetone bath for 10 minutes
   ii. Place the wafer cases and tweezers in a methanol bath for 2-3 minutes
   iii. Rinse with DI water (optional)
   iv. Dry with N_2
b. Diluted Piranha Clean (4/5 H_20 + 1/20 H_2O_2 + 3/20 H_2SO_4)
   i. Add 80 mL of DI water to a glass beaker
   ii. Add 5 mL of 30% Hydrogen Peroxide (H_2O_2)
   iii. Slowly add 15 mL of 96% Sulfuric Acid (H_2SO_4) while gently shaking beaker to stir solution
   iv. Place case/tweezers in solution for 10 minutes
   v. Pour waste in acid drain under running water
c. Rinse in overflow bath

2) Wafer Clean

a. Solvent clean
   i. Place the wafer in an acetone bath for 10 minutes
   ii. Place the wafer in a methanol bath for 2-3 minutes
   iii. Rinse with DI water (optional)
   iv. Dry with N_2
b. Piranha Clean (1/4 H_2O_2 + 3/4 H_2SO_4)
   i. Add 15 mL of 30% Hydrogen Peroxide (H_2O_2) to a glass beaker
   ii. Slowly add 45 mL of 96% Sulfuric Acid (H_2SO_4) while gently shaking beaker to stir solution
   iii. Place sample into solution and remove after 10 minutes
   iv. Pour waste into acid drain under running water
c. Rinse in overflow bath
d. Standard Clean (1/5 H_20_2 + 3/5 H_20 + 1/5 NH_4OH)
   i. Add 30 mL of DI water to a glass beaker
   ii. Add 10 mL of 29% Ammonium Hydroxide (NH_4OH)
   iii. Heat to 70°C ± 5°C on a hot plate
   iv. Remove from hot plate
   v. Add 10 mL of 30% Hydrogen Peroxide (H_2O_2).
   vi. Wait 1 to 2 minutes
   vii. Add sample and remove after 10 minutes
   viii. Pour waste into acid drain under running water

e. Rinse in overflow bath

3) Silanisation

a. Dry sample using the N_2 gun and place in an oven for a few minutes
b. Place in UV/O_3 oven for 15 minutes
    i. Vent with N_2 for 30 seconds before opening oven
c. Prepare silanisation solution 5 minutes before end of UV/O_3
    i. Pour 300 mL of Ethanol into a glass beaker
    ii. Add 15 mL of DI water
    iii. Add 600 µL of 1/3 diluted acetic acid
    iv. Add 6 mL of FluoroSyl Mono silane 660-4 (from Cytonix) and flush bottle with N_2 before closing it. Place solution back in the refrigerator.
d. Silanise wafer
    i. Add sample to prepared solution and remove after 5 minutes
    ii. Rinse sample with Ethanol and dry with N_2 gun
    iii. Bake at 105°C in N_2 oven

4) Teflon Spin

a. Dehydration on hot plate at 110 °C
b. Spin Teflon
    i. 1000 rpm for 30 sec for 1.65 µm coating

5) Bake in Vacuum Oven

a. Place samples in oven and open valve for vacuum.
b. After a vacuum is achieved, open the valves for the nitrogen and allow the pressure to reach ambient.
c. Run the following program

Hb V: 2	rmP.U: min	dwL.U: min	CYC.n: 1
SEG.n: 1	tYPE: rmP.t	Hb: Lo	tGt: 160 dur: 30
SEG.n: 2	tYPE: dwell	Hb: Lo	dur: 20
SEG.n: 3	tYPE: rmP.t	Hb: Lo	tGt: 330 dur: 30
SEG.n: 4	tYPE: dwell	Hb: Lo	dur: 10
SEG.n: 5	tYPE: StEP	Hb: Hi	tGt: 20
SeG.n: 6	tYPE: End	End.t: Stop	

Appendix D: Thermal performance of single phase microchannel flow

The reference case for liquid cooling of electronic components is continuous single-phase liquid flow. The continuous liquid flow is circulated through a microchannel cooler by means of a separate feed pump. Optimisation algorithms are derived for this continuous liquid cooling case (Stevens 2006, 2007). Using that approach, the overall thermal performance of the system can be assessed by estimating the total thermal resistance and the required pumping power. In this way, the thermal performance can be compared to the droplet based cooling system.

Thermal performance analysis of a continuous flow

For the analysis a microchannel heat sink is considered for the cooling of a 10 mm x 10 mm chip that dissipates a heat flux of 100 W. The geometrical parameters of this heat sink are shown in the left hand side of Figure D.1. The allowable pressure drop along the channels is 0.6 bar. The heat transfer and pressure drop analysis are developed under the following assumptions. The heat sink is made of silicon (k = 148 W/mK). Water is used as coolant with constant thermal properties evaluated at room temperature (ρ = 997 kg/m^3, μ = 8.55·10^{-4} Ns/m^2, c_p = 4179 J/kgK and k = 0.613 W/mK). The flow is incompressible and enters the microchannels with a prescribed temperature (T_{in} = 20°C).

In order to assess the overall performance the main counteracting heat transfer phenomena are evaluated leading to a rough estimate for the optimal channel hydraulic diameter, the total thermal resistance and the required pumping power as function of the pressure drop. The thermal resistance of the heat sink consists of the caloric and the convective part:

$$R_{tot} = R_{cal} + R_{conv} \tag{D.1}$$

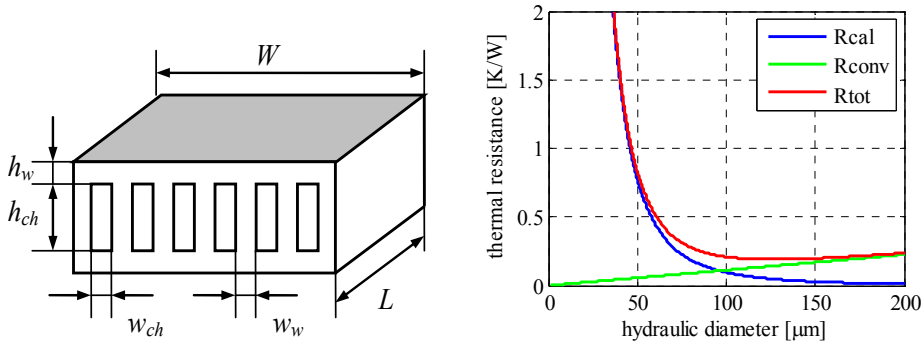

Figure D.1. Heat sink geometrical design parameters (left), Optimal hydraulic diameter for α = 1 and Δp = 0.6 bar (right).

The maximal heat transfer removal is on the one hand determined by the caloric capacity of the coolant given by

$$Q_{cal} = \dot{M} c_p (T_{out} - T_{in}) \tag{D.2}$$

where $\dot{M}$ is the total mass flow through the heat sink, c_p the specific heat of the coolant and T_{in} and T_{out} the inlet and outlet coolant temperature respectively. The average coolant velocity u is determined by the maximum allowable pressure drop Δp along the channels. The velocity u can be obtained from

$$u = \frac{2\,\Delta p\, D_h^2}{\mu\, L\, f\, \mathrm{Re}_D} \tag{D.3}$$

where f is the Darcy friction factor and Re_D the Reynolds number. For fully developed laminar flow $f \cdot Re_D$ equals the Darcy friction factor constant C_{fRe}. The mass flow through the heat sink $\dot{M}$ is determined by the coolant density ρ, the number of parallel channels in the heat sink n, the mean coolant velocity u and the channel dimensions

$$\dot{M} = \rho n w_{ch} h_{ch} u \tag{D.4}$$

The width and height of the channel can be related to the hydraulic diameter using the aspect ratio α. The caloric thermal resistance is then

$$R_{cal} = \frac{(T_{out} - T_{in})}{Q_{cal}} = \frac{2\alpha}{\rho n (1+\alpha)^2} \frac{\mu L C_{f\,\mathrm{Re}}}{\Delta p D_h^4 c_p}\,. \tag{D.5}$$

On the other hand, assuming a constant heat flux to the channel, the convective heat transfer to the coolant

$$Q_{conv} = hA(T_{\max} - T_{out}) \tag{D.6}$$

is determining the total cooling capacity of the system. Here, $h = Nu.k/D_h$ is the convective heat transfer coefficient, Nu the Nusselt number and k the thermal conductivity of the coolant. T_{out} and T_{max} are the coolant outlet temperature and the maximal chip temperature respectively. A is the available area for heat transfer. The convective resistance can be expressed as follows:

$$R_{conv} = \frac{(T_{\max} - T_{out})}{Q_{conv}} = \frac{\alpha}{Nu\; k\; L\; n\; (1+\alpha)^2} \tag{D.7}$$

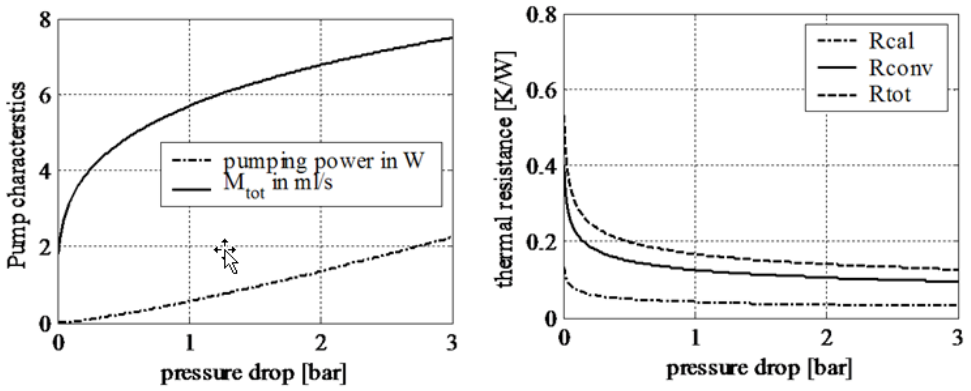

Figure D.2. Pumping power and total mass flow through the cooler as a function of pressure drop for α = 1 (left). Total thermal resistance as a function of pressure drop for square channels (right).

The total thermal resistance of the heat sink becomes the series connection of the caloric and convective thermal resistances as obtained by equations (D.5) and (D.7). Now, the thermal resistance can be evaluated as function of the pressure drop. The right hand side of Figure D.2 shows the evolution of the caloric and convective thermal resistance as function of the pressure drop for square channels. For an increasing pressure drop, the average velocity u, and consequently the flow rate will increase. This increase in pressure drop results in a decrease in the thermal resistance, and thus an enhancement of the cooling performance. However, this comes at the cost of an increased required pumping power W_p. This power can be expressed as follows:

$$W_p = \frac{\dot{M}\Delta p}{\rho} \tag{D.8}$$

The left hand side of Figure D.2 shows the evolution of the flow rate and the required pumping power as function of the pressure drop. The power dissipation at 0.6 bar pressure difference amounts to 300 mW at a total volumetric flow of 5 ml/s. This high power consumption and relatively high pressure drops remain critical issues especially with respect to reliability and control of the cooling system, despite the promise of achieving very low thermal resistances.

References

Acikalin, T.; Wait, S.; Garimella, S.V.; Raman, A., 2004, Experimental Investigation of the Thermal Performance of Piezoelectric Fans, Heat Transfer Eng., Vol. 25, pp. 4-14.

Ahmadi, A.; Nichols, J.; Hoorfar, M.; Najjaran, H.; Holzman, J., 2009, Proc. Of SPIE Def., Sec. and Sens. Conf. 7318, Orlando, Florida.

Armani, M.; Chaudhary, S.; Probst, R.; Walker, S.; Shapiro, B., 2005, Int. J.Robust Nonlinear Control 15, pp. 785-803.

Armani, M.; Walker, S.; Shapiro, B., 2005, Proceedings of the 13th Med.Conf. on Cont. and Aut., Limassol, Cyprus, pp. 131-138.

Arnault, J.; Saada, S.; Nesladek, M.; Williams, O.; Haenen, K.; Bergonzo, P. and Osawa, E., 2008, Diamond nanoseeding on silicon: stability under H2 MPCVD exposures and early stages of growth, Diamond and Related MaterialsVol. 17(7-10), pp. 1143-1149.

Azar, K., 2003, Cooling Technology Options, Part 2, Electronics cooling, Vol. 9(4).

Baelmans, M.; Oprins, H.; Stevens, T.; Rogiers, F., 2007, Digital and continuous liquid cooling for electronic systems, Proceedings of 8th. Int. Conf. on Thermal, Mechanical and Multiphysics Simulation and Experiments in Micro-Electronics and Micro-Systems, EuroSimE, London, UK, April 16-18, 2007, pp. 685-691.

Bahadur, V.; Garimella, S.V., 2006, An energy-based model for electrowetting-induced droplet actuation, J. Micromech. Microeng. 16, pp. 1494-1503.

Baret, J.C.; Seemann, R.; Decre, M.; and Herminghaus, S., 2005, Electroactuation of fluid using topographical wetting transitions, Langmuir, Vol. 21, no. 26, pp. 12218-12221.

Bash, C. *et al.*, 2003, Inkjet Assisted Spray Cooling of Electronics, IPACK2003, Maui, HI, Paper# 35058.

Bejan, A., 2004, Convection Heat Transfer, Wiley, ISBN 0471271500.

Beratlis, N. and Smith, M., 2003, Optimization of Synthetic Jet Cooling for Micro-electronics Applications, Proceedings of 19th SemiTherm Symposium, San Jose, CA, pp. 66-73.

Berge, B.; Peseux, J., 2000, Variable focal lens controlled by an external voltage: an application of electrowetting, Eur. Phys. J. E 3, pp. 159-163.

Berthier, J.; Dubois, P.; Clementz, P.; Claustre, P.; Peponnet, C.; Fouillet, Y., 2007, Sens. Actuators A 134, pp. 471-479.

Bhattacharjee, B.; Najjaran, H., 2010, Droplet position control in digital microfluidic systems, Biomed Microdevices. 2010 Feb;12(1):115-24.

Blake, T.D., 2006, The physics of moving wetting lines, J. Colloid Interface Sci 299:1-13.

Bonn D.; Eggers J.; Indekeu J.; Meunier J. and Rolley E., 2009, Wetting and spreading, Review of Modern Physics, Vol. 81, pp. 739-805.

Brunschwiler, T. *et al.*, 2006, Direct Liquid Jet-Impingment Cooling With Micron-sized Nozzle Array and Distributed Return Architecture, The Tenth Intersociety Conference on Thermal and Thermomechanical Phenomena in Electronics Systems, ITHERM '06, 30 May-2 June 2006, pp.196-203.

Cahill, B.P.; Giannitsis, A.T.; Gastrock, G.; Min, M. and Beckmann, D., 2008, A Dynamic Electrowetting Simulation using the Level-Set Method, Proceedings of the COMSOL Conference 2008 Hannover.

Cassie, A.B.D.; Baxter, S., 1944, Transactions of the Faraday Society, Vol. 40, pp. 546-551.

Chakrabarty, K.; and Su, F., 2006, Digital Microfluidic Biochips: Synthesis, Testing, and Reconfiguration Technique, CRC Press, Boca Raton, FL.

Chang, Y.-H.; Lee, G.B.; Huang, F.C.; Chen, Y.Y.; Lin, J.L., 2006, Integrated polymerase chain reaction chips utilizing digital microfluidics, Biomedical Microdevices, 8, pp. 215-225.

Chatterjee, D.; Hetayothin, B.; Wheeler.; AR, King.; DJ, Garrell, RL, 2006, Droplet-based microfluidics with nonaqueous solvents and solutions, Lab on a Chip, 6 (2), 199-206.

Chen, J.H.; Hsieh, W.H., 2006, Electrowetting-induced capillary flow in a parallel-plate channel. J. Colloid Interface Sci 296:276-283.

Chen, N.; Kuhl, T.; Tadmor, R.; Lin, Q. and Israelachvili, J., 2004, Large Deformations during the Coalescence of Fluid Interfaces, J. N. 2004 Phys. Rev. Lett. 92, 024501.

Cho, S.; Moon, H.; Kim, C.-J., 2003, Creating, transporting, cutting and merging liquid droplets by electrowetting-based actuation for digital microfluidic circuits, J. microelectromech. Syst., Vol. 12, pp. 70-80.

Colgan, E. *et al.*, 2005, A Practical Implementation of Silicon Microchannel Coolers for High Power Chips, Proceedings of 21st SemiTherm Symposium, San Jose, CA, 2005, pp. 1-7.

Cotler, A. *et al.*, 2004, Chip-Level Spray Cooling of an LD-MOSFET RF Power Amplifier, IEEE CPT Trans., Vol. 27, pp. 411-416.

Danneels, J.; Van Ham, B., 2006, Stroming en warmteoverdracht in electrostatisch aangedreven vloeistofdruppels voor electronicakoeling, MSc Dissertation, K.U. Leuven (advisor: prof. M. Baelmans)

de Gennes, P.-G.; Brochard-Wyart, F. and Quere, D., 2004, Capillarity and Wetting Phenomena, Springer, New York.

Decamps, C.; De Coninck, J., 2000, Dynamics of spontaneous spreading under electrowetting conditions, Langmuir 16:10150-10153.

Dussan, E.B., 1977, Immiscible liquid displacement in a capillary tube: the moving contact line, AlChe J. 23, 131.

Extrand, C.W. and Kumagai, Y., 1995, Liquid drops on an inclined plane: The relation between contact angles, drop shape and retentive force, J. Colloid and Interface Sci. 170:515-521.

Faghri, A., 1995. Heat Pipe Science and Technology, US: Taylor and Francis.

Ferziger, J.H.; Peric, M., 1997, Computational Methods for Fluid Dynamics, Springer Verlag, Berlin, pp.59-61.

Fouillet, Y.; Achard, J.L., 2004, Digital microfluidic and biotechnology, C. R. Phys. 5, pp. 577-588.

Gambill, W.R. and Lienhard, J.H., 1989, An Upper Bound for the Critical Boiling Heat Flux, J. of Heat Transfer, Vol. 111, pp. 815-818.

Garimella, S.V. and Sobhan, C.B., 2003, Transport in microchannels - A critical review, Annual Review of Heat Transfer, Vol. 13, pp. 1-50.

Garimella, S.V., 2000, Heat transfer and flow fields in confined jet impingement. Annual Review of Heat Transfer, Vol. XI, pp. 413-494.

Ghosal, U. *et al.*, 2005, High Performance Liquid Metal Cooling Loops, IEEE Semi-Therm 21, San Jose, March 15-17, pp. 16-19.

Gong, J. and Kim, C.-J., 2006, Proc. of 10th Int. Conf. on Min. Systems for Chem. and Life Sci., Tokyo, 1046–1048.

Guyer, E., 1999, Handbook of applied thermal design, CRC press.

Haenen, K.; Lazea, I.; Barjon, J.; D'Haen, J.; Habka, N.; Teraji, T.; Koizumi, S. and Mortet, V., 2009, P-doped diamond grown on (110)-textured microcrystalline diamond: growth, characterization and devices, Journal of Physics: Condensed Matter Vol. 21(36), p. 364204 (10pp).

Hayes, R.A. and Feenstra, B.J., 2003, Video-speed electronic paper based on electrowetting Nature 425, pp. 383-385.

Hectors, D. and Huybrechts, K., 2003, Vloeistofkoeling van elektronicacomponenten door middel van elektrostatisch aangedreven druppels, Thesis, Dept. Werktuigkunde, KULeuven.

Heikenfeld, J. and Steckl, A.J., 2005, High-transmission electrowetting light valves, Appl. Phys. Lett. Vol. 86, pp.151121.

HyperCool-IT project, 2008-2010, SBO project 060830 sponsored by the "Agentschap voor Innovatie door Wetenschap en Technologie in Vlaanderen" (IWT), Belgium, www.hypercool-it.be/

ITRS 2009 Roadmap (www.itrs.net)

Iverson, B.D.; Garimella, S.V., 2008, Recent advances in microscale pumping technologies: a review and evaluation, J. Microfluid. Nanofluid 5:45-174.

Johnson, J.L.; Tan, L.-K., 2004, Metal Injection Molding Of Heat Sinks, Electronics cooling, 10/4.

Johnson, R.E. and Dettre, R.H., 1964, Study of an Idealized Rough Surface, in Contact Angle, Wettability and Adhesion, Washington, DC: American Chemical Society, p. 112.

Jones, B., 2002, On the Relationship of Dielectrophoresis and Electrowetting, *Langmuir*, 2002, 18 (11), pp 4437–4443.

Kakaç, S. *et al.*, 1987, Handbook of single-phase convective heat transfer, Wiley-Interscience, New York.

Kandlikar, S.G. and Grande, W.J., 2004, Evaluation of Single Phase Flow in Microchannels for High Heat Flux Chip Cooling - Thermohydrolic Performance Enhancement and Fabrication Technology, Heat Transfer Engineering, Taylor Francis Inc. 25(8).

Keshavarz-Motamed, Z.; Kadem, L.; Dolatabadi, 2009, A., Effects of dynamic contact angle on numerical modeling of electrowetting in parallel plate microchannels, Journal of Microfluidics and Nanofluidics, DOI 10.1007/s10404-009-0460-3.

Kim, J. and Golliher, E., 2002, Steady State Model of a Micro Loop Heat Pipe, Proceedings of 18th SemiTherm Symposium, San Jose, CA, pp. 137-144.

Klingner, A.; Herminghaus, S.; Mugele, F., 2003, Self-excited oscillatory dynamics of capillary bridges in electric fields, Applied Physics Letters, 82, pp. 4187-4189.

Kuiper, S. and Hendriks, B.H.W., 2004, Variable-focus liquid lens for miniature cameras, Appl. Phys. Lett. 85, pp. 1128-1130.

Lasance, C., 2005, Advances In High-Performance Cooling For Electronics, Electronics Cooling, November 2005.

Laser, D.J.; Santiago, J.G., 2004, A review of micropumps. J. Micromech. Microeng 14(6):35-64.

Lee, J.; Kim, C.-J., 2000, Surface-tension-driven microactuation based on continuous electrowetting, J. Microelectromech. Syst., Vol. 9, pp. 171-180.

Linde Sanchez, A., , 2008, Fabrication of Super-hydrophobic Surfaces MSc Dissertation.

Lu, H.-W.; Bottausci, F.; Bertozzi, A.L.; Meinhart, C.D. and Kim, C.-J., 2008, PIV Investigation of 3-dimensional flow in drops actuated by EWOD, International Conference on Micro Electro Mechanical Systems (MEMS 2008), Vol. 2.

Mahajan, R.; Chia-pin Chiu Chrysler, G., 2006, Cooling a Microprocessor Chip, Proceeding of IEEE, Vol. 94, No. 8, August 2006, pp. 1476-1486.

Martin, 1977, Heat and Mass Transfer between Impinging Gas Jets and Solid Surfaces, Adv. Heat Transfer, Vol. 13, pp. 1-60.

Miner and Ghosal, U., 2004, Cooling of High-Power Density Microdevices Using Liquid

Metal Coolants, Appl. Phys. Lett., Vol. 85, pp. 506-508.

Mohseni, K. and Baird, E., 2007, Digitized heat transfer using electrowetting on dielectric. Nanoscale and Microscale Thermophysical Engineering, 11(1 & 2), pp. 99 – 120.

Mohseni, K., 2005, Effective cooling of integrated circuits using liquid alloy electrowetting, Proceedings of 21st SEMITHERM Symposium, San Jose USA, pp. 20-25.

Moore, G., 1965, Cramming more components onto integrated circuits, Electronics Vol. 38, pp. 114-117.

Mugele, F.; Baret, J.-C., 2005, Electrowetting: from basics to applications, J. Phys.: Condens. Matter 17**,** R705-R774.

Munson, B. R.; Young, D.F.; Okiishi, T.H., 2002, Fundamentals of fluid dynamics, 5th Edition, Wiley.

Nguyen, N.-T.; Huang, X.; Chuan, T.K., 2002, MEMS-micropumps: a review. J. Fluids Eng Trans ASME 124(2):384-392.

Nisar, A.; Afzulpurkara, N.;, Mahaisavariyaa, B.; Tuantranonta, A.; 2008, MEMS-based micropumps in drug delivery and biomedical applications, Sensors and Actuators B: Chemical, Vol 130(2), Pages 917-942.

Oprins, H.; Danneels, J.; Van Ham, B.; Vandevelde, B.; Baelmans, M., 2008, Convection heat transfer in electrostatic actuated liquid droplets for electronics cooling, Microelectronics Journal, 39 (7), pp. 966-974.

Oprins, H.; Danneels, J.; Van Ham, B.; Vandevelde, B.; Baelmans, M., 2007, Convection heat transfer in electrostatic actuated liquid droplets for electronics cooling, Proceedings of THERMES II 2007 (Thermal challenges in next generation electronic systems), Santa Fe, New Mexico, pp. 223-230, ed. S.V. Garimella and A.S. Fleischer, Millpress, Rotterdam, 2007, ISBN 978-90-5966-051-9.

Paik, P.Y.; Pamula, V.K. and Chakrabarty, K., 2004, Thermal effects on droplets transport in digital microfluidics with application to chip cooling, Inter Society Conference on Thermal Phenomena, pp. 649-654.

Paik, P.Y.; Pamula, V.K. and Chakrabarty, K., 2005, Droplet-based hot spot cooling using topless digital microfluidics on a printed circuit board, Proc. IEEE Int. Workshop on Thermal Investigations of ICs and Systems 2005, Belgirate, Lake Maggiore, Italy.

Palm, B., 2001, Heat Transfer in Microchannels, Microscale Thermophysical Engineering 5:155-175, Taylor Francis.

Pamula, V.K.; Chakrabarty K., 2003, Cooling of integrated circuits using droplet-based microfluidics, Proceedings of AOM Great Lakes Symposium on VLSI, pp. 84-87.

Patankar, N., 2003, On the modeling of hydrophobic contact angles on rough surfaces, Langmuir, Vol. 19, pp. 1249-1253.

Patankar, N.; Chen, Y., 2002, Numerical simulation of droplet shapes on rough surfaces, Nanotech 2002, Vol. 1, pp. 116-119.

Peterson, G.P., 1994, An Introduction to Heat Pipes, Canada: John Wiley and Sons, Inc.

Peterson, M.; Fisher, T.; Garimella, S.V. and Schlitz, D., 2003, Experimental Characterization of Low Voltage Field Emission from Carbon-Based Cathodes in Atmospheric Air, Proceedings of IMECE'03, Paper #41775.

Pollack, M.G. *et al.,* 2002, Electrowetting-based actuation of droplets for integrated microfluidics, The royal society of chemistry, Lab Chip, Vol. 2, pp. 96-101.

Pollack, M.G.; Fair, R.B. and Shenderov, A.D., 2000, Electrowetting-based actuation of liquid droplets for microfluidic applications Appl. Phys. Lett. 77, pp. 1725-1726.

Quilliet, C. and Berge, B., 2001, Electrowetting: A recent outbreak Curr. Opin. Colloid Interface Sci. 6 (1).

Quinn A., Sedev R., Ralston J., 2005 Contact Angle Saturation in Electrowetting, J. Phys. Chem. B, Vol. 109 (13), pp 6268–627.

Ren, H.; Fair, R.B.; Pollack, M.G., 2004, Sens. Actuators B 98, pp. 319-327.

Ren, H.; Fair, R.B.; Pollack, M.G.; Schayghnessy, E.J., 2002, Dynamics of electrowetting droplet transport, Sensors and Actuators B 87, pp. 201-206.

Ricks-Laskoski, H.L.; Snow, A.W., 2006, Synthesis and Electric Field Actuation of an Ionic Liquid Polymer, J. Am. Chem. Soc., 128, pp. 12402-12403.

Saeki, F.; Baum, J.; Moon, H.; Yoon, J.-Y.; Kim, C.-J.; Garrell, R.L., 2001, Electrowetting on Dielectrics (EWOD): Reducing Voltage Requirements for Microfluidics, Polym. Mater. Sci. Eng., 85:12-13.

Sagiv, J., 1980, Organized monolayers by adsorption. 1. Formation and structure of oleophobic mixed monolayers on solid surfaces, J. Am/ Chem. Soc., 102(92).

Salenbien R., Glorieux C., Janssens S., Mortet V., Haenen K., 2009, Determination of the thermo-elastic properties of thin nanocrystalline CVD diamond films for heat spreading applications, Therminic 2009

Seemann, R.; Brinkmann, M.; Kramer, E.J.; Lange, F.F.; Lipowsky, R., 2005, Wetting morphologies at microstructured surfaces, Proc Natl Acad Sci U S A.; 102(6): 1848–1852.

Shah, R.K. and Bhatti, M.S., 1987, "Laminar Convection Heat Transfer in Ducts," in, H*andbook of Single-Phase Convective Heat Transfer*, S. Kakac, R.K. Shah and W. Aung, eds., Wiley, 1987.

Shapiro, B.; Moon, H.; Garrell, R.L. and Kim, C.-J., 2003, Equilibrium behaviour of sessile drops under surface tension, applied external fields, and material variations, J. Appl. Phys. 93, pp. 5794-5811.

Sharma, P.K.; Hanumantha Rao, K., 2002, Analysis of different approaches for evaluation of surface energy of microbial cells by contact angle goniometry, Advances in colloid and interface science, Vol. 98, no 3, pp. 341-463.

Shedd, T.A., 2007, Fundamental Behaviors and Limits of Impingement Cooling, SEMI-THERM 2007, pp. 179-183.

Shikhmurzaev, Y.D., 1993, The moving contact line on a smooth solid surface, Int. J. Multi-Phase Flow 19:589-610.

Singhal, V.; Garimella, S.V.; Raman, A., 2004, Microscale pumping technologies for microchannel cooling systems. Appl. Mech. Rev. 57(16):191-221.

Soong, C.Y.; Tzeng, P.Y., 1996, Numerical study on mode-transition of natural convection in differentially heated inclined enclosures, International Journal of Heat Mass Transfer 39, pp. 2869-2882.

Srinivasan, V.; Pamula, V.K.; Fair, F.B., 2004, An integrated digital microfluidic lab-on-a-chip for clinical diagnostics on human physiological fluids, Lab Chip, Vol. 4.

Stevens, T.,; Rogiers, F.; Baelmans, M., 2006, Optimization of micro-channel heat sink geometry, International Heat Transfer Conference ,Sidney, Australia date: Aug 13-18, 2006.

Stevens, T.; Rogiers, F.; Delport, S.; Vleugels, P.; Peirs, J.; Baelmans, M., 2007, Collector pressure losses in micro heat exchangers, Thermal Issues in Emerging Technologies, ThETA 1, Cairo, Egypt, Jan 3-6th 2007.

Stratton, J.A., 1941, Electromagnetic Theory, McGraw-Hill Book Company, New York and London.

Torkkeli, A., 2003, Droplet microfluidics on planar surface, ISBN 951-38-6237-2.

Torkkeli, A.; Saarilahti, J.; Haara, A.; Harma, H.; Soukka, T.; Tolonen, P., 2001, Electrostatic transportation of water droplets on superhydrophobic surfaces, 14th Int. IEEE Conf. on MEMS, 475-8.

Tuckerman, D.B. and Pease, R.F.W., 1981, High performance heat sinking for VLSI, IEEE Electron Device Letters, Vol. EDL-2, pp. 126-129.

Vallet, M.; Vallade, M. and Berge, B., 1999, Limiting phenomena for the spreading of water on polymer films by electrowetting Eur. Phys. J. B 11, pp. 583-591.

Van der Veken G. , 2005, Cooling by means of electro-static actuated liquid flow through micro channels, MSc Dissertation, K.U. Leuven (advisor: prof. M. Baelmans)

Verheijen, H.J.J. and Prins, M.W., 1999, Reversible electrowetting and trapping of charge: model and experiments, Langmuir 15, pp. 6616-6620.

Verplaetsen, F., 1999, Film boiling in the presence of an electric field, PhD thesis, KULeuven.

Verplaetsen, F.; Berghmans, J., 1997, Study of the influence of an electric field on the liquid-vapour interface during film boiling of stagnant fluids, IEEE Transactions on Industry Applications, Vol. 33 (6), pp. 1512-1518.

Walker S.; Shapiro B., 2006, Modeling the Fluid Dynamics of Electro-Wetting On Dielectric (EWOD), Journal of Microelectromechanical Systems, Vol 15, (4), pp 986-1000.

Wang, H.; Hamed, M.S., 2006, Flow mode-transition of natural convection in inclined rectangular enclosures subjected to bidirectional temperature gradients, Int. Journal of Thermal Sciences 45, pp. 782-795.

Wang, K.-L. and Jones, T.B., 2005, Electrowetting Dynamics of Microfluidic Actuation, Langmuir 21 (9), pp. 4211-4217.

Washburn, E.W., 1921, The dynamics of capillary flow., Phys. Rev., 17(13):273.

Washizu, M., 1998, Electrostatic actuation of liquid droplets for microreactor applications, IEEE Transactions on industry applications, Vol. 34, pp. 732-737.

Webb, W. and Ma, C.F., 1995, Single-Phase Liquid Jet Impingement Heat Transfer, Adv. Heat Transfer, Vol. 26, pp. 105-217.

Wenzel, R.N., 1936, Industrial and Engineering Chemistry, Vol. 28, pp. 988-994.

White F.M., 2003, Fluid Mechanics, McGraw–Hill, ISBN 0072402172

Woias, P., 2005, Micropumps—past, progress and future prospects, Sensors Actuat B Chem 105(1):28-38.

Yang, S.; Krupenkin, T.N.; Mach, P. and Chandross, E.A., 2003, Tunable and latchable liquid microlens with photopolymerizable components, Adv. Mater. 15 (11), pp. 940-943.

Yeh, L.T. and Chu, R.C., 2002, Thermal Management of Microelectronic Equipment: Heat Transfer Theory, Analysis Methods and Design Practices, ASME Press, New York.

Yeo, L.; Chang, H.-C., 2008, Electrowetting. In Encyclopedia of Microfluidics and Nanofluidics (ed. D Li), pp. 600-606 (Springer, New York)

Yun, K.S.; Cho, I.J.; Bu, J.U.; Kim, C.-J.; Yoon, E., 2002, A surface-tension driven micropump for low-voltage and low-power operations, J. Microelectromech. Syst. 11, pp. 454-461.

Zhang, C.; Xing, D.; Li, Y., 2007, Micropumps, microvalves, and micromixers within PCR microfluidic chips: advances and trends. Biotechnol Adv 25(5):483-514.

Zienkiewicz, O.C.; Taylor, R.L., 1987, The Finite Element Method, 4th Edition, McGraw Hill, New York.

List of publications

Patent applications

P1. **Oprins H.**, Vandevelde B., Fiorini P., Beyne E., DEVICE FOR COOLING INTEGRATED CIRCUITS, European Patent Application No.: 10165504.1 - 1235, Filing Date: June 10, 2010.

Journal publications

J1. **Oprins, H.;** Danneels, J.; Van Ham, B.; Vandevelde, B.; Baelmans, M., 2008, Convection heat transfer in electrostatic actuated liquid droplets for electronics cooling, Microelectronics Journal, 39 (7), pp. 966-974.

J2. **Oprins, H.**; Nicole, C.C.S.; Van der Veken, G.; Baret, J.-C.; Lasance, C.; Baelmans, M., 2007, On-Chip Liquid Cooling with Integrated Pump Technology, IEEE Transactions on Components and Packaging Technologies, Vol 30. No 2, June 2007, pp. 209-217.

J3. Das, J.; **Oprins, H.**; Ji H.; Sarua, A.; Ruythooren, W.; Derluyn, J.; Kubal, M.; Germain, M.; Borghs, G., 2006, Improved Thermal Performance of AlGaN/GaN HEMTs by an Optimized Flip-Chip Design, IEEE Trans. Electron Devices, vol. 53 (11), Nov. 2006, pp. 2696-2702.

Accepted for publication:

J4. **Oprins, H**.; Srinivasan, A.; Cupak, M.; Cherman, V.; Torregiani, C.; Stucchi, M.; Vandevelde, B.; Van der Plas, G.; Marchal, P. and Cheng, E., Fine grain thermal modelling and expermintal validation of 3D-ICs, Microelectronics Journal, *accepted June 2010.*

J5. Van der Plas, G.; Limaye, P.; Mercha, A.; Loi,I; **Oprins, H.**; Torregiani, C.; Thijs, S.; Linten, D.; Stucchi, M.; Guruprasad, K.; Velenis, D.; Shinichi, D.; Cherman, V.; Vandevelde, B.; Simons, V.; De Wolf, I.; Labie, R.; Perry, D.; Bronckers, S.; Minas, N.; Cupac, M.; Ruythooren, W.; Van Olmen, J.; Phommahaxay, A.; de Potter de ten Broeck, M.; Opdebeeck, A.; Rakowski, M.; De Wachter, B.; Dehan, M.; Nelis, M.; Agarwal, R.; Dehaene, W.; Travaly, Y.; Marchal, P. and Beyne, E., Design issues and considerations for low-cost 3D TSV IC technology, IEEE Journal of Solid-State Circuits, *accepted May 2010.*

Publications in peer-reviewed international magazines

M1. **Oprins, H**., Baelmans, M., 2006, On-chip electrowetting cooling, Electronics Cooling Vol. 12(2), pp.16-20.

Conference publications in proceedings

C1. **Oprins, H.;** Vandevelde B.; Beyne, E.; Borghs, G.; Baelmans, M., 2004, Selective cooling of microelectronics using electrostatic actuated liquid droplets - modelling and experiments, Proceedings of the 10th International Workshop on THERMAL INVESTIGATIONS of ICs and Systems, Sophia Antipolis, France, 29 September - 1 October, 2004, pp. 207-212.

C2. **Oprins, H.**; Nicole, C.C.S.; Baret, J.-C.; Van der Veken, G.; Lasance, C.; Baelmans, M., 2005, On-Chip Liquid Cooling with Integrated Pump Technology, Proceedings of the IEEE Twenty First Annual IEEE Semiconductor Thermal Measurement and Management Symposium (SEMI-THERM), 15-17 March 2005, pp. 347 – 353.

C3. **Oprins, H.**; Danneels, J.; Van Ham, B.; Vandevelde, B.; Baelmans, M., 2007, Convection heat transfer in electrostatic actuated liquid droplets for electronics cooling, Proceedings of THERMES II 2007 (Thermal challenges in next generation electronic systems), Santa Fe, New Mexico, pp. 223-230, ed. S.V. Garimella and A.S. Fleischer, Millpress, Rotterdam, 2007, ISBN 978-90-5966-051-9.

C4. Baelmans, M.; **Oprins, H.**; Stevens, T.; Rogiers, F., 2007, Digital and continuous liquid cooling for electronic systems, Proceedings of 8th. Int. Conf. on Thermal, Mechanical and Multiphysics Simulation and Experiments in Micro-Electronics and Micro-Systems, EuroSimE, London, UK, April 16-18, 2007, pp. 685-691.

C5. Das, J.; Ruythooren, W.; Vandersmissen, R.; Derluyn, J.; **Oprins, H.**; Germain, M.; Borghs, M., 2004, AlGaN/GaN HEMTs: Removal of the Sapphire Substrate using Laser Lift-off, Proceedings of the International Workshop on Nitride Semiconductors, 19-23 July, Pittsburgh, Pennsylvania, USA, 2004.

C6. Das, J.; Ruythooren, W.; Vandersmissen, R.; **Oprins, H.**; Derluyn, J.; Germain, M.; Borghs, G., 2005, Hybrid integration of multi-finger HEMTs: a comparison between flip-chip and substrate removal, Proceedings of The 6th International Conference on Nitride Semiconductors, Bremen, Germany, August 28 – September 2, 2005.

C7. **Oprins, H.**; Das, J.; Vandersmissen, R.; Vandevelde, B.; Germain, M., 2005, Thermal analysis of multi-finger AlGaN/GaN hemts: comparison between flip-chip and substrate removal, Proceedings of the 11th International Workshop on THERMAL INVESTIGATIONS of ICs and Systems, Lake Maggiore, Italy, 27 September - 30 September, 2005, pp. 71-75.

C8. Chen, L.; **Oprins, H.**; Vandevelde, B.; Brizar, G.; Vanderstraeten, D.; Blansaer, E., 2005, Electro-thermal-mechanical analysis of a HiQuad package for high current and high power application, Proceedings of the 11th International Workshop on THERMAL INVESTIGATIONS of ICs and Systems, Lake Maggiore, Italy, 27 September - 30 September, 2005, pp: 173-178.

C9. Das, J.; **Oprins, H.**; Ruythooren, W.; Derluyn, J.; Germain, M.; Borghs, G.; Ji, H.; Sarua, A.; Kuball, M., 2006, A temperature analysis of high-power ALGAN/GAN HEMTS, Proceedings of the 12th International Workshop on THERMAL INVESTIGATIONS of ICs and Systems, Nice, France pp. 38-41, Sep. 2006.

C10. Vandevelde, B.; Brebels, S.; Okoro, C.; **Oprins, H.**; Chen, L.; Christiaens, W. and Vanfleteren, J., 2007, Embedding of chips in flex: a global optimization from thermal, mechanical and electrical RF perspective, Proceedings EMPC, Oulo, Finland, June 17-20, 2007, pp. 25-30.

C11. Gillon, R.; Joris, P.; **Oprins, H.;** Vandevelde, B.; Srinivasan, A.; Chandra, R., 2008, Practical chip-centric electro-thermal simulations, Proceedings of THERMINIC, 24-26 September 2008, Rome, Italy.

C12. Vanaverbeke, F.; Das, J.; Derluyn, J.; **Oprins, H.;** Schreurs, D.; Germain, M.; De Raedt, W., 2009, Layout-optimization of GaN chips, RWW2009, IEEE Topical Symposium on Power Amplifiers for Wireless Communications, January 19 and 20, 2009, San Diego, CA, USA.

C13. **Oprins, H.**; Cupak, M.; Van der Plas, G.; Vandevelde, B.; Marchal, P.; Srinivasan, A. and Cheng, E., 2009, Fine grain thermal modeling of 3D stacked structures, 15th International Workshop on Thermal inverstigations of ICs and Systems – THERMINIC, Leuven, 2009, pp 45-49.

C14. Torregiani, C.; **Oprins, H.**; Vandevelde, B.; Beyne, E. and De Wolf, I., 2009, Thermal analysis of hot spots in advanced 3D-stacked structures, 15th International Workshop on Thermal Investigations of ICs and Systems – THERMINIC, Leuven, 2009, 56-60.

C15. De Wolf, I.; Kalicinski, S.; De Coster, J. and **Oprins, H.**, 2009, Methods to measure mechanical properties of NEMS and MEMS: challenges and pitfalls, MRS: Probing Mechanics at Nanoscale Dimensions, 2009, *invited*.

C16. Torregiani, C.; **Oprins, H**.; Vandevelde, B.; Beyne, E. and De Wolf, I., 2009, Compact thermal modeling of hot spots in advanced 3D-stacked ICs, EPTC 2009.

C17. Van der Plas, G.; Limaye, P.; Mercha, A.; **Oprins, H.**; Torregiani, C.; Thijs, S.; Linten, D.; Stucchi, M.; Guruprasad, K.; Velenis, D.; Shinichi, D.; Cherman, V.; Vandevelde, B.; Simons, V.; De Wolf, I.; Labie, R.; Perry, D.; Bronckers, S.; Minas, N.; Cupac, M.; Ruythooren, W.; Van Olmen, J.; Phommahaxay, A.; de Potter de ten Broeck, M.; Opdebeeck, A.; Rakowski, M.; De Wachter, B.; Dehan, M.; Nelis, M.; Agarwal, R.; Dehaene, W.; Travaly, Y.; Marchal, P. and Beyne, E., 2010, Design Issues and Solutions for Low-cost 3D TSV IC Technology, ISSCC 2010.

C18. Minas, N.; Van der Plas, G.; **Oprins, H.**; Yang, Y.; Okoro, C.; Mercha, A.; Torregiani, C.; Perry, D.; Marchal, P. and Rakowski, M., Characterization of Thermal-Mechanical Stress in 3D Stacked IC for Analog Design, ICMTS (International Conference on Microelectronics Test Structures) 2010.

C19. Srinivasan, A.; **Oprins, H.**; Cheng, E. and Van der Plas, G., Thermal modeling and experimental validation of thermal effects in 3D-ICs, Design, Automation, and Test in Europe conference - 3D Integration Workshop, 2010.

C20. Cupak, M.; **Oprins, H.**; Van der Plas, G.; Marchal, P.; Vandevelde, B.; Srinivasan, A. and Cheng, E., A Practical Approach to Thermal Modeling and Validation of 3D-ICs, DAC 2010.

C21. Katti, G.; Mercha, A.; Stucchi, M.; Tokei, Zs. ; Velenis, D.; Van Olmen, J.; Huyghebaert, C.; Jourdain, A.; Rakowski, M.; Debusschere, I.; Soussan P.; **Oprins, H.**; Dehaene, W.; De Meyer, K.; Travaly, Y.; Beyne, E.; Biesemans, S.; Swinnen, B., Temperature dependent electrical characteristics of Through-Si-Via (TSV) interconnections, IITC 2010.

C22. Srivastava, P.; Das, J.; **Oprins, H.**; Van Hove, M.; Marcon, D.; Cheng, K.; Leys, M.; Decoutere, S.; Mertens, R. and Borghs, G., Self-heating assesment of GAN DHFEts using mono-lithically fabricated 2-DEG resistors, WOCSDICE 2010, Darmstadt, Germany.

Accepted for publication

C22. **Oprins, H.**; Cherman, V.; Torregiani, C.; Stucchi, M., Vandevelde, B. and Beyne, E., 2010, Thermal test vehicle for the validation of thermal modelling of hot spot dissipation in 3D stacked ICs, ESTC2010, *accepted April 2010*.

C23. **Oprins, H.**; Cupak, M.; Van der Plas, G.; Vandevelde, B.; Marchal, P.; Srinivasan, A. and Cheng, E., 2010, Experimental thermal characterisation and model validation of 3D stacked structures, 15th International Workshop on Thermal investigations of ICs and Systems – THERMINIC, Barcelona, 2010, *Accepted June 2010*.

C24. Van der Plas, G.; Thijs, S.; Linten, D.; Guruprasad, K.; Limaye, P.; Mercha, A.; Stucchi, M.; **Oprins, H.**; Vandevelde, B.; Minas, N.; Cupak, M.; M.; Nelis, M.; Agarwal, R.; Dehaene, W.; Travaly, Y.; Marchal, P. and Beyne, E., 2010, Verifying Electrical/Thermal/Thermo-mechanical behavior of a 3D stack – Challenges and Solutions, IEEE Custom Integrated Circuits Conference, September 19 – 22, 2010, San Jose, California, *Accepted June 2010*, *invited*.

Submitted

C25. **Oprins, H.**; Fiorini, P., De Vos, J.; Majeed, B., Vandevelde, B. and Beyne, E., 2010, Modeling, design and fabrication of a novel electrostatically actuated droplet based impingement cooler, PowerMEMS 2010.

Conference and workshop presentations – abstract only

C26. **Oprins, H.;** Danneels J.; Van Ham, B.; Vandevelde, B. and Baelmans, M., 2006, Selective cooling of microelectronics using electrostatic actuated liquid droplets, 5th International Electrowetting Workshop 2006, p.37, Rochester, NY, US, May 30 - June 2, 2006.

C27. **Oprins, H.**; Vandevelde, B. and Baelmans, M., 2007, Cooling of microelectronics using electrostatic actuated liquid droplets, 2nd Thermal management workshop IMAPS, January 31 –Februari 12, 2007, La Rochelle, France.

C28. **Oprins, H.;** Vandevelde, B., 2007, Extraction of thermal properties for electronics packages, NOESIS OPTIMUS World Wide User's Meeting, Leuven, Belgium, June 25 – 26, 2007.

C29. Marchal, P.; **Oprins, H.**; Torregiani, C.; Van der Plas, G.; Srinivasan, A.; Cheng, E., 2009, Modeling thermal and thermo- mechanical stress in 3D Chip stacks, Design for 3D Workshop, 2009.

C30. Beyne,E.; **Oprins,H.**, 2010, Compact thermal modeling of hot spots in 3Dstacked ICs, IMAPS Benelux Spring Event: Thermal and mechanical challenges in power electronics, 16 June, 2010, Eindhoven, Nederland.

C31. Minas, N.; De Wolf, I.; Marinissen, E.; Stucchi, M.; **Oprins, H.**; Mercha, A.; Van der Plas, G.; Velenis, D. and Marchal, P., 2010, 3D Integration: Circuit Design, Test and Reliability Challenges, IEEE International On-Line Testing Symposium IOLTS, 5-7 July 2010, Corfu, Greece.